

2001

Solid state NMR characterization of structural and motional parameter distributions in polyamidoammonium dendrimers

Dariya Ivanovna Malyarenko
College of William & Mary - Arts & Sciences

Follow this and additional works at: <https://scholarworks.wm.edu/etd>



Part of the [Atomic, Molecular and Optical Physics Commons](#), and the [Polymer Chemistry Commons](#)

Recommended Citation

Malyarenko, Dariya Ivanovna, "Solid state NMR characterization of structural and motional parameter distributions in polyamidoammonium dendrimers" (2001). *Dissertations, Theses, and Masters Projects*. Paper 1539623385.
<https://dx.doi.org/doi:10.21220/s2-rhmf-4724>

This Dissertation is brought to you for free and open access by the Theses, Dissertations, & Master Projects at W&M ScholarWorks. It has been accepted for inclusion in Dissertations, Theses, and Masters Projects by an authorized administrator of W&M ScholarWorks. For more information, please contact scholarworks@wm.edu.

**SOLID STATE NMR CHARACTERIZATION OF STRUCTURAL AND MOTIONAL
PARAMETER DISTRIBUTIONS IN POLYAMIDOAMMONIUM DENDRIMERS**

A Dissertation

Presented to

The Faculty of the Applied Science Department

The College of William and Mary in Virginia

In Partial Fulfillment

Of the Requirements for the Degree of

Doctor of Philosophy

by

Dariya Ivanovna Malyarenko

June 2001

UMI Number: 3026408

Copyright 2001 by
Malyarenko, Dariya Ivanovna

All rights reserved.

UMI[®]

UMI Microform 3026408

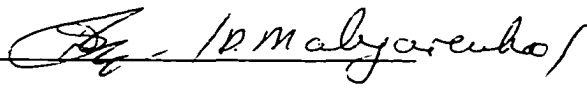
Copyright 2001 by Bell & Howell Information and Learning Company.
All rights reserved. This microform edition is protected against
unauthorized copying under Title 17, United States Code.

Bell & Howell Information and Learning Company
300 North Zeeb Road
P.O. Box 1346
Ann Arbor, MI 48106-1346

APPROVAL SHEET

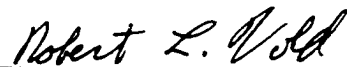
This dissertation is submitted in partial fulfillment of
the requirements for the degree of

Doctor of Philosophy

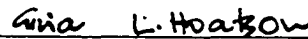


Dariya I. Malyarenko

Approved, June 2001



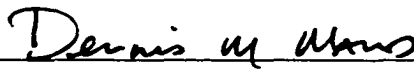
Robert L. Vold, Advisor



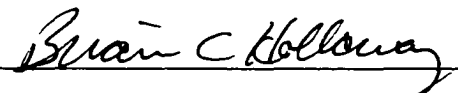
Gina L. Hoatson (Physics)



Robert A. Orwoll



Dennis M. Manos



Brian C. Holloway

To my mother, Svetlana, my father, Ivan, and to the memory of my grandmother, Zinaida

Contents

Acknowledgments	vii
List of Tables	ix
List of Figures	x
Abstract	xiii
1 Dendrimer Research	2
1.1 Motivation	3
1.2 Polyamidoamine Dendrimers	7
1.3 Theoretical and Experimental Investigations	9
1.4 Solid State NMR Experiments	11
1.5 Summary	15
2 NMR Background	17
2.1 Basic NMR Theory and Equipment	18
2.1.1 Spin 1/2 and Spin-1 Nuclei.....	20
2.1.2 Quantum Description and Density Matrix.....	22
2.1.3 NMR Spectrometer and Probe.....	30

2.2	Static Interactions	39
2.2.1	Zeeman Hamiltonian.....	40
2.2.2	Chemical Shielding.....	41
2.2.3	Dipolar Interaction.....	46
2.2.4	Quadrupole Interaction.....	49
2.3	Motion and Relaxation	52
2.3.1	Spectrum Averaging Under Magic Angle Spinning.....	55
2.3.2	Molecular Motion.....	59
2.3.3	Redfield Relaxation.....	63
2.4	Experimental Techniques and Pulse Sequences	66
2.4.1	Quadrupole Echo.....	68
2.4.2	Spin Lattice Relaxation Time Anisotropy.....	70
2.4.3	Deuteron Magic Angle Spinning.....	72
2.4.4	Cross Polarization Magic Angle Spinning.....	74
2.4.5	Rotational-Echo Double-Resonance.....	77
2.5	Summary	83
3	Hydrogen Bonding and Motion in PAMAM Salts	84
3.1	NMR Studies in the Glass Transition Region	85
3.2	Approximation of Fast Molecular Motion	89
3.2.1	Planar Libration.....	90
3.2.2	Fast Rotation and Cone Libration	92
3.3	Hydrogen Bonding	93
3.4	QE Lineshape Assignments	96
3.5	Experimental Results and Simulations	102
3.5.1	Distributions and Lineshapes.....	104
3.5.2	Temperature and Generation Dependence.....	109
3.5.3	Structural Parameters.....	116

3.6	Conclusions	120
4	Relaxation and Dynamics at Interior and Termini of PAMAM Dendrimer	122
4.1	Model Dependent Relaxation Anisotropies	124
4.1.1	SUMS vs. EXPRESS Lineshape Simulations.....	125
4.1.2	Anisotropies for Libration in a Plane and in a Cone.....	130
4.2	Log-Normal Rate Distribution	132
4.3	Unraveling Overlapping Anisotropies	133
4.3.1	Data Fitting Procedures.....	135
4.3.2	Relaxation Anisotropies at Spacers and Branching Sites.....	138
4.3.3	Overlapping Anisotropies Across Ammonium Powder Pattern.....	147
4.4	PAMAM Generation Dependent Kinetics	156
4.4.1	Planar Libration at Branching Sites.....	159
4.4.2	Planar Libration at Spacers.....	160
4.4.3	Fast Rotation of Ammonium Termini.....	162
4.5	Libration of Termini Characterized by ^2H MAS.....	165
4.5.1	Overlapping Side Bands	166
4.5.2	Librational Rate Distribution for Ammonium Termini	169
4.6	Rate Distribution Evolution During Glass Transition	173
4.7	Conclusions	175
5	REDOR Experiment and Analysis Optimization	179
5.1	Planning REDOR for PAMAM Dendrimers	180
5.1.1	^{13}C - ^{15}N Distance Estimation.....	180
5.1.2	Isotope Labeling Strategy.....	182
5.1.3	Observation of ^{13}C versus ^{15}N	183
5.2	Long Distance Measurement with REDOR	185
5.2.1	Reduction of Artifacts.....	186

5.2.2	Proton Decoupling.....	189
5.2.3	Natural Abundance Correction.....	191
5.3	Universal REDOR Curve Calculation	193
5.3.1	Phase Accumulation.....	193
5.3.2	REDOR Dipolar Transform.....	196
5.3.3	Planar Libration and Internuclear Distance Distribution.....	199
5.4	Experimental Results for Model Compounds	205
5.5	Summary	209
6	General Conclusions and Future Research	211
Appendix A	Derivation of Cartesian EFG Tensor Dependence on the Amplitude of Fast Planar Libration	215
Appendix B	T_{1z} Anisotropy Analysis Procedure for Multiple Overlapping Powder Patterns	217
Appendix C	Calculation of Trigonometric Sum in Eq. 5.5	224
	Bibliography	225
	Vita	232

Acknowledgments

This work would never have been completed without the constant support and encouragement of those whose help I would like to acknowledge here. I am grateful to my husband, Evgeniy, for not letting me quit at my most desperate moments and for caring for our family. I am thankful to my parents for enduring my long absence and coping with all the difficulties of their life by themselves; to my daughters, Antonina and Marina, for not being sick too often, sleeping through the nights and letting me take my time at work. I owe a special debt of gratitude to my scientific advisors: Professor Robert Vold, for sharing his ideas, knowledge and experience, being ever enthusiastic, teaching me patience and persistence in research; Professor Gina Hoatson, for providing experimental equipment, maintaining high standards for our research, being always patient, considerate and encouraging whenever I faced scientific or personal problems.

The first three years in the lab I was lucky to work with a wonderful person and knowledgeable graduate student, Sam Varner. I heartily thank him for the many times he would come to the lab, day or night, and help solve any problem, for teaching me basics of C-programming, UNIX system administration, and sharing his confidence. I am also much obliged to other graduate students from our NMR lab: Seregei Kudriavtsev, for building the third spectrometer channel and making REDOR experiments possible; Marco Brown, for showing that electronics can be made to do what it is supposed to. I am grateful to Donghua Zhou for the countless times he helped me to fill high pressure nitrogen cylinders for

temperature dependent experiments and for taking over system administration responsibilities in the lab and giving me peace of mind to write this dissertation; and to Yana Goddard for sharing responsibilities in the lab and being a thoughtful friend.

I appreciate attention, criticism and useful comments from my dissertation committee: Dr. Orwoll, Dr. Manos and Dr. Holloway. My sincere gratitude to Professor Bebout for introducing us to biochemistry and synthesizing doubly labeled CLG for REDOR experiments. I highly appreciate the dedicated work of our librarians, Patricia Hausman and Karen Berquist, thanks to whom there never has been a problem with a reference. I feel forever indebted to our friend, Karen, for helping us settle in Williamsburg, showing the beauties of Virginia and caring for our family like her own. I am thankful to all support staff, Sylvia, Dianne, Marcy and Kathee, for easing all encounters with bureaucracy, and to Ed, John, Kirk and Mel, for making many useful “gadgets”.

I would like to acknowledge Dendritech Inc. for providing free samples of the high generation dendrimers for our research, and Dr. Dvornic, for sharing unpublished results of extensive PAMAM studies. Thanks go to Dr. McDowell, Dr. Mueller and Fred Vogt for useful advice on the experimental details of REDOR during our personal communications, and to Dr. Gullion for showing us working REDOR experiment in his lab at West Virginia University.

List of Tables

3.1	Best Fit Quadrupole Coupling Parameters for Three Powder Patterns of Studied PAMAM Generations at Room Temperature	99
3.2	Best Fit Quadrupole Coupling Parameters for G2, 3, and 9 Experimental QE Spectra at $-30\text{ }^{\circ}\text{C}$ and $+45\text{ }^{\circ}\text{C}$	112
3.3	Fit Relative Intensities and Stoichiometric Expectations for PAMAM Powder Patterns	114
3.4	Fit Line Width and % Total Spectral Intensity for Gaussian and Lorentzian Components	115
3.5	Best Fit Parameters for Three Deuterated Sites of PAMAM Dendrimers	118
4.1	EXPRESS Fit Parameters for R_2ND Groups of All Studied Dendrimer Generations	144
4.2	EXPRESS Fit Parameters for R_3ND^+ Groups of All Studied Dendrimer Generations	145
4.3	EXPRESS Fit Parameters for RND_2^+ Groups of All Studied Dendrimer Generations	151
4.4	Integrated Fit Intensities of Lorentzian and Gaussian Components for All Studied Dendrimer Generations	153
4.5	Average Activation Energies, Logarithms of Collision Frequencies and Rates of Motion for Generation 2, 3 and 9 PAMAM Dendrimers	159
4.6	Best Fit Parameters for Temperature Dependent ^2H MAS Spectra of G2 PAMAM Dendrimer	171

List of Figures

1.1	Specific Deuteration Sites on a Branch of G1 PAMAM Dendrimer.....	14
2.1	Spectrometer Block Diagram	32
2.2	Circuit Diagram of the Triple Resonance (Chemagnetics) Probe	33
2.3	Zeeman Energy Levels and Chemical Shift Anisotropy for the Spin-1/2	45
2.4	Dipolar Shifts and Anisotropy for the Spin-1/2.....	48
2.5	Deuterium Zeeman Levels, Quadrupolar Shifts and Anisotropy	51
2.6	Quadrupole Echo (QE) Pulse Sequence	69
2.7	Inversion Recovery With Quadrupole Echo (IRQE) Detection Pulse Sequence..	70
2.8	Broad-Band Jeener-Broekaert Pulse Sequence	71
2.9	Deuteron Magic Angle Spinning Pulse Sequence and FID	73
2.10	Cross Polarization Pulse Sequence	74
2.11	Rotational-Echo Double-Resonance Pulse Sequence	78
2.12	Simulated REDOR Curve and Its Fourier Transform for $D = 200$ Hz	80
3.1	Temperature Dependent QE spectra of G2 PAMAM dendrimer	86
3.2	DSC Results for G2 PAMAM Dendrimer	87
3.3	Quadrupole Coupling Parameter Dependence on Planar Libration Amplitude ...	91
3.4	Quadrupole Coupling Constant Dependence on Hydrogen Bond Length	95
3.5	Experimental Spectra and Fits for $G2^+-Br^-$ and $G2^+-Cl^-$	97
3.6	RT Spectra and Fits for All Studied PAMAM Generations	100
3.7	1H Solid Echo Spectra of G2 PAMAM Dendrimer	101
3.8	Model Dependent Distributions of Quadrupole Coupling Constants	106
3.9	Experimental QE Lineshapes and Model Dependent Fits for G7 Dendrimer ..	107

3.10 G-Dependence of Quadrupole Coupling Parameters for Three Labeled Sites .	109
3.11 T-Dependent Spectra and Simulations for G2, 3 and 9	111
3.12 Powder Pattern Time and Temperature Hysteresis	115
4.1 Comparison of Simulations for the Model of Site-Dependent Quadrupole Coupling Constants and Site-dependent Populations for Ammonium Powder Pattern of G3 PAMAM Dendrimer at 45 °C	126
4.2 Comparison of SUMS and EXPRESS Lineshape Simulations for G2	128
4.3 Model-Dependent Anisotropies from EXPRESS Simulation	131
4.4 RT Recovery Curves for G1, 3 and 5 at a Few Frequencies	139
4.5 Experimental Recovery Curves and EXPRESS Simulations for Planar Libration at Two Interior Sites Assuming Single Rate or Log-normal Rate Distribution .	140
4.6 T-Dependent Anisotropies of Amide and Tertiary Amine Powder Patterns	142
4.7 Experimental Recovery Curves for Ammonium Rotors of G3 at RT	148
4.8 Fast and Slow Component Quadrupole Order Anisotropies for G3 at 45 °C and G9 at 27 °C	152
4.9 Partially Relaxed Lineshapes, EXPRESS Fits and Unraveled Anisotropies for All Deuterated Sites of G2, 3 and 9 at 35 °C	157
4.10 T-Dependence of Rates and Arrhenius Fits for All Deuterated Sites of G2, G3, and G9	158
4.11 Experimental QE Spectra for G2, 3 and 9 at 55 °C	163
4.12 Experimental ² H MAS Spectrum for G2 at -58 °C Compared With MAS Simulation for Underlying Powder Patterns	167
4.13 Experimental T-Dependent ² H MAS Spectra and Best Fits for Ammonium Termini of G2 Dendrimer	170
4.14 Best Fit Log-Normal Distributions of Cone Libration Rates	172
4.15 T-Dependence and Arrhenius Fits for Average Rates of Termini Libration for Generation 2 Dendrimer	174

5.1	Two Limiting Hydrogen Bond Geometries for Dendrimer Branches	181
5.2	¹³ C CP MAS Experimental Spectra of Deuterated G2 Dendrimer	183
5.3	¹⁵ N CP MAS Experimental Spectrum of Deuterated G2 Dendrimer	184
5.4	Complete REDOR Pulse Sequence With Timing for Efficient Dephasing	187
5.5	π -Pulse Length Tuning Sequence for Spin-1/2	188
5.6	Experimental REDOR FID for 10 % Doubly Labeled 1- ¹³ C- ¹⁵ N-Gly	189
5.7	REDOR Dephasing Efficiency for up to Eight Equally Spaced Dephasing Pulses per Rotor Period	195
5.8	REDOR SCTR Dipolar Transform for Three-Coupling Dephasing Curve	198
5.9	Planar Libration Amplitude Dependence of Dipolar Frequency	200
5.10	Skewed Dipolar Coupling Distributions Corresponding to Gaussian Distributions of Librational Amplitudes or Internuclear Distances	202
5.11	Dipolar Transform for Simulated REDOR Curve Including Planar Libration Amplitude Distribution	203
5.12	Dipolar Transform for Simulated REDOR Curve Including Gaussian Distribution of Internuclear Distances	204
5.13	Experimental REDOR Data and Fits for 10 % Doubly Labeled 2- ¹³ C- ¹⁵ N-Gly and 1- ¹³ C- ¹⁵ N-Gly	205
5.14	Experimental REDOR Data and Fits for 9 % Doubly Labeled Cycloleuciloglycine (CLG) Di-Peptide	206
5.15	SCTR REDOR Dipolar Transform Results for CLG Data	208
B.1	Comparison of Constrained Multiexponential and Unconstrained Biexponential Fits for T-Dependent Recovery Curves at the Horns of G3	218
B.2	Fast and Slow Anisotropies Produced by Unconstrained Biexponential Fits to Experimental and EXPRESS Simulated Data for G3 at 15 and 45 °C	220
B.3	Experimental Recovery Curves and Constrained Multiexponential Fits at Several Frequencies for G2 at 35 °C and G1, 2, 3, 5, 7 and 9 at RT	222

Abstract

The characterization of narrow distributions of structural and motional parameters, and their evolution during the broad glass transition, is performed for deuterated PAMAM dendrimer salts using solid state NMR. The broadening of deuteron quadrupole echo (QE) lineshapes is consistent with the presence of relatively narrow hydrogen bond length distribution ($\sigma_r < 0.25 \text{ \AA}$) at the spacer amide and branching tertiary amine sites. The average hydrogen bond length of $2.15 \pm 0.10 \text{ \AA}$, observed at both interior sites of all generations is evidence of highly uniform intra- and inter-molecular environment. The temperature dependent averaging of the experimental lineshapes is explained on the basis of fast planar librations in the dendrimer interior, and fast rotation and intermediate regime libration (in an asymmetric cone) of the dendrimer termini. While the amplitudes of libration are temperature dependent and higher for low generation dendrimers, the librational rates show Arrhenius behavior only within the glass transition region. In this region, the width of the log-normal distribution of rates increases with temperature at sites associated with chlorine counterions. The largest distributions are still less than one order of magnitude wide. This behavior is very different from the dendrimer in solution and from the linear polymers. Three subclasses of the solid state dendrimer are distinguished on the basis of PAMAM dynamics analysis at the interior and termini deuterated sites. The open structures of low generation materials ($G < 3$) result in interpenetrated environments allowing higher counterion mobility. The intermediate generations ($G = 3-5$) are highly uniform and capable of forming networks of associated termini. The high generation materials ($G > 5$) have crowded backfolded architectures with low internal mobility. This interpretation of the results suggests new applications for the solid PAMAM dendrimers.

Generally useful information on the sensitivity limits of NMR techniques for solid polymer research is obtained. In the regime of fast motion QE lineshapes are highly sensitive to the presence of, even narrow, structural and motional parameter distributions. Average Hamiltonian formalism is adequate for the description of the motional geometry in this regime, with no reference to the rates of motion. The bounds of the "fast regime" are dependent on the motional geometry, and for the case of planar libration extend to rates as low as $\sim 10^6 \text{ s}^{-1}$. The precise characterization of narrow log-normal rate distributions in the intermediate regime can be done using ^2H magic angle spinning (MAS). Deuteron inversion-recovery techniques provide quantitative information on the rates of fast motion, when the overlapping anisotropies from unselectively labeled sites are analyzed using QE lineshape constraints on motional geometry. For multiframe motion, the absolute relaxation time values are determined by the fastest motional rate, while the shape of the anisotropy is influenced both by the motional geometry and by slower motional rates. For PAMAM dendrimer salts, the narrow distributions of structural and motional parameters, as well as averaging by fast planar libration, are negligible. They would not influence distance determination from Rotational Echo Double Resonance (REDOR) experiments.

The discrimination between inter- and intra-molecular hydrogen bonding can be done straightforwardly through selective labeling of dendrimer core and termini and dilution in natural abundance samples according to suggested strategies. The expected internuclear distance of $3.4-4.0 \text{ \AA}$ is well within the sensitivity range of $^{13}\text{C}-^{15}\text{N}$ REDOR, as exemplified by the measurements on small model compounds. One or two equally spaced pulses per rotor period represent the optimum dephasing scheme for proposed REDOR experiments.

**SOLID STATE NMR CHARACTERIZATION OF STRUCTURAL AND MOTIONAL
PARAMETER DISTRIBUTIONS IN POLYAMIDOAMMONIUM DENDRIMERS**

Chapter 1

Dendrimer Research

The field of dendritic macromolecules is developing at the interface of different scientific disciplines. Its growth has been stimulated by practical needs for materials with new properties as well as by theoretical advances in understanding the symmetry and self-regularity underlying many complex natural phenomena in different physical systems and living organisms. During the last few years this field has grown dramatically, finding numerous applications and penetrating into many spheres of science and technology. Polymer engineers, biochemists, pharmacologists and surface scientists are exploring a common interest in dendritic polymers [1-3]. Each scientific field tends to look at dendrimers from different but complementary perspectives.

Most of the practical applications of dendrimers in biochemistry or medicine rely on precise understanding of the dendrimer interior and surface architecture, the extent of chain end folding, the degree of interpenetration between neighboring molecules, and distributions of structural and motional parameters. But even with considerable progress in development and refinement of polymerization techniques [1-3], the field still lacks a complete theoretical explanation of dendrimer structure, motion and bulk properties. Solving this problem could

save experimental time and allow researchers to predict, rationalize or design new practical applications. The way to achieve this is to identify and characterize microscopic origins of dendrimer bulk properties. This is the point where the experimental methods of condensed matter physics should be applied. At this stage the analysis of experimental results requires knowledge not only of the materials being studied, but also of the fundamentals of the experimental techniques employed.

This chapter is intended as a review of recent developments, experimental investigations and theoretical models in the area of dendrimer research and applications. Fundamental definitions and concepts that are discussed in later chapters will also be introduced. In order to show how our solid state NMR study of polyamidoammonium (PAMAM) dendrimer salts [4-6] fits in the framework of dendritic research, the relevant literature overview will be presented in detail. This will be followed by brief discussion of the relevant solid state NMR theory, experiments and our results.

1.1 Motivation

The synthesis of dendrimers (starting in 1979) was the first successful attempt to achieve control over the structure of a polymeric system in three dimensions [2]. Until this time nature had held the monopoly on this type of synthesis. The natural synthesis of many biologically important three-dimensional polymers, such as proteins or enzymes, is known to be well controlled to give a molecular architecture with a specific and highly efficient function. In biochemistry, the development of synthetic three-dimensional macromolecules was attempted not only to study and mimic foundations laid by nature, but also to build new nanoscopic biocompatible molecular devices. These synthetic dendritic molecules were much more compact than folded linear biological polymers of the same molecular weight. This property, combined with tailorable functionality and capability for active site creation for metal incorporation, makes dendrimers both good models for the investigation of

intramolecular interactions in biological systems and possible candidates for immunodiagnostics or drug-delivery agents [7, 8]. As building blocks for larger megamolecular structures [9], dendrimers appear to follow the basic rules common for proteins and polynucleic acids (DNA, RNA). In addition, their high degree of symmetry allows for self-assembly [10] - yet another biologically and technically important phenomenon.

Although the dendritic growth occurs in three dimensions, the resulting structures do not fill all the space inside their boundaries. Instead, they are micelle-like, highly channeled, and rich in voids which allows for the incorporation of small molecules [1, 11]. In fact dendrimers are fractals, possessing “fractional” dimensionality between 2.0 (square) and 3.0 (cube). The mathematics of fractals has theoretically predicted the principles of such an architecture. Fractals describe many natural structures of non-integral dimensionalities, such as clouds, coastlines or micelles. Their growth is governed by the symmetry of the system and characterized by self-similarity. As fractals, dendrimers provide a tool for validating many general mathematical hypothesis of fractal science.

The web-like structure of the dendrimer interior offers new possibilities for micelle chemistry. In contrast to traditional micelles, dendritic micelles are not dynamic associations of molecules, but static covalently bound structures very similar to natural systems. For example, an increase in ionic strength of the medium would change the aggregation number and size of traditional micelles but not of dendritic particles [2]. Some dendritic micelles can not only encapsulate small compounds, but also solubilize hydrophobic molecules in aqueous solution to an equal or greater extent than traditional surfactants [12, 13]. The molecular size of dendritic micelles changes depending on the pH (acidity) of the solution and solvent properties. It is interesting that the radii of high generation dendrimer electrolytes show little dependence on pH [14], while low generation dendrimers are less susceptible to solvent quality changes [15, 16]. This ability of dendritic micelles to swell or contract is governed by the interior and terminal group interaction with the environment. It is

indicative of molecular flexibility implying a non-entangled architecture dependent on solvent properties.

Chemical and physical properties of dendritic polymers distinguish them from their linear analogs and determine their applications. The key to these properties is in the dendrimer synthesis. By definition, dendrimers are hyperbranched polymers with well defined molecular composition and a step-wise repetitive reaction sequence. They differ from other hyperbranched polymers by their ability to form compact, highly symmetric structures. Dendrimers are characterized by a very regular tree-like architecture growing from a core. This resemblance to a tree explains the origin of their name. There are two main procedures for dendrimer synthesis: convergent and divergent [1, 2]. Convergent synthesis involves a step growth from the core outwards, while divergent synthesis proceeds inwards to the core, assembling branched blocks into one final product molecule.

In either form of synthesis the structural units and the dendrimer core can be of arbitrary chemical composition, but they should have multifunctional ends for further branching at the next step of the polymer growth. Currently over thirty different interiors have been synthesized [2, 3]. They may accommodate carbon, nitrogen, oxygen, silicon, phosphorous or metals. Bulky structural blocks of a short length containing rings or stiff interatomic linkages may provide more rigidity to the structure, while longer linear blocks including alkyl chains with "soft" linkages naturally allow more flexibility and entanglement [1, 2].

At each succeeding step of polymerization more structural units (spacers) are added to the branching sites of previously formed molecule. The product of each polymerization step is called a "generation" and assigned a number, G , according to the step number. Thus, for each generation the number of available branching sites at the surface is fixed by the generation number. Entanglement and surface crowding may limit the ideal growth of the dendrimer to a certain G depending on the building monomer length and geometry. The surface of a product dendritic molecule can be modified to insure desired reactivity; more than 100 surface modifications have been reported [2, 3] to date.

Until recently the most widely used synthetic polymers have been linear, with little or no branching. The control over chain length and branching is a very important factor determining many bulk properties of a polymer, such as solubility, rigidity, crystallinity and even conductivity. Upon completion of the synthesis, the polymer in solution may have macromolecules of widely varying chain length and molecular weight, M . Plotting the number of molecules with a certain chain length as a function of the chain length reveals a distribution, which can be characterized by its mean value and width at the half height. These microscopic structural distributions govern polymer bulk properties and are of great importance for engineering applications.

Most macromolecules in solution will have a chain length equal or close to the mean, in the range specified by the distribution width. This width is characterized by the ratio of the weight average to the number average molecular weight, $\frac{\overline{M}_w}{\overline{M}_n}$, called polydispersity. In contrast to conventional synthetic polymers dendrimers can be synthesized as nanoscale monodisperse materials, with \overline{M}_w and \overline{M}_n almost equal, implying extremely narrow molecular weight distributions. Therefore, narrow distributions of microscopic and bulk properties are expected. Such an accurate control over the molecular architecture coupled with possibility for selective reactive group functionalization suggests many applications in nano-chemistry. These include nanocatalysts [17, 18], layered reaction substrates [19, 20], and separation media [21, 22].

The chemical and physical response of dendrimers to the changes in environment is strongly dependent on their structure and composition. The presence of many chain ends and branched architecture allows for extremely high reactivity, solubility and miscibility together with low intrinsic viscosity [2, 3]. In contrast to linear or branched polymers, dendrimer intrinsic viscosity, $[\eta]$, does not obey a power law growth with increasing molecular weight, M , corresponding to log-log linear relationship $\log[\eta] \propto \log M$. Instead for dendrimers this log-log relationship is a bell shaped curve with the maximum slightly

below $M = 5000$ amu (between $G = 3.0$ and 4.0). This behavior can be explained if the higher generation dendrimers assume a spherical shape [23, 24]. The largest molecules synthesized typically have diameters greater than 10 nm [25, 26].

Despite the difference in solution properties, thermal properties of solid dendrimers and functionally analogous linear polymers are remarkably similar. The variation of dendrimer glass transition temperature, T_g , with molecular weight and chain-end composition has been shown to follow a modified version of the chain-end free volume theory developed for linear polymers [2, 27]. After reaching a certain generation, due to the large number of the chain ends, the free volume is expected to be fixed, and T_g growth stops. This kind of behavior, with T_g increasing for lower generations and remaining constant for $G > 4.0$, has been observed experimentally [27]. In addition, pure dendrimers exhibit rather wide (10-15 °C) glass transition regions, notwithstanding their narrow molecular weight distributions [27]. A plausible explanation accounting for the fixed free volume with increasing generation number is that for high generations some of the chain ends may fold back into the dendrimer interior.

1.2 Polyamidoamine Dendrimers

Most experimental work and theoretical analysis on dendritic structure have been conducted on polyamidoamine dendrimers [28]. These dendrimers were among the first representatives of their class available for research due to their comparatively cheap synthesis, first performed between 1985 and 1986 [28]. They are also known by the name starburst polymers, referring to the star-like symmetry of their growth. Starburst dendrimers typically possess a three-functional (ammonia) or four-functional (diamine) core [29]. Their branches (spacers) are composed of alkyl chains of different lengths with amide connectivity to the next branching site.

Typical representatives of the “starburst” family are PAMAMs, which contain a biologically important amino acid (β -alanine) as a repeating unit in their structure. They are polymerized from the ethylenediamine core ($\text{H}_2\text{N}-\text{CH}_2-\text{CH}_2-\text{NH}_2$), branch at tertiary amine sites ($-\text{N}<$), and have double the number of reactive surface groups with each succeeding generation. For example, after nine iterations the product molecule, $G = 9.0$, has 4×2^9 terminal groups, a molecular weight of 467,162, and a measured diameter of 12.4 nm [25]. In addition, these dendrimers have an extremely narrow distribution of sizes, $\frac{\overline{M}_w}{\overline{M}_n} = 1.0003 - 1.0005$, exceptional even for the polymers of their class. This indicates that incomplete arm defects, if present, can be only a tiny fraction of a percent and would hardly interfere with experimental studies of the dendrimer structure.

Each step of the β -alanine PAMAM growth involves two chemical reactions. The first reaction is the addition of two metal acrylate monomers (e.g. sodium acrylate $\text{CH}_2=\text{CH}-(\text{CO})-\text{O}-\text{Na}$) at each amine site ($-\text{NH}_2$), in which a vinyl double bond opens, and both amine hydrogens are replaced by the carboxylate group [$-\text{CH}_2-\text{CH}_2-(\text{CO})-\text{ONa}$]. The next reaction is amidation of the resulting amino acid with a release of NaOH base, in which another molecule of ethylenediamine is added to each terminal [$-(\text{CO})\text{ONa}$] group to form an amide linkage, [$-(\text{CO})\text{NH}-$], and a new polyamine. After these two reactions each of the resulting amine terminated branches of integer generation will look like [$-\text{CH}_2-\text{CH}_2-(\text{CO})-\text{NH}-\text{CH}_2-\text{CH}_2-\text{NH}_2$]. If the last step of the polymer growth involves the first reaction only, the “half integer” carboxylate terminated generations are produced.

The dimensions of the resulting molecules, determined by size exclusion chromatography, increase from 1 to 10 nm for generations 0.0 through 9.0 [30]. The solvent accessible area of PAMAM macromolecules grows from 29% for $G = 4.0$ to 69% and

124% for $G = 5.0$ and 6.0 respectively [30]. This indicates a highly channeled, micelle-like interior in a polar solvent.

The glass transition temperature also increases with the generation number, and thus with the molecular weight: from $-11\text{ }^{\circ}\text{C}$ for $G = 0.0$ to the asymptotic value of $+14\text{ }^{\circ}\text{C}$ for $G > 4.0$ [27]. After the fourth generation, molecular weight does not appear to effect T_g , which is interpreted as the segmental motions in the dendrimer reaching their limiting amplitudes around $G = 4.0$. The results of rheological studies showed that molecular density of PAMAM has a minimum around $G = 4.0$. This may be explained by a transition to a spherical shape occurring for higher generation dendrimers [23, 24].

Relatively complex constituents and precise synthesis make PAMAM dendrimers good model compounds for studying intramolecular processes in biological polymers, and for developing a theory of the growth, structure and dynamics of dendritic polymers as a class. The amide connectivity of the dendrimer interior stabilizes the structure by hydrogen bonding, a phenomenon also found to be important for protein folding [31]. Many suggested applications rely on PAMAM's biocompatibility. These include drug delivery systems [7, 8], sequestering [32], MRI contrasting agents[33], and surface modifiers [34]. Correlations between the structure and mobility of PAMAM dendrimers [35-39] and their useful properties [7, 8, 32-34] are therefore of great interest.

1.3 Theoretical and Experimental Investigations

Several theoretical models of dendrimer structure and growth have been proposed. The kinetic model [40], which considers dendritic growth as a random three dimensional process, predicts that during formation of the dendrimer molecules reactive terminating groups can be found both on the polymer surface and in its interior at any polymerization step for all generations. As a result, the molecules are channeled all the way through and do not form a rigid shell at the surface.

According to the model of self consistent fields [41], which takes into account the balance of forces at the branching sites, the ideal starburst growth of the dendrimer can proceed without termini folding back, but only for a limited number of generations. This number depends on the length of the polymer spacer, and its flexibility. For PAMAM, for instance, the model predicts the possibility of ideal growth up to generations $G = 8-10$.

The estimation of the moment of inertia as a result of molecular dynamics simulations [37] has suggested that the dendrimer shape symmetry increases from hemispherical to spherical with growing generation number. This supports yet another picture of dendrimers with open structures for low generations, the formation of a "surface layer" around generation 3-4, and the transition to the globular shape with extensive channeling and voids in the interior for higher generations.

Substantial experimental evidence has been accumulated which supports the existence of a structural change to a spherical shape in solution [35-37, 39, 42-46]. The results of molecular dynamics simulations are supported by experimental studies of NMR relaxation of small guest molecules in dendrimer solutions [37]. Recent Small Angle Neutron (SANS) [38] and Small Angle X-ray Scattering (SAXS) [39] investigations and photoinduced electron transfer experiments [42] also confirmed these simulations. Together with counterion mirroring [47], these studies suggest extended dendron configurations for dendrimers in solution. For generation 7-10 polyamidoamine dendrimers SAXS exhibited features characteristic of nearly monodisperse, spherical particles with uniform internal segment densities and much higher regularity than that of dilute hyperbranched polymer solutions [39]. For the lower generations, an accurate determination of particle shape and internal density distribution was not possible due to absence of higher order scattering features. Liquid state NMR studies have revealed a flexible dendrimer exterior and compact core [35, 36]. The measured distributions of relaxation times were three decades wide. With the surface groups being more mobile than interior groups, chain end localization and shell

rigidity remains in question. It is likely that the interpretation of the results heavily depends on solvent interactions [15, 16, 48, 49].

Although direct spectroscopic measurements of dendrimer structures are complicated by the lack of long-range order, much indirect information has been gained by monitoring the mobility of metal complexes incorporated in the dendrimer interior and surface [43, 44]. This provides evidence of an open structure for low generations, and a more compact architecture for high generation dendrimers consistent with a change in dendrimer surface morphology around generation 3 [43, 44]. However, incorporation of foreign material may cause the change in dendrimer behavior. Thus, the conclusions lack generality.

At present the understanding of dendrimers resulting from experimental research and theoretical predictions sketches a picture of a channeled, fractal-like molecule with a regular distribution of voids in the interior, an open architecture for lower generations and a sphere-like structure for higher generations in solution. The nature of the edge of the sphere is vague. Most probably it consists not only of terminal groups, but also of several neighboring inner layers. Temperature [23, 24], solvent interactions [16, 48, 49], and interpenetration between neighboring molecules [25, 26] may alter the shell properties, making it look more or less rigid. The shell formation might be accompanied by chain end folding back into the "pre-surface" layer, thus allowing more mobility for the terminal groups left at the surface.

1.4 Solid State NMR Experiments

Until now all experimental work on PAMAM dendrimers was done in solution where the solvent interactions and overall molecular "tumbling" motions complicate and obscure the observations of internal motion and structure of the polymer. Although most of the current applications involve the dendrimer in solution, solid state studies might provide better insight into PAMAM's intrinsic structure and dynamics, resolve theoretical

ambiguities, and suggest new applications. Experiments on dry PAMAM dendrimers are complicated due to high hygroscopicity of the material, and have been done only above their T_g [24]. Due to very narrow molecular size distributions, dendrimers can be characterized more precisely than most linear polymers. However, the fractal-like dendrimer architecture lacks long-range order and therefore cannot be investigated by crystallographic techniques. Solid state nuclear magnetic resonance (NMR) provides a powerful combination of experimental techniques for this purpose.

The chemical composition of the PAMAM dendrimers allows for efficient exchange of hydrogen atoms with deuterons in solution at functionally important interior amide and surface amine N-H sites. Changes in the intermolecular environments, accompanying any structural transition or molecular motion in a deuterated sample, produce reorientation and redistribution of local electric fields interacting with deuteron nuclear spin. The spin behavior can be monitored by deuteron quadruple echo (QE) spectroscopy, and the resulting lineshapes are determined by the molecular motion. Therefore, information on the distribution of amide hydrogen bond lengths as well as on the motion at the PAMAM surface and interior can be obtained.

Deuteron relaxation studies are distinguished by sensitivity to a wide range of motional rates, ranging from seconds to picoseconds [50-52]. Structural transitions in dendrimers and other polymers are naturally accompanied by changes in the amplitudes and rates of molecular motion [50, 53-55]. Deuteron relaxation is an excellent choice of technique to quantitatively characterize these dynamical processes. For complex dynamical processes with multiple motions the sensitivity to a particular motional regime can be enhanced by application of deuteron magic angle spinning (MAS) technique. ^2H MAS provides a way to discriminate between motional processes on the scale from milliseconds to nanoseconds [56]. The distribution of rates of molecular motion may also be characterized from ^2H relaxation and MAS studies [6].

In principle, the intra- versus inter-molecular distances in solid dendrimers can be measured by rotational-echo double-resonance (REDOR) method [57, 58]. REDOR distance determination experiments would require specific site isotope labeling, for example with ^{15}N in the dendrimer core and ^{13}C at the branches. Selective labeling is generally expensive. In choosing the place for isotope labeling the effects of temperature dependent molecular motion should be considered with care (this will be discussed in Chapter 5). Experimental optimization schemes have to be developed beforehand and checked for sensitivity to distribution of motional and structural parameters for proper data interpretation. To obtain a complete quantitative picture of PAMAM motion and structure a combination of the experimental solid state NMR techniques should be applied.

To monitor the temperature dependence of motional and structural parameter distributions in dendrimers we prepared solid deuterated PAMAM salts. This had an advantage of $\sim 20^\circ$ increase in glass transition temperature of the samples, bringing the experiments into the room temperature range. However, salt formation produced increased hygroscopicity to the materials. Thus, all the experiments had to be done with the dendrimers carefully dried and packed in moisture proof containers. For the experiments described in this thesis, amine terminated StarburstTM dendrimers (ethylene-diamine core) of generations 1 through 3 were obtained from Aldrich as 5g of 20 wt.% solutions in methyl alcohol. Generations 5, 7 and 9 were synthesized as 0.8 g of 15-25 wt.% methanol solutions and kindly donated for experiments by Dendritech Inc. (Michigan Molecular Institute, [59]). All pure dendrimers were stored in a refrigerator when not in use. Two samples of deuterated PAMAM salts were prepared for each of the dendrimer generations $G = 1, 2, 3, 5, 7$ and 9 . Deuteration of each sample was done in four steps: (1) 2 ml HCl and 2 ml D_2O were added to the methanol solution; (2) the sample was dried under nitrogen at 60°C for 24 hours; (3) 2 ml D_2O were added and step 2 repeated; (4) step 3 was repeated and the sample was dried under vacuum at 20°C for three days (with the solvent trap cleaned every

3 to 5 hours). At each deuteration step, chemical exchange in solution was allowed to proceed at least for 12 hours to ensure equilibration. Theoretically, 97 to 99 % deuteration should be achieved. The use of a strong acid results in deuteration of all terminal ammonium, RND_3^+ , sites and at least partial deuteration of tertiary amine sites [60], R_3ND^+ . Stoichiometric ratios $\text{R}_2\text{ND}:\text{R}_3\text{ND}^+:\text{RND}_3^+$ are $2:1:3(1-2^{-G-1})^{-1}$ according to the structures illustrated in Fig.1.1. For infinitely grown dendrimer the ratio would be 2:1:3. Dry dendrimers were powdered, packed into 5 mm outer diameter Wilmad glass sample tubes, and sealed in a glove bag under nitrogen to avoid moisture. Sealed tubes containing approximately 200 mg of sample were stored at ambient temperature. MAS experiments were done on G2 dendrimer packed in 5 mm zirconia rotor with finned teflon spacers.

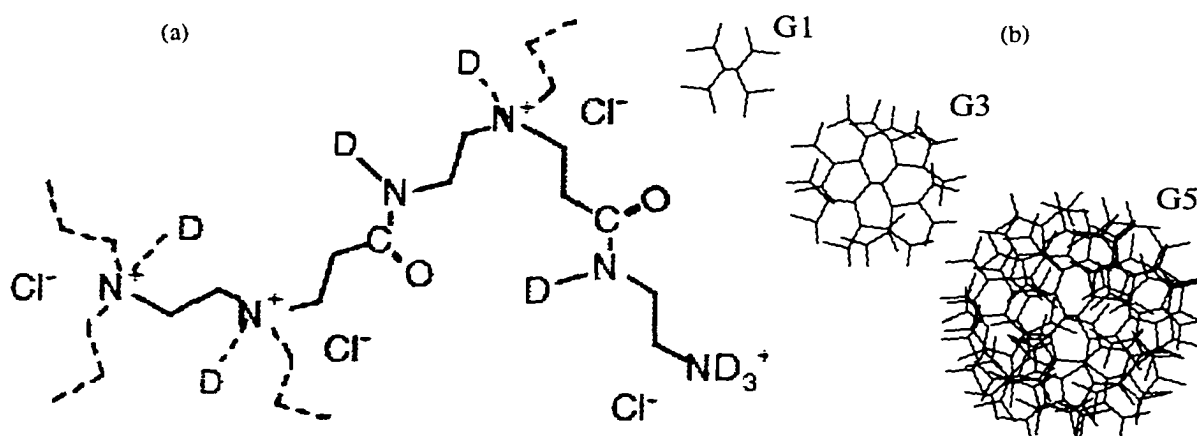


Figure 1.1
(a) PAMAM branch (one of eight for G1) showing deuteration at specific secondary amide, and interior and surface tertiary amine sites; (b) cartoon illustrations for G1, G3 and G5.

Excess DCl in solution should result in complete deuteration of interior tertiary amine branching sites in addition to the ammonium termini [60]. However, the extent of deuteration was not controlled and it is possible that some sites lose deuterons during solvent removal. Deuteration at low acid concentrations, at least for low generation materials, can be expected to occur predominantly at the branching sites two spacers apart due to effects of electrostatic repulsion [60]. Thus it is possible that deuteration occurs in part “by

layers" (e.g. at termini and at generation 0 sites for G2), and for high generation dendrimers the accessible layers might not penetrate close to the dendrimer core. This may cause discrepancy between measured relative intensities of spectral features and stoichiometric expectations.

Our study of quadrupole echo lineshapes spectra for deuterated PAMAM salts [4], provided evidence of thermally activated planar librational motion in the dendrimer spacers and branching points, and a composite, two-frame motion of ammonium termini, RND_3^+ . These motions competed with the stabilizing influence of hydrogen bonds at interior amide (R_2ND) and deuterated tertiary amine (R_3ND^+) sites in the course of the broad glass transition. The balance between these competing trends correlated to a progression from the open, interpenetrated structures of low generation dendrimers to more symmetric, backfolded molecular architecture for high generations. The rates and activation energies of internal dendrimer motions (librations and rotation) during glass transition were quantified on the basis of anisotropic, temperature dependent relaxation data [5]. ^2H MAS lineshapes contributed quantitative information on libration of the dendrimer termini and permitted characterization of surprisingly narrow distributions of libration rates of the dendrimer spacers [6]. Finally, the acquired knowledge about structural and motional parameter distributions was used for optimization of experimental REDOR conditions.

1.5 Summary

Ongoing investigation of the dendrimer structure and application development requires an interdisciplinary effort. PAMAM has proved to be a good model compound for dendrimer structure investigation due to high precision synthesis and relatively simple structure, with nonetheless biologically important units and interactions. A considerable number of experimental and theoretical research makes it one of the most studied

dendrimers in solution and thus a preferred subject for further research in the area of dendritic polymers and extension to solid state. Flexible structural units and stabilizing amide connectivity provide possibilities for the explicit monitoring of the balance between intramolecular motion and hydrogen bonding in the transition to backfolded structures for high generations.

Solid PAMAM dendrimers with excluded solvent interactions allow to describe intrinsic dendrimer behavior and validate theoretical predictions. Characterization of the distribution of microscopic structural and motional parameters and their temperature evolution is of general interest for PAMAM engineering applications. Our solid state NMR studies of PAMAM salt characterize generation dependent changes in starburst behavior below, as well as within, the glass transition region. In the following chapters of this dissertation the techniques employed will be introduced and the results of quadrupole echo lineshapes, relaxation time anisotropies and deuteron MAS experiments for deuterated PAMAM salts will be analyzed. Their implications for theories of dendrimer formation and solid state morphology, as well as polymer research on the whole, will be highlighted.

Chapter 2

NMR Background

Nuclear Magnetic Resonance (NMR) is a powerful spectroscopic method probing the interaction of radio-frequency (RF) electromagnetic (EM) radiation with matter. In an external magnetic field, the transitions between different spin angular momentum quantum states of the nuclei can be matched by RF photons. Therefore, information about the spin system encoded in RF signals can be detected and analyzed with high accuracy. NMR spectra are sensitive to perturbations of the energy levels caused by a variety of intramolecular interactions, in addition to the strongest interaction, with the external magnetic field. This makes NMR an indispensable tool for many scientific disciplines.

Solid state NMR allows investigation of spatially anisotropic spin interactions, which reflect molecular structure, order and motion. The information about molecular orientations is encoded in the orientation dependent spectra. Reorientation of the interaction tensors, which accompanies molecular motion, can be monitored through the solid NMR spectra to provide microscopic details of motional rates and trajectories. This orientation dependence is not preserved in liquid state NMR spectra because fast isotropic tumbling of molecules averages out the orientational dependence of the spin interactions.

This chapter describes basic NMR principles and experimental techniques relevant to the present study of structural and motional parameter distributions in PAMAM dendrimer salts. The introduction to NMR theory, equipment and important static interactions is followed by the discussion of the formalism for motional modulation of the interactions, and description of experimental techniques and pulse sequences applied to obtain the data presented in this dissertation.

2.1 Basic NMR Theory and Equipment

NMR can detect changes in the nuclear spin angular momentum, $\bar{\mathbf{I}}$, energy state associated with changes of magnetic dipole moment, $\bar{\mathbf{M}}$. These two quantities are related by the fundamental expression [61]

$$\bar{\mathbf{M}} = \gamma \hbar \bar{\mathbf{I}} \quad [2.1]$$

Where $\hbar = 1.055 \times 10^{-34} \text{ J} \cdot \text{s}$ is Planck's constant, and γ , the gyromagnetic ratio is characteristic of the observed nucleus. Angular momentum is a quantum property of the nucleus. In three-dimensional space, with fixed (x, y, z) coordinate frame, it should be regarded as a vector operator $\bar{\mathbf{I}} = \mathbf{I}_x \bar{e}_x + \mathbf{I}_y \bar{e}_y + \mathbf{I}_z \bar{e}_z$. The eigenvalues of this operator define the observable quanta of angular momentum about three space fixed axes. Matrix elements for transitions from initial, $|\Gamma m'\rangle$, to final, $|\Gamma m\rangle$, quantum state are given by,

$$\langle \Gamma m | \mathbf{I}_z | \Gamma m' \rangle = m \delta_{mm'} \delta_{\Gamma\Gamma'} \quad [2.2]$$

$$\langle \Gamma m | \mathbf{I}_x | \Gamma m' \rangle = \frac{1}{2} \delta_{\Gamma\Gamma'} (\delta_{mm'+1} \sqrt{(I+m)(I-m+1)} + \delta_{mm'-1} \sqrt{(I-m)(I+m+1)}) \quad [2.3]$$

$$\langle \Gamma m | \mathbf{I}_y | \Gamma m' \rangle = \frac{i}{2} \delta_{\Gamma\Gamma'} (-\delta_{mm'+1} \sqrt{(I+m)(I-m+1)} + \delta_{mm'-1} \sqrt{(I-m)(I+m+1)}) \quad [2.4]$$

Here, “ I ” and “ m ” define the quantum numbers associated with the total angular momentum and its z-projection, \mathbf{I}_z , respectively [62]. Since only certain discrete values of the

z-component are observable, a nucleus with spin I has $(2I+1)$ states associated with operator \mathbf{I}_z .

When a macroscopic assembly of nuclear spins is placed in a strong static magnetic field, $\vec{B} = B_0\vec{e}_z$, the spin magnetic dipole moments tend to align parallel to the field, thus achieving the lower energy state. The Hamiltonian operator, \mathbf{H} (the quantum analog of the classical interaction energy), for this system is

$$\mathbf{H} = -\gamma\hbar\mathbf{I}_zB_0 = -\hbar\omega_0\mathbf{I}_z \quad [2.5]$$

$$\omega_0 = \gamma B_0 = 2\pi\nu_0 \quad [2.6]$$

where ν_0 is the Larmor frequency. Thus, the allowed energy levels are $\langle m_i | \mathbf{H} | m_i \rangle$

$$E_i = -m_i\hbar\omega_0 \quad [2.7]$$

Occupation of each eigenstate of the Hamiltonian is subject to constraints of thermal (Boltzmann) equilibrium of the ensemble of nuclear spins. Since the intensity of the observed transition between nuclear spin energy levels in a bulk sample is proportional to the difference in populations, NMR sensitivity is determined by

$$p_i - p_j = N \frac{1 - e^{-\frac{\hbar\omega_0}{k_b T}}}{1 + e^{-\frac{\hbar\omega_0}{k_b T}}} \quad [2.8]$$

Where p_i is a population of an i -th quantum state, N , the number of nuclear spins in the ensemble, k_b , Boltzmann constant, and, T , the sample temperature. Under usual NMR experimental conditions - less than 10 Tesla external magnetic field, close to room temperature ($T = 300$ K) - the Boltzmann factor is much less than one and the population difference between two energy levels can be approximated by $N\Delta E(2k_b T)^{-1}$. For instance, for a spin $I = 1/2$ nucleus resonating at 300 MHz, the excess of spins aligned parallel to the field ($m = 1/2$) over those anti-parallel to it ($m = -1/2$) is extremely small, $2.4 \times 10^{-5}N$. This result implies that only 20-30 spins in a million will contribute to an observed NMR signal. This small difference determines relatively low NMR sensitivity and larger sample volumes

required compared to other spectroscopic techniques, such as infrared or ultraviolet radiation absorption.

For the solid samples, the sensitivity at a certain frequency is further decreased by the presence of anisotropic spin-spin interactions which, in general, lead to the spread of intensity over a broad frequency range. Due to all these sensitivity drawbacks, additional effort is required in the development of technically demanding NMR equipment and experimental techniques. It is noteworthy that a stronger magnetic field, larger gyromagnetic ratio and lower temperature help to establish higher population difference and achieve more intense NMR signals.

2.1.1 Spin-1/2 and Spin-1 Nuclei

Spinless isotopes ($I = 0$) do not possess magnetic moments (Eq. 2.1) and are invisible to NMR. Nuclear angular momentum arises from the coupling of the spin and orbital angular momenta of its nucleons: protons and neutrons. Each nucleon has a spin of $1/2$ (when the fundamental unit of angular momentum, the Planck constant, is set equal to one). Since proton and neutron spins cannot pair with each other, nuclei with an even number of protons and neutrons always have zero angular momenta (e.g. ^{12}C , ^{16}O). If both the number of protons and neutrons are odd, the nuclei have integer spin (e.g. ^2H , ^{14}N). When the number of protons or neutrons is odd while the other is even, the nuclei possess half-integer spins (e.g. ^1H , ^{13}C , ^{15}N , ^{17}O).

Even when a particular nucleus has no spin, some of its isotopes may have angular momentum and thus can be detectable by NMR, as is the case with carbon-13 and oxygen-17. However, isotopes with spin are often of low natural abundance (1.11 % in case of ^{13}C), and this will decrease NMR sensitivity. In a typical NMR experiment the resonance of one particular isotope is observed. The difference between resonance frequencies for nuclei of different elements is usually much greater than the range of frequencies produced by a

single isotope. Also, the band width of EM radiation produced by the spectrometer pulses is limited.

The nuclei possessing spins higher than $1/2$ have quadrupole moments (eQ) arising from a non-spherical nuclear electronic charge distribution. The interaction between the quadrupole moment and the surrounding electric field gradient tensor (EFG) dominates NMR spectra of such nuclei. The smallest eQ is observed for deuterium ($I = 1$) and leads to the resonance frequency range of at most 300 kHz. Other spin-spin interactions are negligible for deuterons, but low natural abundance of this nucleus (0.015 %) makes isotopic enrichment of the samples mandatory for ^2H NMR. For ^{14}N ($I = 1$), the eQ is six times that of deuterium, and spectral ranges in excess of a megahertz are produced. The observation of such a broad frequency range is rarely practical, and isotope substitution by ^{15}N ($I = 1/2$, 0.37 % natural abundance) is often performed for NMR investigation. The anisotropic interactions for ^{15}N lead to the spectral ranges of less than 10 kHz. For hydrogen and carbon-13 the typical observed frequency ranges are 70 and 20 kHz respectively.

In planning NMR experiments utilizing isotopic substitution it is often useful to estimate the achievable sensitivity for a particular nucleus. The nucleus with the highest sensitivity is hydrogen [63]. Since intensity of the NMR transition is proportional to energy level population difference (Eq. 2.8 and its approximation below), and a square of RF frequency, the sensitivity for a certain nucleus in respect to hydrogen will be approximately proportional to the cube of the ratio of their gyromagnetic constants [63]. Thus, it can be estimated that ^2H and ^{13}C show approximately one hundred, and ^{15}N – one thousand, times lower sensitivity than protons [63]. The experimental solid state NMR spectra of these nuclei are to be analyzed to investigate PAMAM dendrimer salts in the following chapters. The lower sensitivity usually means that longer experiments have to be performed to ensure reasonable signal-to-noise (S/N) ratios. Since the coherent NMR signal grows proportionally to the number of acquisitions, while the incoherent noise grows

proportionally to the square root of this number, increasing the number of NMR scans, N_s , allows $\sqrt{N_s}$ increase in S/N ratio. To double S/N by coherent averaging a four-fold increase in the number of scans (and thus in time) is required.

The multiplicity for $I = 1/2$ nucleus is 2, and for $I = 1$ nucleus is 3, therefore, two and three spin energy levels respectively will be observed for them in an external magnetic field. Thus, for these isotopes the x, y and z- components of the spin angular momentum, (Eqs. 2.2-2.4) are matrices 2x2 and 3x3:

$$I = \frac{1}{2}, \quad \mathbf{I}_x = \begin{pmatrix} 0 & \frac{1}{2} \\ \frac{1}{2} & 0 \end{pmatrix}, \quad \mathbf{I}_y = \begin{pmatrix} 0 & -\frac{i}{2} \\ \frac{i}{2} & 0 \end{pmatrix}, \quad \mathbf{I}_z = \begin{pmatrix} \frac{1}{2} & 0 \\ 0 & -\frac{1}{2} \end{pmatrix} \quad [2.9]$$

$$I = 1, \quad \mathbf{I}_x = \begin{pmatrix} 0 & \frac{1}{\sqrt{2}} & 0 \\ \frac{1}{\sqrt{2}} & 0 & \frac{1}{\sqrt{2}} \\ 0 & \frac{1}{\sqrt{2}} & 0 \end{pmatrix}, \quad \mathbf{I}_y = \begin{pmatrix} 0 & -\frac{i}{\sqrt{2}} & 0 \\ \frac{i}{\sqrt{2}} & 0 & -\frac{i}{\sqrt{2}} \\ 0 & \frac{i}{\sqrt{2}} & 0 \end{pmatrix}, \quad \mathbf{I}_z = \begin{pmatrix} 1 & 0 & 0 \\ 0 & 0 & 0 \\ 0 & 0 & -1 \end{pmatrix} \quad [2.10]$$

2.1.2 Quantum Description and Density Matrix

In a quantum mechanical description, the wavefunction of the nucleus is defined by a linear combination of eigenstates of its Hamiltonian. In a static external magnetic field along the laboratory z-axis the energy levels are the eigenvalues of \mathbf{I}_z , m , of the Zeeman Hamiltonian (Eq. 2.7). For spin-1/2 and spin-1 nuclei the eigenvalues are (+1/2, -1/2) and (+1, 0, -1), and the state vector will have two and three components respectively

$$|\psi(t)\rangle = \sum_{k=1}^{2I+1} C_k(t) |m_k\rangle \quad [2.11]$$

where the coefficients are normalized such that $\sum_{k=1}^{2I+1} |C_k(t)|^2 = 1$ for all t . In order to describe experimental NMR quantum mechanically, we must identify the observable quantities. Since NMR spectroscopy monitors the changes in sample magnetization, the observed quantities

are the expectation values of magnetization operator components. They are proportional to angular momentum expectation values (Eq. 2.1), and according to convention, when $\hbar \equiv 1$,

$$\langle \bar{\mathbf{M}}(t) \rangle = \gamma \langle \psi(t) | \bar{\mathbf{I}} | \psi(t) \rangle \quad [2.12]$$

The time evolution of a wave function is governed by the Shroedinger equation [64]

$$i \frac{\partial}{\partial t} |\psi(t)\rangle = \mathbf{H} |\psi(t)\rangle \quad [2.13]$$

And its solution for a state vector [64] is:

$$|\psi(t)\rangle = e^{-i\mathbf{H}t} |\psi(0)\rangle \quad [2.14]$$

where the exponential operator is called a "propagator" because it propagates the influence of system Hamiltonian on the initial state at time zero to a final state at time t . According to Eqs. 2.9 and 2.12, the initial expectation values for the three magnetization components ($t = 0$) in external magnetic field (Eq. 2.5) for spin-1/2 system are

$$\begin{aligned} \langle \mathbf{M}_x(0) \rangle &= \frac{\gamma}{2} (C_1^* C_2 + C_2^* C_1), \quad \langle \mathbf{M}_y(0) \rangle = i \frac{\gamma}{2} (C_1 C_2^* - C_1^* C_2), \\ \langle \mathbf{M}_z(0) \rangle &= \frac{\gamma}{2} (|C_1|^2 - |C_2|^2) \end{aligned} \quad [2.15]$$

and for the spin-1 nucleus (Eqs. 2.10 and 2.12):

$$\begin{aligned} \langle \mathbf{M}_x(0) \rangle &= \frac{\gamma}{\sqrt{2}} (C_1^* C_2 + C_2^* C_1 + C_2^* C_3 + C_3^* C_2), \\ \langle \mathbf{M}_y(0) \rangle &= i \frac{\gamma}{\sqrt{2}} (C_1 C_2^* - C_1^* C_2 + C_3^* C_2 - C_2^* C_3), \\ \langle \mathbf{M}_z(0) \rangle &= \frac{\gamma}{2} (|C_1|^2 - |C_3|^2) \end{aligned} \quad [2.16]$$

In both cases the expectation value of the magnetization operator has the same time dependence (Eq. 2.14), given below

$$\begin{aligned} \langle \mathbf{M}_x(t) \rangle &= \langle \mathbf{M}_x(0) \rangle \cos \omega_0 t + \langle \mathbf{M}_y(0) \rangle \sin \omega_0 t \\ \langle \mathbf{M}_y(t) \rangle &= \langle \mathbf{M}_y(0) \rangle \cos \omega_0 t - \langle \mathbf{M}_x(0) \rangle \sin \omega_0 t \\ \langle \mathbf{M}_z(t) \rangle &= \langle \mathbf{M}_z(0) \rangle \end{aligned} \quad [2.17]$$

It follows that in external magnetic field the observed nuclear magnetization precesses at ω_0 around the direction of the field counterclockwise with the frequency determined by the

strength of the applied field and gyromagnetic constant of the nucleus (Eq. 2.6). This precession frequency corresponds to the transition between the angular momentum eigenstates, and is referred to as the Larmor frequency.

Manipulation of the system states in NMR experiments can be achieved by changing the states of the spin angular momentum operator. Due to invariance to rotation about its axis, angular momentum is conserved [65]. Therefore, infinitesimal rotation through angle $d\alpha$ around x, y or z-axis in the spin space can be described by application of the corresponding operator $[1-i(d\alpha)\mathbf{I}_{x,y,z}]$. Then, the sequence of N small rotations amounting to a finite angle rotation $\alpha = Nd\alpha$ is described as a product of N infinitesimal rotation operators, which in the limit $N \rightarrow \infty$ converges to an exponential rotational operator [62],

$$\mathbf{R}_{x,y,z} = e^{-i\alpha\mathbf{I}_{x,y,z}} \quad [2.18]$$

Any rotation of the system can be accounted for by Euler coordinate transformations. According to the Rose convention (adopted in this dissertation) the *coordinate axis rotation* is a "passive" one and involves negative (clockwise) rotation angles. Euler transformations are described by "active" system rotation through angle $0 \leq \gamma \leq 2\pi$ about the z-axis, then through angle $0 \leq \beta \leq \pi$ about a new y-axis, followed by rotation through $0 \leq \alpha \leq 2\pi$ about a new z-axis. The matrix representation for a full Euler rotation operator can be obtained analytically since it corresponds to the transition operator between two quantum states $|Im\rangle$ and $|I'm'\rangle$

$$\langle I' m' | \mathbf{R} | Im \rangle = \langle I' m' | e^{-i\alpha\mathbf{I}_z} e^{-i\beta\mathbf{I}_y} e^{-i\gamma\mathbf{I}_z} | Im \rangle = e^{-im'\gamma} e^{-im'\alpha} d_{m'm}^{(I)}(\beta) \delta_{I'I} \quad [2.19]$$

$$d_{m'm}^{(I)}(\beta) = \sum_{n=0}^{\infty} \frac{1}{n!} (-i\beta)^n \langle m' | \mathbf{I}_y^n | m \rangle \quad [2.20]$$

After re-grouping odd and even terms into sub-series and making use of Eq. 2.9 and 2.10, the matrix representation for rotation operator about the y-axis for spin-1/2 and spin-1 nuclei can be found [62]:

$$d^{(1)}(\beta) = \begin{pmatrix} \cos \frac{\beta}{2} & -\sin \frac{\beta}{2} \\ \sin \frac{\beta}{2} & \cos \frac{\beta}{2} \end{pmatrix} \quad [2.21]$$

$$d^{(1)}(\beta) = \begin{pmatrix} \cos^2 \beta & -\sqrt{2} \cos \beta \sin \beta & \sin^2 \beta \\ \sqrt{2} \cos \beta \sin \beta & 1 - 2 \sin^2 \beta & -\sqrt{2} \cos \beta \sin \beta \\ \sin^2 \beta & \sqrt{2} \cos \beta \sin \beta & \cos^2 \beta \end{pmatrix} \quad [2.22]$$

According to the Euler formalism, the rotation around x-axis can be rewritten as a composite rotation involving \mathbf{R}_z and \mathbf{R}_y operators:

$$\mathbf{R}_x = e^{-i\phi \mathbf{I}_x} = e^{-i\frac{\phi}{2} \mathbf{I}_z} e^{-i\phi \mathbf{I}_y} e^{i\frac{\phi}{2} \mathbf{I}_z} \quad [2.23]$$

Knowing the matrix representations for all rotation operators allows straightforward characterization of the change in spin system quantum state in response to a perturbation. For instance, if the spin-1 system is prepared in state $C_1(0) = 1$, $C_{2,3}(0) = 0$ ($\langle \mathbf{I}_x(0) \rangle = \langle \mathbf{I}_y(0) \rangle = 0$, $\langle \mathbf{I}_z(0) \rangle = 1$), after RF irradiation at frequency ω_1 with phase \mathbf{I}_x , such that $\omega_1 t = \pi/2$, the evolution of the state vector is

$$\left| \psi\left(\frac{\pi}{2\omega_1}\right) \right\rangle = \mathbf{R}_x \left| \psi(0) \right\rangle = \left(\frac{1}{2}, \frac{i}{\sqrt{2}}, -\frac{1}{2} \right) \quad [2.24]$$

Expectation values of the spin angular momentum, $\langle \mathbf{I}_x(t) \rangle = \langle \mathbf{I}_z(t) \rangle = 0$, $\langle \mathbf{I}_y(t) \rangle = 1$, show that the applied field has caused spin magnetization to rotate from z to y-axis.

Since the operator symmetry properties and transformations are frequently used in solid state NMR for the description of spin-spin interactions, the derived matrix representation for rotation operator, \mathbf{R} , is useful for evaluating Hamiltonian manipulations. Many interactions can be written in terms of vector-tensor products [61]. These may then be transformed into combinations of spherical irreducible tensors of rank 2 (e.g. traceless symmetric part of a Cartesian tensor), rank 1 (e.g. any vector or anti-symmetric part of a Cartesian tensor), and rank 0 (e.g. trace of a Cartesian tensor – scalar, invariant to rotations). The M -th component of the spherical irreducible tensors of rank L , $T_M^{(L)}$, obeys the following rule upon coordinate transformation [65]:

$$T_m^{(L)}(NEW) = \mathbf{R}T_m^{(L)}(OLD)\mathbf{R}^{-1} = \sum_{m'=-L}^L D_{m'm}^{(L)}T_{m'}^{(L)}(OLD) \quad [2.25]$$

$$D_{m'm}^{(L)} = e^{-i(m'\alpha+m\gamma)}d_{m'm}^{(L)}(\beta) \quad [2.26]$$

Here $D_{m'm}^{(L)}(\alpha, \beta, \gamma)$ are Wigner rotation matrix elements (e.g. calculated for the rank $L = 1$ in Eq. 2.22), which are tabulated for $L = 2$ by Brink and Satchler [65].

Measurements of isolated spins are rarely feasible. Real NMR experiments mostly monitor the evolution of a large number of spins represented by a statistical mechanical ensemble. For non-interacting spins, the state of each nucleus in an ensemble is a linear combination of the single spin eigenstates. For mixed ensembles the result of a measurement is given by the weighted average of expectation values [64]. The ensemble average of the magnetization operator is

$$\langle \bar{\mathbf{M}} \rangle = \sum_i p_i \langle \psi_i | \mathbf{M} | \psi_i \rangle \quad [2.27]$$

where $|\psi_i\rangle$ are the state vectors of the system, and p_i their fractional populations. These states are not necessarily orthogonal and their number may be different from the number of eigenstates. The fractional populations satisfy the normalization condition, $\sum_i p_i = 1$. The state vectors of the system can be expanded into linear combinations of an orthonormal basis set of the system Hamiltonian eigenfunctions, $|\phi_n\rangle$,

$$|\psi_i\rangle = \sum_n |\phi_n\rangle \langle \phi_n | \psi_i \rangle = \sum_n C_n |\phi_n\rangle \quad [2.28]$$

Then the ensemble average expectation value of spin magnetization is

$$\langle \bar{\mathbf{M}} \rangle = \sum_i p_i \sum_{n,m} \langle \psi_i | \phi_n \rangle \langle \phi_n | \mathbf{M} | \phi_m \rangle \langle \phi_m | \psi_i \rangle = \sum_{n,m} \rho_{nm} M_{nm} = \text{Tr}(\rho \mathbf{M}) \quad [2.29]$$

$$\rho_{nm} = \langle \phi_n | \rho | \phi_m \rangle = \sum_i p_i \langle \phi_n | \psi_i \rangle \langle \psi_i | \phi_m \rangle \quad [2.30]$$

$$\rho = \sum_i p_i |\psi_i\rangle \langle \psi_i| \quad [2.31]$$

Since the trace of a matrix is independent of basis set the ensemble average expectation value of spin magnetization (as well as any other operator) is invariant to representation. The operator ρ is the ensemble average probability of spin states; its matrix representation (Eq. 2.30) ρ_{nm} is referred to as the density matrix. The elements of the density matrix contain information about the spin ensemble. The diagonal terms describe the populations of each eigenstate, while off diagonal terms describe phase coherence of the spins in the ensemble. In an NMR experiment the signal observed after application of an RF pulse corresponds to \mathbf{I}_x , because it involves dipolar transitions. These are represented by non-zero elements whose indices differ by one, $\rho_{nn\pm 1}$.

For an isolated spin-1/2 system the density matrix is 2x2, so higher quantum coherences are not possible. For an isolated spin-1 and higher, multiple quantum coherences can be created, but are not directly observable. For n coupled nuclear spins, I_k , the dimensionality of the system density matrix is determined by $\prod_{k=1}^n (2I_k + 1)$. The density operator is unitary (its inverse is equal to a complex conjugate transpose – adjoint operator), $\rho^+ = \rho^{-1}$. When the system is at thermal equilibrium in a static magnetic field, no signal is observed using RF radiation. This is a consequence of the spin precession being phase incoherent at thermal equilibrium, and information about the phase correlation between stationary eigenstates is lost. All off-diagonal terms are zero, and the diagonal elements of the equilibrium density matrix, $\rho(\infty)$, are determined by a Boltzmann population distribution

$$\rho_{nn}(\infty) = \frac{e^{-\frac{E_n}{k_b T}}}{\sum_n e^{-\frac{E_n}{k_b T}}} \quad [2.32]$$

For the system in static magnetic field at temperatures above one Kelvin, the high temperature approximation is valid

$$\rho_{nn}(\infty) = \frac{1}{2I+1} \left(1 - \frac{m_n \gamma B_0}{k_b T} \right) \quad [2.33]$$

The constant term with no time dependence can be disregarded, and the reduced density operator corresponding to the second term is

$$\rho(\infty) = \frac{\gamma B_0 \mathbf{I}_z}{(2I+1)k_b T} \quad [2.34]$$

For example, the ensemble average equilibrium magnetization components for the spin-1/2 and spin-1 systems can be calculated according to Eqs. 2.29 and 2.34

$$\langle \overline{\mathbf{M}}_{x,y} \rangle (I=1/2 \text{ or } 1) = 0, \quad \langle \overline{\mathbf{M}}_z \rangle (I=1/2) = \frac{\gamma^2 B_0}{4k_b T}, \quad \langle \overline{\mathbf{M}}_z \rangle (I=1) = \frac{2\gamma^2 B_0}{3k_b T} \quad [2.35]$$

Thus, no transverse magnetization can be detected at equilibrium for these systems. To create observable magnetization, the state of the spin ensemble should be changed to non-equilibrium involving single quantum coherence density matrix elements, $\rho_{n \pm 1}$.

The time evolution of the density matrix is of great importance for analysis of NMR experimental data. The time dependence of the expansion coefficients of the quantum state vector (Eq. 2.13) is,

$$i \frac{\partial}{\partial t} \langle \phi_m | \psi \rangle = \sum_l \langle \phi_m | \mathbf{H} | \phi_l \rangle \langle \phi_l | \psi \rangle \quad [2.36]$$

Now taking time derivative of the density matrix elements, we obtain

$$\frac{\partial}{\partial t} \langle \phi_n | \rho | \phi_m \rangle = \frac{\partial}{\partial t} \sum_i p_i \langle \phi_n | \psi_i \rangle \langle \psi_i | \phi_m \rangle = -i \sum_l (H_{nl} \rho_{lm} - \rho_{nl} H_{lm}) = i \langle \phi_n | [\rho, \mathbf{H}] | \phi_m \rangle \quad [2.37]$$

$$\frac{\partial}{\partial t} \rho = i[\rho, \mathbf{H}] \quad [2.38]$$

For a time-independent Hamiltonian, integration of the above differential equation results in the solution

$$\rho(t) = e^{-i\mathbf{H}t} \rho(0) e^{i\mathbf{H}t} \quad [2.39]$$

Thus, knowledge of the Hamiltonian and the density matrix at a single time allows the time evolution of the density matrix to be calculated.

In NMR, the Hamiltonian typically consists of a large time-independent interaction, \mathbf{H}_0 , and much smaller time dependent part $\mathbf{H}_1(t)$. To simplify calculations by excluding the large time dependent contribution, the interaction representation of density matrix is introduced

$$\rho^* = e^{-i\mathbf{H}_0 t} \rho e^{i\mathbf{H}_0 t} \quad [2.40]$$

Notice that for the reduced density matrix, $\text{Tr}(\rho^*) = 0$. This operator can be expanded into linear combination of a suitable basis set of $[(2I+1)^2-1]$ operators (equal to the number of the independent ρ_{nm}^* components). For spin-1/2 the basis set consists of three operators, while for spin-1, eight operators are needed.

The equation of motion in the interaction representation is

$$\frac{\partial}{\partial t} \rho^* = i[\rho^*, \mathbf{H}_1^*] \quad [2.41]$$

where \mathbf{H}_1^* is the interaction Hamiltonian:

$$\mathbf{H}_1^* = e^{i\mathbf{H}_0 t} \mathbf{H}_1 e^{-i\mathbf{H}_0 t} \quad [2.42]$$

For a large static field it is possible to perform a transformation of this type into a reference frame rotating about the laboratory z-axis. If the rotation rate of this reference frame is chosen to be equal to the Larmor frequency, any RF field applied at the Larmor frequency will appear to be static in this frame. Such an interaction frame is referred to as the rotating reference frame (RRF). Henceforth, the reduced density matrix and interaction Hamiltonian will always be described in this reference frame, and "*" will be omitted.

To solve the equation of motion for the density matrix we integrate from $t' = 0$ to $t' = t$,

$$\rho(t) = \rho(0) + i \int_0^t [\rho(t'), \mathbf{H}_1(t')] dt' \quad [2.43]$$

This integral equation for ρ can be solved iteratively using successive approximation, as long as \mathbf{H}_1 is small compared to \mathbf{H}_0 . The formal solution is given by,

$$\rho(t) = \rho(0) + i \int_0^t [\rho(0), \mathbf{H}_1(t')] dt' + \int_0^t dt' \int_0^{t'} dt'' [[\rho(0), \mathbf{H}_1(t'')], \mathbf{H}_1(t')] \quad [2.44]$$

2.1.3 NMR Spectrometer and Probe

In order to detect a time-dependent magnetic moment, a coil is placed around the sample, with its axis perpendicular to the static magnetic field. The precessing magnetization induces a tiny, but measurable, current in the sample coil due to the time-varying magnetic flux through its windings. This analog signal can be recorded, digitized, and processed to produce the spectrum.

As discussed in previous section, the phase incoherence of spin ensemble at thermal equilibrium leads to the cancellation of observable magnetization in the xy -plane. To tip the bulk magnetization from the z -axis and introduce detectable components in the xy -plane, an oscillating current in the sample coil creates a magnetic field, \vec{B}_1 , perpendicular to the laboratory z -direction, around which the nuclear moments start to precess. This oscillating field is gated to produce a pulse with a sinc-function excitation profile. The frequency range of this excitation is approximately proportional to the inverse of a pulse length. Thus, short pulses cover broader frequency ranges, which is useful for the detection of NMR spectra in solids, which have large anisotropic interactions. High power levels must be used with short pulses to induce detectable phase coherence, but practical pulse lengths are limited to longer than a microsecond because of rise times in the tuned probe circuits. Thus, the widest frequency coverage that can be achieved using single pulse is less than one megahertz. However, this bandwidth is sufficient to measure all spectral components of hydrogen-1, carbon-13, nitrogen-15 and hydrogen-2 isotopes in independent experiments for the PAMAM dendrimer salt samples studied in this dissertation.

The duration of the pulse and its intensity determines how far the magnetization vector is rotated from equilibrium. A pulse that rotates magnetization by 90° (called a 90 degree pulse, or $\pi/2$ pulse) results in the largest signal, since all of the magnetization is in the xy -plane. All above considerations pertain to the frame rotating at the Larmor frequency in the laboratory frame. The direction in which \vec{B}_1 points in the RRF depends on the pulse phase.

Therefore, the NMR spectrometer must be capable of controlling both the length and the phase of the pulses to coherently manipulate and detect the spin states of the system.

In this study the method used to acquire NMR spectra is pulsed Fourier transform NMR. The signal is generated by irradiating the sample with a short, intense pulse of RF radiation. The response of the sample to the pulse, called a free induction decay (FID), is the sum of the responses of all the nuclei resonant in the sample. The Fourier transform of this time domain FID gives an NMR spectrum. The frequency of a peak in the NMR spectrum corresponds to a particular value of the energy difference of two spin states of the nucleus ($I = 1/2$). The integrated intensity of the peak is proportional to the number of nuclei resonating at that particular frequency.

The spectrometer used for this research (shown schematically in Fig. 2.1) is a custom-built solid state pulsed FT NMR instrument based on 7.048 Tesla magnet (OXFORD). The magnet has a superconducting coil immersed in liquid helium surrounded by vacuum isolation and nitrogen cooling dewar. The magnet bore has a custom-built temperature monitoring system to ensure proper operational conditions and avoid destruction of thermal isolation leading to uncontrollable boil off of cooling liquids. For the normal regime of operation the in-bore temperatures should be maintained in the range from +4 to +40 °C. A static magnetic field of 7 Tesla generated by the persistent current (36 A) in the superconducting magnet removes degeneracy of nuclear energy levels. At this field protons resonate at 300.07 MHz, deuterons at 46.06 MHz, carbon-13 at 75.46 MHz, and nitrogen-15 at 30.41 MHz.

RF pulse generation equipment (transmitter) and signal detection circuitry (receiver) in the spectrometer are controlled by TTL signals from the pulse programmer (Libra, Tecmag) according to the pulse sequence loaded into its memory. A computer interface (MacNMR, Tecmag) allows the user to specify the pulse sequence and to digitize and manipulate the collected data. The pulse programmer uses a 10 MHz clock, and thus has a timing resolution of 100 ns. During experiments the FID voltage is sampled periodically and the

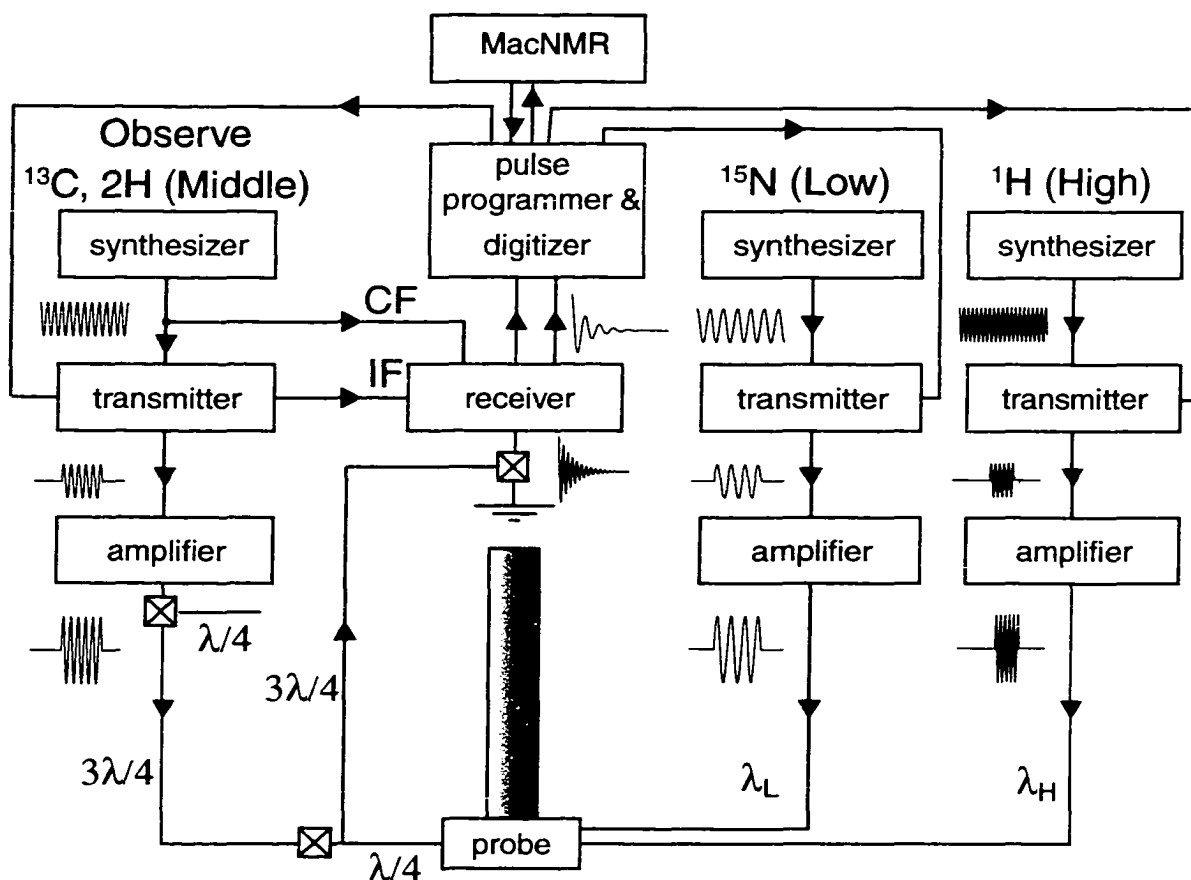


Figure 2.1

Block diagram of the custom-built NMR spectrometer used to perform single, double and triple resonance experiments. The cables to and from the probe are cut to a precise length depending on the Larmor frequency of irradiated nucleus. Crossed diodes insulate the receiver from the high-power pulse, and direct the weak NMR signal to the detecting circuit. The FID is demodulated in the receiver with the signals from the transmitter in "observe" channel, and then digitized by the pulse programmer and can be processed on the computer using the manufacturer's software (MacNMR, version 5.9).

value is stored in the computer as a binary number. The time interval between sampling points, the dwell time, DW , determines the frequency range detected (the width of the spectrum, SW). The highest frequency that can be accurately represented is the Nyquist frequency, $\nu_N = (2 \times DW)^{-1}$ [66]. Frequencies outside the interval $-\nu_N \leq \nu \leq \nu_N$ must be filtered out of the analog signal before digitization. Otherwise they will be aliased into the spectrum at another frequency, $\pm \nu_N + \nu$.

The spectrometer operates in a heterodyne mode. This design minimizes interference of extraneous Larmor frequency signals during both pulse generation and signal detection. To produce an RF pulse, a continuous wave oscillating signal from the stable frequency synthesizer at Larmor plus intermediate frequency (ν_{IF}) is gated by an electronic switch controlled by the pulse programmer. The gating pulses at intermediate frequency ($\nu_{IF} = 30$ MHz) are mixed with the continuous carrier frequency ($\nu_{CF} = \nu_0 + \nu_{IF}$) to produce Larmor frequency pulses, when the upper side band ($\nu_0 + 2\nu_{IF}$) is removed with band pass filters. The transmitter can produce pulses of arbitrary phase with respect to the demodulating (IF) signal. Thus, the RF field in the sample coil can be made to point in any direction in the xy-plane of RRF. After a band pass filtering, the Larmor frequency pulses are amplified and transmitted through coaxial cable (50Ω) to the probe, which contains the sample coil. For multiple resonance experiments several nuclei have to be irradiated simultaneously at their Larmor frequencies. This requires that the spectrometer have several synthesizers, transmitters and amplifiers (Fig. 2.1). For double and triple resonance experiments described in this dissertation the pulse power levels in the triple resonance probe were a few hundred Watts. To achieve uniform excitation of wide line deuterium spectra, the power levels in excess of a kilowatt were applied to the high power, single channel deuterium probe.

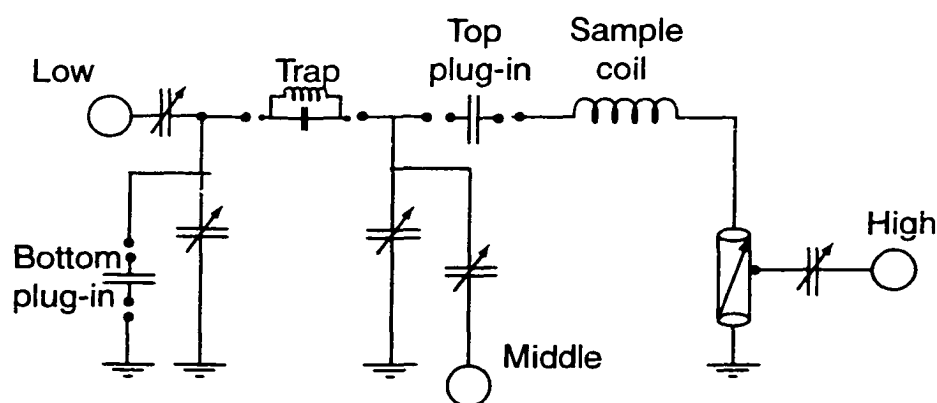


Figure 2.2
Circuit diagram of the triple resonance (Chemagnetics) probe. Three circuits are independently tunable through the choice of plug-in capacitor and trap values, and by adjustment of the variable capacitors. All circuits share an inductor, the sample coil.

NMR probes house resonant circuits that are tuned to match the output impedance of the amplifier and impedance of the cables, at the Larmor frequency. This maximizes the power being transmitted to the probe and minimizes the reflected power. The probe used for double and triple resonance experiments has three tuned circuits that share the sample coil, as shown in Fig. 2.2. This arrangement allows pulses to be simultaneously applied to more than one nuclear species, as well as tune the probe over a wide range of Larmor frequencies by changing the plug-in capacitors and using different channels. The presence of three channels, however, lowers the maximum pulse power accessible. The high power single channel deuteron probe was essentially a L - C - R circuit [67, 68] with a 5 mm coil as the inductor. The probes are capable of withstanding high power pulses (hundreds of Volts) and detection of induced low intensity signals (fraction of a microvolt). Ring down times of the probe circuit after application of high power pulses preclude immediate acquisition of NMR FID. The relaxation time of the circuit, t_r , is proportional to the probe quality factor [68]

$$Q = \frac{2\pi\nu_0 L}{R} \quad [2.45]$$

$$t_r = \frac{Q}{\pi\nu_0} \quad [2.46]$$

$$BW = \frac{\nu_0}{Q} \quad [2.47]$$

where ν_0 is the Larmor frequency of the applied pulse. The bandwidth of the probe, BW (the range of frequencies with little attenuation), is inversely proportional to Q -factor. Therefore, a tradeoff must usually be achieved between ring down time and probe bandwidth, BW , by choosing a coil with appropriate inductance, L , and resistance, R , in the observed frequency range. The experimentally determined Q -factors for deuteron and triple resonance probe are 105 and 220 respectively. Their corresponding ring down times at deuteron Larmor frequency are approximately 20 and 40 μ s. The experimentally determined

probe characteristics follow the relation Eq. 2.46 only qualitatively because non-ideal probe circuitry and other electric components (in receiver line) contribute to measured values.

The triple resonance probe (Chemagnetics) has magic angle spinning capabilities. The sample is contained between a Teflon spacer and bottom cap in the middle of a cylindrical zirconia rotor, with Kel-F turbine top cap. For experiments with air or moisture sensitive compounds finned spacers and bottom caps have to be used. The end caps and spacers are made from materials possessing no signals at the observed frequency in MAS NMR experiments and low thermal expansion coefficients. Clean, dry air or nitrogen forced through small holes in the stator blows on a turbine causing it to turn. The spinning frequency is controlled by a tachometer circuit which monitors the changes in the LED intensity reflected by dark marks painted on the bottom of the rotor. The tachometer output regulates the air valves of the Chemagnetics spin rate controller, and the stable spinning (± 2 Hz) can be achieved for up to 12 kHz.

The temperature around the coil is regulated by passing preheated or precooled nitrogen gas. The temperature is precisely adjusted and maintained to 0.01 °C by a feedback temperature controller (DRC-91CA LakeShore). In the high power deuteron probe, the platinum resistor sensor is placed ~1 cm away from the coil. For this probe calibration showed that the measured and real sample temperatures were equal (to ± 0.5 °C) after 15-20 minutes of thermal equilibration ($T_{\text{real}} = T_{\text{meas}}$). However, the accessible temperature range is only -50 to +100 °C due to poor thermal isolation. In the triple resonance probe, the temperature sensor is placed in the removable variable temperature (VT) stack at least 3 cm above the coil. The stack provides better thermal isolation since the cooling purge gas is passed between the inner tube containing the heater and the outer shield. Since the VT gas path is different from the spinning gas path, heating or cooling the sample does not interfere much with the spinning stability. The operational temperature range for Chemagnetics probe is from -150 to 250 °C. The real sample temperature corresponding to the set one had to be determined through calibration. This was done for different spinning rates, since the

spinning causes frictional heating of the sample. This calibration was performed using ^{207}Pb NMR on lead nitrate, a compound with a known linear temperature dependence of its chemical shift, δ_{iso} . The two points needed to fix the intercept of the calibration line were determined from NMR measurements of the melting points for D_2O ($T_m = 0\text{ }^\circ\text{C}$) and deuterated stearic acid ($T_m = 71\text{ }^\circ\text{C}$). The resulting calibration lines for MAS probe spinning at 0.0, 4.0, and 7.5 kHz are given below.

$$T_{\text{real}}(0.0\text{ kHz}) = (3.1 \pm 0.3) + (0.94 \pm 0.01)T_{\text{meas}} \quad [2.48]$$

$$T_{\text{real}}(4.0\text{ kHz}) = (7.1 \pm 0.4) + (0.94 \pm 0.01)T_{\text{meas}} \quad [2.49]$$

$$T_{\text{real}}(7.5\text{ kHz}) = (12.0 \pm 0.3) + (0.94 \pm 0.01)T_{\text{meas}} \quad [2.52]$$

The heater elements for both probes are nickel wires with magnesium oxide insulation (ARI Industries [69]). They are capable of carrying 1.9 and 5.0 A of current for the deuteron and triple resonance probes respectively. Adequate current levels and heater powers (155 W and 500 W) are provided by a Kepco power supply (Model ATE 150-3.5M). Its output current is regulated by the input voltage (0 to 10 V) from the Lakeshore temperature controller, changing in response to the resistance readings from (110 Ω) platinum resistor sensor.

The coils in the probes which produce the time dependent RF fields are also used to detect precessing magnetization after the pulse. The NMR free induction decay (FID) signal is a voltage ($\sim 1\text{ }\mu\text{V}$) induced in the coil by time-varying magnetization vector. This tiny analog FID signal is passed into a preamplifier (30 dB gain) which is protected by crossed diodes to ground and, following additional high gain broad band amplification (60 dB), into the heterodyne receiver, and the demodulator. Demodulation in the receiver shifts all the frequencies from the RF range (10 – 1000 MHz) to the audio frequency range (0 – 500 kHz). Audio frequency signals are much easier to amplify, filter, and digitize. The NMR

signal is demodulated in two steps: first with carrier frequency and then phase coherently with intermediate frequency (30 MHz) reference signal from the transmitter. Demodulation effectively corresponds to observation in the RRF. The phase difference between the receiver and reference signal determines where the induced magnetic field points in the rotating frame. The IF demodulation step is performed in quadrature, resulting in the separation of the real and imaginary signal components. The two components are then sent through matched audio amplifier, low pass analogue filters and digitized by two analog to digital converters in the Libra pulse programmer. To improve S/N ratio coherent signal averaging is done in the Libra memory, and phase cycling is used to reduce spectral artifacts.

A complex Fourier transform of NMR signal has both positive (faster than RRF) and negative (slower than RRF) frequencies. This doubles the range of signals that can be acquired with a particular dwell time. Thus, for typical deuteron spectra from -200 to $+200$ kHz (400 kHz full spectral width) a dwell time of $2.5 \mu\text{s}$ is appropriate to avoid aliasing. Discrete sampling and the finite length of the time-domain data set may limit frequency resolution especially when FT spectra have only a few points defining the resonance peak. Rather than increase the number of acquisition points (acquisition time) it is often useful to increase digital resolution by zero-filling time-domain data sets and subsequently increasing the number of points in FT spectra for the fixed spectral width [66].

A few spectral artifacts may arise due to hardware limitations. In quadrature detection there may be a difference in baseline offset between two channels, which causes the presence of a prominent peak at the center of FT spectrum. A baseline correction is applied to bring each channel offset to zero before FT in such cases. Due to a fixed time delay between excitation and detection, t_0 (which depends on the electronics ring-down time) the phases of the acquired signal may vary with frequency in the FT spectrum because of the linear phase shift, ωt_0 , accumulated during the delay. In such cases, if experimental techniques avoiding the influence of the delay are not available, constant and linear phase

correction are applied to FT spectra [66]. This computerized procedure is equivalent to rotation of real and imaginary components of the complex spectra by the angle $\phi(\omega) = \phi_0 + k(\omega - \omega_p)$ in xy-plane. The rate of the phase change with frequency is given by k , and ω_p is a pivot frequency (corresponding to the line with no distortion after the constant phase correction by ϕ_0) with respect to which the phase is growing linearly.

For a single FID the intrinsic signal to noise ratio (S/N) is dependent on spectrometer electronics. For most samples single scan S/N is not enough for quantitative study. Thousands of FIDs may be required to increase S/N by coherent averaging in long experiments. Spectral lines are sometimes artificially broadened in an effort to boost the S/N and save experimental time. The quantitative characterization of the artificially broadened spectra should be still possible when the broadening does not compromise resolution, i.e. does not smear the difference between distinct resonances in the spectrum. Moderate broadening (a few hundred hertz) is usually acceptable for most deuteron solid state NMR spectra, since this is smaller than the line width associated with the anisotropic quadrupolar interactions. In a process, known as apodization, the FID is multiplied by a function, usually a decaying exponential, prior to FT. As a result, the width of each line in the spectrum increases, since the multiplication of the functions in a time domain corresponds to convolution of their Fourier transforms in a frequency domain [66]. The effect of convolution is to distribute the intensity of each point in the spectrum thus smoothing the jagged random noise. Notwithstanding the line broadening, some features that are obscured by noise may show up clearly after apodization. The amount of line broadening in Hz, $\Delta\nu$, applied to the spectrum is the full width at half maximum intensity of the Fourier transform of the apodizing function. For the decaying exponential, $\exp(-\pi\Delta\nu t)$, the Fourier transform is a Lorentzian [66] with a maximum at $\nu = 0$ and half maximum at $\Delta\nu$. For Gaussian apodization [66], $\exp(-t^2\Delta\nu^2\pi^2(4\log_2)^{-1})$, the spectra are convoluted with the Gaussian of half maximum at $\Delta\nu$.

2.2 Static Interactions

In addition to external magnetic field, internal fields in the sample influence nuclear energy levels. For spin-1/2 and spin-1 nuclei, these fields originate from the interaction of the nuclear magnetic dipole moment with the surrounding electrons (\mathbf{H}_σ) and with other magnetic dipoles (\mathbf{H}_D). For $I \geq 1$, the nuclear electric quadrupole moment interacts with the electric field gradient at the site of the nucleus. These interactions are of relevance for ^1H , ^{13}C , ^{15}N and ^2H NMR experiments on the dendrimers which will be discussed in the following chapters. The total Hamiltonian describing time-independent states of the nuclear system is a sum of the static Hamiltonians for each of these interactions

$$\mathbf{H} = \mathbf{H}_Z + \mathbf{H}_\sigma + \mathbf{H}_D + \mathbf{H}_Q \quad [2.51]$$

$$\{10^7 - 10^8 \text{ Hz}\} \quad \{10^3 - 10^4 \text{ Hz}\} \quad \{10^1 - 10^5 \text{ Hz}\} \quad \{10^4 - 10^6 \text{ Hz}\}$$

where \mathbf{H}_Z is the Hamiltonian determining the Zeeman interaction with static external field, \mathbf{H}_σ is the chemical shielding of the nucleus by local electron density, \mathbf{H}_D describes the dipole interactions, and \mathbf{H}_Q is the quadrupolar term for $I > 1/2$. The approximate interaction strengths listed below the Hamiltonians are valid for the present study. It is obvious that chemical shielding, dipolar and quadrupolar interactions (strength $\ll 10^7$ Hz) can be considered as perturbations to the Zeeman Hamiltonian. The effect of these perturbing interactions is the source of information about local environments of the resonating nucleus in the solid state.

All of the above-mentioned interactions can be written in terms of Cartesian vector-tensor products $\vec{V}_1 \mathbf{T} \vec{V}_2$, from which sums of the spherical irreducible tensor products can be constructed [62, 70]. The general form of interaction Hamiltonian is,

$$\mathbf{H}_{\text{int}} = \sum_{l=0}^{l_{\text{max}}} \sum_{m=-l}^l (-1)^m A_{-m}^{(l)} T_m^{(l)} \quad [2.52]$$

The maximum rank of the tensor involved in the interaction description, l_{\max} , is determined by the selection rules for allowed quantum transitions between stationary spin states. This construction is useful since it allows separation of any interaction into two parts: one depending only on the nuclear spin operators ($A_m^{(l)}$), and the other depending on the electronic states and spatial coordinates of the interacting local fields ($T_m^{(l)}$). In addition, coordinate transformations of these tensors can be done using Wigner rotation matrix formalism (Eq. 2.25).

2.2.1 Zeeman Hamiltonian

The strongest interaction which removes nuclear energy level degeneracy in external magnetic field is the Zeeman interaction (cf. Eq. 2.5). In terms of spherical irreducible tensors (Eq. 2.52), \mathbf{H}_Z can be written as follows:

$$\mathbf{H}_Z = A_0^{(0)} T_0^{(0)}, \quad A_0^{(0)} = B_0 \mathbf{I}_z, \quad T_0^{(0)} = -\gamma \quad [2.53]$$

Being a scalar, $T_0^{(0)}$ is preserved during coordinate transformations. Thus, as expected, Zeeman energy levels are never anisotropic (transition frequencies are independent of the system geometry). As was discussed in section 2.1.2, the effect of the Zeeman interaction is the presence of two (spin-1/2) and three (spin-1) equally spaced energy levels with the frequency difference between neighboring levels given by Larmor frequency of magnetization precession around the external field. The gyromagnetic ratios and Larmor frequencies are known for all magnetically active isotopes. In the rotating reference frame (RRF), usually used in solid state NMR experiments, the Zeeman resonance frequency is shifted to zero.

2.2.2 Chemical Shielding

When placed in an external magnetic field, electrons in molecules produce complicated current loops inducing magnetic fields opposing (in most cases) the applied field. Due to this diamagnetic effect, electrons are said to "shield" the nucleus from external magnetic field. Chemical shielding tensor depends on electronic current density in the vicinity of the nucleus, which is determined by the many-electron molecular wave function describing the electronic state under the influence of electrostatic potentials and the static magnetic field [71]. The electron density localization is highly dependent on the chemical bonds in the molecule. As a result, chemically distinct nuclei experience different chemical shielding. If the local electronic surrounding of a particular group is almost the same in different molecules, the chemical shielding for this group will not change much from compound to compound. This property is widely used for the assignment of the resonances in solution state NMR spectra of molecules with unknown structure from the known chemical shifts of different functional groups.

For a particular nucleus, the size of the chemical shielding interaction is proportional to the strength of the applied external magnetic field. To facilitate the comparison of spectra acquired using different static magnetic fields, the resonance frequencies are expressed in dimensionless units, called chemical shifts. They are reported in parts per million (ppm) relative to the frequency of a reference compound. The standard reference compound for carbon-13 and proton NMR is tetramethylsilane (TMS) which has an unusually high chemical shielding. The chemical shift, δ , is calculated from the resonance frequencies of the compound, ν , and TMS, ν_{TMS} , at the same field strength by [63]:

$$\delta = \frac{\nu - \nu_{TMS}}{\nu_{TMS}} \times 10^6 \quad [2.54]$$

The range of chemical shifts for ^{13}C spans a few hundred ppm, while for proton spectra it is of order 10 ppm. The greater the chemical shift, the higher the observed NMR frequency, and the lower the chemical shielding at the observed site.

Chemical shielding is anisotropic. Empirically, it is described by a second-rank tensor or a corresponding quantum mechanical operator. In general, the chemical shielding tensor is not symmetric, but it can be decomposed into symmetric and anti-symmetric parts. The anti-symmetric part has negligible effect on NMR spectra [70]. For the symmetric real-valued matrix there exists special principle axes system (PAS), where this matrix is diagonal, $\sigma_{ij}(\text{PAS}) = \sigma_{ij}\delta_{ij}$. Therefore, NMR measurements of the chemical shielding tensor in a laboratory-fixed frame (LAB) may allow determination of the tensor components in its PAS frame, as well as the PAS frame orientation with respect to the static magnetic field. The chemical shielding Hamiltonian in a laboratory fixed frame in the general case is [61]:

$$\mathbf{H}_\sigma = \gamma \bar{\mathbf{I}} \sigma \bar{\mathbf{B}} \quad [2.55]$$

It can be rewritten in terms of the irreducible spherical tensor products according to Eq. 2.52, where $l_{\text{max}} = 2$, and tensor components are [70]

$$\begin{aligned} A_{\pm 2}^{(2)} &= \frac{1}{2} [B_x \mathbf{I}_x - B_y \mathbf{I}_y \pm i(B_x \mathbf{I}_y + B_y \mathbf{I}_x)], & A_{\pm 1}^{(2)} &= \mp \frac{1}{2} [B_x \mathbf{I}_z - B_z \mathbf{I}_x \pm i(B_y \mathbf{I}_z + B_z \mathbf{I}_y)], \\ A_0^{(2)} &= \sqrt{\frac{2}{3}} [B_z \mathbf{I}_z - \frac{1}{2}(B_x \mathbf{I}_x + B_y \mathbf{I}_y)], & A_{\pm 1}^{(1)} &= B_z \mathbf{I}_x - B_x \mathbf{I}_z \pm \frac{i}{2}(B_z \mathbf{I}_y - B_y \mathbf{I}_z), \\ A_0^{(1)} &= -\frac{i}{\sqrt{2}} (B_y \mathbf{I}_x - B_x \mathbf{I}_y), & A_0^{(0)} &= -\frac{1}{\sqrt{3}} (B_x \mathbf{I}_x + B_y \mathbf{I}_y + B_z \mathbf{I}_z) \\ T_{\pm 2}^{(2)} &= \frac{1}{2} (\sigma_{xx} - \sigma_{yy}) \pm i\sigma_{xy}, & T_{\pm 1}^{(2)} &= \mp (\sigma_{xz} \pm i\sigma_{yz}), & T_0^{(2)} &= \sqrt{\frac{2}{3}} (\sigma_{zz} - \frac{1}{2}(\sigma_{xx} + \sigma_{yy})), \\ T_{\pm 1}^{(1)} &= 0, & T_0^{(1)} &= 0, & T_0^{(0)} &= -\frac{1}{\sqrt{3}} (\sigma_{xx} + \sigma_{yy} + \sigma_{zz}) \end{aligned} \quad [2.57]$$

Usually the direction of the external field is taken to be along the laboratory z-axis. Furthermore, the chemical shielding is only a small perturbation (Eq. 2.51) to the Zeeman Hamiltonian. Thus, to the first order, the \mathbf{A} terms proportional to \mathbf{B}_x , \mathbf{B}_y , and \mathbf{I}_x , \mathbf{I}_y , (which do

not commute with \mathbf{I}_z) may be ignored. Therefore, the expression for the chemical shielding Hamiltonian in the laboratory frame simplifies to

$$\mathbf{H}_\sigma(LAB) = A_0^{(0)}T_0^{(0)}(LAB) + A_0^{(2)}T_0^{(2)}(LAB) = \gamma_z B_z \sigma_{zz} \quad [2.58]$$

This shows that in the laboratory fixed frame chemical shielding frequencies are proportional to Larmor frequencies (Eq. 2.6).

In a PAS frame chemical shielding tensor, σ , is diagonal, and can be described by three conventional quantities, σ_{iso} , η and σ_{33} , related to its PAS values in the following way:

$$\sigma_{iso} = \frac{1}{3}Tr(\sigma), \quad \eta = \frac{\sigma_{11} - \sigma_{22}}{\sigma_{33} - \sigma_{iso}}, \quad \sigma_{11} \leq \sigma_{22} \leq \sigma_{33} \quad [2.59]$$

The T components (Eq. 2.57) in the PAS system can be rewritten in terms of the characteristic chemical shielding parameters

$$\begin{aligned} T_{\pm 2}^{(2)}(PAS) &= \frac{\eta}{2}(\sigma_{33} - \sigma_{iso}), & T_{\pm 1}^{(2)}(PAS) &= 0, & T_0^{(2)}(PAS) &= \sqrt{\frac{3}{2}}(\sigma_{33} - \sigma_{iso}), \\ T_{\pm 1}^{(1)}(PAS) &= 0, & T_0^{(1)}(PAS) &= 0, & T_0^{(0)} &= -\sqrt{3}\sigma_{iso} \end{aligned} \quad [2.60]$$

Applying the coordinate frame transformation $(\alpha_{PL}, \beta_{PL}, 0)$ to the spherical irreducible tensors (Eqs. 2.25 and 2.26), to rotate PAS) into LAB, an expression for σ_{zz} , in terms of the PAS values of the chemical shielding tensor (Eq. 2.59) can be found [61],

$$\mathbf{H}_z(LAB) = A_0^{(0)}d_{00}^{(0)}(\beta_{PL})T_0^{(0)}(PAS) + A_0^{(2)} \left[\begin{aligned} &d_{00}^{(2)}(\beta_{PL})T_0^{(2)}(PAS) \\ &+ d_{20}^{(2)}(\beta_{PL})T_2^{(2)}(PAS)(e^{-i2\alpha_{PL}} + e^{i2\alpha_{PL}}) \end{aligned} \right] \quad [2.61]$$

$$\sigma_{zz} = \frac{\sigma_{33} - \sigma_{iso}}{2} \left(\frac{2\sigma_{iso}}{\sigma_{33} - \sigma_{iso}} + 3\cos^2 \beta_{PL} - 1 + \eta \sin^2 \beta_{PL} \cos 2\alpha_{PL} \right) \quad [2.62]$$

For a single crystal, with known orientation of its symmetry axis with respect to external magnetic field, the three PAS components of the chemical shielding tensor can be directly determined from the orientation dependence of sharp peaks in the experimental spectrum, since only distinct orientations $(\alpha_{PL}, \beta_{PL})$ will be present. However, for many samples it is not possible to grow single crystals large enough for (low sensitivity) NMR experiments. In

addition, many solid materials, like glassy amorphous polymers, do not have a regular crystal structure. Powdered crystalline and rigid glassy samples show a continuous distribution of orientations of the chemical shielding PAS, or so called "chemical shielding anisotropy" (CSA). As a result, spectral lines from such substances are distributed over a range of resonance frequencies. Notwithstanding diminished resolution, the spectrum contains information on all possible orientations, and has a characteristic lineshape referred to as a "powder pattern". Equation 2.62 shows that, for particular orientations of PAS chemical shielding tensor with respect to LAB system, the σ_{PAS} components can be directly measured from the spectrum,

$$\sigma_{\underline{z}}(\beta_{\text{PL}} = 0) = \sigma_{33}, \quad \sigma_{\underline{z}}(\beta_{\text{PL}} = \frac{\pi}{2}, \alpha_{\text{PL}} = 0) = \sigma_{11}, \quad \sigma_{\underline{z}}(\beta_{\text{PL}} = \frac{\pi}{2}, \alpha_{\text{PL}} = \frac{\pi}{2}) = \sigma_{22} \quad [2.63]$$

It turns out that the experimental CSA powder pattern spectra has intensity discontinuities which occur exactly at these orientations.

For CSA powder spectrum the intensity at a given frequency is proportional to the probability to find a randomly chosen nucleus at an orientation corresponding to this frequency or, equivalently, to $\sigma = \sigma_{\underline{z}}(\text{LAB})$ (Eq. 2.62). Therefore, frequency dependent intensity distribution constituting powder can be predicted from the σ -dependent orientational probability, $P(\Omega)$,

$$I(\sigma) = \frac{dP(\Omega(\sigma))}{d\sigma} \quad [2.64]$$

The probability of finding a certain orientation in an isotropic distribution (e.g. in case of the powdered sample) is:

$$dP(\Omega(\sigma)) = \frac{\sin \beta(\sigma) d\beta d\alpha}{4\pi} \quad [2.65]$$

It is obvious that more spins can be found at the orientation $\beta = \beta_{\text{PL}} = \pi/2$ than at $\beta_{\text{PL}} = 0$. Thus the lowest intensity corresponds to $\sigma_{\underline{z}}(\beta_{\text{PL}} = \pi/2) = \sigma_{33}$. For the simple case of an axially symmetric chemical shielding tensor, $\sigma_{11} = \sigma_{22}$ ($\eta = 0$), the analytical frequency

dependence of CSA intensity is easy to evaluate using Eq. 2.62 and substituting $\sin\beta d\beta = d(-\cos\beta)$ in Eq. 2.65 by

$$d(\cos\beta(\sigma)) = d\sqrt{\frac{2\sigma - 3\sigma_{iso} + \sigma_{33}}{3(\sigma_{33} - \sigma_{iso})}} = d\sqrt{\frac{\sigma - \sigma_{11}}{\sigma_{33} - \sigma_{11}}} \quad [2.66]$$

$$I(\sigma) = \frac{1}{2\sqrt{(\sigma_{33} - \sigma_{11})(\sigma - \sigma_{11})}} \quad [2.67]$$

Then, to find an observed digitized spectral intensity we need to integrate over a frequency bin $\Delta\nu = 2xSW/\text{points}(\text{FID})$, corresponding to $\Delta\sigma$:

$$I(\sigma_i) = \int_{\sigma_i - \frac{\Delta\sigma}{2}}^{\sigma_i + \frac{\Delta\sigma}{2}} I(\sigma) d\sigma = \frac{\sqrt{\sigma_i + \frac{\Delta\sigma}{2} - \sigma_{11}} - \sqrt{\sigma_i - \frac{\Delta\sigma}{2} - \sigma_{11}}}{\sqrt{\sigma_{33} - \sigma_{11}}} \quad [2.68]$$

Thus, for $\sigma_{11} \leq \sigma \leq \sigma_{33}$, the highest intensity will correspond to $\nu = \nu_0\sigma_{11}$ (ν_0 is the Larmor frequency). Then it will decrease according to a square-root law to the minimum value at $\nu = \nu_0\sigma_{33}$.

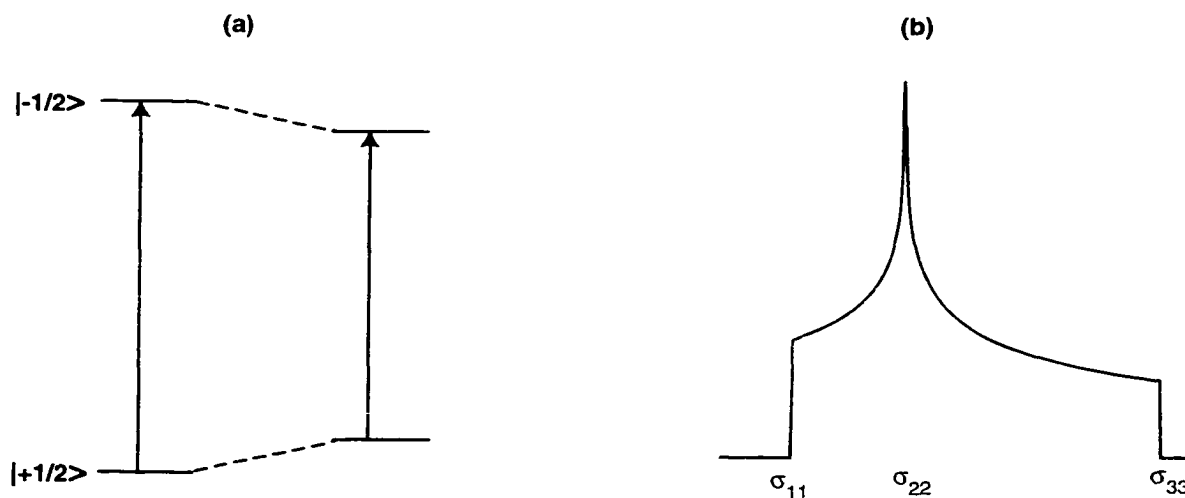


Figure 2.3
Zeeman energy levels for the spin-1/2 eigenstates, and the shifts caused by the chemical shielding interaction (a). The anisotropy of this interaction results in a powder pattern (b).

In the case of non-symmetric chemical shielding tensor the analytical expression can be written to incorporate the α_{PL} -dependence in Eq. 2.67. Since $\alpha = \alpha_{\text{PL}}$ appears only as the argument of squared trigonometric functions ($\cos 2\alpha = \cos^2 \alpha - \sin^2 \alpha$ in Eq. 2.62), the integration and normalization can be restricted to the first quadrant.

$$I(\sigma) = \frac{1}{\pi} \int_0^{\frac{\pi}{2}} \frac{d\alpha}{\sqrt{(\sigma_{33} - \sigma_{11} \cos^2 \alpha - \sigma_{22} \sin^2 \alpha)(\sigma - \sigma_{11} \cos^2 \alpha - \sigma_{22} \sin^2 \alpha)}} \quad [2.69]$$

This expression can be rewritten in the form of complete elliptic integral [61, 70], or efficiently evaluated numerically using SUMS algorithm [72]. An example of CSA powder pattern, calculated with SUMS, and the effect of the chemical shielding on the Zeeman energy levels are shown in Fig. 2.3 (b) and (a). The range of the observed chemical shifts (Eq. 2.54) in solid powdered samples spans from $\delta_{33} \sim -\nu_0 \sigma_{33}$ to $\delta_{11} \sim -\nu_0 \sigma_{11}$. The characteristic discontinuities in the chemical shielding spectrum correspond to σ_{11} , σ_{22} and σ_{33} , in order of increasing frequency.

2.2.3 Dipolar Interaction

Two magnetic dipole moments, $\bar{\mu}_1$ and $\bar{\mu}_2$, interact with the classical energy [73],

$$E = \frac{(\bar{\mu}_1, \bar{\mu}_2)}{r^3} - 3 \frac{(\bar{\mu}_1, \bar{r})(\bar{\mu}_2, \bar{r})}{r^5} \quad [2.70]$$

where \bar{r} is the vector from $\bar{\mu}_1$ to $\bar{\mu}_2$. Two nuclei in external magnetic field will behave as quantum dipoles, and their interaction is described by a quantum mechanical Hamiltonian,

$$\mathbf{H}_D = \bar{\mathbf{I}}^{(1)} \mathbf{D} \bar{\mathbf{I}}^{(2)} \quad [2.71]$$

$$D_{ij} = \frac{\gamma_1 \gamma_2}{r^3} (\delta_{ij} - 3\bar{e}_i \bar{e}_j) \quad [2.72]$$

in which D_{ij} are the components of Cartesian dipole coupling tensor, and the dipolar moments are replaced by operators [61]

$$\bar{\mathbf{M}}^{(1)} = \gamma_1 \hbar \bar{\mathbf{I}}^{(1)}, \quad \bar{\mathbf{M}}^{(2)} = \gamma_2 \hbar \bar{\mathbf{I}}^{(2)} \quad [2.73]$$

$\bar{\mathbf{I}}^{(1)}$ and $\bar{\mathbf{I}}^{(2)}$ are spin angular momentum operators of the two nuclei, and γ_1 and γ_2 are their gyromagnetic ratios. For an isolated $\bar{\mathbf{I}}^{(1)} \dots \bar{\mathbf{I}}^{(2)}$ spin pair the dipolar Hamiltonian can be written in terms of the second rank irreducible spherical tensors [52]

$$\mathbf{H}_D = \sum_{m=-2}^2 (-1)^m A_{-m}^{(2)} T_m^{(2)} \quad [2.74]$$

where the operators in spin (**A**) and real (**T**) space are

$$A_{\pm 2}^{(2)} = \frac{1}{2} \mathbf{I}_{\pm}^{(1)} \mathbf{I}_{\pm}^{(2)}, \quad A_{\pm 1}^{(2)} = \mp \frac{1}{2} (\mathbf{I}_z^{(1)} \mathbf{I}_{\pm}^{(2)} + \mathbf{I}_z^{(2)} \mathbf{I}_{\pm}^{(1)}), \quad A_0^{(2)} = \frac{1}{\sqrt{6}} (3 \mathbf{I}_z^{(1)} \mathbf{I}_z^{(2)} - \bar{\mathbf{I}}^{(1)} \bar{\mathbf{I}}^{(2)}) \quad [2.75]$$

$$T_{\pm 2}^{(2)}(PAS) = T_{\pm 1}^{(2)}(PAS) = 0, \quad T_0^{(2)}(PAS) = -\sqrt{6} \omega_D \quad [2.76]$$

$$\omega_D = \frac{\gamma_1 \gamma_2}{r^3} \quad [2.77]$$

Here ω_D is a dipolar coupling constant for the spins separated by the distance r , $\mathbf{I}_{\pm} = \mathbf{I}_x \pm i \mathbf{I}_y$ are raising and lowering operators for the spin I nucleus. Since \mathbf{H}_D exerts only a small perturbation on Zeeman energy levels (Eq. 2.51), to the first order the **A** terms proportional to \mathbf{I}_x or \mathbf{I}_y , not commuting with $\mathbf{H}_z = -\gamma_1 B_0 \bar{\mathbf{I}}^{(1)} - \gamma_2 B_0 \bar{\mathbf{I}}^{(2)}$, can be ignored. The strength of the dipolar interaction grows with increasing gyromagnetic constants and decreasing internuclear distance. For instance, in case of a directly bonded carbon-proton spin pair ($r = 1.1 \text{ \AA}$) the dipolar strength is about 25 kHz. In a polycrystalline sample the orientation dependence of dipolar interaction results in a powder pattern spectrum observed in a laboratory fixed frame (similar to CSA case (Eq. 2.67)), due to the $\cos^2 \beta$ dependence of the resonance frequencies:

$$T_0^{(2)}(LAB) = d_{\infty}^{(2)}(\beta_{PL}) T_0^{(2)}(PAS) = -\frac{\sqrt{6}}{2} \omega_D (3 \cos^2 \beta_{PL} - 1) \quad [2.78]$$

In case of two spin-1/2 system, dipolar coupling to spin $I^{(2)}$, which has two eigenstates, will split each level of spin $I^{(1)}$ in two as illustrated in Fig. 2.4 (a). With respect to the central Larmor frequency transition for $I^{(1)}$, two symmetric lines will be observed in the dipolar spectrum for each powder orientation, producing a characteristic Pake doublet (see Fig. 2.4 (b)). Due to axial symmetry of the dipolar interaction ($T_{\pm 2}^{(2)} = 0$), the powder pattern is symmetric, and its width depends on the dipolar coupling strength, ω_D (Eq. 2.77).

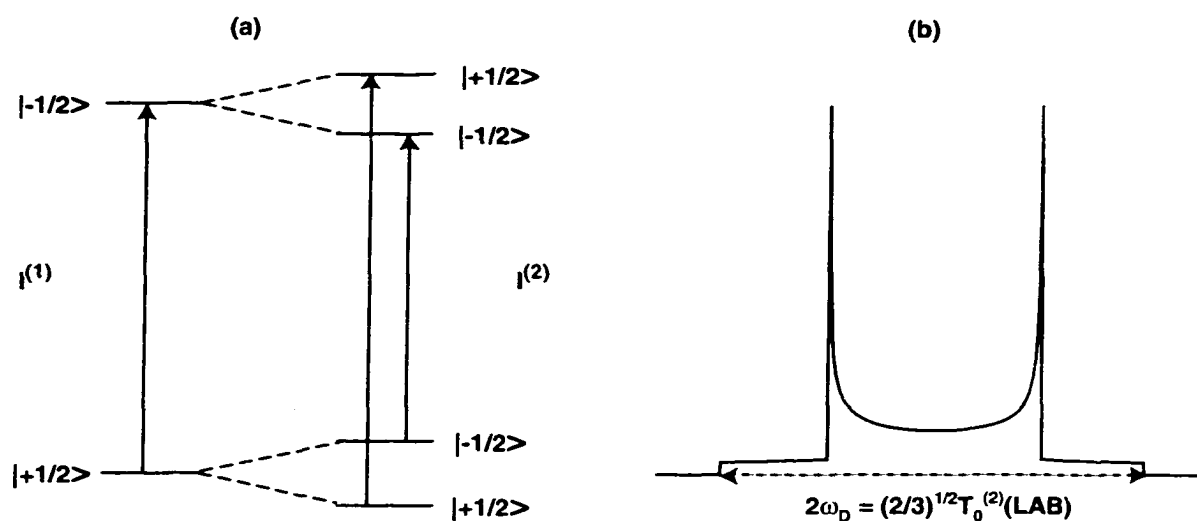


Figure 2.4

(a) The shift of Zeeman energy levels for $I^{(1)}$ nucleus due to dipolar interaction with $I^{(2)}$ nucleus in case of a single spin-1/2 pair. (b) Axially symmetric dipolar Pake doublet powder pattern observed in case of a powdered sample.

In case of multiple dipolar coupled spin pairs with different internuclear distances, the spectrum would comprise many overlapping Pake doublets, producing broad unstructured lines. For heteronuclear spin pairs such an undesirable broadening can be removed by applying long decoupling pulses at the Larmor frequency of the $I^{(2)}$ spins, while $I^{(1)}$ signal is acquired. If the applied decoupling field is stronger than dipolar interaction, the latter is effectively averages to zero. This technique is known as RF decoupling. When Larmor frequencies of dipolar coupled spins are very different (e.g. for protons $\nu_0^H = 300.07$ MHz, and for carbons $\nu_0^C = 75.46$ MHz), the application of the decoupling field does not

influence the observed signal. In case of homonuclear spin pairs ($I^{(2)}$ and $I^{(1)}$ are the same nucleus), the spectra can be considerably influenced by dipolar coupling especially if the spins are close in space. In such cases, low natural abundance of the observed spin (e.g. 1 % for ^{13}C) assures that the internuclear distances are too long to significantly influence the spectra.

2.2.4 Quadrupolar Interaction

The classical interaction energy between the nucleus and surrounding electrons can be readily factored into multipole expansions dependent on electron and nuclear coordinates separately [71], because of the 10^5 ratio between electron orbital and nuclear radius. The angle dependence of the interaction is contained in spherical harmonics (eigenfunctions of angular momentum operator [61]), which are irreducible spherical tensors [62]. The quantum mechanical Hamiltonian for quadrupolar interaction of spin-1 system (deuteron), can therefore be written in the form (Eq. 2.52, $l = l_{\text{max}} = 2$) [52]:

$$\mathbf{H}_Q = \bar{\mathbf{I}}\mathbf{Q}\bar{\mathbf{I}} = \sum_{m=-2}^2 (-1)^m A_{-m}^{(2)} T_m^{(2)} \quad [2.79]$$

$$Q_{ij} = \frac{eQ}{2I(2I-1)} \frac{\partial^2 V}{\partial x_i \partial x_j}, \quad x_i, x_j = x, y, z \quad [2.80]$$

$$A_{\pm 2}^{(2)} = \frac{1}{2} \mathbf{I}_{\pm}^2, \quad A_{\pm 1}^{(2)} = \mp \frac{1}{2} (\mathbf{I}_z \mathbf{I}_{\pm} + \mathbf{I}_{\pm} \mathbf{I}_z), \quad A_0^{(2)} = \frac{4}{\sqrt{6}} (3\mathbf{I}_z^2 - \bar{\mathbf{I}}\bar{\mathbf{I}}) \quad [2.81]$$

$$T_{\pm 2}^{(2)}(PAS) = \frac{\eta\chi}{4}, \quad T_{\pm 1}^{(2)}(PAS) = 0, \quad T_0^{(2)}(PAS) = \frac{\sqrt{6}\chi}{4} \quad [2.82]$$

$$\chi = e^2 q_{zz} Q \quad [2.83]$$

$$\eta = \frac{q_{xx} - q_{yy}}{q_{zz}} \quad [2.84]$$

Here \mathbf{Q} is the Cartesian quadrupole coupling tensor (symmetric, traceless), eQ is the nuclear quadrupole moment, V is orientation dependent electrostatic potential produced by the electrons surrounding the nucleus, V_{ij} defines the elements of the electric field gradient tensor (EFG), and q_{ii} are the components of \mathbf{Q} in its principle axes system, $\chi \geq 0$ (in Hz) is called a quadrupole coupling constant, and $0 \leq \eta \leq 1$ is a unitless asymmetry parameter of EFG tensor, when its PAS components satisfy the inequality: $|q_{xx}| \leq |q_{yy}| \leq |q_{zz}|$. Spin (\mathbf{A}) and spatial (\mathbf{T}) operators are separated in the spherical irreducible tensor representation.

For deuterons, the quadrupolar interaction is dominant, and dipolar and chemical shielding interactions are negligible in comparison. Its strength is still order of 10^{-3} smaller than Zeeman term (Eq. 2.51). Therefore, it produces a shift of the Zeeman levels (Fig. 2.5 (a)), which can be calculated using the first order time independent perturbation theory.

$$E_m = E_m^{(0)} + \Delta E_Q = E_m^{(0)} + H_Q^{mm} = E_Z^m + E_Q^m \quad [2.85]$$

The full quadrupole Hamiltonian in RRF is

$$H_Q = \begin{pmatrix} \frac{1}{\sqrt{6}} T_0^{(2)} & \frac{1}{\sqrt{2}} T_{-1}^{(2)} & T_{-2}^{(2)} \\ \frac{1}{\sqrt{2}} T_{+1}^{(2)} & -\frac{2}{\sqrt{6}} T_0^{(2)} & -\frac{1}{\sqrt{2}} T_{-1}^{(2)} \\ T_2^{(2)} & -\frac{1}{\sqrt{2}} T_{+1}^{(2)} & \frac{1}{\sqrt{6}} T_0^{(2)} \end{pmatrix} \quad [2.86]$$

Thus, the shifts for the three deuteron ($I = 1$) Zeeman energy levels ($|-1\rangle$, $|0\rangle$, $|+1\rangle$) to first order are:

$$\Delta E_Q^{-1,+1} = \frac{1}{\sqrt{6}} T_0^{(2)} \quad [2.87]$$

$$E_Q^0 = -\frac{2}{\sqrt{6}} T_0^{(2)} \quad [2.88]$$

This means that instead of single transition at the Larmor frequency, two transitions symmetrically shifted by $\pm \frac{3}{\sqrt{6}} T_0^{(2)}$ in respect to Zeeman frequency (or zero in RRF) will show up in the spectra, as illustrated in Fig. 2.5.

As in the cases of the chemical shielding and dipolar coupling, for powders, an orientation dependent distribution of doublets will be observed in deuteron spectrum.

$$T_0^{(2)}(LAB) = \sum_{m=-2}^2 D_{m0}^{(2)}(\Omega_{PL}) T_m^{(2)}(PAS) = d_{00}^{(2)}(\beta_{PL}) T_0^{(2)}(PAS) + d_{20}^{(2)}(\beta_{PL}) T_2^{(2)}(PAS) (e^{-i2\alpha_{PL}} + e^{i2\alpha_{PL}}) \quad [2.89]$$

where Ω_{PL} are Euler angles relating the PAS and the LAB frames, and the components of Wigner rotation matrices, $D_{ij}^{(2)}(\Omega_{PL})$, for the second rank spherical tensor transformation are tabulated in Brink and Satchler [65].

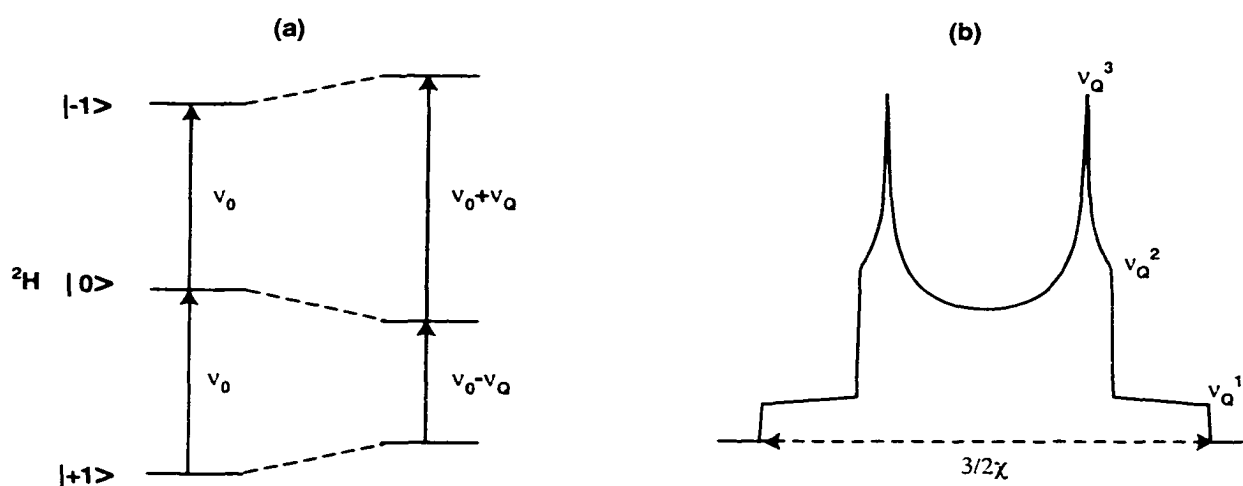


Figure 2.5

(a) Zeeman ^2H levels and quadrupolar shifts. (b) Powder pattern resulting from the two overlapping anisotropies of quadrupolar transitions. The values of quadrupole coupling parameters can be found from discontinuity positions (ν_Q^1 , ν_Q^2 , and ν_Q^3) according to Eqs. 2.91 and 2.92.

It is convenient to characterize the experimentally observed resonances in deuteron spectra by the distance between quadrupolar doublet components

$$2\nu_Q = \sqrt{6} T_0^{(2)}(LAB) = \frac{3}{4} \chi [3 \cos^2 \beta_{PL} - 1 + \eta \sin^2 \beta_{PL} \cos 2\alpha_{PL}] \quad [2.90]$$

The frequency positions of the powder pattern discontinuities, indicated in Fig. 2.5 (b), provide information on the quadrupole coupling parameters:

$$\chi = \frac{4}{3} \nu_Q^1(\beta_{PL} = 0) \quad [2.91]$$

$$\eta = \frac{\nu_Q^2(\beta_{PL} = \frac{\pi}{2}, \alpha_{PL} = \frac{\pi}{2}) - \nu_Q^3(\beta_{PL} = \frac{\pi}{2}, \alpha_{PL} = 0)}{\nu_Q^1(\beta_{PL} = 0)} \quad [2.92]$$

The points of the highest, ν_Q^3 , and lowest, ν_Q^1 , spectral intensity are usually referred to as "horns" and "shoulders" of the powder pattern. Since the quadrupole coupling parameters describe the electric field gradient tensor at the nucleus, experimental deuteron spectra and their temperature dependence mirror microscopic changes in the local electronic environment.

2.3 Motion and Relaxation

The quantum states of spin ensembles evolve under the system Hamiltonian, which is the product of nuclear spin operators and electronic space operators, depending on the system geometry (Eq. 2.52). This prompts for two ways of quantum state manipulation: either through spin coordinates, or through the system geometry. Rotation of the spin angular momentum can be achieved by application of RF pulses (e.g. Eq. 2.24), with the phase and strength specified by pulse sequence. This will be discussed in the next section. The spatial part of the system Hamiltonian is altered by the changes in spin orientations with respect to laboratory fixed coordinates. This changes are induced by random internal molecular motion, or by forced external sample reorientation (such as sample spinning or flipping). The effect of such motions on the observed spectra will be discussed in the following subsections.

In a quantum mechanical system energy is absorbed through changes in quantum states. When placed in external magnetic field bulk magnetization is created due to the Boltzmann distribution favoring population of magnetic moments parallel to the field (Eq. 2.35). If external field is removed, the population difference between spin-up and spin-down states is no longer equilibrium, and the system will minimize the energy by relaxing to a new equilibrium state with no bulk magnetization. In the absence of RF perturbation, the magnetization will relax back to equilibrium along the z-axis. The time constant characterizing magnetization relaxation after the perturbation is removed, is called

longitudinal or spin-lattice relaxation time, T_1 . The ratio of equilibrium population, p_{eq} , difference at initial, p_0 , and any other time, p_t , has an exponential time dependence [63]

$$\frac{p_{eq} - p_t}{p_{eq} - p_0} = \exp\left(-\frac{t}{T_1}\right) \quad [2.93]$$

In practice a time period of $5T_1$ is enough for 99 % system magnetization to return to equilibrium. This is important system characteristic, since it limits the rate of acquisition in NMR experiment. If the time interval between collection of FIDs is insufficient for full system relaxation, saturation may occur, and no signal will be observed. It means that equilibrium population distribution with the presence of bulk magnetization is not achieved, and thus, cannot be detected, because RF irradiation equalized level populations through the absorption of the photons.

In systems with two energy levels, there is only one path for spin-lattice relaxation, however for systems with three levels (e.g. deuterons), there are two, depending on the nature of RF perturbation. When the applied RF field simply inverts spin-1 populations (Zeeman order, $\langle \mathbf{I}_z \rangle$), the equilibration goes through a combination of one and two quantum spin flips, characterized by a single time constant T_{1z} :

$$\langle \overline{\mathbf{M}}(t) \rangle \propto \langle \overline{\mathbf{I}}_z(t) \rangle = \langle \overline{\mathbf{I}}_z(\infty) \rangle - \left(\langle \overline{\mathbf{I}}_z(\infty) \rangle - \langle \overline{\mathbf{I}}_z(0) \rangle \right) \exp\left(-\frac{t}{T_{1z}}\right) \quad [2.94]$$

If instead the initial population distribution corresponds to quadrupolar order ($\rho(0) = \langle \mathbf{Q}_z \rangle \sim A_0^{(2)}$ (Eq. 2.81)) equilibrium is reached solely via single quantum transitions, and is characterized by the time constant T_{1Q} :

$$\langle \overline{\mathbf{M}}(t) \rangle \propto \langle \overline{\mathbf{Q}}_z(t) \rangle = \langle \overline{\mathbf{Q}}_z(0) \rangle \exp\left(-\frac{t}{T_{1Q}}\right) \quad [2.95]$$

Spin-lattice relaxation of a nuclear spin occurs by dissipation of excess energy into non-spin degrees of freedom (i.e., into the "lattice"). Since spin-lattice coupling is very weak, it is permissible to assume that the lattice is always at thermal equilibrium and has infinite heat capacity in comparison to the spins. Energy is transferred between the spins and the lattice

via stimulated absorption or emission of photons. The fluctuations in the magnetic and electric fields arise as a consequence of random molecular motion. Modulation of the orientation dependent spin interactions gives an efficiency of relaxation, which depends on the square of the interaction strength. Thus, when magnetic dipole-dipole interaction is the dominant relaxation mechanism, T_1 is inversely proportional to a square of dipolar constant, ω_D^2 (Eq. 2.77). If the quadrupole coupling of the spins to electric field gradients dominates relaxation, the rate of equilibration grows as a square of quadrupole coupling constant, χ^2 (Eq. 2.83). In addition, the relaxation rates depend on the power spectrum of fluctuations at the relevant frequencies: ω_0 for one-quantum spin flips and $2\omega_0$ for two-quantum spin flips.

The power spectrum of local field fluctuations is often characterized by spectral densities of motions. The relaxation rate depends on the spectral density at the Larmor frequency (and its multiples for multiple-quantum spin flips). If the fluctuation rate is either very fast or very slow on this time scale the relaxation time will be long, since not many fluctuations will have the appropriate frequency components to induce stimulated emission. When the motional rate is comparable to the Larmor frequency the relaxation is fastest, because more fluctuations have the appropriate frequency components. Therefore, the temperature dependence of T_1 exhibits a minimum when the motional rate is equal to the Larmor frequency ($k = \nu_0$) [74], its absolute value depending on the details of the spin interactions. Thus, measuring the relaxation time yields detailed information about molecular motion.

Another relaxation process important for NMR experiments is spin-spin (transverse) relaxation, characterized by T_2 . This time describes how individual spins in an ensemble lose their phase coherence after RF irradiation disappears. This process can be visualized as the magnetization vectors dephasing in the xy-plane of the RRF:

$$\langle \overline{\mathbf{M}}_{xy}(t) \rangle \propto \langle \overline{\mathbf{I}}_+(t) \rangle = \langle \overline{\mathbf{I}}_+(0) \rangle \exp\left(-\frac{t}{T_2}\right) \quad [2.96]$$

Spin-spin dephasing is much faster (< 1 ms for solids) than spin-lattice relaxation. It is facilitated by energy conserving, simultaneous flip-flops of two spins in an ensemble, when their phase does not change but they start to accelerate in opposite directions. The oscillating local magnetic and electric fields slightly augmenting or diminishing the external field felt by the different nuclei cause the opposite direction of precession in the RRF. The same is true when the B_0 field is slightly inhomogeneous over the dimensions of the sample. T_2 relaxation is driven by the tendency of the system to spontaneously achieve a state with maximum entropy in the absence of "organizing" forces. Short transverse relaxation times in solid samples give rise to corresponding signal broadening in the frequency domain.

2.3.1 Spectrum Averaging Under Magic Angle Spinning

Magic angle spinning (MAS) is a method used to increase resolution in solid state NMR spectra by selective averaging the anisotropic interactions [70]. If the sample is spun rapidly about an axis oriented at the angle $\theta_m = \arccos\left(\frac{1}{\sqrt{3}}\right) = 54.7^\circ$ with respect to the external magnetic field, all second rank, anisotropic interactions (such as those discussed in section 2.2 above) are averaged, giving high resolution, "liquid-like" spectra [75]. In liquids anisotropic interactions are averaged by fast isotropic random tumbling of the molecules. In solids this averaging is mimicked by fast spinning about a special axis, whose "magic" properties of averaging second rank spherical tensor interactions is realized by imparting an appropriate periodic time dependence to the spatial components of the interaction Hamiltonians. For the static interactions relevant to the dendrimer studies in this dissertation (Eq. 2.51), the secular Hamiltonian in the RRF frame (henceforth referred to as LAB frame) can be written in a generalized form: $\mathbf{H} = A_0^{(0)}T_0^{(0)} + A_0^{(2)}T_0^{(2)}$. The first term is present only for \mathbf{H}_q (Eq. 2.51). Since, this term is invariant to coordinate transformations ($D_{00}^{(0)} = 1$), the effect of MAS on all above mentioned static interaction Hamiltonians in the LAB frame can be derived in general solely from $T_0^{(2)}(\text{LAB})$.

In the LAB frame the spatial component of the generalized Hamiltonian can be described by two consecutive coordinate transformations: from PAS to rotor fixed axes system (RAS), $\Omega_{PR} = \Omega(0, \beta_{PR}, \gamma(t))$, followed by RAS to LAB, $\Omega_{RL}(0, \theta_m, 0)$. Although the active rotation of the rotor is described by angle $\alpha_{PR}(t)$ around the rotor axis, the coordinate transformation is passive, and so that γ_{PR} time dependence should be considered instead. Due to cylindrical symmetry of the system, α_{PR} is irrelevant. Since the rotor orientation in LAB is fixed, α_{RL} and γ_{RL} can be put equal to zero without loss of generality. Azimuthal and polar angles γ_{PR} and β_{PR} describe the interaction tensor (PAS) orientation within the rotor. Due to the rotation, the azimuthal angle will be time dependent, $\gamma_{PR}(t) = \alpha + \omega_r t$, where $\omega_r = 2\pi\tau_r^{-1}$ is the rotor frequency. In the laboratory fixed frame the rotor axis is oriented at the magic angle, θ_m , with respect to the Zeeman field. The set of Wigner transformations for $T_0^{(2)}$ is given by

$$T_0^{(2)}(LAB) = \sum_{k=-2}^2 D_{k0}^{(2)}(\Omega_{RL}) \sum_{p=-2}^2 D_{pk}^{(2)}(\Omega_{PR}) T_p^{(2)}(PAS) \quad [2.97]$$

Here $T_0^{(2)}(LAB)$ and $T_p^{(2)}(PAS)$ are the components of the interaction tensor in the LAB and PAS fixed frames respectively. Due to the symmetry of the interactions, $T_{\pm 1}^{(2)}(PAS) = 0$ for chemical shielding (Eq. 2.60), dipolar (Eq. 2.76) and quadrupolar (Eq. 2.82) tensors. This allows simplification of Eq. 2.97:

$$\begin{aligned} T_0^{(2)}(LAB) = & T_2^{(2)}(PAS) \sum_{k=-2}^2 D_{k0}^{(2)}(\Omega_{RL}) (D_{-2k}^{(2)}(\Omega_{PR}) + D_{2k}^{(2)}(\Omega_{PR})) \\ & + T_0^{(2)}(PAS) \sum_{k=-2}^2 D_{k0}^{(2)}(\Omega_{RL}) D_{0k}^{(2)}(\Omega_{PR}) \end{aligned} \quad [2.98]$$

Substitution of Wigner matrix elements and utilization of their symmetry properties [65], helps to factor out the time dependent terms of $T_0^{(2)}(LAB)$:

$$\begin{aligned} T_0^{(2)}(LAB) = & \left[\frac{1}{2} T_0^{(2)}(PAS) - \frac{1}{\sqrt{6}} T_2^{(2)}(PAS) \begin{pmatrix} \sin^2 \beta_{PR} \cos 2(\alpha + \omega_r t) \\ -\sqrt{2} \sin 2\beta_{PR} \cos(\alpha + \omega_r t) \end{pmatrix} \right] \\ & + \frac{2}{\sqrt{6}} T_2^{(2)}(PAS) \cos 2(\alpha + \omega_r t) \end{aligned} \quad [2.99]$$

From this expression, it can immediately be seen that all the Hamiltonians are periodically modified by $\omega_r t$, so that $\mathbf{H}(t=0) = \mathbf{H}(t = n\tau_r)$, for any number, n , of rotor periods. In other words, each interaction will be refocused once per rotor period. In general, this leads to rotational side bands (at the multiples of the rotor frequency) in the Fourier transformed spectra [76]. The spectral intensity distribution (Eq. 2.64) among the spinning side bands (SSB) will also depend on the rotor frequency [76]. Since the total intensity of the observed nucleus is conserved, the smaller the number of side bands, the higher their intensity, and the higher the sensitivity. Imprecise setting of the magic angle will cause deviations from Eq. 2.99, reintroduction of $\theta_m \neq \beta_{RL}$ -dependent terms, and SSB broadening. This can be used for precise experimental setting of θ_m by adjusting the angle until the narrowest line width is achieved.

For each specific interaction in Eq. 2.51, the corresponding MAS Hamiltonian is explicitly written below (Eq. 2.99),

$$\mathbf{H}_\sigma = \mathbf{I}_z B_0 \left[\sigma_{iso} + \frac{\sigma_{33} - \sigma_{iso}}{2} \left[\left(1 - \frac{\eta}{3} \right) \begin{pmatrix} \sin^2 \beta_{PR} \cos 2(\alpha + \omega_r t) \\ -\sqrt{2} \sin 2\beta_{PR} \cos(\alpha + \omega_r t) \end{pmatrix} + \frac{2\eta}{3} \cos 2(\alpha + \omega_r t) \right] \right] \quad [2.100]$$

$$\mathbf{H}_D = \frac{1}{2} \omega_D (3\mathbf{I}_z^{(1)} \mathbf{I}_z^{(2)} - \bar{\mathbf{I}}^{(1)} \bar{\mathbf{I}}^{(2)}) \begin{pmatrix} \sin^2 \beta_{PR} \cos 2(\alpha + \omega_r t) \\ -\sqrt{2} \sin 2\beta_{PR} \cos(\alpha + \omega_r t) \end{pmatrix} \quad [2.101]$$

$$\mathbf{H}_Q = \frac{\chi}{2} (3\mathbf{I}_z^2 - \bar{\mathbf{I}}) \left[\left(1 - \frac{\eta}{3} \right) \begin{pmatrix} \sin^2 \beta_{PR} \cos 2(\alpha + \omega_r t) \\ -\sqrt{2} \sin 2\beta_{PR} \cos(\alpha + \omega_r t) \end{pmatrix} + \frac{2\eta}{3} \cos 2(\alpha + \omega_r t) \right] \quad [2.102]$$

When the interaction strength, determined by the terms preceding $f(\gamma_{PR}(t), \beta_{PR})$, is small compared to ω_r , the time average of the Hamiltonian will depend only on the time average of

f over a rotor period. Let us consider this average in case of dipolar Hamiltonian. Over the time t_2 the observed spin acquires the "dipolar" phase [77],

$$\phi_D(t_2) = \int_0^{t_2} \omega_D(t) dt = \pm \frac{D}{4\omega_r} \left(\begin{array}{l} \sin^2 \beta_{PR} [\sin 2(\alpha + \omega_r t) - \sin 2\alpha] \\ -2\sqrt{2} \sin 2\beta_{PR} [\sin(\alpha + \omega_r t) - \sin \alpha] \end{array} \right) \quad [2.103]$$

Here $D = \omega_D(\text{PAS})(2\pi)^{-1}$ (ω_D is given in Eq. 2.75) is measured in Hz. It can be seen that over the rotor period, $t_2 = \tau_r$, the accumulated phase is zero. This result can be easily generalized for chemical shielding and quadrupolar Hamiltonians as well. In case of \mathbf{H}_D , there remains an observable transition in MAS spectrum at the isotropic chemical shift, σ_{iso} . This way a chemical shift resolution, comparable to liquid state NMR, can be achieved in solids. However, as was noted above, the average Hamiltonian formalism can be applied only for very high rotor speeds or low interaction strengths [76]. On the basis of Eqs. 2.100-2.102, these conditions can be quantitatively satisfied, with tolerable accuracy, when the rotor frequency exceeds twice the full width of corresponding static powder pattern ($\nu_r > \{2(\sigma_{33}-\sigma_{11})\nu_0 \text{ or } 4\nu_D \text{ or } 3\chi\}$).

For the present study of polyamidoammonium dendrimer salts, the spinning rates in MAS experiments were 4-5 kHz. At such rates (and even at the maximum technically achievable at present, $\nu_r \sim 40$ kHz), the first order deuteron quadrupolar interaction (~ 250 kHz) can never be completely averaged. The ^{13}C - ^{15}N heteronuclear, and ^1H - ^1H , ^{13}C - ^{13}C , and ^{15}N - ^{15}N remote ($r > 2 \text{ \AA}$) homonuclear dipolar couplings are averaged in most cases, while ^{13}C - ^1H direct heteronuclear couplings cannot be averaged by MAS only. The chemical shielding strength for ^{15}N of amine and amide groups [78] allows observation of isotropic chemical shifts under MAS. The same is true for methyl and methylene carbons [78], while for carbonyl groups, 2-3 side bands are typically observed in ^{13}C MAS experiments with 20 kHz spectral width.

2.3.2 Molecular Motion

Since potential energy functions in solids typically consist of deep wells, internal molecular motion is usually modeled by thermally activated jumps among discrete orientations or sites. Typically, these are thermally activated Markovian processes, and as temperature increases, the jump rate increases. The characteristic activation energy, E_A , can be found from measuring rate constants, k , as a function of temperature and using the Arrhenius relation:

$$k = A \exp\left(-\frac{E_A}{k_B T}\right) \quad [2.104]$$

where the pre-exponential factor, A , is the frequency of collisions in the absence of an activation barrier. The activation energy and collision frequency are found as the slope and intercept of the logarithmic best fit jump rate versus inverse temperature.

In general, the slow, intermediate and fast motional regimes are defined according to the relative magnitudes of the frequency difference between interchanging sites, i and j ($\Delta\nu_{ij} = \nu_i - \nu_j$), and the motional rate, k_{ij} . For two transitions, corresponding, for instance, to two orientations in a powder pattern, no motional averaging occurs when rate is much smaller than the frequency difference, $k_{ij} \ll \Delta\nu_{ij}$, and two distinct lines are observed in NMR spectrum. If the motional rate is comparable to the splitting, $k_{ij} \sim \Delta\nu_{ij}$, the probability of random jumps between the two transitions during the experiment is spread over the frequency range between them in a Gaussian-like manner, centered at the average frequency, $(\nu_i + \nu_j)/2$, and a motionally broadened line is observed. Finally, when the rate is much larger than the splitting, $k_{ij} \gg \Delta\nu_{ij}$, the lines are completely averaged and collapse into a single sharp transition at the average frequency. Thus, in powders the fast regime deuteron spectrum is identical to a slow regime intensity distribution (Eq. 2.90) except for the averaged values of quadrupolar coupling parameters (Eqs. 2.91-2.92). In the fast regime, these averaged values provide information on the geometry of motion independent of an

exact motional rate. In the intermediate regime differential broadening of the various doublets results in lineshapes which are characteristic of both motional trajectories and rates.

When motion is sufficiently fast, the spins experience an average Hamiltonian, rather than an orientation dependent distribution of static Hamiltonians responsible for the powder pattern observation. The general idea is that the Euler angles describing powder orientations are now time dependent even in the static sample (no MAS) due to internal motions. These time dependence is averaged on the scale of fast motion, so that the observed spectra reflect the transitions corresponding to "average" orientations. In case of the quadrupolar interaction (Eq. 2.79), the average Hamiltonian experienced by spins is:

$$\langle H_Q(LAB) \rangle_t = A_0^{(2)} \langle T_0^{(2)}(LAB) \rangle_t = A_0^{(2)} \sum_{k=-2}^2 \langle D_{k0}^{(2)}(\Omega_{PL}(t)) \rangle_t T_k^{(2)}(PAS) \quad [2.105]$$

Invoking the ergodic hypothesis allows replacement of the time averaged Wigner rotation matrix elements, $D_{ij}^{(2)}(\Omega(t))$, by their ensemble average (equivalent to powder average) values for a model dependent geometry of the motion:

$$\langle D_{ij}^{(2)}(\Omega(t)) \rangle_t = \langle D_{ij}^{(2)}(\Omega(t)) \rangle_\Omega = \int_0^{2\pi} d\alpha \int_0^{2\pi} d\gamma \int_0^\pi d\beta \sin \beta P(\Omega) D_{ij}^{(2)}(\alpha, \beta, \gamma) \quad [2.106]$$

Here $P(\Omega)$ is a normalized probability of the certain orientation, $\Omega(\alpha, \beta, \gamma)$, defined by the motional model. In case of jumps between discrete orientations, the integral in Eq. 2.106 reduces to a sum. Thus, for qualitatively similar models this probability is different for continuous diffusion and discrete Markovian jumps.

When a deuteron continuously librates in a cone of half angle β_c , the observed quadrupolar frequencies (Eq. 2.90) will be modified by averaging of the H_Q with the uniform probability

$$P(\Omega) = \left(\int_0^{2\pi} d\alpha \int_0^{2\pi} d\gamma \int_0^{\beta_c} d\beta \sin \beta \right)^{-1} = \frac{1}{4\pi^2(1 - \cos \beta_c)} \quad [2.107]$$

The ensemble averages of $D_{00}^{(2)}(\Omega_{PL})$ and $(D_{20}^{(2)}(\Omega_{PL}) + D_{-20}^{(2)}(\Omega_{PL}))$ [65] describing the molecular motion (Eq. 2.89) are:

$$\langle D_{00}^{(2)}(\Omega_{PL}) \rangle_{\Omega} = \frac{4\pi^2}{4\pi^2(1 - \cos \beta_c)} \int_0^{\beta_c} \frac{1}{2} (3 \cos^2 \beta - 1) d(-\cos \beta) = \frac{1}{2} \cos \beta_c (1 + \cos \beta_c) \quad [2.108]$$

$$\begin{aligned} \langle D_{20}^{(2)}(\Omega_{PL}) \rangle_{\Omega} + \langle D_{-20}^{(2)}(\Omega_{PL}) \rangle_{\Omega} &= \sqrt{\frac{3}{2}} \frac{2\pi}{4\pi^2(1 - \cos \beta_c)} \\ &\times \int_0^{2\pi} \cos 2\alpha d\alpha \int_0^{\beta_c} (1 - \cos^2 \beta) d(-\cos \beta) = 0 \end{aligned} \quad [2.109]$$

This means that in the LAB frame motionally averaged asymmetry parameter is zero, $\eta = 0$ (Eqs. 2.109, 2.90) and the quadrupole coupling is reduced by libration in a cone to the average value:

$$\langle \chi \rangle = \frac{1}{2} \cos \beta_c (1 + \cos \beta_c) \chi_{PAS} \quad [2.110]$$

If the same model is considered for discrete jumps between four sites: $\Omega_1(0, \beta_c^{(4)}, 0)$, $\Omega_2(120^\circ, \beta_c^{(4)}, 0)$, $\Omega_3(240^\circ, \beta_c^{(4)}, 0)$, and $\Omega_4(0, 0, 0)$, with uniform probability $P(\Omega) = 1/4$, the average asymmetry parameter is still zero, but the quadrupole coupling is now reduces by different angle dependent factor:

$$\langle \chi \rangle = \frac{\chi_{PAS}}{4} \sum_{i=1}^4 \frac{1}{2} (3 \cos^2 \beta_i - 1) = \frac{\chi_{PAS}}{4} \left(1 + \frac{3}{2} (3 \cos^2 \beta_c^{(4)} - 1) \right) \quad [2.111]$$

Comparing Eq. 2.110 and 2.111, we see that different librational amplitudes $\beta_c \neq \beta_c^{(4)}$ may be responsible for the same observed averaging of quadrupole constant in case of continuous motion and discrete jumps. In fact, the relation between these amplitudes can be calculated,

$$\beta_c^{(4)} = \arccos \sqrt{\frac{4}{9} \cos \beta_c (1 + \cos \beta_c) + \frac{1}{9}} \approx \beta_c - 5^\circ \quad [2.112]$$

This shows that the same reduction of quadrupole coupling is achieved with approximately 5° smaller cone amplitudes in case of a four-site jump approximation.

The average Hamiltonian theory, valid for fast motion, provides no quantitative information about the actual motional rates and thus, can not be extended to the slow and intermediate motion regimes. A complete description of the time evolution of spin system, accounting for spin dynamics, relaxation and motion in any motional regime, requires the solution of the stochastic Liouville-von Neumann equation [51] for the spin density operator (Eq. 2.41):

$$\frac{d}{dt}\rho(t) = (i\Omega + \mathbf{R} + \mathbf{K})[\rho(t) - \rho(\infty)] = \mathbf{L}[\rho(t) - \rho(\infty)] \quad [2.113]$$

Where $\rho(\infty)$ is the equilibrium spin density matrix, \mathbf{L} is the time independent Liouville operator. $\Omega = [\rho, \langle \mathbf{H}_0 \rangle]$, is a diagonal operator of site frequencies determined for deuterons by the time independent quadrupolar interaction Hamiltonian, and $\mathbf{R} = [\rho, \mathbf{H}_1(t)]$ is a relaxation operator in RRF. \mathbf{K} is a kinetic exchange matrix, whose elements are the jump rates from site j to i , k_{ij} . In case of random stationary Markovian motion the matrix equation 2.113 represents a set of coupled, first-order differential equations for the density matrix elements.

Assuming that a nucleus jumps instantaneously between N sites, the complete spin density super-operator is constructed as a direct product of the individual spin density matrices for each site. For deuteron, each site has nine density matrix elements, and the dimension of \mathbf{L} is $9N$ [51]. The elements of the exchange matrix, \mathbf{K} , satisfy the condition of detailed balance:

$$k_{ii} = -\sum_{i \neq j} k_{ij} \quad [2.114]$$

The time evolution of observed signal is given by $\mathbf{M}(t) = \text{Tr}(\rho(t)\mathbf{I}_+)$, so only a submatrix elements of ρ (ρ_{12} and ρ_{23}) have to be considered. Accordingly, the equation for magnetization will be

$$\dot{\mathbf{M}}(t) = \mathbf{L}\mathbf{M}(t) \quad [2.115]$$

Its formal solution is given by,

$$\mathbf{M}(t) = e^{\mathbf{L}t}\mathbf{M}(0) \quad [2.116]$$

The frequencies of precession for each site, contained in $\mathbf{\Omega}$, are defined by the crystallite orientation with respect to the external magnetic field and individual site orientations within the crystallite. When site populations are not equal, \mathbf{K} is not symmetric ($p_i k_{ij} = p_j k_{ji}$), but can be diagonalized after a diagonal similarity transformation [67] $U_{ij} = p_i^{1/2} \delta_{ij}$. The symmetrized matrix has orthogonal eigenvectors, \mathbf{X} , and its eigenvalues, λ , can be found numerically. Therefore, the solution can be written,

$$\mathbf{M}(t) = \mathbf{U} \mathbf{X} e^{\lambda t} \mathbf{X}^{-1} \mathbf{U}^{-1} \mathbf{M}(0) \quad [2.117]$$

It can be used for evaluation of the magnetization evolution between pulses in a generic multipulse NMR experiment. The effect of pulses can be included as boundary conditions for successive time intervals. This algorithm, implemented in software package EXPRESS [55, 67], was used for calculations of quadrupole echo (QE) lineshapes and T_{1Z} , T_{1Q} anisotropies for relaxation experiments on PAMAM dendrimers. The corresponding pulse sequences are discussed in the proceeding section. EXPRESS assumes that the jump rates are sufficiently fast so that the difference in site-specific spin-lattice relaxation rates are averaged to a common value. It is capable of modeling multi-axis jump motions for a sequence of up to four "jumping frames". A similar approach to the solution of stochastic Liouville equation (Eq. 2.115) was used in the MAS simulation program (written by Dr. Kristensen [79, 83], which calculates the deuteron magnetization evolution under magic angle spinning in the presence of Markovian jump motion [56, 79].

2.3.3 Redfield Relaxation

For fast molecular motion quantitative information about motional rates can be extracted by finding the analytic solution for the spin density matrix equation of motion (Eq. 2.44). In the fast regime the measured anisotropic spin-lattice relaxation times can be predicted using Redfield theory. Its basic assumption is that there exists a time t such that the Hamiltonian

$\mathbf{H}_1(t)$ fluctuates over all possible values, and the average value is zero, $\langle \mathbf{H}_1(t) \rangle_t = 0$, while $\rho(t)$ changes only slightly (ρ and \mathbf{H} are in the interaction representation (Eqs. 2.40 and 2.42)). So, for the time average of the derivative of the density matrix in Eq. 2.44, only the second term contributes to ρ evolution.

$$\frac{d}{dt} \rho = i \overline{[\rho(0), \mathbf{H}_1(t)]} - \int_0^t \overline{[[\rho(0), \mathbf{H}_1(t')], \mathbf{H}_1(t)]} dt' = - \int_0^t \overline{[[\rho(0), \mathbf{H}_1(t')], \mathbf{H}_1(t)]} dt' \quad [2.118]$$

Using standard quantum mechanics to expand the commutators in this term in the eigenstate basis set of \mathbf{H}_0 [61], the time derivative of the ab -th density matrix element can be written as,

$$\frac{d}{dt} \rho_{ab}(t) = \sum_{c,d} R_{abcd} e^{i2\pi(\nu_a - \nu_b - \nu_c + \nu_d)t} \rho_{cd}(t) \quad [2.119]$$

where R_{abcd} are the Redfield relaxation super-operator elements in the interaction representation. This relation is known as Redfield equation [80], which is formally equivalent to the stochastic Liouville equation (Eq. 2.113) in the fast motional regime. It is assumed that non-secular terms ($\nu_a - \nu_b \neq \nu_d - \nu_c$) are negligible, and so the exponential factors in Eq. 2.19 are unity. Supermatrix elements of the relaxation operator can be written in terms of the spectral densities

$$R_{abcd} = J_{abcd}(\Delta\nu_{bd}) + J_{abcd}(\Delta\nu_{ac}) - \delta_{bd} \sum_p J_{pcpa}(\Delta\nu_{pc}) - \delta_{ac} \sum_p J_{pbpd}(\Delta\nu_{pd}) \quad [2.120]$$

$$J_{abcd}(\nu) = \int_0^\infty G(\tau) e^{-i2\pi\nu\tau} d\tau \quad [2.121]$$

$$G(\tau) = \overline{H_{1ab}(t)H_{1cd}(t+\tau)} \quad [2.122]$$

Here $\tau < t$ is a correlation time for the motionally induced fluctuations of the Hamiltonian such that for the times longer than τ , $\overline{H_{1ab}(t)H_{1cd}(t+\tau)} \rightarrow 0$, and within τ , Redfield coefficients are time independent. This allows replacement of the upper limit of integration in Eq. 2.121 by infinity. The correlation function $G(\tau)$ is even, and its long time limit is zero. Physically, the spectral density is a measure of fluctuation power at the frequency ν .

For deuterons, if the quadrupolar Hamiltonian is represented in terms of the second rank irreducible spherical tensors (Eq. 2.79), it is possible to calculate the explicit form of the spectral densities in terms of correlation functions for orientation determining tensor components [55, 67], $T_m^{(2)}(t)$,

$$J_{abcd}(\nu) = [T_0^{(2)}(PAS)]^2 \sum_{m,m'=-2}^2 (-1)^{m+m'} \langle a|A_{-m}|b\rangle \langle c|A_{-m'}|d\rangle^* j_{mm'}(\nu) \quad [2.123]$$

$$j_{mm'}(\nu_{mm'}) = [T_0^{(2)}(PAS)]^{-2} \int_0^\infty \overline{T_m^{(2)}(LAB, t) T_{m'}^{(2)*}(LAB, t + \tau)} e^{-i2\pi\nu - \tau} d\tau \quad [2.124]$$

When the time dependent conditional probability, $P(\Omega_0; \Omega, \tau)$, of the transition between two orientations, $\Omega_0(\alpha_0, \beta_0, \gamma_0)$ and $\Omega(\alpha, \beta, \gamma)$, is specified by the motional model, the correlation function in Eq. 2.124 can be calculated in terms of the ensemble average of the Wigner rotation matrix elements

$$\begin{aligned} \overline{T_m^{(2)}(LAB, t) T_{m'}^{(2)*}(LAB, t + \tau)} &= \sum_{k,k'=-2}^2 T_k^{(2)}(PAS) T_{k'}^{(2)*}(PAS) \\ &\times \int_{\Omega_0} P(\Omega_0) D_{km}^{(2)}(\Omega_0) d\Omega_0 \int_{\Omega} P(\Omega_0; \Omega, \tau) D_{k'm'}^{(2)*}(\Omega) d\Omega \end{aligned} \quad [2.125]$$

The correlation time is determined by the jump rate, $\tau = k^{-1}$. For instance, in case of the hard collision model, when conditional probabilities are exponential functions of the correlation time, the spectral densities are Lorentzians. In the fast motion limit, $\nu\tau \ll 1$, they are inversely proportional to the jump rate.

The elements of the relaxation super-matrix are the transition probabilities between different spin states, described by the density matrix elements (Eq. 2.119). When measuring the relaxation of Zeeman order (Eq. 2.94), the time evolution of z-magnetization $\langle \mathbf{I}_z \rangle = \text{Tr}(\rho(t) \mathbf{I}_z) = (\rho_{11} - \rho_{33})$ is monitored. When quadrupole order relaxation is studied (Eq. 2.95), $\langle \mathbf{Q}_z \rangle = \text{Tr}(\rho(t) \mathbf{Q}_z) = \rho_{11} + \rho_{33} - 2\rho_{22}$ is changing in time. The corresponding relaxation rates are written in terms of spectral densities as follows:

$$T_{1z}^{-1} = R_{1122} + 2R_{1133} = \frac{3\pi^2}{2} \chi^2 (j_1(\nu_0) + 4j_2(2\nu_0)) \quad [2.126]$$

$$T_{1Q}^{-1} = 3R_{1122} = \frac{9\pi^2}{2} \chi^2 j_1(\nu_0) \quad [2.127]$$

The spectral density functions can be calculated for a given model (Eq. 2.125) and substituted into Eqs. 2.126 and 2.127 to compare with experimentally measured anisotropic relaxation rates. The motional model is validated by adjusting its parameters until they produce the best fit to experimental data. As was pointed out in the previous subsection, in case of fast motion, the jump amplitudes can be determined separately by the average Hamiltonian simulation of lineshape parameters (Eq. 2.105). Then, by fitting relaxation data, the rates of the motion can be analytically calculated with the aid of the Redfield theory. This approach was not used exclusively in the present dissertation due to mixed time scales of motion and complex overlapping lineshapes. Nevertheless, taking advantage of its implications allowed rapid preliminary numerical simulations.

2.4 Experimental Techniques and Pulse Sequences

The ability to precisely control the creation of population differences and coherent superpositions of eigenstates makes NMR a very powerful spectroscopic tool. In general, a "tailored" non-equilibrium spin system state can be prepared by the application of radio frequency pulses of suitable lengths, intensities and phases. The system is then allowed to evolve under the influence of its internal Hamiltonian. After that, coherence transfer occurs through relaxation or molecular motion during the mixing period, and single quantum coherences (the only coherences directly observable by NMR) are created by the RF pulses. Finally, the resulting signal is acquired during the detection time. Thus, a timeline of events that occur in an NMR experiment, called a "pulse sequence", is subdivided into four time periods [81]: preparation, evolution, mixing and detection. These time lines are used to visualize exactly how a particular experiment is performed.

In the absence of molecular motion, the spin evolution can be calculated using the reduced density matrix expanded in a set of basis operators. The choice of operators for the spin-1/2 system is naturally I_x , I_y and I_z . The magnetization is detected by application of RF pulse to rotate the equilibrium magnetization $M_z \sim I_z$ away from the static field. The detected transverse magnetization is proportional to a linear combination of I_x and I_y . The conventional spin-1 basis set is comprised of the operators I_x , I_y , I_z , $Q_x = I_z I_x + I_x I_z$, $Q_y = I_z I_y + I_y I_z$, $Q_z = \frac{1}{\sqrt{3}}(3I_z^2 - I^2)$, $D_x = I_x^2 - I_y^2$, and $D_y = I_x I_y + I_y I_x$. The two quadrupole transitions can be pictured as two magnetization vectors, with precession frequencies in RRF of $\pm\nu_Q$. If these two "magnetization" vectors are parallel they form the **I**-components, and when they are anti-parallel **Q**-components are formed. Magnetization proportional to I_x , I_y , Q_x and Q_y describes single quantum coherences, which are detectable by NMR. The operators D_x and D_y describe double quantum coherences between the $|+1\rangle$ and $|-1\rangle$ states, and can be inferred only by conversion into one of the observable quantum states.

Ideally, the step by step propagation of the reduced density matrix in time can be calculated by invoking Eq. 2.39 with time independent Hamiltonians acting on the spin ensemble at certain time periods of the pulse sequence. RF Hamiltonians during preparation, mixing and detection are usually designed to tip spin magnetization by a known angle by applying a pulse of a well defined phase and duration (e.g. Eq. 2.24). In the simplest case, when the strength of the RF field is B_1 , and its phase is ϕ , this Hamiltonian can be written as

$$\mathbf{H}_{\text{RF}} = \mathbf{H}_1 = \gamma B_1 \mathbf{I}_\phi = \omega_1 \mathbf{I}_\phi \quad [2.128]$$

In practice, the length and strength of RF pulses can be controlled with limited precision. This leads to the creation of small extraneous coherences during imperfect pulse irradiation. Undesirable spectral artifacts due to these electronics limitations are minimized by phase cycling the pulses. A phase cycle works by selectively changing the sign of specific terms in the density matrix on successive NMR scans. This allows unwanted coherences to sum to zero and the desired signal to be coherently averaged.

Some experimental techniques employed for the dendrimer characterization described in this dissertation, such as quadrupole echo, T_{1Z} and T_{1Q} anisotropy measurements, ^{13}C CP MAS, have been used in our laboratory for a long time. The full details, including artifact suppressing phase cycles and limitations for deuteron QE, relaxation measurements and MAS experiments can be found in Ph.D. dissertations of Tse, 1995 [67], Brown, 1997 [82], and Kristensen, 1995 [83]. The ^{13}C CP MAS fundamentals and hardware requirements are described by Varner, 1999 [84]. The above mentioned techniques will be briefly reviewed in the following subsections using density matrix formalism to describe how RF pulses help to create, manipulate and observe non-equilibrium spin ensembles. More details will be provided for Rotational-Echo Double-Resonance (REDOR) experiment since this dissertation describes the first introduction of this technique in our solid state NMR laboratory.

2.4.1 Quadrupole Echo

In the simplest NMR experiment, the magnetization detection is done by applying a single RF pulse to rotate the magnetization from the z-axis to the transverse plane where the resulting FID is detected. The initial state of the spin ensemble will be described by normalized equilibrium density matrix (Eq. 2.34), $\rho(0) = \mathbf{I}_z$. For instance, in case of RF pulse with x-phase and length τ_p , the RF Hamiltonian (Eq. 2.128) is $\mathbf{H}_1 = \omega_1 \mathbf{I}_x$, and the magnetization flip angle $\theta = \omega_1 \tau_p$. According to Eq. 2.39, the density matrix immediately after the pulse is [61]:

$$\rho(0^+) = e^{-i\theta \mathbf{I}_x} \mathbf{I}_z e^{i\theta \mathbf{I}_x} = \cos \theta \mathbf{I}_z - \sin \theta \mathbf{I}_y \quad [2.129]$$

The RF pulse of the length $\tau_p = \pi(2\omega_1)^{-1}$ is called a "90 degree pulse". Its length is set experimentally by maximizing the conversion of \mathbf{I}_z into an observable transverse magnetization ($\rho(0^+) = -\mathbf{I}_y$, when $\theta = \pi/2$).

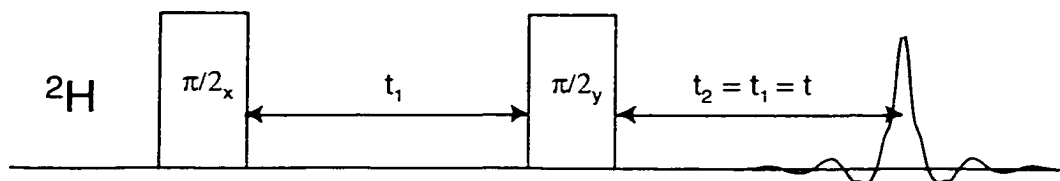


Figure 2.6
Quadrupole echo (QE) pulse sequence used to detect Zeeman order for deuterons.

For broad deuteron powder patterns, the FID induced by the application of an RF pulse will die off quickly. Thus, much signal intensity is lost due to the electronic "dead time" right after the pulse. If undistorted FIDs are to be recorded, it is necessary to refocus the magnetization outside the dead time interval. This is achieved by using two-pulse quadrupole echo (QE) sequence, $[\pi/2]_x - t_1 - [\pi/2]_y - t_2 - \text{ACQ}$ [85-87], shown in Fig. 2.6. After the first 90 degree pulse the density matrix is proportional to $-\mathbf{I}_y$. During the pulse spacing, t_1 , the density matrix evolves under the quadrupolar Hamiltonian, \mathbf{H}_Q (Eq. 2.79). As a result, the density matrix oscillates between \mathbf{I}_y and \mathbf{Q}_x at the quadrupole frequency $\omega_Q = 2\pi\nu_Q$ (Eq. 2.90):

$$\rho(t_1^-) = -\cos(\omega_Q t_1) \mathbf{I}_y + \sin(\omega_Q t_1) \mathbf{Q}_x \quad [2.130]$$

The application of the next 90 degree pulse with y-phase and subsequent free precession under the \mathbf{H}_Q during t_2 results in the density matrix

$$\begin{aligned} \rho(t_1 + t_2) = & -\cos(\omega_Q t_1) [\cos(\omega_Q t_2) \mathbf{I}_y - \sin(\omega_Q t_2) \mathbf{Q}_x] \\ & - \sin(\omega_Q t_1) [\cos(\omega_Q t_2) \mathbf{Q}_x + \sin(\omega_Q t_2) \mathbf{I}_y] \end{aligned} \quad [2.131]$$

When, $t_1 = t_2 = t$, the magnetization refocuses, and the density matrix is identical to that following the first 90 degree pulse,

$$\rho(2t) = -\mathbf{I}_y = \rho(0^+) \quad [2.132]$$

This way an undistorted FID can be acquired (ignoring relaxation that occur during $2t$ period). Since QE echo avoids distortion and allows observation of \mathbf{I}_z by converting it into \mathbf{I}_y , this sequence is of general use for quadrupolar magnetization detection as a part of a

more complicated pulse sequence. If performed as a function of the pulse spacing, t , QE can measure the dephasing time (T_2) of transverse magnetization.

2.4.2 Spin Lattice Relaxation Time Anisotropy

To measure Zeeman spin lattice relaxation time, an initial, 180 degree pulse inverts the equilibrium populations and the spins are left to relax for a variable delay time, τ , after which the QE sequence is used to detect the magnetization. The three pulse inversion recovery quadrupole echo detection (IRQE) pulse sequence, $[\pi]_x - \tau - [\pi/2]_x - t - [\pi/2]_y - t - \text{ACQ}$, used for T_{1z} measurements is shown in Fig. 2.7.

The initial pulse inverts the density matrix

$$\rho(0^+) = e^{-i\pi I_z} \rho(0^-) e^{-i\pi I_z} = -\rho(0^-) \quad [2.133]$$

After the inversion during the delay time, τ , the spins reestablish thermal equilibrium by interaction with fluctuating local fields in the lattice,

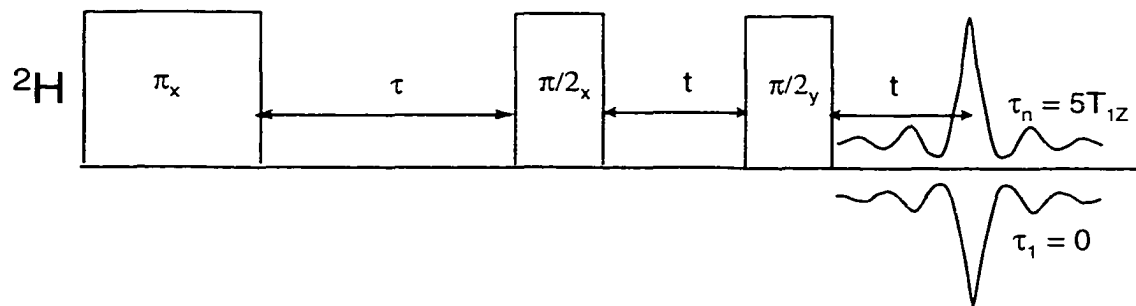


Figure 2.7
Inversion Recovery with Quadrupole Echo (IRQE) detection pulse sequence.

$$\rho(\tau) = \mathbf{I}_z \left(1 - 2 \exp \left[-\frac{\tau}{T_{1z}} \right] \right) \quad [2.134]$$

The QE pulse pair is then used to convert z-magnetization into observable single quantum coherences. In order to have efficient inversion over the entire frequency spectrum, the initial

pulse has to have a uniform excitation profile. Otherwise, pulse efficiency corrections should be made when analyzing the partially relaxed powder patterns. The T_{1Z} analysis is performed at a variety of positions on the powder lineshape. The variation of relaxation time as a function of frequency gives the anisotropy.

Quadrupolar order, Q_z , is described by a state in which only one of the two transitions has been inverted. For the spin-1 system, Q_z relaxes independently of I_z with the relaxation time, T_{1Q} . The broadband Jeener-Broekaert (BBJB) sequence [88, 89], was extended for solid state applications by adding a refocusing 90 degree pulse at the end and constructing appropriate phase cycle for artifact suppression [90], $[\pi/2]_x - 2t_p - [3\pi/8]_{\bar{y}} - 2t_p - [\pi/4]_y - t_p - [\pi/4]_y - \tau - [\pi/4]_{\bar{y}} - t - [\pi/2]_{\bar{y}} - t - \text{ACQ}$ (Fig. 2.8), is capable of uniform excitation of quadrupolar order over a significantly wide frequency range without producing Zeeman order. The bandwidth of uniform excitation is controlled by changing the excitation delay, t_p [67]. The first four pulses prepare quadrupolar order. During the relaxation delay, τ , this order decays exponentially (Eq. 2.95). Then the 5th and 6th pulses create and refocus the detectable single quantum coherences.

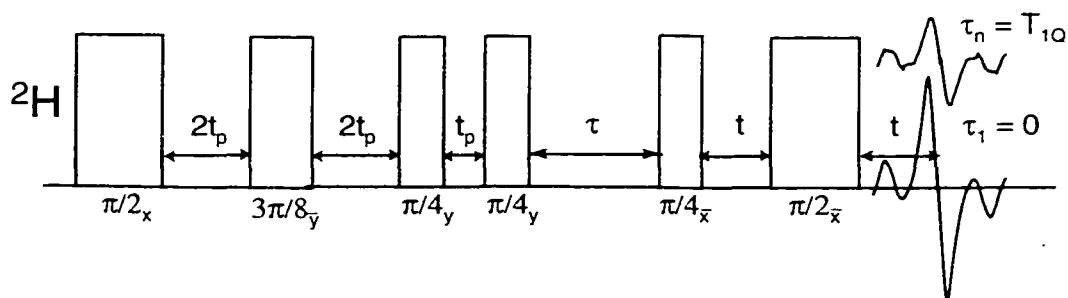


Figure 2.8
Broad-band Jeener-Broekaert (BBJB) sequence for monitoring relaxation of quadrupolar order.

After the first preparation pulse and $2t_p$ quadrupolar order evolution period, the density matrix is given by Eq. 2.130. Following three pulses and $3t_p$ evolution periods the broadband excitation is achieved [67],

$$\begin{aligned}
\rho(5t_p^+) = & \left(-\frac{\sqrt{3}}{2} \mathbf{Q}_z + \frac{1}{2} \mathbf{D}_x \right) \begin{pmatrix} \left[\cos^2(2\omega_Q t_p) + \frac{1}{\sqrt{2}} \sin^2(2\omega_Q t_p) \right] \sin(\omega_Q t_p) \\ -\frac{1}{2\sqrt{2}} \sin(2\omega_Q t_p) \cos(\omega_Q t_p) \end{pmatrix} \\
& - \mathbf{I}_y \begin{pmatrix} \left[\cos^2(2\omega_Q t_p) + \frac{1}{\sqrt{2}} \sin^2(2\omega_Q t_p) \right] \cos(\omega_Q t_p) \\ + \frac{1}{2\sqrt{2}} \sin(2\omega_Q t_p) \sin(\omega_Q t_p) \end{pmatrix} \\
& + \mathbf{Q}_x \frac{1}{2} \left(1 - \frac{1}{\sqrt{2}} \right) \cos(2\omega_Q t_p) \sin(2\omega_Q t_p)
\end{aligned} \quad [2.135]$$

The unwanted \mathbf{I}_y , \mathbf{Q}_x and \mathbf{D}_x coherences are removed by appropriate phase cycling [67, 90].

Thus, only the pure quadrupolar order term, \mathbf{Q}_z , is left after the relaxation delay, t :

$$\rho(5t_p + \tau^-) = -\frac{\sqrt{3}}{2} \mathbf{Q}_z \exp\left(-\frac{\tau}{T_{1Q}}\right) \begin{pmatrix} \left(\cos^2(2\omega_Q t_p) + \frac{1}{\sqrt{2}} \sin^2(2\omega_Q t_p) \right) \sin(\omega_Q t_p) \\ -\frac{1}{2\sqrt{2}} \sin(2\omega_Q t_p) \cos(\omega_Q t_p) \end{pmatrix} \quad [2.136]$$

The last two mixing pulses and two periods of free precession under a quadrupolar Hamiltonian produce an echo independent of frequency ω_Q value

$$\rho(5t_p + \tau + 2t) = \frac{1}{4} \mathbf{Q}_z - \frac{\sqrt{3}}{4} \mathbf{D}_x + \frac{\sqrt{3}}{2} \mathbf{Q}_y \quad [2.137]$$

Additional phase cycling ensures that only \mathbf{Q}_y is retained. It can be detected without distortions due to spectrometer dead time. The zero time of the Fourier transform corresponds to a zero crossing in the imaginary channel.

2.4.3 Deuteron Magic Angle Spinning

An alternative to use of quadrupole echo is provided by the deuteron magic angle spinning experiment. This experiment retains information about the quadrupole coupling (from sideband intensity envelope) and provides additional information on slow and intermediate dynamics from sideband linewidths [79, 83]. Deuteron MAS is performed with application of a single 90° excitation pulse. During acquisition the density matrix evolves under quadrupolar Hamiltonian, H_Q , which is periodically modulated by MAS (Eq. 2.102).

Thus, every rotor period the magnetization is refocused to $-I_y$ since at that time $\nu_Q(n\tau_r) = \nu_Q(0)$ (Eq. 2.132, $t = \tau_r/2$). For deuterium MAS the single pulse sequence with a rotary echo train is shown in Fig. 2.9.

Due to transverse magnetization relaxation, the echo amplitudes are attenuated with increasing number of rotor periods. The Fourier transform of the experimental FID

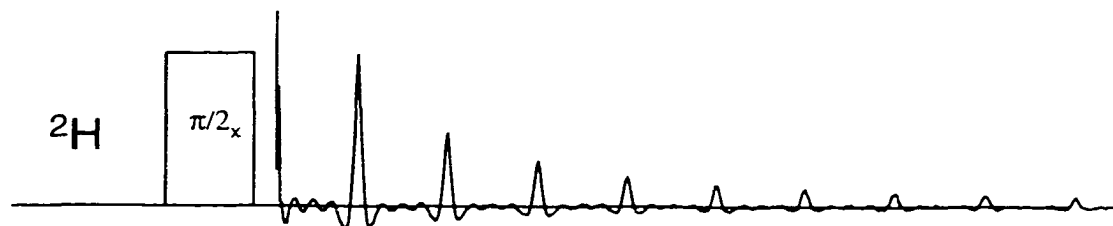


Figure 2.9
Single pulse experiment with MAS for deuterium, and outgoing rotational quadrupole echo train.

produces a lineshape and intensity profile reminiscent of the QE lineshape consisting of the Lorentzian shaped sidebands at multiples of the rotor frequency, their width determined by the rate of echo attenuation. Similar to QE, the MAS lineshape envelope intensity is dependent on quadrupole coupling parameters (Eqs. 2.83, 2.84). In addition, the line's widths are modified by MAS (Eq. 2.102), and for deuterons this is especially sensitive to molecular motion in the intermediate regime [79], corresponding to short T_2 values and, consequently, broad sidebands. If the sideband width is relatively narrow compared to the chemical shift differences for chemically distinct deuterons, ^2H MAS has an additional benefit of providing chemical shift resolution for overlapping powder patterns. Chemical shift range for deuterons in ppm is on the same order as for protons, ~ 10 ppm. This means, for instance, that to observe the chemical shift between R_2ND and RND_3^+ deuterons (~ 3 ppm), corresponding approximately to 140 Hz, the MAS side band width should not exceed 50-60 Hz. For correct interpretation of side band width and broadening it is extremely important that the magic angle is set with the best possible precision.

2.4.4 Cross Polarization Magic Angle Spinning

For spin-1/2 nuclei magic angle spinning has the effect of increasing spectral resolution due to the averaging of moderate chemical shift and heteronuclear dipolar coupling anisotropies (Eqs. 2.100 and 2.101). The higher the spinning speed, the more efficient averaging and higher sensitivity can be achieved. However, in most cases for homonuclear dipolar couplings of close spins the routinely reachable rotor frequencies (< 15 kHz) are not enough to defeat spectral broadening. Here, low natural abundance of observed nucleus is helpful, since rare spins are far apart in space. However, the detection of low intensity NMR signal presents a problem. In such cases, it is desirable to couple MAS with the cross polarization from protons in a double resonance experiment [75]. The corresponding pulse sequence is shown in Figure 2.10.

Pulses are applied independently for two nuclei at their different Larmor frequencies, and due to frequency limited excitation profiles these do not interfere significantly. The

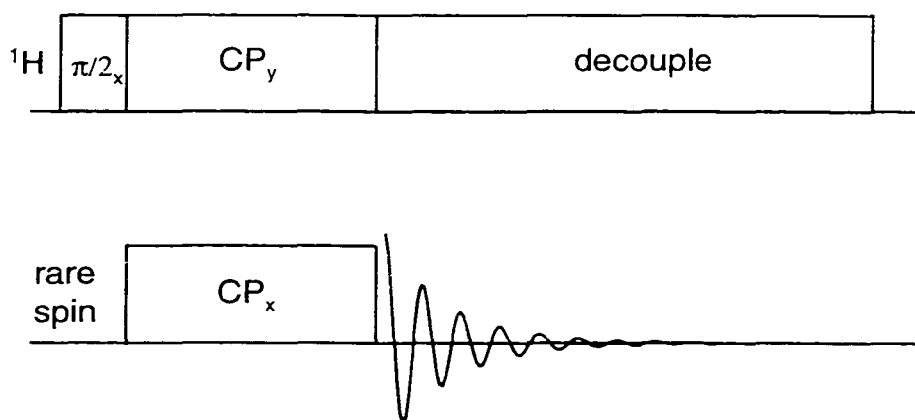


Figure 2.10

The cross polarization pulse sequence. Proton magnetization is transferred to the rare spin during the contact pulse (CP). During observation high power proton decoupling is used to average direct dipolar coupling of protons to observed spins.

experiment starts by applying a 90 degree pulse to the nucleus of high natural abundance and sensitivity, I, chosen to serve as a magnetization sink. The created transverse

magnetization (Eq. 2.129) is then spin locked along its axis for a period, τ_{CP} , by application of a long (CP) pulse with the same y -phase as the I-magnetization. Simultaneously, the RF pulse at the Larmor frequency of the rare spin nucleus, S, is applied with an amplitude chosen to match the energy of the magnetization sink nucleus in RRF. When the Hartman-Hahn condition, $\gamma_I B_1^I = \gamma_S B_1^S$, is met [91], mutual spin flips of two nuclei conserve energy. During this user specified, contact time, τ_{CP} , single quantum coherences among rare spins are created via the dipolar coupling with abundant spins [61]. Once the pulse is off the rare spin magnetization is observed. During the acquisition time the abundant nucleus is continuously irradiated at its Larmor frequency (usually much higher than that of the rare spin, since higher sensitivity results for higher γ). This helps effectively average dipolar interaction of directly bonded spins, which is otherwise problematic with currently accessible MAS speeds. This is known as high power decoupling, and has the effect of keeping the abundant nucleus magnetization rotating fast in the RRF of observed nucleus, so that its time average value is close to zero on the time scale of the observed nucleus.

At thermal equilibrium the bulk magnetization of the spin-1/2 nucleus is given in Eq. 2.35. The I-spin magnetization in the RRF is equal to the equilibrium magnetization, meaning that $B_0/T = B_1^I/T_1^I$. Since S-spins are rare, after cross polarization, their spin temperature is very close to that of I-spins (large thermal reservoir). The Hartman-Hahn match ensures that the applied $B_1^S = B_1^I \gamma_I / \gamma_S$. Therefore, the signal enhancement is given by the ratio of cross polarized magnetization to equilibrium magnetization for S-spin, $M_1^S / M_0^S = \gamma_I / \gamma_S$. Thus, for instance by carbon-13 – proton cross polarization, the carbon signal can be enhanced by nearly a factor of four. Efficient cross polarization occurs as long as the thermal equilibrium is maintained between S and I-spins. The I-spin energy may dissipate due to the contact with lattice as well (T_1 process). In addition, since a single signal acquisition is not sufficient for experiments, the spin-lattice relaxation time, T_1 , of the polarizing nucleus determines recycle delay in CP MAS. This helps to further reduce

experimental time, since often T_1 for rare S-spins (e.g. ^{13}C , ^{15}N) are 10-100 times longer than for I-spins (e.g. ^1H).

The CP MAS technique [75] can be efficiently applied to enhance experiment sensitivity for low natural abundance nuclei (such as ^{13}C or ^{15}N) dipolar coupled to nuclei with high natural abundance and sensitivity, like protons. The CP MAS pulse sequence may also be used as a preparation step in more complicated sequences, where enhanced resolution and signal-to-noise ratio are major issues.

The observation of spin-1/2 nucleus chemical shifts using CP MAS usually requires spectral width less than 30 kHz, and individual peak width is order of 10-100 Hz, the outcoming FIDs last long in most cases. The problem of spectrometer dead time can be solved by simply discarding the first few FID points before Fourier transformation. This does not effect the observed peak intensities very much, but will produce phase distortions [66]. To defeat the latter, a spin echo (SE) can be used after cross polarization. As with QE, the idea is to let magnetization evolve under the system Hamiltonian after cross polarization for some time, t , and then apply a 180 degree pulse of the phase corresponding to the magnetization phase right after τ_{CP} . This pulse has the effect of reversing the magnetization dephasing, and brining it back to initial state at time t after the pulse. The system Hamiltonian, e.g. in case of ^{13}C natural abundance experiment, is the chemical shielding Hamiltonian under MAS (Eq. 2.100), $\mathbf{H}_\sigma = \omega_\sigma^{\text{MAS}} \mathbf{I}_z$. Let us assume that $\rho(\tau_{CP})$ is proportional to \mathbf{S}_y , then with $\theta = \omega_\sigma^{\text{MAS}} t$, the density matrix evolution after the contact pulse is described by

$$\begin{aligned} \rho(\tau_{CP} + 2t) &= e^{-i\theta \mathbf{S}_z} e^{-i\theta \mathbf{S}_y} e^{-i\theta \mathbf{S}_z} \mathbf{S}_y e^{i\theta \mathbf{S}_z} e^{i\theta \mathbf{S}_y} e^{i\theta \mathbf{S}_z} \\ &= \cos \theta (\cos \theta \mathbf{S}_y - \sin \theta \mathbf{S}_x) + \sin \theta (\cos \theta \mathbf{S}_x + \sin \theta \mathbf{S}_y) \quad [2.138] \\ &= \mathbf{S}_y = \rho(\tau_{CP}) \end{aligned}$$

Thus, at time t after the echo pulse, the magnetization is refocused and can be acquired with no interference from electronics ring down.

2.4.5 Rotational-Echo Double-Resonance

Measuring dipolar interactions between coupled spins allows internuclear distances to be determined (Eq. 2.75). This is especially valuable for glassy polymers (like PAMAM dendrimers) or other large macromolecular systems (e.g. enzymes) lacking high-quality single crystals. For such systems, X-ray distance measurements can not be performed, and NMR becomes the primary source of distance constraint information. For a heteronuclear spin pair, the distance measurement can be straightforwardly performed by the Rotational-Echo Double-Resonance (REDOR) method [77]. This method has the advantage of preserving chemical shift resolution while recovering weak dipolar interactions. The experiment is performed with the sample in a rotor oriented at the magic angle to external field. The rotor is spun at a frequency of several kHz, enough to provide high resolution of chemical shifts with complete averaging of dipolar couplings (which for ^{13}C - ^{15}N pair are typically less than 1 kHz).

The reintroduction of weak dipolar interaction is achieved by application of rotor synchronized dephasing π -pulses to an unobserved nucleus, while for the observed spin the simple spin echo cross polarization MAS experiment is performed (Fig. 2.11). The echo pulse is applied at the rotor period to refocus isotropic chemical shift and to eliminate undesirable dephasing from scalar coupling and off-resonance effect [77]. The dephasing pulse changes the sign of the secular spin operator $A_0^{(2)}$ (Eq. 2.75) at the time of its application, t_1 , so that the dipolar Hamiltonian averaged over the rotor period is no longer zero [77]. If the dephasing pulse is applied at half a rotor period (as shown in Fig.2.11), the dipolar phase accumulated over the rotor period, depending on the dipolar frequency D (Eq. 2.101), is

$$\phi_D = \int_0^{\frac{\tau_r}{2}} \omega_D(t) dt - \int_{\frac{\tau_r}{2}}^{\tau_r} \omega_D(t) dt = \pm 2\sqrt{2} \sin 2\beta \sin \alpha \quad [2.139]$$

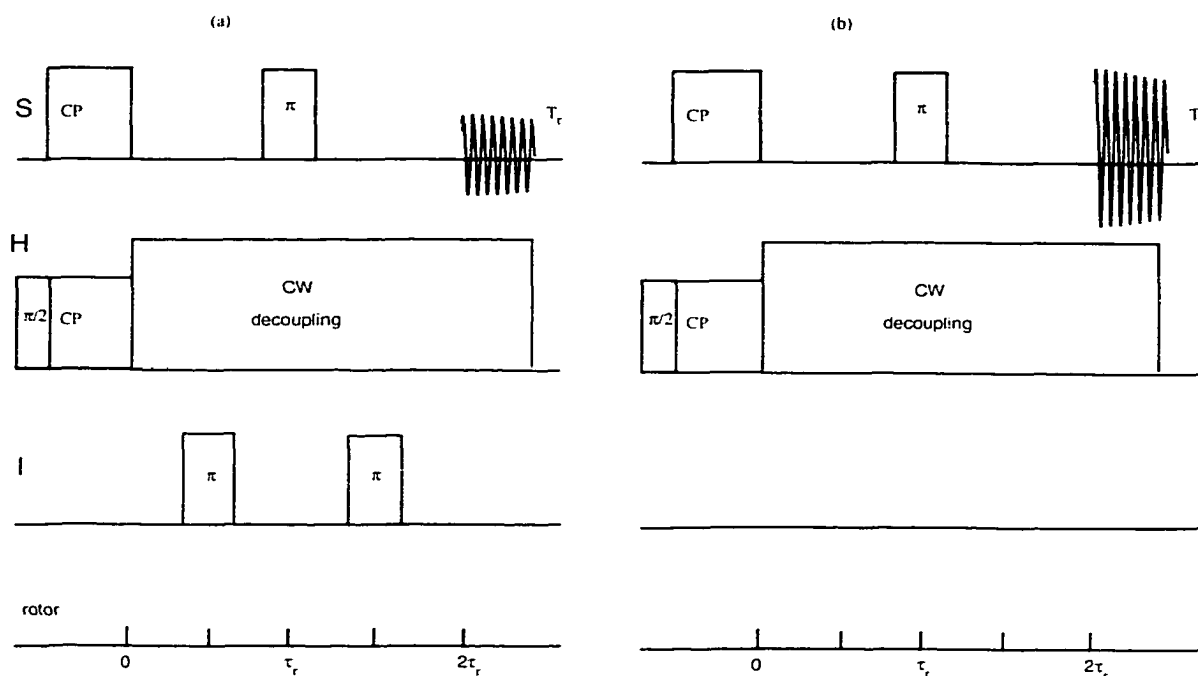


Figure 2.11

Simple REDOR pulse sequence. "S" stands for an observed spin. "H" is a proton magnetization sink through the cross polarization (CP). Protons are then decoupled by continuous wave (CW) field before a recycle delay, T_r . I-spin magnetization is dephased by π -pulses every half a rotor period. In the absence of dephasing pulses (b), the full spin echo is observed after two rotor periods, $2\tau_r$, accumulated dipolar phase is zero. With the application of dephasing pulses (a), the dipolar phase accumulates, and the observed echo is reduced.

In general, due to periodic time dependence of the dipolar frequency during MAS, its average over the rotor period is zero (Eq. 2.103). So, for any time, t_1 , the accumulated phase

$$\int_{t_1}^{\tau_r} \omega_D(t) dt = - \int_0^{t_1} \omega_D(t) dt = -\theta \quad [2.140]$$

Therefore, the dipolar evolution of the system over the rotor period, with application of 180 degree x-pulse at time t_1 , can be described by the operator [92]

$$\mathbf{U}(\tau_r) = e^{-i\theta \mathbf{S}_z I_z} e^{-i\pi I_x} e^{i\theta \mathbf{S}_z I_z} = e^{-i2\theta \mathbf{S}_z I_z} e^{-i\pi I_x} \quad [2.141]$$

According to Eq. 2.29, the observed magnetization $\langle \mathbf{S}_+ \rangle$ after one rotor period, τ_r , when the change in system states is described by propagator $\mathbf{U} = \mathbf{U}(\tau_r)$, is

$$\langle \mathbf{S}_+(\tau_r) \rangle = \text{Tr}(\boldsymbol{\rho}(\tau_r) \mathbf{S}_+) = \text{Tr}(\mathbf{U} \boldsymbol{\rho}(0) \mathbf{U}^{-1} \mathbf{S}_+) = \text{Tr}(\mathbf{U} \mathbf{S}_+ \mathbf{U}^{-1} \boldsymbol{\rho}(0)) \quad [2.142]$$

The initial density matrix after the preparation period can be written in terms of observed, S, and dephased, I, magnetization

$$\boldsymbol{\rho}(0) = \boldsymbol{\rho}_S(0) + \boldsymbol{\rho}_I(0) = M_0^I \mathbf{I}_z + M_0^S \mathbf{S}_x \quad [2.143]$$

Substituting Eq. 2.141 into Eq. 2.142, we get [61]

$$\begin{aligned} \langle \mathbf{S}_+(\tau_r) \rangle &= \text{Tr}(e^{i\pi \mathbf{I}_z} e^{i2\theta \mathbf{S}_z \mathbf{I}_z} \mathbf{S}_+ e^{-i2\theta \mathbf{S}_z \mathbf{I}_z} e^{-i\pi \mathbf{I}_z} \boldsymbol{\rho}(0)) \\ &= \text{Tr}([\cos \frac{\theta}{2} - i2 \mathbf{I}_z \sin \frac{\theta}{2}]^2 \mathbf{S}_+ \boldsymbol{\rho}(0)) = \text{Tr}(e^{-i2\theta \mathbf{I}_z} \boldsymbol{\rho}(0)) \end{aligned} \quad [2.144]$$

Now, by using an expansion valid for spin-1/2 particles [61],

$$e^{-i2\theta \mathbf{I}_z} = \mathbf{1} \cos \theta - i2 \mathbf{I}_z \sin \theta \quad [2.145]$$

the observed magnetization can be expressed as

$$\begin{aligned} \langle \mathbf{S}_+(\tau_r) \rangle &= \cos \theta [\text{Tr}(\mathbf{S}_+ \boldsymbol{\rho}_I(0)) + \text{Tr}(\mathbf{S}_+ \boldsymbol{\rho}_S(0))] \\ &\quad - i2 \sin \theta [\text{Tr}(\mathbf{I}_z \mathbf{S}_+ \boldsymbol{\rho}_I(0)) + \text{Tr}(\mathbf{I}_z \mathbf{S}_+ \boldsymbol{\rho}_S(0))] = \cos \theta \langle \mathbf{S}_+(0) \rangle \end{aligned} \quad [2.146]$$

Consequently, the ratio of observed S-spin transverse magnetization after dipolar dephasing, S_+^r to that in the absence of dephasing, S_+^0 , depends only on accumulated dipolar phase

$$\frac{S_+^r}{S_+^0} = \cos \theta \quad [2.147]$$

According to the pulse sequence shown in Fig. 2.11, $\theta = \phi_D$ (Eq. 2.139). Without dephasing pulses, the signal observed after two rotor cycles will be attenuated only by T_2 (Eq. 2.96) effects: $S_+^0(2\tau_r) = M_0^S \exp(-2\tau_r/T_2)$. With the dephasing pulses, the reduced echo will be observed: $S_+^r(2\tau_r) = M_0^S \exp(-2\tau_r/T_2) \cos(2\phi_D)$, for a single internuclear vector orientation. Maximum echo reduction achievable for a single pulse per rotor period is obtained with dephasing pulses timed at half a rotor period [93]. Pulses applied before or after this time would produce smaller REDOR dephasing. The direct measurement of dipolar dephasing is done by taking the ratio of reduced to full echo signals. In case of a glassy or powdered samples with isotropic distribution of dipolar coupled spin pair

orientations, the observed REDOR dephasing after N rotor cycles is calculated by performing the standard powder average

$$\frac{S_r}{S} = \int_{\Omega} \frac{S_+^r}{S_+^0} d\Omega = \frac{1}{4\pi} \int_0^{2\pi} d\alpha \int_0^{\pi} d\beta \sin \beta \cos(N\phi_D) \quad [2.148]$$

Numerical evaluation of the double integral in Eq. 2.148 with an assumed value for the dipolar coupling, D , followed by comparison with the experimentally measured S_r/S , provides a way to determine the S-I internuclear distance. Complex Fourier transform (FT) of REDOR data acquired over many rotor cycles gives a dipolar Pake doublet (Fig. 2.12), with the difference between extremes equal to $\frac{2\sqrt{2}}{\pi} D$ (in case of a single dephasing pulse in the middle of a rotor period [77]). This allows approximate estimation of the dipolar coupling directly from the FT of the experimental data provided long data sets with good signal to noise can be acquired.

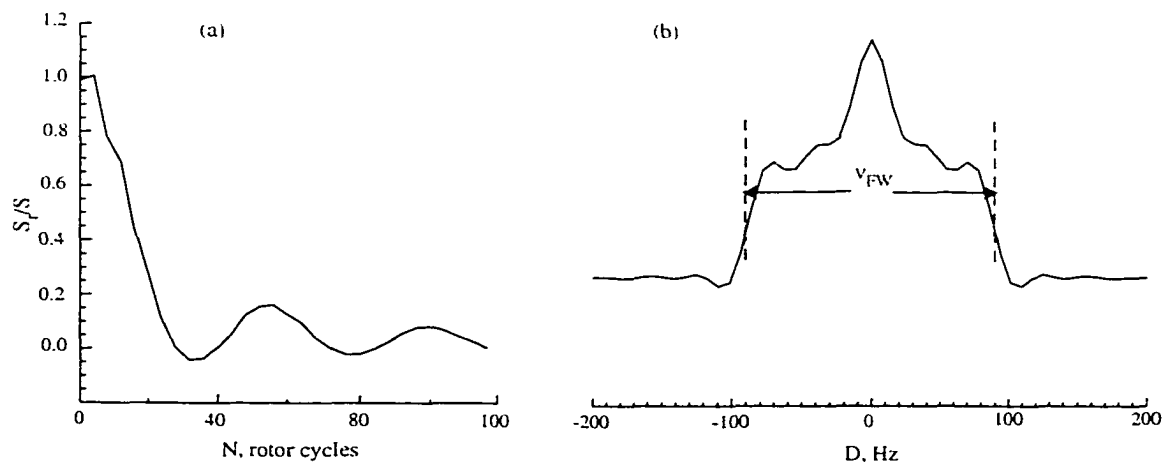


Figure 2.12

Simulated REDOR curve (a) and its Fourier transform (b) for $D = 200 \text{ Hz} \approx 1.11v_{FW}$. 30 points for REDOR curve were calculated by numerical double integration of Eq. 2.148 according to Simpson's rule [94] for every fourth rotor cycle, $\tau_r = 250 \mu\text{s}$, $SW = 500 \text{ Hz}$. 20 % noise was added to the simulated data. The data were zero filled to 128 points before FT.

To save experimental time, REDOR data sets usually have to be truncated in the time-domain. Such abrupt truncation causes sinc-function modulation wiggles that appear on either side of the main peak in corresponding frequency-domain spectra [66]. These

troublesome wiggles are effectively reduced by Blackman-Harris apodization [95], which attenuates the first wiggle lobe by as much as 67 dB. Such a three-point window function can be written for i -th point of REDOR curve as follows [66]:

$$F(i) = 0.424 + 0.497 \cos\left(\frac{i\pi \text{step}}{N}\right) + 0.079 \cos\left(\frac{i2\pi \text{step}}{N}\right) \quad [2.149]$$

where "step" is the step in rotor cycles, and N , is the total number of the rotor cycles sampled. The half-width of the broadening in the frequency domain due to Blackman-Harris apodization is approximately $(N\tau_r)^{-1}$ [66].

REDOR formalism can be applied for the case of multiple isolated spin pairs, $S^{(j)}-I^{(j)}$, with different internuclear distances (or their continuous distribution) [96]. The "isolation" condition requires that the spin operators for different spin pairs commute: $[I^{(j)}, I^{(k)}] = 0$, $[S^{(j)}, S^{(k)}] = 0$, and $[I^{(j)}, S^{(k)}] = 0$. Then the observed magnetization for the spin system (Eq. 2.146) reduces to a sum

$$\langle S_+(\tau_r) \rangle = \sum_j \cos \theta_j \langle S_+(0) \rangle_j \quad [2.150]$$

Therefore, the observed dephasing is a sum of REDOR curves

$$\frac{S_r}{S} = \frac{1}{4\pi} \sum_j f_j \int_0^{2\pi} d\alpha \int_0^\pi d\beta \sin \beta \cos(N\phi_D(D_j)) \quad [2.151]$$

$$f_j = \frac{\langle S_+(0) \rangle_j}{\sum_j \langle S_+(0) \rangle_j} \quad [2.152]$$

In such cases, the direct comparison of simulated multiple REDOR curves with experimental data is possible but time consuming, and the FT procedure is no longer capable of providing quantitative information. However, new efficient REDOR dipolar transform methods, which allow quantitative characterization of multiple internuclear distances, have recently become available [97]. This will be discussed in more detail in Chapter 5 of this dissertation.

For long distance measurement, REDOR sensitivity is limited by low dephasing efficiency, such that noticeable echo reduction is observed only after many rotor cycles. The

need for longer dephasing may compete with low signal-to-noise due to T_2 effects. In such cases, it may sometimes be possible to increase sensitivity and lower systematic errors by measuring the distances between nuclei with higher gyromagnetic constants (like ^{13}C - ^{31}P or ^{13}C - ^{19}F instead of ^{13}C - ^{15}N).

REDOR experiments for spin-1/2 – spin-1 pairs are likewise possible [98, 99]. If spin-1 is observed, while spin-1/2 is dephased, the resulting dephasing is the same as described above (Eq. 2.148). If instead, spin-1 is chosen to dephase, application of π -pulses changes its three states: $|-1\rangle \rightarrow |+1\rangle$, $|0\rangle \rightarrow |0\rangle$; $|+1\rangle \rightarrow |-1\rangle$, so that the magnetic quantum number modulus is incremented by -2, 0 and +2 respectively. Therefore, the observed REDOR signal for a single internuclear vector assumes the form

$$\frac{S_+^r}{S_+^0} = \frac{1}{3}(1 + 2 \cos 2N\phi_D) \quad [2.153]$$

For a spin-1 nucleus, the first order quadrupole interaction is large. For instance, in case of a static deuteron typical quadrupole coupling constants are 160-200 kHz. The deuteron is a good choice of label for REDOR experiments, since it has very low background contribution (0.2 % natural abundance), and can be exchanged for protons in complex organic molecules to establish distance constraints. Due to reasonably high gyromagnetic ratio and twice dephasing efficiency (Eq. 2.147), deuteron REDOR can provide better sensitivity to long internuclear distances. Unfortunately, the large first order quadrupole interaction makes this experiment technically demanding [99]. Equation 2.153 is strictly correct only under the assumption of very strong " δ " π -pulses, providing perfect excitation. In most commercial triple resonance probes the pulse power levels are limited, and the full deuteron powder spectrum cannot be excited. Recently, the ways around this problem have been invented introducing composite excitation and dephasing pulses in the deuteron channel [100-102].

When the deuteron is the observed nucleus, a single 90 degree excitation pulse is applied, and the magic angle spinning spectrum consists of a quadrupole side band pattern. The dipolar coupling can then be measured (Eq. 2.148), if intensity from all side bands is integrated. Alternatively, the rotor synchronous acquisition can be performed [98] with and without dephasing pulses on the spin-1/2 nucleus, directly producing the REDOR curve. There are a few complications for such experiments. One is that the background signal from the spin-1/2 nucleus (e.g. ^{13}C) close to deuteron label can be strong enough to interfere with dephasing from the labeled site. Another is connected with the fact that the deuteron spectrum may not provide enough chemical shift resolution in case of overlapping powder patterns. In many cases selective deuteron labeling is not feasible, especially for materials with hydrogen bonding, where hydrogens are easily exchanged for deuterons at all sites simultaneously (e.g. for PAMAM dendrimers). Therefore, the above mentioned experiment with dephasing pulses on quadrupole nucleus is of greater practical utility, despite being more technically demanding than simple spin-1/2 – spin-1/2 REDOR.

2.5 Summary

This chapter provides the description of NMR theory, equipment and experimental techniques used for studying PAMAM dendrimer structure and dynamics. It contains a quantum mechanical description of important internuclear interactions for spin-1/2 and spin-1 nuclei observed in the dendrimers. The discussion of the effects of motional averaging on these interactions and measured relaxation times highlights great utility of the solid state NMR techniques in the investigation of the dendrimer structure and molecular motion. The basic concepts and vocabulary commonly used for the description of relevant NMR experiments are introduced. The quantum mechanical basis of the dynamics simulation algorithms for software packages (SUMS, EXPRESS, MAS), used in experimental data analysis, has been discussed.

Chapter 3

Hydrogen Bonding and Motion in PAMAM Salts

The equilibrium structure of a material is determined by stabilizing inter- and intramolecular interactions competing with destabilizing thermally activated molecular motion. Solid state NMR techniques (described in the previous chapter) allow simultaneous investigation of both static and dynamic aspects of this competition. Thus, characterization of structure and dynamics of polymers is an important application of deuterium NMR. The goal is to connect the microscopic quantum mechanical properties with the known or desired bulk properties. Revealing such correlations is essential and eventually this could help direct the synthesis towards meeting desired physical specifications.

This chapter is devoted to the first experimental characterization of solid dendrimer architecture using temperature and generation dependent spectra which are connected to molecular motion. Models for the consistent description of experimental results are introduced and validated. This is followed by assignment of the overlapping QE lineshapes. The spectral overlap is caused by non-selective deuteration of PAMAM salts (as described in Chapter 1). Next, the lineshape simulation procedure is introduced, and an algorithm for extracting the characteristic distribution parameters responsible for the experimentally

observed powder pattern broadening is presented. The rest of the chapter explains the implications of observed temperature and generation dependence of the structural parameters for the morphology of deuterated PAMAM ammonium chloride dendrimer salts.

For six PAMAM generations the solid state deuterium NMR data obtained are interpreted to obtain a qualitatively complete picture of the dendrimer structure and motional amplitudes. Lineshape analysis provides information on the distribution of amide hydrogen bond lengths between the dendrimer spacers at secondary amide sites, and at deuterated tertiary amine branching sites. Both flexible structural units and stabilizing amide connectivity with counterion attraction govern PAMAM transition from an interpenetrated extended structure for low generations to a more symmetric backfolded architecture for high generations. In the course of this transition it is possible to explicitly investigate the balance between destabilizing effect of planar intra-molecular librational motion, cone libration of terminal groups and constructive trends of hydrogen bonding. Most of the material presented in this chapter is published in *Macromolecules*, **33** (2000) [4].

3.1 NMR Studies in the Glass Transition Region

Due to the sensitivity of the solid state NMR experiments to molecular dynamics, a complete material characterization by NMR requires knowledge of the thermal range studied in connection with bulk dendrimer properties. Therefore, temperature dependent spectra should not be interpreted without comparison with bulk measurements such as differential scanning calorimetry (DSC).

Appropriate experimental settings for QE lineshape acquisition have to provide adequate spectral coverage, good signal-to-noise ratios, short recycle delays, and minimize transverse relaxation effects [4]. Elevated temperatures were attained by flowing heated air around the sample coil, and low temperatures were attained using nitrogen gas cooled from a boil-off

dewar. Comparison of room temperature spectra obtained with recycle delays of 5 s and 20 s indicated that a 5 s recycle time was adequate for essentially complete relaxation of all spectral features. At higher temperatures shorter recycle delays were sufficient. The relative errors in total intensity of different spectra due to electronic instabilities over the 24 hour acquisition period were estimated to be less than 5 %.

The temperature dependent QE spectra of the G2 dendrimer are shown in Figure 3.1. A relatively narrow central component emerges on top of broad powder patterns, with intensity increasing for temperatures above 20 °C. Similar qualitative changes in the spectra were observed for all generations, although in different temperature ranges. In deutron spectra narrow components are usually observed when the orientation inequivalence of transition frequencies (Eq. 2.90) is removed by rapid, isotropic motional processes. This liquid-like behavior may involve parts of the sample where stabilizing interactions have been broken by thermally activated molecular motion. The anisotropy wide deutron powder patterns can be associated with rigid material, either polycrystalline or amorphous.

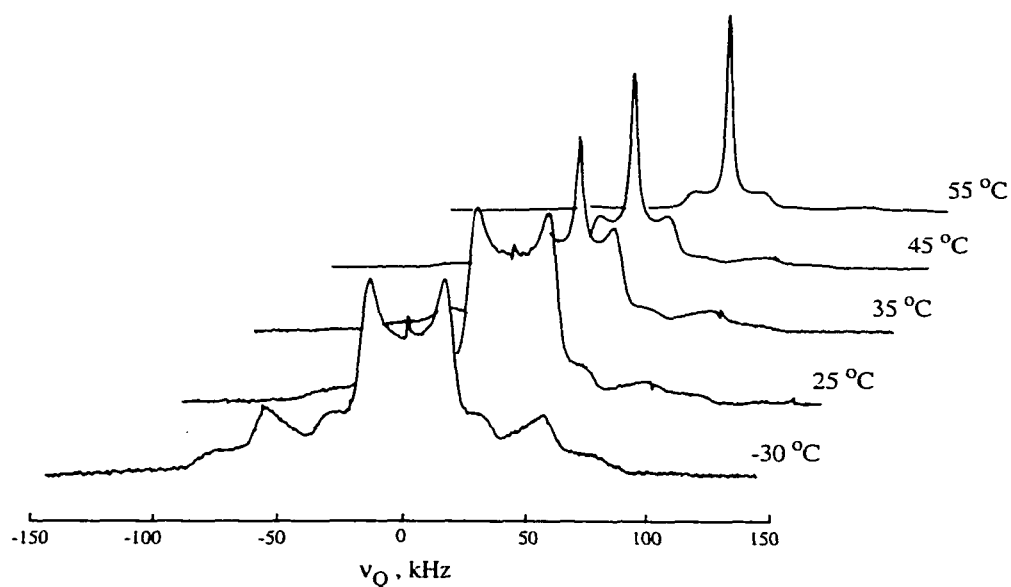


Figure 3.1
Temperature dependent quadrupole echo spectra of generation 2 PAMAM chloride dendrimer salt.

Solid amine terminated dendrimers are known to be entirely amorphous, with broad glass transition temperatures starting at $-11\text{ }^{\circ}\text{C}$ for G0 to $13\text{ }^{\circ}\text{C}$ for $G > 4$ [3]. DSC data for G2 dendrimer salts, presented in Figure 3.2, also reveal no evidence of a crystalline transition. Instead, the onset of a broad change in heat capacity ($21\text{ }^{\circ}\text{C}$ – $71\text{ }^{\circ}\text{C}$) coincides with the first appearance of the narrow component of the deuteron lineshape. This component continues to grow with increasing temperature up to $65\text{ }^{\circ}\text{C}$, where the sample begins to flow (data not shown). We therefore associate this spectral feature with the onset of the broad glass transition. Quantitative DSC measurements on all samples were hampered by the extremely hygroscopic nature of PAMAM salts, but our NMR data demonstrate that the salt formation raises T_g by about $24\text{ }^{\circ}\text{C}$ relative to the pure unionized polymers [103]. This is qualitatively in accord with theoretical predictions [103].

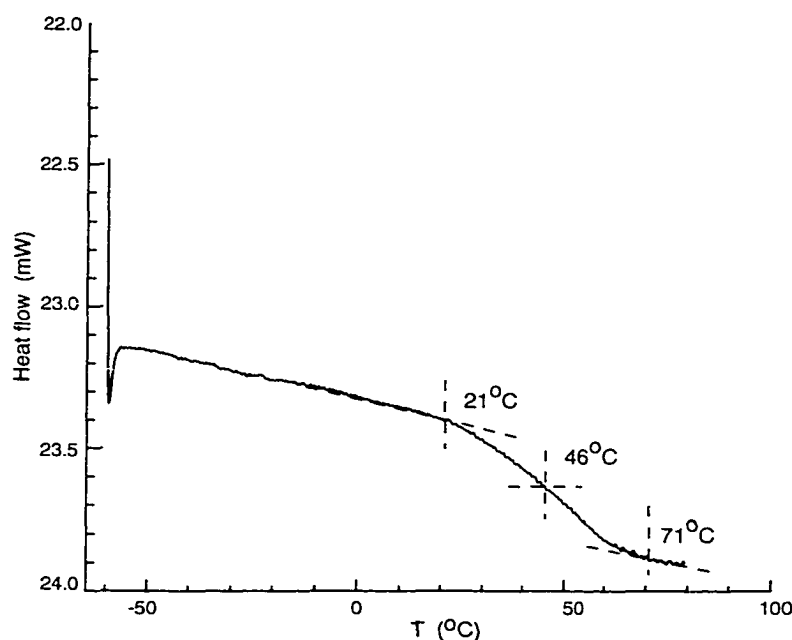


Figure 3.2

Differential scanning calorimetry curve for G2 deuterated PAMAM dendrimer salt. This curve was obtained on a 10 mg sample (dried under vacuum and packed under nitrogen) using a Perkin Elmer Pyris-1 calorimeter, scanning from -60 to $+80\text{ }^{\circ}\text{C}$ at $10\text{ }^{\circ}\text{C}/\text{min}$.

Another fact worth noticing is the wide temperature range of the glass transition. Although in salts it is much wider (~ 50 °C) than in pure dendrimers (~ 15 °C [27]), the origins might not be very different. Broad glass transition regions in linear polymers are usually associated with nonuniform structures coming from wide distributions of chain lengths. This cannot provide a reasonable explanation for practically monodisperse dendrimers. Moreover, our deutron NMR studies (discussed in subsequent sections) indicate relatively narrow distributions of librational amplitudes and rates for PAMAM dendrimer salts. Perhaps the wider transition found for salts is associated with the increased complexity of their electrostatic interactions.

Close investigation of temperature dependent powder patterns suggests that changes of quadrupole coupling parameters (discontinuity splitting and asymmetry) occur in the course of the broad glass transition. The line widths do not appear to undergo major modifications, which would be characteristic of motion in the intermediate regime. Slow motion, if present, would dictate long recycle delays (> 10 s) for signal observation, which is not the case. Therefore, in the first approximation, the glass transition behavior of the amorphous PAMAM salts can be described assuming fast molecular motion as the origin of the temperature dependent lineshape evolution within the glass transition region.

Unselective deuteration and salt preparation results in the overlap of contributions from chemically distinct deuterated sites. As has been noted in Chapter 1, PAMAM structure allows deutron exchange at the dendrimer terminal ammonium, spacer amides and branching point tertiary amine groups to be achieved by simple exchange in solution. Different motions and thus temperature dependent trends are possible for the different sites. This could provide another explanation for the wide glass transition in bulk dendrimer salts.

3.2 Approximation of Fast Molecular Motion

Averaging of observed quadrupole coupling parameters by fast molecular motion can be described using irreducible spherical tensors [65]. In the principle axes system (PAS) of the electric field gradient tensor, the quadrupole coupling constant and asymmetry parameter are defined by the constant tensor components $T_m^{(2)}(\text{PAS})$ with $m = 0, \pm 1$ (Eq. 2.82). These quantities are related to their counterparts in laboratory fixed coordinates by a series of Euler rotations. Thus if $\Omega_{\text{PM}}(\alpha_{\text{PM}}, \beta_{\text{PM}}, \gamma_{\text{PM}})$ denotes a transformation which rotates the PAS frame onto a set of molecule fixed axes (e.g. fixed to the dendrimer branch), $\Omega_{\text{MD}}(\alpha_{\text{MD}}, \beta_{\text{MD}}, \gamma_{\text{MD}})$ denotes a rotation from molecule fixed axes to a dendrimer-fixed frame, and $\Omega_{\text{DL}}(\alpha_{\text{DL}}, \beta_{\text{DL}}, \gamma_{\text{DL}})$ denotes a rotation from dendrimer-fixed axes to laboratory fixed axes, the tensor elements in the laboratory frame are given by

$$T_m^{(2)}(\text{LAB}) = \sum_{a=-2}^2 D_{am}^{(2)}(\Omega_{\text{DL}}) \sum_{b=-2}^2 D_{ba}^{(2)}(\Omega_{\text{MD}}) \sum_{c=-2}^2 D_{cb}^{(2)}(\Omega_{\text{PM}}) T_c^{(2)}(\text{PAS}) \quad [3.1]$$

Here, $D_{ij}^{(2)}(\Omega)$ is the (j, k) element of the second rank Wigner rotation matrix for the transformation Ω . To calculate the equilibrium spectrum, $T_0^{(2)}(\text{LAB})$ must be averaged over fast motions (Eq. 2.105). The time independent Euler transformation Ω_{DL} defines the dendrimer orientation in a powder sample, while both remaining transformations are time dependent due to molecular motion. Assuming that it is permissible to average these motions independently, the averaged tensor element in the LAB system is given by

$$\begin{aligned} \langle T_0^{(2)}(\text{LAB}) \rangle &= \sum_{a=-2}^2 D_{a0}^{(2)}(\Omega_{\text{DL}}) \sum_{b=-2}^2 \langle D_{ba}^{(2)}(\Omega_{\text{MD}}) \rangle \sum_{c=-2}^2 \langle D_{cb}^{(2)}(\Omega_{\text{PM}}) \rangle T_c^{(2)}(\text{PAS}) \\ &\equiv \frac{\sqrt{6}}{8} \langle \chi \rangle (3 \cos^2 \beta_{\text{DL}} - 1 + \langle \eta \rangle \sin^2 \beta_{\text{DL}} \cos 2\alpha_{\text{DL}}) \end{aligned} \quad [3.2]$$

$$\langle D_{ij}^{(2)}(\Omega) \rangle = \int_{\Omega} D_{ij}^{(2)}(\Omega) P(\Omega) d\Omega \quad [3.3]$$

where angular brackets mean ensemble average due to molecular motion, $\langle \chi \rangle$ and $\langle \eta \rangle$ are observed average quadrupole coupling parameters, and $P(\Omega)$ is a model dependent probability of orientation Ω .

3.2.1 Planar Libration

For the deuterons at the dendrimer spacers and branching sites large amplitude motion is prohibited by steric constraints. Restricted fast libration in a plane is a plausible type of motion for these groups [54]. For such motion it can be assumed, without loss of generality, that the dendrimer- and molecule-fixed frames coincide. The transformation $\Omega_{MD}(\alpha_{MD}, \beta_{MD}, \gamma_{MD})$ in Eq. 3.2 reduces to the identity operator, collapsing the sum over index b . The largest component of the EFG tensor, q_{zz} , is coincident with the N-D bond axis to a high degree of approximation [54, 104]. Following Usha et.al. [54], we assume that libration occurs in a plane containing the N-D bond perpendicular to q_{yy} , such that q_{yy} remains invariant. As an extension to previous calculations [105], we will consider the case of nonzero intrinsic asymmetry parameter, $\eta_{PAS} \neq 0$, characteristic e.g. of amide groups [54, 104]. The transformation $\Omega_{PM}(\alpha_{PM}, \beta_{PM}, \gamma_{PM}) = \Omega_{PM}(0, \phi(t), 0)$, and effects of libration on the observed quadrupole coupling parameters are easy to evaluate by averaging Eq. 3.2 over the one-dimensional arc, $-\phi_0 \leq \phi \leq \phi_0$, with uniform probability $(2\phi_0)^{-1}$.

$$\begin{aligned} \langle T_0^{(2)}(LAB) \rangle &= d_{00}(\beta_{DL}) (\langle d_{00}(\phi) \rangle T_0^{(2)}(PAS) + 2 \langle d_{20}(\phi) \rangle T_2^{(2)}(PAS)) \\ &+ 2 \cos 2\alpha_{DL} d_{20}(\beta_{DL}) (\langle d_{20}(\phi) \rangle T_0^{(2)}(PAS) + [\langle d_{22}(\phi) \rangle + \langle d_{2-2}(\phi) \rangle] T_2^{(2)}(PAS)) \\ &\equiv d_{00}(\beta_{DL}) \langle T_0^{(2)}(MOL) \rangle + 2 \cos 2\alpha_{DL} d_{20}(\beta_{DL}) \langle T_2^{(2)}(MOL) \rangle \end{aligned} \quad [3.4]$$

$$\langle d_{ij}(\phi) \rangle = \frac{1}{2\phi_0} \int_{-\phi_0}^{\phi_0} d_{ij}(\phi) d\phi \quad [3.5]$$

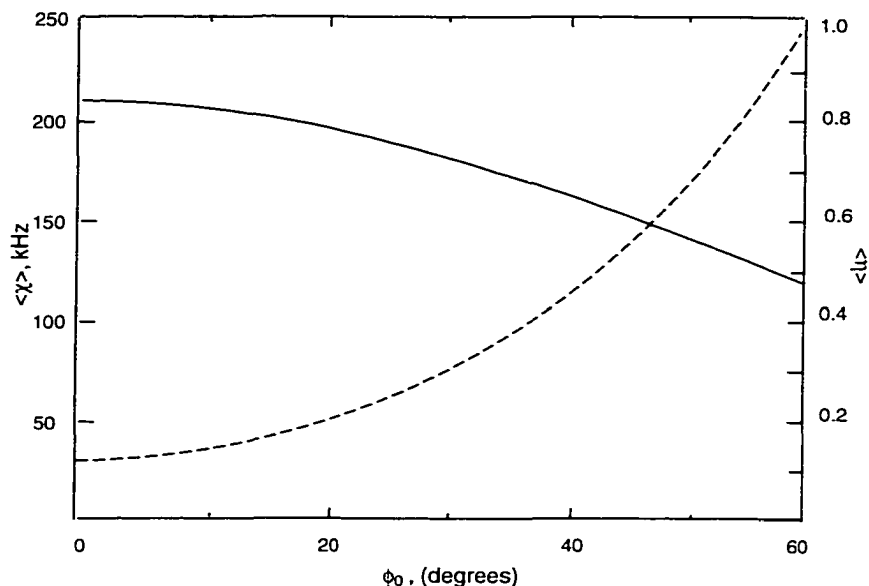


Figure 3.3

Average quadrupole coupling constant, $\langle \chi \rangle$ (solid line), and asymmetry parameter, $\langle \eta \rangle$ (dashed line), dependence on libration amplitude for the planar libration of ND bond (Eqs.3.6, 3.7) with $\chi_{PAS} = 210$ kHz and $\eta_{PAS} = 0.12$ (characteristic values for amide groups).

This procedure gives the following analytical expressions for the average quadrupole coupling constant and a motionally induced asymmetry parameter:

$$\langle \chi \rangle = \frac{1}{2} \chi_{PAS} [(\langle c^2 \rangle - 1)(1 - \eta_{PAS}) + 2\langle c^2 \rangle] \quad [3.6]$$

$$\langle \eta \rangle = \frac{\eta_{PAS}(1 + \langle c^2 \rangle) - 3(\langle c^2 \rangle - 1)}{(\langle c^2 \rangle - 1)(1 - \eta_{PAS}) + 2\langle c^2 \rangle} \quad [3.7]$$

$$\langle c^2 \rangle = \frac{1}{2} \left(1 + \frac{\sin(2\phi_0)}{2\phi_0} \right) \quad [3.8]$$

Here, $\langle c^2 \rangle$ is the ensemble average of $\cos^2\phi(t)$. To ensure freedom from algebraic errors which can plague this sort of calculation, it was verified that identical answers were obtained using Cartesian tensors and 3x3 orthogonal Euler rotation matrices [105] (Appendix A).

3.2.2 Fast Rotation and Cone Libration

When fast rotation about a three-fold symmetry axis is combined with isotropic libration of the axis in a cone, integration over Ω_{PM} (with constant probability 1/3) ensures that the average asymmetry parameter is zero, and the quadrupole coupling constant is reduced by a factor $d_{00}(\beta_{PM})$. Further, integration over Ω_{MD} , to account for the libration in a cone, with uniform probability $[4\pi^2(1-\cos\beta_{MC})]^{-1}$ (Eq. 2.107), gives the average quadrupole coupling constant,

$$\langle \chi \rangle = \frac{1}{4} \chi_{PAS} (3 \cos^2 \beta_{PM} - 1) \cos \beta_{MD} (1 + \cos \beta_{MD}) \quad [3.9]$$

Here, β_{PM} is the angle between the Z-axis of the principle axes frame and the three-fold rotation axis and β_{MD} is the half-angle of the cone. For this model, inversion of Eq. 3.8 yields the following expression,

$$\beta_{MD} = \arccos \left(-\frac{1}{2} + \sqrt{\frac{1}{4} + 2 \frac{\langle \chi \rangle}{\frac{1}{2} \chi_{PAS} (3 \cos^2 \beta_{PM} - 1)}} \right) \quad [3.10]$$

This model is appropriate for the deuterons of the dendrimer termini. Additional considerations would be needed to account for temperature dependent nonzero asymmetry parameters, if observed, with decreasing quadrupole coupling constant. The asymmetry may be caused by inequivalence of the rotational and librational sites, when the probability $P(\Omega)$ is no longer uniform. For instance, there can be deviations from the cone libration symmetry due to preference of the sites with stronger attraction to chlorine anion in PAMAM. The same may hold true for rotational sites. In fact, to describe non-zero asymmetry parameter, probabilities of both librational and rotational orientations should be nonuniform.

3.3 Hydrogen Bonding

The presence of the amine, amide, and ammonium proton donors, as well as carbonyl and chlorine proton acceptors in PAMAM salts, ensures that hydrogen bonding is a very important factor for structural stability. If classified by strength, hydrogen bonds are intermediate between covalent and van der Waals forces [106]. Although Coulombic attractions between polar groups contribute to its strength, the hydrogen bond is more complex than just classical electrostatic attraction. Its formation involves a lone electron pair of the acceptor atom pulled toward the bridging donor proton. The consequences of such interaction are directionality and constrained geometry of the bond as well as subtle shifts of electron density from the proton acceptor to the donor group. Rather than residing on the bridging proton, the electron density becomes distributed throughout the donor group. The total density associated with the central hydrogen undergoes a decrease when the bond is formed.

Electron density shifts which arise from the H-bonding in deuterated compounds result in perturbation of the electric field gradient (EFG) tensor "deshielding" the bridging deuteron. These changes in the EFG tensor correlate with the length of the hydrogen bond [107]. In general, these correlations are anisotropic. A simple, consistent empirical relation has been found only for the largest component of EFG tensor, q_{zz} , in principle axes system (PAS) of the observed deuteron, in the absence of molecular motion. If it is assumed that redistribution of the electron density occurs predominantly along the direction of the hydrogen bond, coinciding with z-direction in PAS, the Taylor expansion for q_{zz} component along z-direction is,

$$\begin{aligned}
 q_{zz}(z = z(r^{-1})) &= q_{zz}(z(0)) + r^{-1} \left. \frac{\partial}{\partial r} q_{zz}(z(r^{-1})) \right|_{r^{-1}=0} \\
 &\quad + r^{-2} \left. \frac{\partial^2}{\partial r^2} q_{zz}(z(r^{-1})) \right|_{r^{-1}=0} + \dots \\
 &= q_{zz}^0 - r^{-3} q_{zz}^0 + O(r^{-5})
 \end{aligned}
 \tag{3.11}$$

Where r is the distance between deuteron and acceptor nucleus.

From this expansion we can see that q_{zz}^0 describes the principle EFG component for infinitely separated donor-acceptor pair, and depends only on the electron environment of the deuteron. The coefficient of the second term should depend mostly on acceptor electronic state, since its lone pair electron density shift will determine the gradient $\frac{\partial}{\partial z} q_{zz}$ around the deuteron donor. Because, $\chi \sim q_{zz}$ (Eq. 2.83), the quadrupole coupling constant can be related to hydrogen bond distance, r , by an expression of the form

$$\chi_{PAS} = A - Br^{-3} \quad [3.12]$$

where A and B are empirical constants in kHz and distance r is in Å.

In case of PAMAM salts studied in this dissertation, r is the distance from the deuteron to the X-acceptor atom in a N-D...X hydrogen bond, and X can be oxygen, chlorine or bromine anion. This model completely ignores the asymmetry parameter [107-109]. The experiments confirmed that constants $A > 0$ and $B > 0$ are related to the state of orbital hybridization of hydrogen donor and acceptor atoms respectively [107, 109]. For tetrahedrally bonded nitrogen, $RND_3^+ \dots Cl^-$, $A = 239$ kHz and $B = 728$ kHz are rather well established values [108] (solid line fit in Fig. 3.4a), and for the purpose of simulations we adopted them for the branching points $R_3ND^+ \dots Cl^-$. For spacer secondary amides, $R_2ND \dots O$, there is less agreement in the literature. Some authors interpret data using the intercept value $A = 282$ kHz [54, 104], which was found to be valid for $RND_2 \dots O$ groups [108, 110-113], as illustrated in Fig. 3.4d. Attempts [114] to refine the correlation (Eq. 3.12) for secondary amide deuterons by including corrections for non-linear hydrogen bonds were not very successful. In this regard it must be noted that quadrupole coupling constants determined indirectly from relaxation measurements in solution (assuming a zero asymmetry parameter) are likely to be significantly different from the principle axes values in the solid required by Eq.3.12. Long relaxation times and limited sensitivity have precluded extensive accumulation of reliable solid state quadrupole coupling parameters for

secondary amide containing compounds with known structures. Nevertheless, if we assume that the slope, B , is still determined by the oxygen-acceptor atom, we can conclude on the basis of a few reports [54, 104] that a more appropriate intercept would be $A = 260$ kHz, as illustrated in Fig. 3.4c.

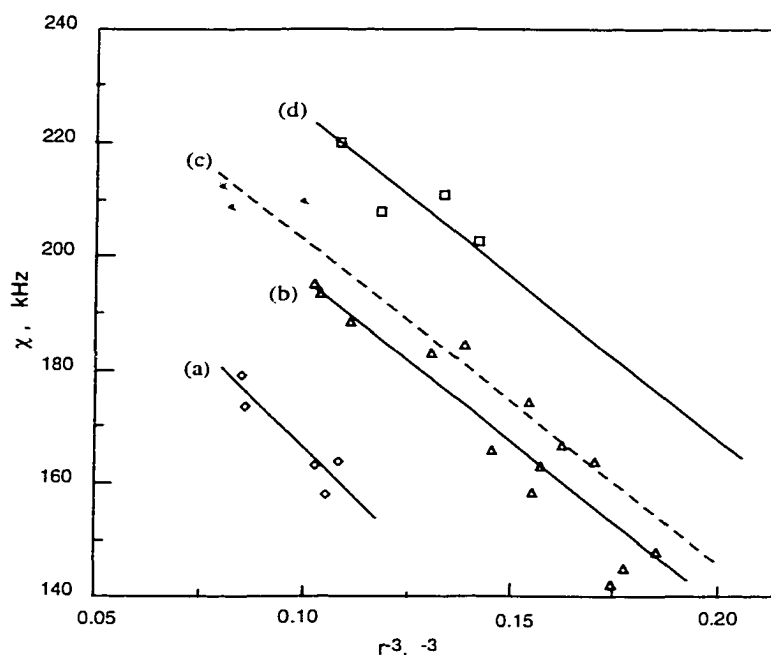


Figure 3.4

Dependence of quadrupole coupling constant, χ , on the inverse cube of the YD...X hydrogen bonding length, r . Points are experimental data: YD = ND⁺, X = Cl⁻ [108] (diamonds), YD = ND⁺, X = O [108, 109] (triangles), YD = RND₂, X = O [108, 110-113] (squares), YD = R₂ND, X = O [54, 104] (stars). Lines are linear fits with intercept and slope: (a) $A = 239$, $B = 728$ [108]; (b) $A = 253$, $B = 572$ [109]; (c) $A = 260$, $B = 572$; (d) $A = 282$, $B = 572$ [108]. In (c), the best fit A was found with the slope fixed at 572 as described in the text.

The value $B = 572$ kHz for oxygen is well established by the data for RND₃⁺...O [108, 109] (Fig.3 b) and for RND₂...O [108, 110-113] (Fig.3d). The fact that a few outlying points from the RND₃⁺...O line come close to the secondary amide line (Fig. 3.4c) may indicate some as yet poorly understood differences among zwitterionic RND₃⁺ deuterons. Note also that for these deuterons, the best fit intercept $A = 253$ kHz is very different from

$A = 239$ kHz (Fig. 3.4a) found for ionic solids [108, 109], even though the nitrogen-donors are tetrahedrally hybridized in both cases. In view of these limitations hydrogen bond length obtained from deuteron QE spectra can not be given much quantitative credence, but may nevertheless reveal interesting and useful qualitative trends.

3.4 QE Lineshape Assignments

QE spectra of all dendrimer generations consist of broad, overlapping powder patterns arising from three types of deuterons in rigid environments, plus two narrow peaks of different width in the center originating from more mobile parts of the sample. Our spectral assignments are based on literature values of quadrupole coupling parameters for deuterons bonded to nitrogens in different hybridization states [54, 104, 108, 109, 115, 116], confirmed by experiment on the G2 dendrimer in which Cl^- counterions were substituted with Br^- .

On the basis of literature values of quadrupole coupling parameters for similar materials [54, 104, 108, 109, 115, 116], the two widest powder patterns, which are observed for all generations, are assigned to secondary amide and protonated tertiary amine deuterons, respectively. Deuteration of tertiary amine sites was ensured during our preparation procedure (Chapter 1) by the excess of strong acid, and confirmed by measurements conducted on generation 2 dendrimers with counterion substitution. For quantitative interpretation of the changes in QE spectra upon anion substitution, the overlapping broad powder patterns were simulated to fit observed motionally averaged quadrupole coupling parameters, $\langle\chi\rangle$, $\langle\eta\rangle$, and line width, σ_χ , using SUMS algorithm [72, 84]. Results are shown in Figure 3.5.

Substitution of Br^- (Fig. 3.5a) for Cl^- (Fig. 3.5b) resulted in a noticeable decrease of $\langle\chi\rangle$ for deuterons at both the branching amine and amide sites, from 161 kHz (Fig. 3.5(b1)) to 149

kHz (Fig. 3.5(a1)) and 201 kHz (Fig. 3.5(b2)) to 192 kHz (Fig. 3.5(a2)), respectively. The observed changes for deuterons in the dendrimer interior demonstrate that the anions are not

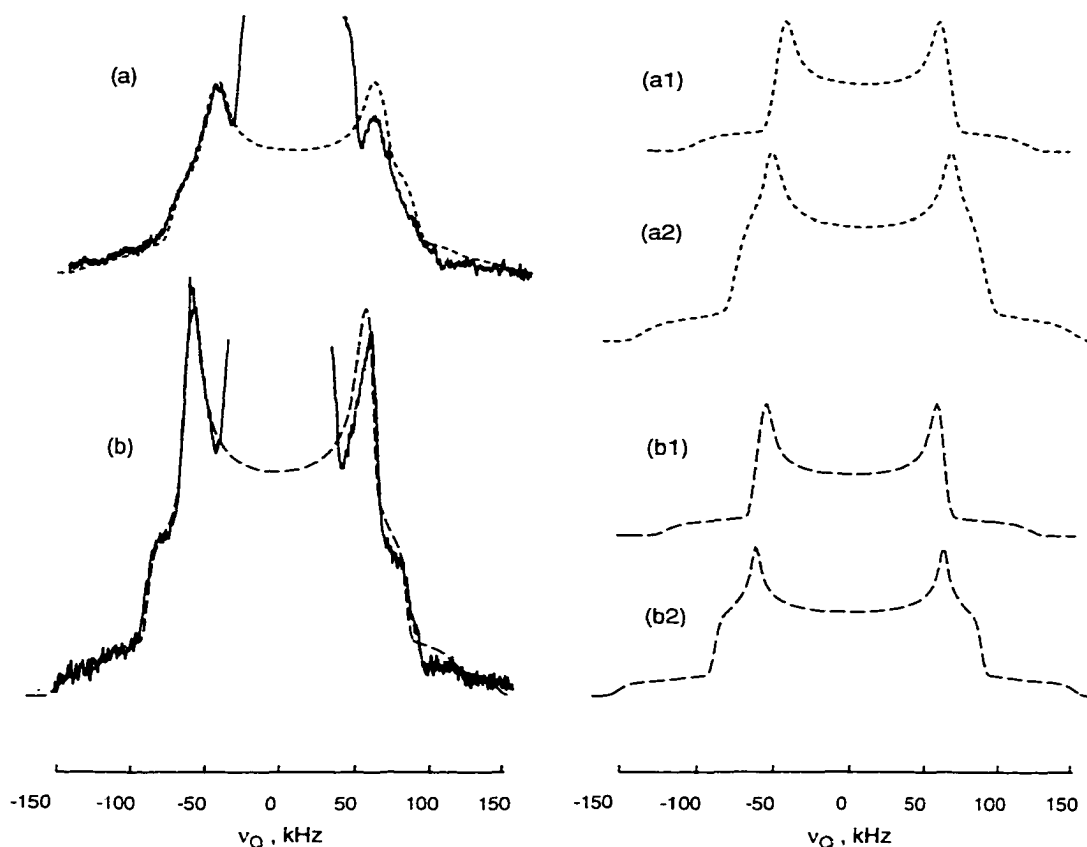


Figure 3.5

Experimental spectra (solid lines) and fits (dashed lines) assuming broadening due to Gaussian distribution of quadrupole coupling constants with averaging due to planar librations of the dendrimer spacer for underlying powder patterns of (a) brominated, and (b) chlorinated generation 2 dendrimers at $-30\text{ }^{\circ}\text{C}$. Inserts show the separate powder patterns whose sum best fits the experimental data. (a1) fit for $\text{R}_3\text{ND}^+\dots\text{Br}^-$, $\langle\chi\rangle = 149\pm 2\text{ kHz}$, $\langle\eta\rangle = 0.07\pm 0.01$, $\sigma_\chi = 10\pm 1\text{ kHz}$, integrated intensity = 1.0 ± 0.1 , $\eta_{\text{PAS}} = 0.05$, $\chi_{\text{PAS}} = 152\pm 3\text{ kHz}$, $\phi_0 = (11\pm 4)^\circ$, $\bar{r} = 2.03\pm 0.06\text{ \AA}$; (a2) fit for R_2ND , $\langle\chi\rangle = 192\pm 2\text{ kHz}$, $\langle\eta\rangle = 0.16\pm 0.01$, $\sigma_\chi = 11\pm 1\text{ kHz}$, integrated intensity = 2.0 ± 0.4 , $\eta_{\text{PAS}} = 0.12$, $\chi_{\text{PAS}} = 199\pm 3\text{ kHz}$, $\phi_0 = (15\pm 4)^\circ$, $\bar{r} = 2.1\pm 0.1\text{ \AA}$; (b1) fit for $\text{R}_3\text{ND}^+\dots\text{Cl}^-$, $\langle\chi\rangle = 161\pm 2\text{ kHz}$, $\langle\eta\rangle = 0.05\pm 0.01$, $\sigma_\chi = 8\pm 1\text{ kHz}$, integrated intensity = 1.0 ± 0.1 , $\eta_{\text{PAS}} = 0.05$, $\chi_{\text{PAS}} = 161\pm 3\text{ kHz}$, $\phi_0 = (1\pm 1)^\circ$, $\bar{r} = 2.11\pm 0.03\text{ \AA}$; (b2) fit for R_2ND , $\langle\chi\rangle = 201\pm 2\text{ kHz}$, $\langle\eta\rangle = 0.17\pm 0.01$, $\sigma_\chi = 6\pm 1\text{ kHz}$, integrated intensity = 1.7 ± 0.4 , $\eta_{\text{PAS}} = 0.12$, $\chi_{\text{PAS}} = 210\pm 3\text{ kHz}$, $\phi_0 = (17\pm 2)^\circ$, $\bar{r} = 2.25\pm 0.1\text{ \AA}$.

confined to the dendrimer surface. For the secondary amide sites the approximate 10 kHz decrease in $\langle\chi\rangle$ observed upon substitution of Br^- for Cl^- is most probably caused by a decrease of hydrogen bond length (Eq. 3.12). This hypothesis is supported by the fact that the decrease in average hydrogen bond length at these sites is very close to the difference in diameters between Cl^- and Br^- anions, $\Delta r = 0.14 \pm 0.02 \text{ \AA}$. Within experimental error, the same holds true for hydrogen bonds at protonated branching sites, for which $\Delta r = 0.09 \pm 0.04 \text{ \AA}$. The slightly larger changes in average hydrogen bond length found for secondary amide sites suggest greater flexibility of spacers compared to the branch points. The observed increase in powder pattern distribution widths from 6 to 11 kHz may correspond to a wider distribution of hydrogen bonding environments in the brominated sample.

Numerical inversion of Equation 3.7 can be used to estimate the planar libration amplitude from the best fit motionally averaged asymmetry parameter, $\langle\eta\rangle$, if a value is assumed for η_{PAS} (see caption to Fig. 3.5). According to this procedure, the small change in asymmetry parameter upon counterion substitution, from $\langle\eta\rangle = 0.17$ to 0.16 for $\text{R}_2\text{ND}\dots\text{O}$, corresponds to a negligible decrease in librational amplitude (17° to 15°) of the dendrimer spacers. Larger changes in libration amplitude (1° to 11°) found for R_3ND^+ groups could be associated with less efficient packing around the larger anion, perhaps arising from reduced electrostatic interactions.

In calculations of the average hydrogen bond distances for the brominated sample, the A and B parameters of the quadrupole coupling-hydrogen bond relation, Eq. 3.12, were assumed to be the same as for the chlorinated G2 dendrimer $\text{R}_3\text{ND}^+\dots\text{Cl}^-$. This is reasonable since the χ_{PAS} values for $\text{RND}_3^+\dots\text{Cl}^-$ and $\text{RND}_3^+\dots\text{Br}^-$ are similar [115, 116], and the hybridization symmetry is preserved upon anion substitution. The assumed values of η_{PAS} , used for quantitative estimation of libration amplitudes, require further justification. These quantities can be measured only at very low temperatures for “static” deuterons, whose long relaxation times ($\geq 10 \text{ s}$) would imply prohibitively long experiments. On the basis of literature citations for secondary amide [54, 104] and static ammonium [108, 109, 115, 116] deuterons and our own

measurements at $-30\text{ }^{\circ}\text{C}$, reasonable maximum PAS values for the asymmetry parameters, η_{PAS} , of R_2ND and R_3ND^+ are estimated to be 0.12 and 0.05, respectively. These values depend on the electronic environment around the dendrimer spacer, which we assume to be independent of dendrimer generation. If the assumed values of η_{PAS} are too large, the calculated libration amplitudes and hydrogen bond lengths will be underestimated, but qualitative conclusions about the observed trends will not be affected.

For all dendrimer generations the narrowest powder patterns present in the spectra (Fig. 3.6) are assigned to motionally averaged deuterons of terminal $\text{RND}_3^+\dots\text{Cl}^-$ groups. Room temperature values of the RND_3^+ characteristic quadrupole parameters, together with those for the RND_2 and R_3ND^+ powder patterns, are summarized in Table 3.1. In principle, the relative total intensities of spacer secondary amide to branching tertiary amine to terminal ammonium powder patterns can be calculated from the known stoichiometry for each dendrimer generation (Chapter 1). For instance, for G2, they should be 2:1:3.429, while for G9 2:1:3.003 is expected.

Table 3.1

Best fit quadrupole coupling parameters for three powder patterns of studied PAMAM generations at room temperature

G#	RND_3^+			R_3ND^+			R_2ND		
	$\langle\chi\rangle$ $\pm 0.5,$ kHz	σ_χ $\pm 0.5,$ kHz	$\langle\eta\rangle$ ± 0.005	$\langle\chi\rangle$ $\pm 2,$ kHz	σ_χ $\pm 1,$ kHz	$\langle\eta\rangle$ ± 0.01	$\langle\chi\rangle$ $\pm 2,$ kHz	σ_χ $\pm 1,$ kHz	$\langle\eta\rangle$ ± 0.01
G1	48.5	5.0	0.110	156	10.5	0.08	200	8	0.16
G2	48.5	5.0	0.115	157	8	0.09	198	9	0.18
G3	49.0	4.0	0.100	161	11	0.12	190	10	0.18
G5	48.5	5.0	0.110	154	8	0.08	198	9	0.18
G7	49.0	5.4	0.110	156	10.5	0.09	203	11	0.13
G9	49.0	5.4	0.110	156	10.5	0.07	204	10	0.14

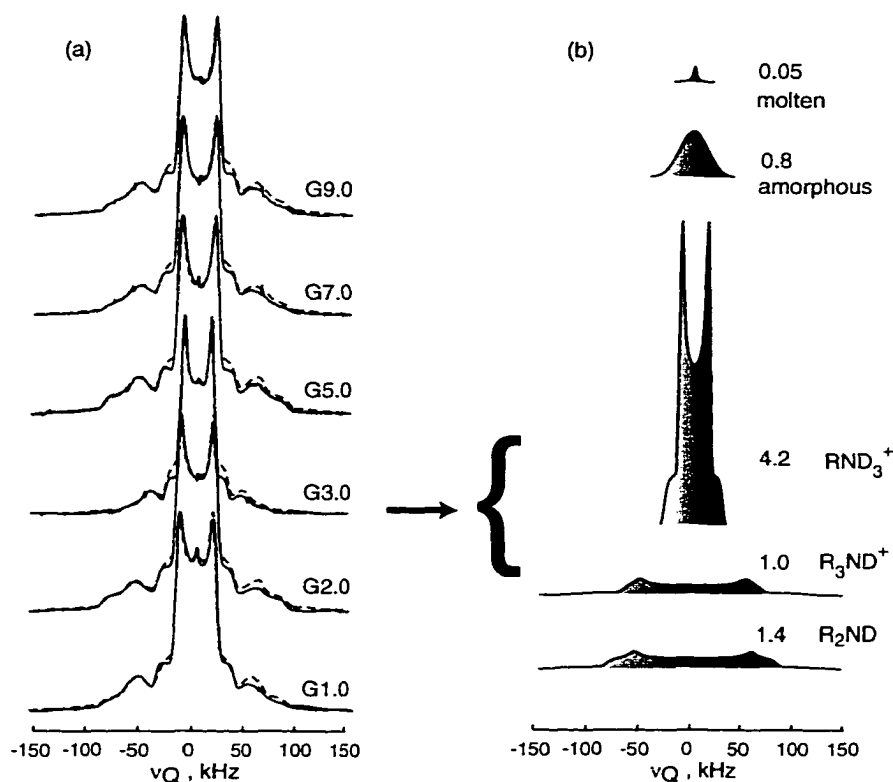


Figure 3.6

(a) room temperature experimental spectra (solid lines) and fits (dashed lines) for all generations studied; (b) deconvoluted fit for G3 with corresponding integrated intensities. The best fit quadrupole coupling parameters are listed in Table 3.1.

It is likely that rapidly tumbling residual solvent contributes some intensity to the narrow central features at high temperature (see Fig. 3.6 (deconvoluted spectrum)). Estimation of this contribution has been done from proton spin echo (SE) spectra (Fig. 3.7), obtained at room temperature on the deuterated G2 sample several months after preparation. The spectrum in Figure 3.7a shows the results of the proton SE experiment without sample spinning. The 5 kHz wide feature can be distinguished on top of a 40 kHz wide blob. The latter is associated with the non-exchangeable protons of the rigid glassy dendrimer (mostly $-\text{CH}_2-$). They relax slowly and do not reach full intensity even after 5 s recycle delay. The broadening comes from both dipolar coupling and chemical shielding anisotropy. The narrower 5 kHz feature can be associated with segments in motion which relax faster, but have partially preserved anisotropic interactions.

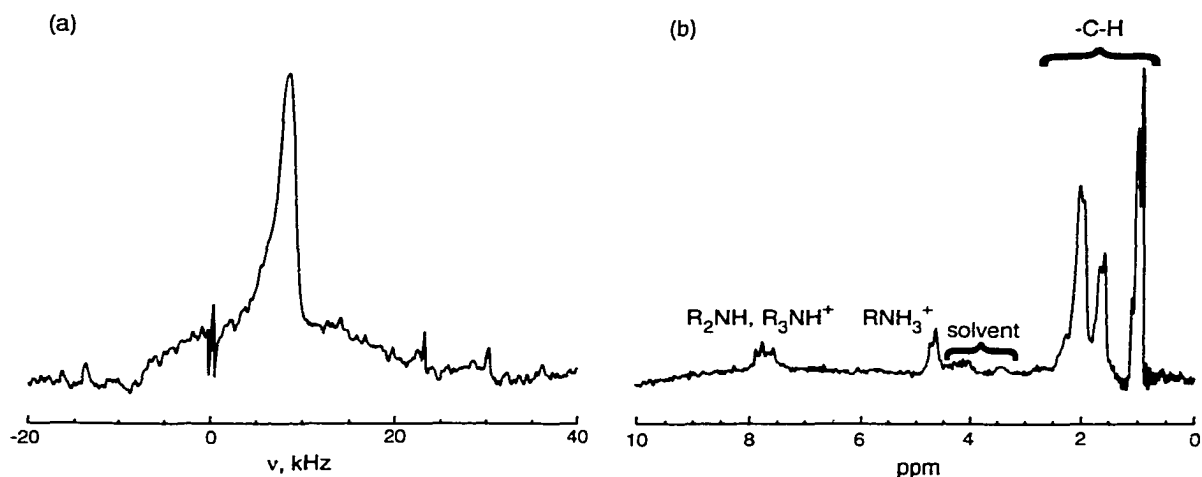


Figure 3.7

Experimental spectra for proton solid echo in G2 PAMAM chloride dendrimer: (a) no spinning, SW = 50 kHz, 1024 acquisition points, 300 Hz exponential apodization, 4.5 μ s 90 degree pulse, 2000 transients, 5 s recycle delay; (b) MAS at 5 kHz, SW = 10 kHz, 1024 acquisition points (zero filled to 4096 points for FT), 5 μ s 90 degree pulse, 52000 transients, 1 s recycle delay (spectrum (b) referenced to TMS).

Magic angle spinning of the sample at 5 kHz helps to further average these interactions and yields a resolved spectrum of the narrow component (Fig. 3.7b). The peaks close to 0 ppm arise from $-\text{CH}_2-$ protons, which will not contribute to the deuteron lineshapes. The rest of the peaks belong to protons which are exchangeable with deuterons. Assignments are based on literature chemical shift compilations [63, 78, 117]. The relative intensity of the solvent peaks, which may have counterparts in deuteron spectra, is measured to be less than 20 % of the total N-H contributions. Therefore, in the deuteron spectrum at most 20 % of the narrow spectral feature at room temperature may come from residual solvent. Since this feature contributes less than 10 % total QE intensity, the contribution of residual solvent is less than 2% of the total deuteron spectral intensity. This falls within experimental error, and cannot increase with the temperature. However, a small amount of solvent still may exert a noticeable plasticizing effect on the surrounding regions of the sample even below T_g . This

might be observed in some spectra as a motionally averaged contribution at temperatures well below the glass transition region.

3.5 Experimental Results and Simulations

To account for the observed finite width of experimental powder patterns, distributions of structural and motional parameters causing the detected distribution of spectral intensity were included in simulations. Data manipulation and simulation was performed on Indigo2 and O2 Silicon Graphics workstations using the commercially available data visualization package PV-WAVE and locally written C-programs. Exponential apodization, corresponding to 500 Hz Lorentzian broadening, was applied to the experimental time domain signals. The data were then left shifted, by spline interpolated fractions of a dwell time if necessary, so that a point occurred precisely at the top of the echo. This procedure is less prone to introduction of baseline artifacts than the alternative of linear phase correction after Fourier transformation. A frequency independent phase correction of 5-15 degrees was used to minimize the signal in the out of phase channel. The relatively small residual asymmetry in the Fourier transformed spectra probably arises from instrumental artifacts not fully eliminated by phase cycling.

Lineshapes were simulated using the SUMS algorithm [72], in which frequency domain spectra with finite asymmetry parameter are efficiently computed by summing sets of axially symmetric subspectra. Broadened lineshapes were modeled by expressing both the quadrupole coupling constant, χ , and the asymmetry parameter, η , of the electric field gradient tensor, in terms of a single, model dependent parameter κ which was assumed to have a Gaussian distribution, $G(\kappa)$. The explicit relation between κ and quadrupole coupling parameters depends on the different motional models used. Normalized lineshapes $I(\nu)$ were computed from the expressions

$$I(\nu) = p(\nu) f(\nu) \sum_i S(\chi(\kappa_i), \eta(\kappa_i), \nu) G(\kappa_i) \Delta\chi \quad [3.13]$$

$$G(\kappa_i) = N^{-1} \exp\left(-\frac{1}{2} \left[\frac{\kappa_i - \bar{\kappa}}{\sigma_\kappa} \right]^2\right) \quad [3.14]$$

$$N = \int_x G(\kappa(\chi)) d\chi \quad [3.15]$$

$$p(\nu) = \frac{\sin^3\left(\frac{\pi}{2} \sqrt{1 + 4\nu^2 \tau_{90}^2}\right)}{\sqrt{(1 + 4\nu^2 \tau_{90}^2)^3}} \quad [3.16]$$

$$f(\nu) = \left[1 + Q^2 \frac{(\nu - \nu_0)^2}{\nu_0^2} \right]^{-1} \quad [3.17]$$

where $\Delta\chi$ is increment of χ , τ_{90} is the length of the 90 degree pulse, $\nu_0 = 46.06$ MHz is the deuteron Larmor frequency, Q is the probe quality factor and $S(\chi, \eta, \nu)$ is the SUMS formula [72] for a powder pattern with specified values of χ and η . Each value of the summation index in Eq. 3.13 refers to a subspectrum defined in the SUMS algorithm. The function $p(\nu)$ corrects the simulated lineshape for effects of finite pulse width [87], and $f(\nu)$ accounts for the finite bandwidth of the probe. The functional form of $f(\nu)$ corresponds to a Lorentzian response function, with full width at half height equal to ν_0/Q . Both corrections are needed to achieve adequate fits to the experimental lineshapes at frequencies $|\nu - \nu_0| \geq 100$ kHz. For example, at 100 kHz away from the center of the powder patterns, $p(\nu) = 0.84$ for the 1.6 μs 90 degree pulses used in our experiments, and $f(\nu) = 0.83$ for $Q = 105$. The probe Q -value of 105, which was used in all the simulations of dendrimer spectra, was determined by SUMS fitting an experimental powder pattern of a deuterated polyethylene test sample.

Equation 3.13 requires that successive values of κ correspond to equal increments of the quadrupole coupling constant, $\Delta\chi$. This increment was set equal to the frequency step

between successive points in the experimental spectrum; this facilitates computing the lineshape with a sufficiently accurate weighting function to permit comparison with the experimental spectrum. The model dependent expressions for $\chi(\kappa)$ were inverted analytically or numerically to obtain explicit expressions for $\kappa(\chi)$, which were then used, with visual estimates of the average quadrupole coupling parameters, $\langle\chi\rangle$ and $\langle\eta\rangle$, to determine $\bar{\kappa}$, the centroid of a Gaussian distribution in κ . The SUMS routine was incorporated into a set of C-functions which compute distributions of weights, corresponding to the model chosen in the main program, within the limits determined by desired accuracy and physical constraints.

Normalized lineshapes for each type of deuteron were calculated using trial values of the distribution width. Weighted sums of these lineshapes were compared with experimental spectra, and the distribution width and relative weights for each type of deuteron were adjusted by trial and error to achieve the minimum mean square deviation between the weighted sum and experimental lineshapes. Unfortunately, direct computerized nonlinear least squares fit [84] would not converge for many broadened overlapping powder patterns, since there were three fit parameters ($\langle\chi\rangle$, $\langle\eta\rangle$ and σ_κ) for each of them. Nevertheless, this routine can be successfully applied in case of single broadened powder pattern. Each simulation of full experimental spectrum required about 300 powder pattern calculations, but this took only a few seconds due to the high efficiency of the SUMS algorithm.

3.5.1 Distributions and Lineshapes

The final lineshape intensity distribution should reflect the peculiarities of the skewed distribution, $G(\kappa(\chi))$, as determined by the functional relation $\chi(\kappa)$. In principle, comparison of simulated lineshapes to experimental results should provide tests of the different models accounting for the observed intensity distribution. In practice, wider distributions allow for

better distinction, because as shown in Fig. 3.8, the differences in skew are then more pronounced. The selection of a particular model based on only slightly broadened lineshapes is likely to be ambiguous.

Four models were explored. In model I, a simple Gaussian distribution of quadrupole coupling constants is assumed, i.e., $\kappa = \chi$ (solid lines in Fig.2). In this case, the first guess for the distribution width, σ_χ , can be taken as the apparent half-width of the powder pattern horn, and its centroid is simply $\langle\chi\rangle$. Though simple and straightforward, this model can only express the presence of a distribution and gives no indication of its physical origin. More realistic models II, III, and IV associate the distribution with libration on a planar arc, libration in a cone, and hydrogen bond length, respectively.

For the hydrogen bonding model (IV) the parameter κ is taken to be r , distance from the deuteron to the X-acceptor atom in a N-D...X hydrogen bond. The non-linear relation between r and χ (Eq. 3.11) implies that a Gaussian distribution in r produces the skewed distribution in χ , shown as long dashed lines in Fig. 3.8. Distribution of librational cone angles corresponds to $\kappa = \beta_{MD}$ (Eq. 3.9). The most probable angle, $\bar{\kappa} = \beta_c$, for the model of cone libration can be estimated from Eq. 3.10 for the known value of χ_{PAS} and the best fit experimental $\langle\chi\rangle$. The quadrupole coupling constants in PAS, χ_{PAS} , can be found in literature [108, 116], or measured experimentally at very low temperatures where molecular motion ceases. Its value will determine the hydrogen bond length according to Eq. 3.12. The planar libration is defined by $\kappa = \beta_{PM}$.

The mean of a Gaussian distribution of $\bar{\kappa} = \phi_0$ can be determined by choosing a plausible value for η_{PAS} , such that numerical inversion of Eq. 3.7 reproduces the experimentally observed value for $\langle\eta\rangle$. Then χ_{PAS} can be estimated from Eq. 3.6 using the observed $\langle\chi\rangle$. Finally, Eq. 3.12 may be solved to determine the average hydrogen bond length.

Effects of libration on the hydrogen bond length derived from librational models can be directly accounted for by replacing A and B in Eq. 3.12 by their “motionally reduced”

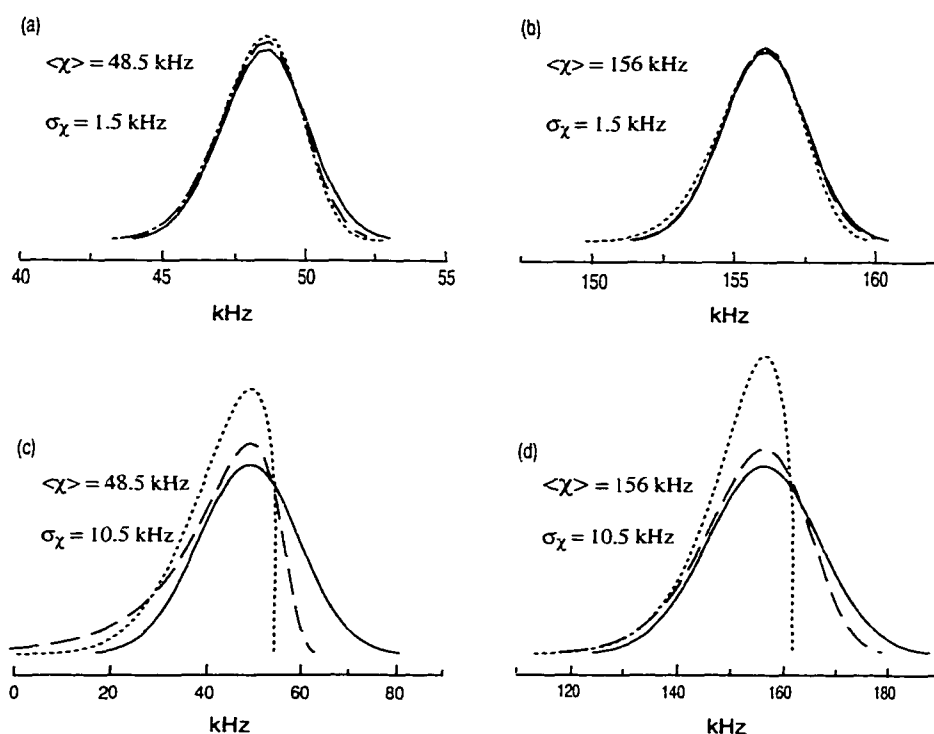


Figure 3.8

Normalized distributions of quadrupole coupling constants. $\langle\chi\rangle = 48.5\text{ kHz}$ corresponds to RND_3^+ deuterons, and $\langle\chi\rangle = 156\text{ kHz}$ - to R_3ND^+ deuterons. Gaussian distribution of χ in model I (solid lines), Gaussian distribution of arc amplitudes in model II (dotted lines (b) and (d)) Gaussian distribution of cone angles in model III (dotted lines (a) and (c)), or hydrogen bond lengths in model IV (dashed lines). Note that nonlinear relation between χ and the bond lengths or angles for models II, III and IV leads to skewed distributions, especially for wide distributions as illustrated by 2c and 2d.

equivalents AF and BF, where the factor $F = \langle\chi\rangle/\chi_{\text{PAS}}$ is determined from Eqs. 3.6 or 3.9 for libration in a plane or in a cone, respectively. Then the best fit $\langle\chi\rangle$ substitutes χ_{PAS} in Eq. 3.12. Its analytical inverse yields the hydrogen bond length. This approximate procedure ignores the distribution of libration amplitudes. It effectively reduces both the centroid and the width of the χ_{PAS} distribution ascribed to the hydrogen bond length. If no librational corrections are applied, the derived values of σ_r and \bar{r} for hydrogen bonding will be underestimated.

The errors in model dependent parameters reported in this Chapter were calculated by standard error propagation methods starting from estimated uncertainties for the observables. The absolute error for the amplitude of cone libration, $\Delta\beta_c$, was found to be less than 5° . Uncertainties in the χ_{PAS} values are equal to the corresponding experimental errors in the average quadrupole coupling constants measured from the spectra. The uncertainty in the amplitude of planar libration amplitude grows with decreasing angle, ϕ_0 . The uncertainty in the average hydrogen bond length, Δr , is determined mainly by the planar libration amplitude and is higher for larger ϕ_0 .

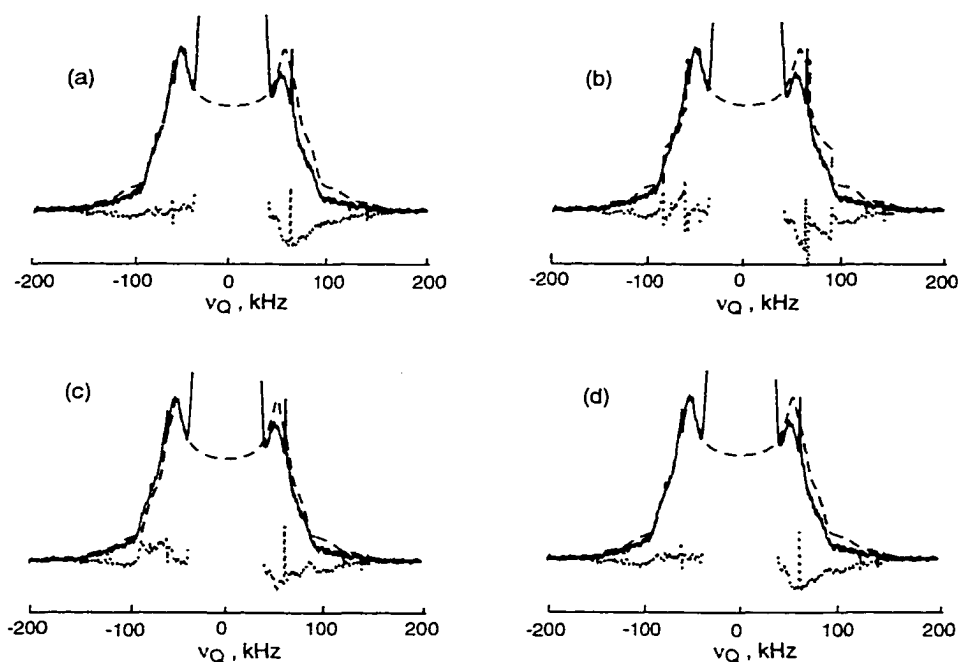


Figure 3.9

Experimental (solid lines) and simulated (dashed lines) powder patterns for G7 dendrimer at ambient temperature (24 °C). Differences between simulations and experiments are shown as dotted lines. All spectra here were simulated with two overlapping powder patterns; $\langle\chi\rangle = 203$ kHz, $\langle\eta\rangle = 0.13$ and $\langle\chi\rangle = 156$ kHz, $\langle\eta\rangle = 0.09$ respectively. In (a), a Gaussian distributions of χ (model I) were assumed, with $\sigma_\chi = 10.7$ kHz and 10.5 kHz for the R_2ND and R_3ND^+ powder patterns respectively. In (b), libration on an arc (model II) was characterized by $\sigma_\phi = 7.5^\circ$ and 7° , and in (c), libration in a cone (model III) was used with $\sigma_\beta = 10^\circ$ and 9° . In (d), a Gaussian distributions of hydrogen bond length (model IV) were used with $\sigma_r = 0.12$ and 0.09 Å.

Typical experimental spectra, calculated lineshapes, and their difference for the two widest powder patterns of the generation 7 dendrimer at room temperature are shown in Fig.3.9. The best fit quadrupole coupling parameters were found to be $\langle\chi\rangle = 203\pm 2$ kHz and $\langle\eta\rangle = 0.13\pm 0.01$ for the widest pattern, and $\langle\chi\rangle = 156\pm 2$ kHz and $\langle\eta\rangle = 0.09\pm 0.01$ for the narrower one. The best fit distribution widths for the wide and narrow patterns of different models are: $\sigma_\chi = 10.7$ kHz and 10.5 kHz (model I, Fig. 3.9a), $\sigma_\phi = 7.5^\circ$ and 7° (model II, Fig. 3.9b), $\sigma_\beta = 10^\circ$ and 9° (model III, Fig. 3.9c), and $\sigma_r = 0.12$ and 0.09 Å (model IV, Fig. 3.9d), respectively. The distributions of hydrogen bond length were calculated including the effects of planar libration as described above.

It is noteworthy that, compared with a symmetric distribution of χ -values, both librational and hydrogen bond length distributions are biased toward the lower frequencies (Fig. 3.8, short and long dashed lines), but for wide distributions the libration models require a cutoff at high frequencies. This gives the higher frequencies greater weight and produces characteristic sharp features in the lineshapes, Fig. 3.9b and 3.9c, which are not present in the experimental data. The fits using distributions of hydrogen bond lengths are marginally better than those using a symmetric distribution of quadrupole coupling constants. Therefore, the physical origin of experimental quadrupole coupling parameter distribution at the dendrimer spacer and branching points is predominantly the intradendrimer distribution of hydrogen bond lengths. The distribution widths for quadrupole coupling constants of RND_3^+ groups at ambient temperature are approximately 5 kHz, roughly half of those for the other sites for which rapid three-fold rotation is absent (see Table 3.1). For such narrow distributions, Figs. 3.8a and 3.8b show that it is hard to discriminate between libration of the three-fold axis and hydrogen bond distances as the underlying source of the distribution. Thus, preference of hydrogen bond length or cone libration amplitude distribution for terminal ammonium groups is not warranted by the precision of the data. Any or both of the two models are applicable here.

3.5.2 Temperature and Generation Dependence

The best fit generation dependent quadrupole coupling parameters at room temperature (24 °C) before and after annealing at 55 °C, and at -30 °C (for G = 2, 3, and 9) are shown in Figure 3.10. At ambient temperature, a minimum value of $\langle\chi\rangle$ for the R_2ND sites is found for generation 3 (Fig. 3.10a), and smaller asymmetry parameters are observed for higher

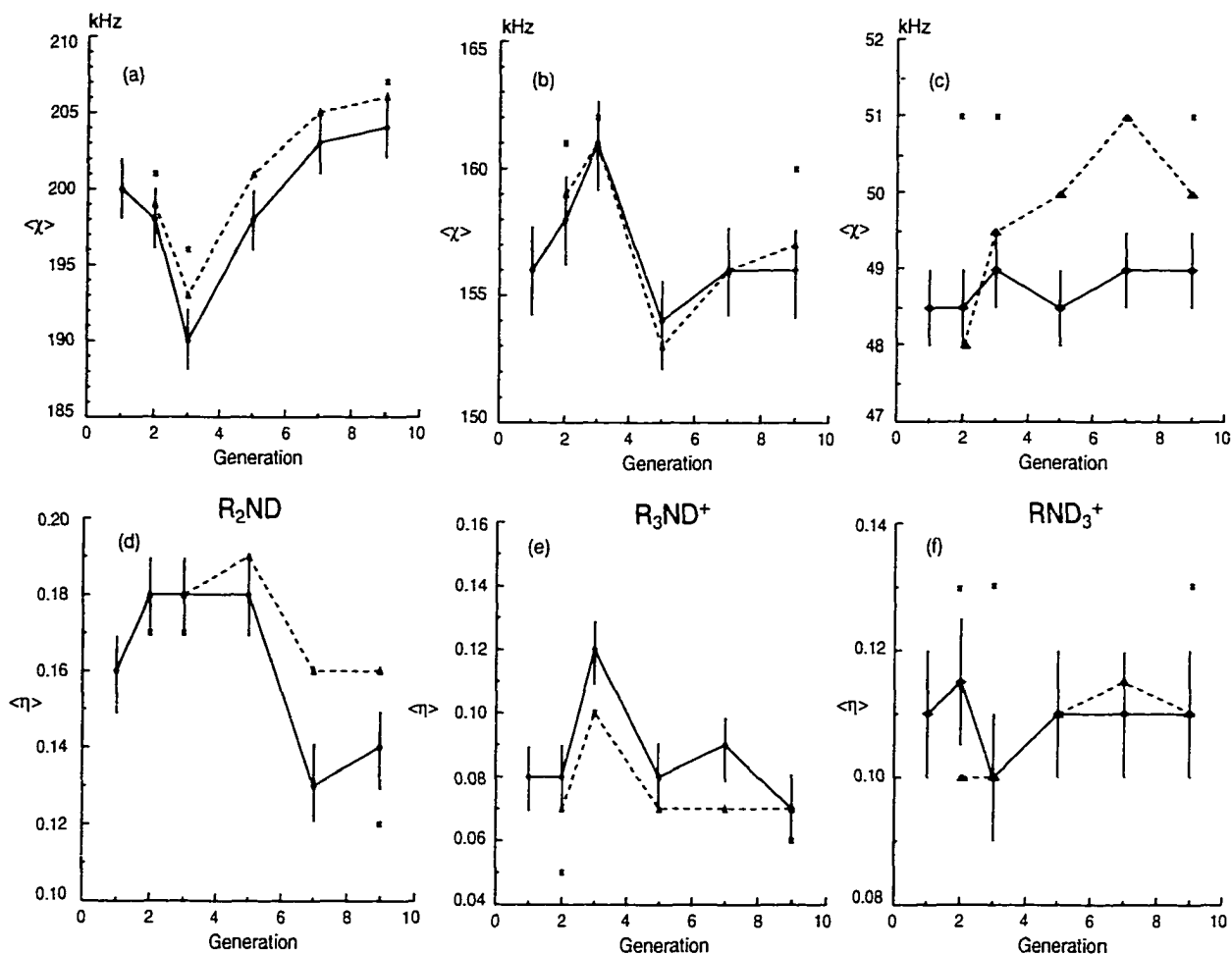


Figure 3.10

Generation dependence of quadrupole coupling parameters for three overlapping powder patterns: (a) and (d) R_2ND , (b) and (e) R_3ND^+ , and (c) and (f) RND_3^+ . Lines connecting the points are drawn to guide the eye: room temperature data for fresh samples (solid lines), data obtained at room temperature after annealing at 55 °C for two days (dashed lines); data at -30 °C (stars). Error bars for the points connected by solid lines also apply to the other points for the same material.

generations (Fig. 3.10d). At R_3ND^+ sites, generation 3 shows a maximum value of both $\langle\chi\rangle$ and $\langle\eta\rangle$ (Figs. 3.10b and 3.10e). No generation dependence is observed for the quadrupole coupling parameters of the terminal ND_3^+ groups for fresh materials studied at room temperature (the third column in Fig. 3.10 (solid lines)): $\langle\chi\rangle = 49\pm 0.05$ kHz and $\langle\eta\rangle = 0.110\pm 0.005$. Comparing to $\langle\eta\rangle$ at -30°C , Fig. 3.10 (stars), it can be seen that the sign of the changes in asymmetry with increasing temperature is opposite for interior and terminal groups. The decreasing finite $\langle\eta\rangle$ at termini reports on difference of their dynamics from dynamics in dendrimer interior, but can not be explained within the framework of symmetric cone libration and fast three-fold rotation model III. For deuterated interior sites, deviations of the asymmetry parameters from their PAS values are in agreement with model II, and must reflect the amplitudes of librational motion according to Eq. 3.7.

It is interesting that even though the librational amplitudes are about the same for amide sites of generations 2, 3 and 5, generation 3 has an average coupling constant, $\langle\chi\rangle = 190$ kHz, which is much smaller than the values for other generations. Simultaneously, at room temperature the tertiary amine sites of generation 3 show the smallest reduction of average quadrupole coupling constant but they have the largest asymmetry parameter. These observations suggest that the motion of generation 3 dendrimers is different, in some as yet unspecified way, from that of the other generations.

Over the temperature range of 75°C , $\langle\chi\rangle$ values for all sites of generations 2, 3 and 9 (Fig. 3.11, Table 3.2) decrease uniformly with increasing temperature. This is accompanied by a noticeable decrease in $\langle\eta\rangle$ for RND_3^+ deuterons and an increase in $\langle\eta\rangle$ for the other sites. For R_2ND and R_3ND^+ deuterons, the model of asymmetric planar libration is fully consistent with the temperature dependent data, and with our observation of relatively short relaxation times [54], $T_{1Z} < 1$ s, for these deuterons.

The nonzero asymmetry parameters exhibited by RND_3^+ are inconsistent with a simple symmetric rotor picture, and demonstrate the necessity for modification of model III. Under conditions of fast motion, when rates are much higher than the static quadrupole splitting, nonzero asymmetry parameters can arise if populations for the cone “sites”, used to define the ND_3^+ axis, are not equal, i.e., if the probability of orientation within the cone is nonuniform. Another source of residual asymmetry is unequal populations or different χ_{PAS} values of the sites defining three-fold jumps of the ND_3^+ group. For 2-site (planar) libration of the RND_3^+ rotation axis, the observed asymmetry parameter should increase [116] with increasing temperature. Our observation of the opposite tendency rules out this explanation.

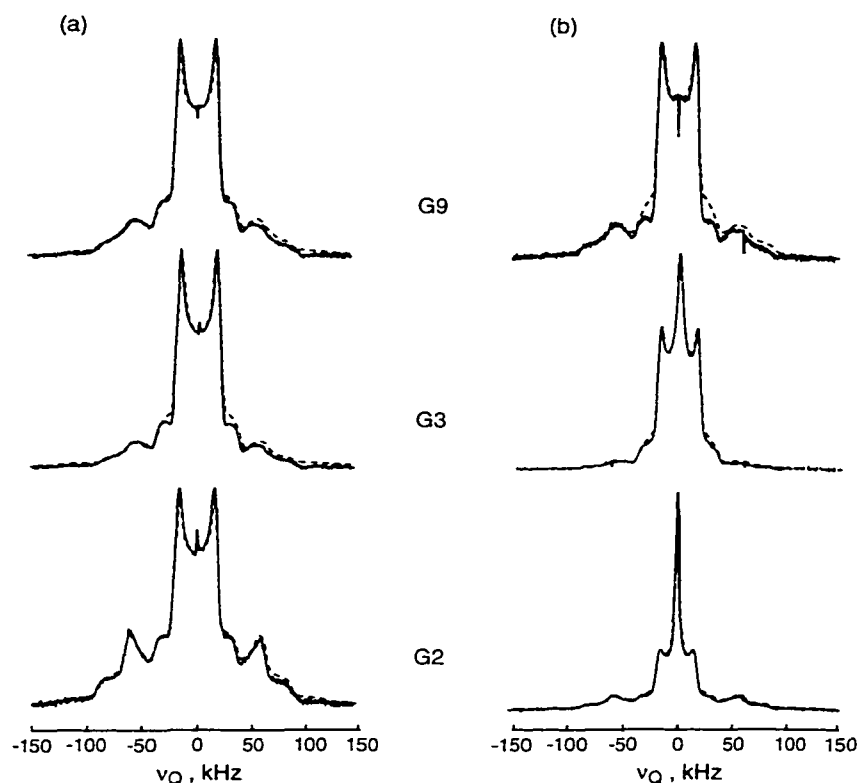


Figure 3.11

Experimental spectra (solid lines) and simulations (dashed lines) for three PAMAM generations at -30°C (a) and 45°C (b). The best fit parameters are listed in Table 3.2.

Table 3.2

Best fit quadrupole coupling parameters for G2, 3, and 9 experimental QE spectra at $-30\text{ }^{\circ}\text{C}$ and $+45\text{ }^{\circ}\text{C}$ (see Fig. 3.11)

G & T	RND_3^+			R_3ND^+			R_2ND		
	$\langle\chi\rangle$ $\pm 0.5,$ kHz	$\langle\eta\rangle$ ± 0.01	σ_χ $\pm 0.5,$ kHz	$\langle\chi\rangle$ $\pm 2,$ kHz	$\langle\eta\rangle$ ± 0.01	σ_χ $\pm 1,$ kHz	$\langle\chi\rangle$ $\pm 2,$ kHz	$\langle\eta\rangle$ ± 0.01	σ_χ $\pm 1,$ kHz
G2									
-30°C	51	0.13	4.6	161	0.05	8.3	201	0.17	6.3
+45°C	46.5	0.10	5.0	158	0.07	7.4	197	0.18	7.8
G3									
-30°C	51	0.13	4.7	162	0.10	10.5	196	0.17	7.5
+45°C	49	0.095	4.0	159	0.13	11.5	194	0.20	9.7
G9									
-30°C	51	0.13	4.6	160	0.06	12.7	207	0.12	8.6
+45°C	48	0.08	5.4	156	0.07	10.5	204	0.17	8.7

Instead, the asymmetry seems to be the result of unequal rotation and libration site populations, which implies nonuniform probabilities and nonideal geometries for motional averaging (Eqs. 3.3 and 3.9). Such skewed geometries may arise from one of the ammonium ND bonds orienting towards the chloride anion. The other two ammonium deuterons could be partially hydrogen bonded to carboxylic oxygens. This would cause unequal χ_{PAS} and η_{PAS} values simultaneously with unequal site populations. Then, the observed decrease in $\langle\eta\rangle$ with increasing temperature could be explained simply as an increase in the symmetry of rotation and cone libration.

To avoid introducing too many independent parameters, the RND_3^+ spectra were simulated using a single, phenomenologically determined value for the motionally averaged asymmetry parameter $\langle\eta\rangle$. Distributions of $\langle\chi\rangle$ were included in the simulation as specified by model III, a Gaussian distribution of cone angles (cf. Eqs. 3.9 and 3.10). The angle between PAS and molecule fixed Z axes was assumed to be $\beta_{\text{MP}} = 70.5^\circ$ [116], and for each generation χ_{PAS} was fixed at the value derived by applying the planar libration model II (cf. Eqs. 3.6-3.8) to interior R_3ND^+ sites. We believe that χ_{PAS} values determined for rigid interior $\text{R}_3\text{ND}^+ \dots \text{Cl}^-$ sites provide a reasonable approximation for RND_3^+ deuterons due to

similar symmetry and hybridization states for both groups [108, 116]. Within experimental error, these values turned out to be temperature independent for each generation, which is expected if the model is right. Quite a large difference was found between generation 3, for which $\chi_{\text{PAS}} = 171 \pm 3$ kHz, and all other generations, for which $\chi_{\text{PAS}} = 162 \pm 3$ kHz. This reflects intrinsic structural peculiarities of generation 3, and will be further discussed in terms of calculated average librational amplitudes and hydrogen bond distances.

Adequate fits of all lineshapes in the middle of the spectra required addition of Gaussian and Lorentzian lines of different width. An increase in intensity of these components, at the expense of the three powder patterns, was observed with increasing temperature (see for $T = -30$ and $+45$ °C in Fig. 3.11 and Tables 3.3, 3.4). The stoichiometric and measured relative intensities of the three overlapping powder patterns, as well as the parameters for Gaussian and Lorentzian components are listed in Tables 3.3 and 3.4. In most cases, simulations for generations greater than 2 yielded total intensities for interior deuteron sites that were smaller than would be expected from stoichiometry (Table 3.3, first column). In the powder patterns deviations of the integrated relative intensities from calculated values (based on the known stoichiometry) arise, in part, from incomplete deuteration at the branching sites. This would be expected if the deuteration of interior sites proceeds by layers [60] (see description of sample preparation in Chapter 1). If the rate and amplitude of spacer R_2ND librational motion of the branches attached to undeuterated R_3N sites is significantly smaller than that on branches involving R_3ND^+ sites, secondary amide deuterons on the former could go undetected because of very long relaxation times [54] (> 100 s). Experimental quadrupole echo spectra obtained with 5 s recycle delays were superimposable on those with 20 s recycle delay, but the presence of a small fraction of deuterons with much longer relaxation times cannot be excluded.

For all generations, the integrated intensities of both Gaussian and Lorentzian components increase with increasing temperature. As described above, the appearance of narrow peaks in the middle of the spectrum is associated with the onset of the glass

transition. DSC measurements show that for G2 the transition starts near room temperature (Fig. 3.2). The presence of Gaussian component at low temperatures can be related to residual solvent plasticization effect (Fig. 3.7). At higher temperatures the Gaussian feature is probably associated with partially rigid regions undergoing large amplitude intramolecular motion. The formation of these regions may be a prerequisite of a wide temperature range for rigid glass to molten glass transition in PAMAM dendrimer salts. The fact that this component grows more for G3 than for low (G2) and high (G9) generations with increasing temperature indicates higher flexibility of G3 structure. This would be consistent with a picture of little interpenetration and backfolding for generation 3 molecules. The Lorentzian component appears at higher temperatures in respect to Gaussian. It must be associated with molten dendrimer regions above T_g . Its fraction at lower temperatures is lower for higher generations. This is consistent with higher T_g for high generation materials. A similar increase of T_g with generation number has been observed for amine-terminated PAMAM dendrimers [3, 23, 24, 27].

Table 3.3

Fit relative intensities and stoichiometric expectations for PAMAM powder patterns

Generation	Temperature	I(RND ₃ ⁺):I(R ₃ ND ⁺ + R ₂ ND) Stoichiometry vs. Fit		I(R ₂ ND):I(R ₃ ND ⁺) Stoichiometry vs. Fit	
G1	RT	1.333	1.2±0.3	2	1.0±0.3
	-30°C	1.143	0.6±0.3	2	1.7±0.5
	RT	1.143	1.2±0.3	2	3.4±0.5
G2	+45°C	1.143	0.8±0.3	2	1.5±0.4
	-30°C	1.067	2.1±0.8	2	1.2±0.4
	RT	1.067	1.7±0.7	2	1.4±0.4
G3	+45°C	1.067	2.9±1.2	2	1.4±0.4
G5	RT	1.016	1.0±0.3	2	2.8±0.5
G7	RT	1.004	1.3±0.6	2	1.2±0.3
	-30°C	1.001	1.1±0.3	2	1.0±0.3
	RT	1.001	1.2±0.3	2	1.4±0.4
G9	+45°C	1.001	1.1±0.3	2	2.0±0.4

Table 3.4

Fit line width and % total spectral intensity for Gaussian and Lorentzian components

Generation	Temperature	Gaussian		Lorentzian	
		$\nu_{1/2} \pm 1$, kHz	I, %	$\nu_{1/2} \pm 0.5$, kHz	I, %
G1	RT	12	9 \pm 5	2	1 \pm 0.5
	-30°C	14	6 \pm 3	-	0.0
G2	RT	14	7 \pm 3	2	0.2 \pm 0.2
	+45°C	12	8 \pm 4	2	21 \pm 5
G3	-30°C	14	2 \pm 1	-	0.0
	RT	14	10 \pm 5	2	0.6 \pm 0.3
G5	+45°C	14	21 \pm 5	3	13 \pm 5
G7	RT	14	3 \pm 2	2	0.3 \pm 0.2
G9	-30°C	14	5 \pm 3	2	0.4 \pm 0.2
	RT	14	8 \pm 4	-	0.0
G9	RT	14	4 \pm 2	2	0.3 \pm 0.2
	+45°C	14	10 \pm 5	2	0.4 \pm 0.2

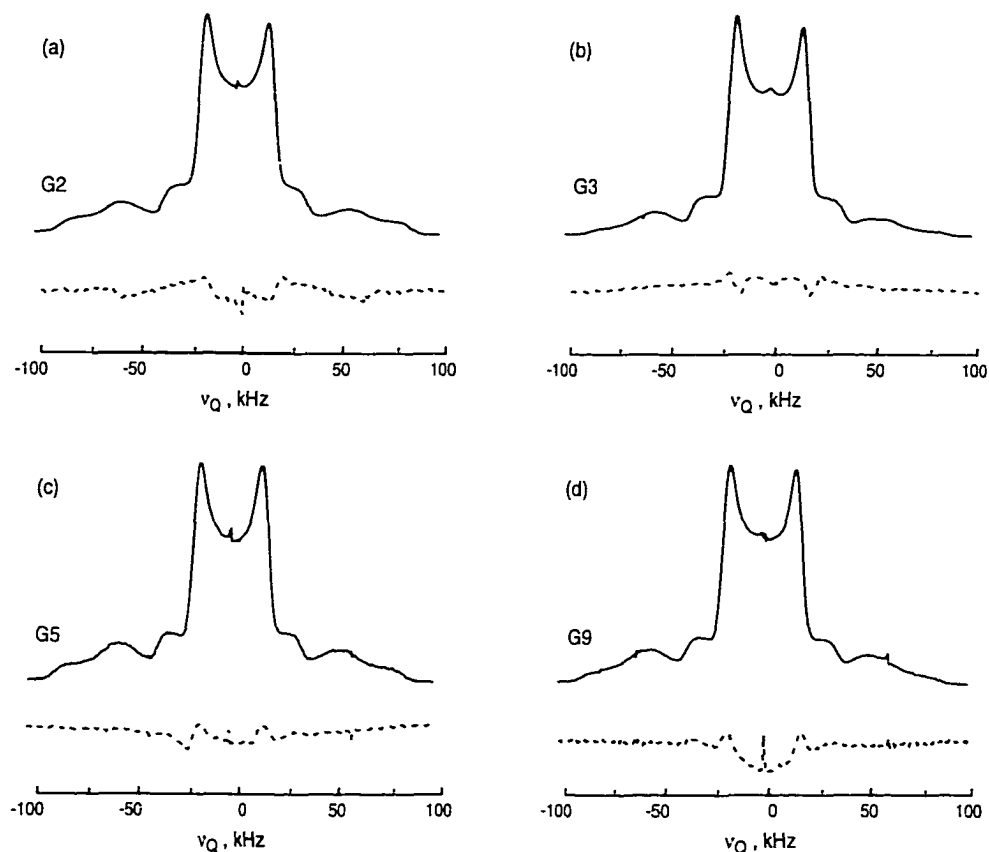


Figure 3.12

Powder pattern behavior after annealing at 55 °C for two days for generations G2 (a), G3 (b), G5 (c) and G9 (d). Solid lines are powder patterns for fresh samples. Dashed lines are difference spectra, “fresh” minus “annealed”.

A slight temperature and time hysteresis was observed for the fractions of mobile component, which is not unusual for amorphous polymers. As can be seen from Figs. 3.10 and 3.12, for annealed samples the changes in lineshapes involved not only the middle of the spectra, but also the overlapping powder patterns. The fraction of rigid material decreased after the samples annealed at 55 °C were cooled back to room temperature. Similar decreases progressed slowly in samples stored at ambient temperature over the period of a year. However, the magnitude of the observed changes are close to experimental error, and further speculation is not warranted.

3.5.3 Structural Parameters

The structural and motional parameters derived from the best fits to experimental spectra are listed in Table 3.5. Although the quantitative characterization of hydrogen bond length (on the basis of Eq. 3.12) should be treated with caution, the numbers are reasonable and some qualitative conclusions can be drawn. From simple geometric considerations (bond lengths [54] and angles [118]), the minimum hydrogen bond length between secondary amide deuteron and carboxylic oxygen of the same spacer in "cis" configuration is estimated to be 2.45 Å. However, even this minimum value is significantly larger than all the values for interior deuterons (Table 3.5). Since "trans" amide configuration is usual, the calculated "minimum" distance for the same branch is expected to be even longer. Therefore, the experimental spectra reveal information about hydrogen bonding between neighboring spacers of the same or different dendrimer molecules.

Although X-ray data for PAMAM model compounds is lacking, this interpretation is consistent with X-ray determination of hydrogen bond distances in other model dendrimers with amide terminal groups, for which N...O distances 2.84 ± 0.08 Å were found for intramolecular hydrogen bonds and 2.94 ± 0.05 Å for intermolecular hydrogen bonds [119]. The fact that \bar{r} turns out to be essentially temperature independent for all generations

provides further strong support for the validity of models II and IV. For high and low generations, the hydrogen bond length at the branching R_3ND^+ sites, $\bar{r} = 2.1 \text{ \AA}$, is only slightly smaller than at the spacer RND_2 sites, $\bar{r} = 2.2 \text{ \AA}$. The smallest difference is found for generation 3. This suggests a uniform distribution of local structures throughout the dendrimer, which is further confirmed by comparatively narrow distribution widths, $\sigma_r < 0.2 \text{ \AA}$. Recalling the effect of anion substitution, it is possible that equilibrium distance between RND_3^+ groups and associated anions imposes a steric constraint on the ability of secondary amide groups to participate in hydrogen bonding, and thus determines the structural order for the whole dendrimer molecule. This implies that the dendrimer structure can be expected to change somewhat so as to accommodate various included materials [37, 43, 44].

Librational amplitudes are equal, within experimental error, at both interior sites and are slightly larger for dendrimer termini. Therefore, in accord with the physically reasonable picture, dendrimer mobility increases from the center outwards. For generations 5 and greater the librational amplitudes at interior and termini are slightly smaller, indicating more rigid or crowded structures. With the temperature increasing from -30 to $+45 \text{ }^\circ\text{C}$, the motional amplitudes increase at all deuterated sites (Table 3.5). For generation 2, the amplitude of planar libration increases more at R_3ND^+ sites (from 1° to 11°), while for high generation 9 greater increase is found for the R_2ND sites (from 1° to 13°). For generation 3 the temperature dependencies of the librational amplitudes, as well as their values are almost uniform throughout the dendrimer, the same being true for the hydrogen bond lengths. It is noteworthy that absolute values of the librational amplitude depend on assumed value of η_{PAS} . Nevertheless, the observed temperature changes and trends are independent of assumptions.

Table 3.5

Best fit parameters for three deuterated sites of PAMAM dendrimer

G \ par	RND ₃ ⁺		R ₃ ND ⁺			R ₂ ND		
	$\beta_r, ^\circ$	σ_β $\pm 2^\circ$	$\phi_n, ^\circ$	$\sigma_{\pm 0.01},$ \AA	$\bar{r}, \text{\AA}$	$\phi_n, ^\circ$	$\sigma_{\pm 0.02},$ \AA	$\bar{r}, \text{\AA}$
G1 RT	21±5	9	14±3	0.09	2.1±0.1	16±2	0.11	2.21±0.07
G2 RT	21±5	9	16±2	0.07	2.1±0.1	19±2	0.12	2.2±0.1
recent	22±5	9	11±4	0.06	2.12±0.06	19±2	0.11	2.25±0.1
-30°C	16±5	8.5	1±1	0.07	2.11±0.03	17±2	0.09	2.25±0.1
+45°C	25±5	10	11±4	0.06	2.11±0.06	19±2	0.11	2.2±0.1
G3 RT	25±3	6	21±2	0.12	2.2±0.1	19±2	0.11	2.1±0.1
recent	24±3	6.3	18±2	0.08	2.2±0.1	19±2	0.12	2.16±0.1
-30°C	22±3	8.6	19±2	0.11	2.2±0.1	17±2	0.10	2.2±0.1
+45°C	25±3	6.3	23±2	0.12	2.2±0.1	23±2	0.13	2.22±0.12
G5 RT	21±4	10	14±3	0.07	2.08±0.08	19±2	0.12	2.23±0.11
recent	18±4	11	11±4	0.06	2.06±0.06	20±2	0.13	2.31±0.11
G7 RT	20±4	10	16±2	0.09	2.1±0.1	8±4	0.13	2.18±0.04
recent	16±4	11.5	11±4	0.09	2.09±0.06	15±3	0.17	2.3±0.1
G9 RT	20±4	10	11±4	0.09	2.09±0.06	11±4	0.13	2.21±0.05
recent	18±4	11.5	11±4	0.09	2.10±0.06	15±3	0.17	2.3±0.1
-30°C	16±4	8.5	8±4	0.11	2.11±0.04	1±1	0.12	2.21±0.03
+45°C	22±4	10	11±4	0.09	2.09±0.06	17±2	0.13	2.3±0.1

Amide hydrogen bond libration is a measure of the restricted mobility of the dendrimer arms, while libration of the amine hydrogen bonds reports primarily on the motion of the counterion. Thus, the open structure of generation 2 allows thermal energy to be dissipated by increasing Cl⁻ mobility, while interpenetration between neighboring molecules hinders the motional freedom of the dendrimer arms. In contrast, the compact, folded structure of generation 9 spatially restricts Cl⁻ mobility and thermal energy preferentially increases the mobility of the dendrimer network. For generation 3, mobility and hydrogen bonding is uniform at all sites, indicating that this material most probably is neither folded nor extensively interpenetrated. Consequently, nominally identical hydrogen bond lengths

between the dendrimer spacers observed for generations 1, 2, 5, 7, and 9 can be explained by interpenetration of neighboring molecules for low generations ($G < 3$), and by intramolecular backfolding for high generations ($G \geq 5$). The onset of a transition, to a more symmetric, folded state at generation 3, hinders intermolecular penetration, but does not involve extensive backfolding either.

The extent of time and temperature hysteresis is clearer from the analysis of structural parameters, marked “recent” room temperature data, listed in Table 3.5. For high generations ($G > 3$) a slight increase in average hydrogen bond length and distribution width, together with smaller librational amplitudes of the termini, were observed after annealing. It is possible that there was sufficient thermal energy for some dendrimer arms to back-fold in the interior during the heat treatment, thus slightly widening and crowding voids in the interior. This would create less uniform structures and more hindrance to librational motion.

The slight increase in distribution width with increasing temperature observed for most deuterated sites of generation 2, 3 and 9 dendrimers (Tables 3.2 and 3.5) may indicate that some part of lineshape broadening is connected to the distribution of motional parameters (e.g. the rates of molecular motion). However, the effect falls within experimental error for QE lineshape method, and cannot be characterized even qualitatively from available experimental data. Other deuteron solid state NMR experiments [50-52, 56], sensitive to the dendrimer kinetics should provide a way for quantitative characterization of such distributions, if present. It should be noted, however, that their contribution to the observed line width is minor, compared to the distribution of hydrogen bond length.

3.6 Conclusions

Temperature dependent deuteron quadrupole echo lineshapes of integer generations, $G = 1, 2, 3, 5, 7, 9$ of PAMAM chloride salts are characteristic of rigid amorphous materials undergoing broad glass transitions between 25 °C and 65 °C. Adequate fits QE lineshapes were obtained by assuming Gaussian distributions of hydrogen bond lengths for interior $R_2ND...O$ and $R_3ND^+...Cl^-$ deuterons, and Gaussian distributions of librational cone angles for motion of the C_{3v} axis of terminal RND_3^+ groups. The estimated average hydrogen bond lengths at both types of interior sites are 2.2 ± 0.15 Å, independent of generation number. For G2 the spectra obtained upon anion substitution of Cl^- by Br^- demonstrate that both types of hydrogen bonding are counterion dependent. The hydrogen bond length at both interior sites decreased with increasing anion radius. In the temperature range from -30 to +60 °C the decreases in quadrupole coupling constants and increases in observed asymmetry parameters at the interior sites are ascribed to effects of planar libration. In the dendrimer interior the average libration amplitude increases with temperature and decreases with increasing generation. Analytical expressions for description of motion dependent changes in experimentally observed quadrupole coupling parameters in case of planar libration with finite asymmetry of PAS EFG tensor are derived. These were successfully applied for calculations of libration amplitudes in PAMAM interior by fitting to experimental data. From the temperature dependence for libration amplitudes it was concluded that thermal energy is dissipated in counterion mobility for low generations and in mobility of the dendrimer spacers for high generations. In addition to three-fold rotation, asymmetric cone libration is required to explain the observed temperature dependent asymmetry parameters of terminal ND_3^+ groups.

Our results suggest that the lower generation PAMAM dendrimer salts appear to form a loose, trembling web of interpenetrating neighboring molecules. This is consistent with REDOR results for benzyl ether dendrimers [57]. Some backfolding for low generations

cannot be ruled out by our data, but the structure is certainly open enough to allow significant counterion motion. For higher generations, back-folding should be more extensive, leading to lower libration amplitudes. The dendrimer structures are stabilized by hydrogen bonding between protonated tertiary amines and chloride anions at the branching points and, to some extent, between amide and carboxylic oxygen atoms of neighboring branches. The average hydrogen bond distance was approximately the same for both types of bonding and its distribution is narrow, indicating highly uniform environments. The fraction of molten amorphous material is small at low temperatures (8 ± 5 %), but with increasing temperature grows more for low generation materials, perhaps due to their lower T_g . The breaking of stabilizing hydrogen bonds results in increasing amplitudes of motion inside the polymer network, up to the point where material starts to flow. Around generation 3, steric crowding at the dendrimer surface hinders deep interpenetration between neighboring molecules. The structural change to a folded architecture may occur over several generations ($G = 3-5$) [37] and is probably a generic property of dendritic polymers. The derived hydrogen bond distributions are narrow for all dendrimer generations, $\sigma_r < 0.2$. No appreciable distributions of librational amplitudes are present for the PAMAM interior. The wide temperature range of the glass transition must therefore be connected not to the wide range of motional and structural parameters, but to the hyperbranched nature of the dendrimer.

Spectra of low and high generation materials exhibit the same characteristic features, which allows equally detailed characterization of all generations. This task has been problematic for other experimental methods [38, 39]. Similar quadrupole coupling and motional parameters are found for low and high generation dendrimers, which implies that intermolecular penetration and intramolecular backfolding both reduce dendrimer mobility. Quantitative estimation of the amplitudes of libration and hydrogen bond lengths was achieved, with a degree of accuracy reasonable for complex polymeric systems.

Chapter 4

Relaxation and Kinetics at Interior and Termini of PAMAM dendrimer

This chapter quantifies the rates, distributions and activation energies of internal dendrimer motions (libration and rotation) on the basis of anisotropic, temperature dependent T_{1Z} and T_{1Q} relaxation data and ^2H MAS experiments. The analysis is complicated by the presence of overlapping powder patterns originating from unselective deuteron labeling. However, such labeling is easy to implement and has the benefit that a single experiment provides information on chemically and spatially different sites simultaneously. The approach developed here for analysis of relaxation data may be useful for other unselectively labeled materials with relatively narrow distributions of structural and dynamical parameters.

Results reported in this chapter provide a definition of three dendrimer subclasses: low, intermediate, and high generation, on the basis of local segmental dynamics in these solid, glassy polymers. Low generation (G2) PAMAM dendrimer salts have similar segmental dynamics to high generation (G9) materials, but are more extensively plasticized by

protonation at the branching sites. Surface crowding without extensive backfolding is characteristic of intermediate (G3) dendrimer salts, and in the solid this facilitates the formation of an extensive intermolecular network of hydrogen bonded termini. This unique behavior of solid, intermediate generation dendrimers has a counterpart in solution, where a well known transition occurs from unfolded, open structures at low generation to globular, backfolded morphology for high generation dendrimers. For solid, high generation ($G \geq 5$) dendrimer salts, the arms are deeply backfolded and span the dendrimer interior to the same extent as the interpenetrated arms of low generations. In contrast to theoretical predictions of the dense shell formation [103], but in agreement with kinetic growth models [40], the generation dependence of segmental chain dynamics revealed by deuterium NMR does not support the existence of a dense surface shell for high generation materials. In general, hydrogen bonding in PAMAM dendrimers strongly affects activation energies for spacer and branch site libration.

The chapter is organized as follows. First, the application limits for the motional models and structural and motional parameters, derived from the static QE lineshape simulations, to the dynamics studies are set. This knowledge helps considerably speed up the relaxation data analysis by predicting relaxation anisotropies for the corrected motional models. Next, the notion of log-normal rate distribution is introduced. It partially accounts for the nonexponential behavior of experimental recovery curves as well as spinning side band broadening in deuterium magic angle spinning experiments. The procedure for unraveling overlapping anisotropies is discussed in great detail in the following section and complemented by Appendix B. Then, generation dependent kinetics revealed by the relaxation data analysis is described. The next section is devoted to the experimental MAS study of the termini libration for G2 dendrimer, which is followed by discussion of temperature evolution of librational rate distributions at interior and surface of PAMAM dendrimers during broad glass transition. The concluding section summarizes the acquired

information and compares it with theoretical predictions about dendrimer morphology and suggested engineering applications.

The simulation of experimental data presented in this chapter were performed using EXPRESS [55, 67] and MAS [56] simulation packages with the aid of PV-WAVE data visualization subroutines. Much of the material described in this chapter was published in *Macromolecules*, **33(20)** (2000) [5], and second manuscript was submitted to *Macromolecules*, in March 2001 [6].

4.1 Model Dependent Relaxation Anisotropies

The time scale of molecular motion in polymeric systems can be determined from the study of spin relaxation. Polymer kinetics is often quantified by fitting experimental data to the numerically solved stochastic Liouville-von Neumann equation for the relevant motional model. In this equation the motion is described by random jumps between discrete spin orientations, "sites". These techniques allows study of polymer kinetics dependent on motional amplitudes and rates, as well as on characteristic quadrupole coupling parameters and site populations. Unfortunately, it has two drawbacks: too many independent fit parameters and long calculation times (proportional to the square of the number of sampled orientations). The rates, site populations, Euler angles describing site orientations, and principal axis values of quadrupole coupling parameters, χ_{PAS} (Eq. 2.83), and η_{PAS} (Eq. 2.84), for each spectral feature can be varied in the simulations. Therefore, when possible, it is essential to acquire prior knowledge about motional models and constraints on fit parameters from other experiments before the analysis of relaxation data. In case of PAMAM dendrimers, this was achieved by the analysis of static temperature and generation dependent QE lineshapes, which have been extensively described in the preceding chapter.

4.1.1 SUMS vs. EXPRESS Lineshape Simulations

It is useful to start by comparing lineshape simulations according to fast SUMS [72] and slower EXPRESS [55, 67] algorithm. The major differences should result from violation of assumptions about the fast motion scale and continuity of motional trajectories (see sections 2.3.2 and 3.2) adopted in SUMS. In contrast, EXPRESS considers only discrete orientations, and includes finite motional rates which may influence the resulting lineshapes depending on the regime of molecular motion.

For ammonium deuterons the previously described (Chapter 3) two-frame motional model of fast three-fold rotational jumps in combination with continuous libration of the rotation axis in a cone, has to be modified to allow discrete four-site jumps, slower rates of cone libration and higher populations at one of the three-fold sites as well as at one of the peripheral four-fold sites to account for the observed finite asymmetry parameter. This modification helps to introduce nonuniform orientation probability, $P(\Omega)$, and reproduce the experimentally observed decreases in motionally averaged $\langle\eta\rangle$ of the RND_3^+ deuterons with increasing temperature. The lineshapes simulated with larger numbers of librational cone sites (≥ 7) were not considerably different from those with four sites in a cone. Therefore, the latter were found adequate for the description of termini libration.

Population differences can be introduced in EXPRESS lineshape calculations and MAS side band simulations of the dendrimer kinetics. At any given temperature, it is also possible to fit the lineshape by maintaining equal populations, and allowing site-to-site differences in principal axes values of the quadrupole coupling parameters χ_{PAS} (by ~ 40 kHz) and in η_{PAS} (by ~ 0.04). Figure 4.1 illustrates this point for G3 at 45 °C. However, fitting the observed temperature dependence of $\langle\chi\rangle$ and $\langle\eta\rangle$ in this fashion requires the unphysical assumption of temperature dependent PAS quadrupole parameter values. Equally good and physically more reasonable fits are obtained by assuming site and temperature independent PAS

values, and allowing the relative populations of the sites to become more nearly equal with increasing temperature.

The quadrupole coupling parameters for all RND_3^+ sites were set to $\chi_{\text{PAS}}=165$ kHz and $\eta_{\text{PAS}}=0.06$, in accord with literature citations [115, 116, 120]. The simulated spectra were convoluted with a Gaussian of 3 kHz half width, which produced broadened lineshapes

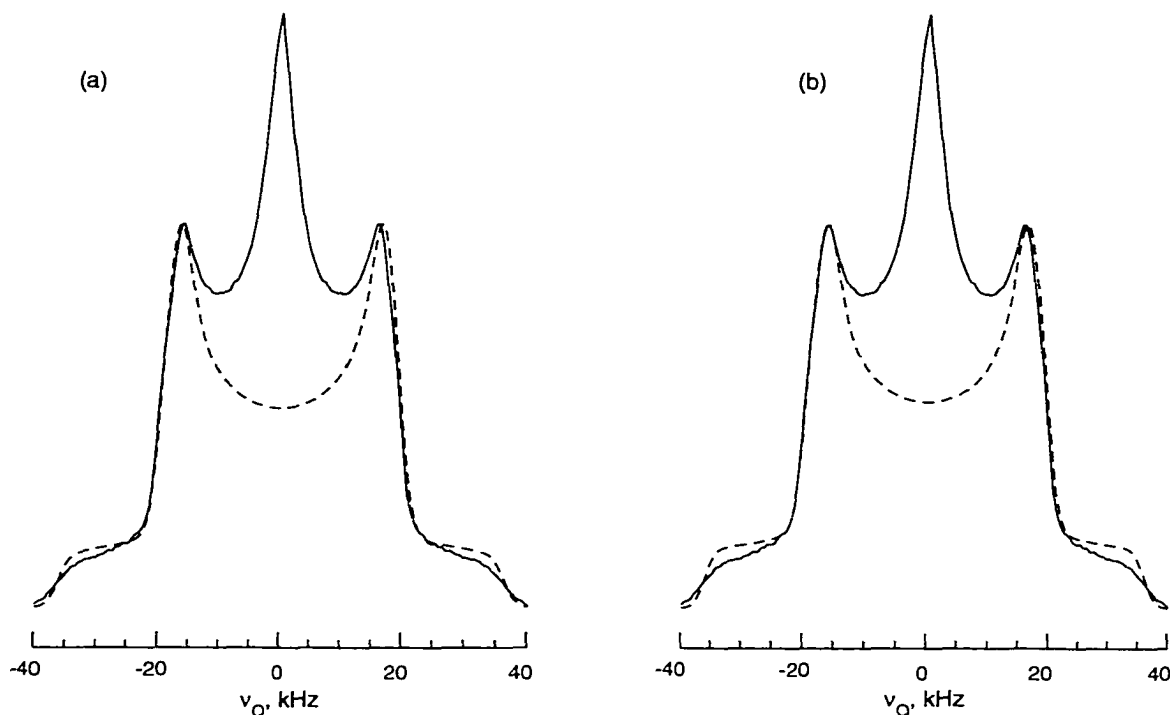


Figure. 4.1

Central part of experimental spectrum (solid) for PAMAM G3 at 45 °C compared with a two-frame motion simulation (dashed) for RND_3^+ component only. (a) model using jumps between 3 rotational and 4 librational sites of unequal site populations, p , with invariant quadrupole coupling parameters: $\chi_{\text{PAS}} = 165$ kHz, $\eta_{\text{PAS}} = 0.06$, $k_c = 10^6$ s⁻¹, $k_3 = (3.0 \pm 0.3) \times 10^{10}$ s⁻¹, $\beta_c = 23^\circ \pm 3^\circ$ (cone angle), $p_3 = (0.327, 0.327, 0.346)$, $p_c = (0.03, 0.03, 0.03, 0.91)$. (b) model of unequal quadrupole parameters with equal site populations: $\chi_{\text{PAS}} = (150, 150, 190)$, $\eta_{\text{PAS}} = (0.04, 0.04, 0.08)$ (each set repeated four times for the cone sites), $k_c = 10^6$ s⁻¹, $k_3 = (2.4 \pm 0.3) \times 10^{10}$ s⁻¹, $\beta_c = 10^\circ \pm 3^\circ$. Gaussian apodization of 3 kHz and exponential apodization of 0.5 kHz were applied to all simulated spectra. The Euler coordinates, $\Omega(\alpha, \beta, \gamma)$, for the three rotation sites were: $\Omega_1(0^\circ, 70.5^\circ, 0^\circ)$, $\Omega_2(120^\circ, 70.5^\circ, 0^\circ)$, $\Omega_3(240^\circ, 70.5^\circ, 0^\circ)$; and for the four cone sites: $\Omega_1(0^\circ, 0^\circ, 0^\circ)$, $\Omega_2(0^\circ, \beta_c, 0^\circ)$, $\Omega_3(120^\circ, \beta_c, 0^\circ)$, $\Omega_4(240^\circ, \beta_c, 0^\circ)$.

hardly distinguishable from previous SUMS results (Fig. 3.11, G3 at 45 °C), where cone librational angle distributions had been assumed. The ~ 2 kHz smaller Gaussian broadening is required, comparing to the SUMS simulations in Chapter 3 (see Table 3.2, G3 at 45 °C), because of the motional broadening resulting from slow cone axis libration is explicitly included in EXPRESS calculations.

It is natural to expect a noticeable change in ammonium PAS quadrupole coupling parameters from site to site due to different lengths of hydrogen bonds [108]. However, we consider the smaller number of variable parameters, which results from assuming site independent values, to be more appropriate for our simulations, in accord with the practice established by other authors [115, 116, 120]. Extensive simulations, one of which is shown in Fig. 4.1, confirm that this assumption can lead to a slight (15-25 %), overestimation of motional rates, but the effect is marginally within the experimental uncertainty limits (10-30 %). Overestimation of the librational amplitude, on the other hand, is rather large. If site dependent quadrupole coupling parameters were allowed, the best fit librational angles would be 10° to 15° smaller for all data sets, and the difference in populations would be correspondingly smaller. Therefore, while the librational amplitudes and site populations cited later in this chapter fit the data, the quoted values represent upper limits only.

For generation 2 equilibrium lineshapes, simulated with SUMS [72] (upper dashed trace) and EXPRESS [55, 67] (lower dotted trace) for the same motional models, are shown at 25 °C in Fig. 4.2a and at 45 °C in Fig. 4. 2b. Individual powder patterns for RND_3^+ , R_2ND , and R_3ND^+ deuterons simulated using EXPRESS (dotted lines) and SUMS (dashed lines) are also shown to the right of the experimental spectra (solid lines) and fits. For planar librations at the spacers and branching points, the number of sites on the arc was fixed to six equally probable orientations in EXPRESS. This was enough to ensure that the simulated lineshapes do not change considerably with increasing number of sites on the arc. In contrast, SUMS assumed no discretization of orientations along the arc when planar libration amplitudes were derived. Both algorithms yield acceptable fits to the overall

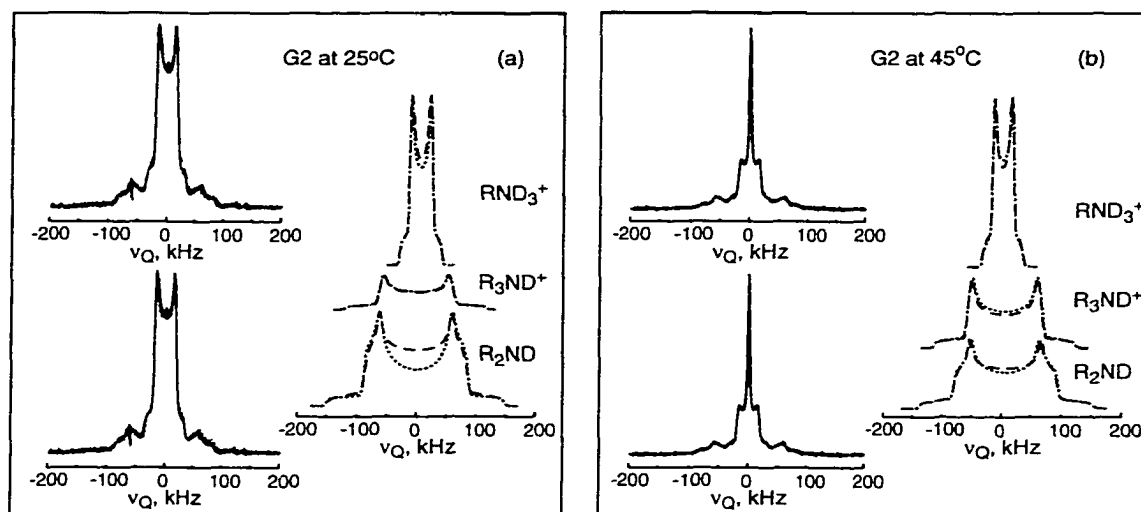


Figure 4.2

Experimental lineshapes (solid lines) and simulations (dashed and dotted) for G2: (a) at 25 °C and (b) at 45 °C, using SUMS (dashed trace) and EXPRESS (dotted trace). To the right of experimental lineshapes deconvoluted spectra of each deuteron site are compared for the two algorithms (see discussion in the text). See Tables 4.1-4.3 for corresponding EXPRESS fit parameters. The SUMS fit parameters are cited in Tables 3.1-3.5 (Chapter 3).

spectrum, but some small differences can be seen for individual contributions, especially at lower temperature (Fig. 4.2a).

Compared with SUMS results, explicit inclusion of slow libration of the ammonium C_{3v} symmetry axis in the EXPRESS calculations produces marginally better fits at the shoulders of the RND_3^+ powder pattern, and minor intensity changes in the middle. A weak dependence of the simulated equilibrium lineshape constraints this librational rate to 10^5 - 10^7 s^{-1} . So, in all simulations for ammonium deuterons the rate of their C_{3v} axis libration was fixed at the average value, $k_c = 10^6$ jumps per second. Including the axis motion in the simulation results in approximately 1-2 kHz broadening of the lineshape. The consideration of a log-normal librational rate distribution for ammonium termini may contribute some additional lineshape broadening as well. Thus, Gaussian apodization of these simulated spectra was ~ 2 kHz smaller than when the motion is assumed to be fast.

Intensity deviations are more pronounced in the middle of the R_2ND powder patterns. This tendency is also observed for other dendrimer generations. The effect of such misfits

amounts to less than a 5% overestimation of the mobile fraction (Gaussian plus Lorentzian peaks) compared with SUMS results. This did not significantly increase the uncertainties in the motional rates derived from the EXPRESS simulations, which were the ultimate goal of this investigation. Therefore, the equilibrium lineshape parameters determined from relatively fast SUMS simulations provided a good starting point for computationally intensive EXPRESS dynamics simulations.

For the secondary amide deuterons the main reason for loss of intensity in the center of the EXPRESS simulated spectra (Fig. 4.2) is the comparatively low number of librational jump sites (6). This saves computational time, but leads to correspondingly large angle jumps, especially for large librational amplitudes (as is in the case of G2 spacers). Also, we did not include any distribution of hydrogen bond lengths, which produce skewed distributions of intensities in the powder patterns (Chapter 3). The amount of Gaussian apodization used with EXPRESS simulations was fixed to the same value (7 kHz) for all data sets, even though the actual width of the powder patterns varied slightly with temperature and generation number. As was the case with ammonium termini powder pattern, additional 1-2 kHz broadening was coming from explicitly including the finite rate of libration into EXPRESS lineshape simulation of planar libration at the dendrimer interior.

It is noteworthy that at interior sites, the librational rate $k_l \sim 10^6 \text{ s}^{-1}$ is on the order of the deuteron Larmor frequency. Thus, planar librations fall in the category of "intermediate regime" molecular motion. However, judging from the appearance of the spectra, no major lineshape changes are observed when the librational rates increase to 10^8 - 10^9 s^{-1} compared to 10^5 - 10^7 s^{-1} . In this regard, it seems reasonable to reconsider the definition of slow intermediate and fast motional regime in application to this particular model of molecular motion. For libration in a plane with a given arc amplitude, the maximum possible change in quadrupole coupling parameters is dependent only on the librational amplitude (cf. Eqs. 3.6, 3.7). Under moderate librational amplitudes ($< 20^\circ$), the frequency shift of discontinuities in quadrupole echo spectra is less than 20 kHz compared to PAS values. Molecular motion

will influence such lineshapes when its rate is on the order of that frequency shift, $k_1 \sim 10^4 \text{ s}^{-1}$. This means that the above-mentioned librational rates higher than 10^6 s^{-1} are effectively "fast" for the libration on a planar arc.

In contrast, in case of three-fold rotation around ammonium symmetry axis, the amplitude of the motion is determined by the angle between ND bond and C_{3v} , 70.5° , which is fixed by the orbital hybridization constraints in covalent bonding. This geometry allows quadrupole spectra discontinuity shifts in excess of 100 kHz, meaning that intermediate regime spreads over the rates of 10^4 - 10^6 s^{-1} . Thus, in general, the fast regime for molecular motion should be determined not on the basis of the rate compared to deuteron resonance frequency and full spectrum width, but in application to a particular motional model dictating the maximum frequency range of possible averaging. According to the latter definition, both interior libration and termini rotation in PAMAM dendrimers pertain to the fast motional limit. It is therefore not surprising that the motional parameters describing the QE lineshapes calculated by SUMS under the assumption of fast molecular motion, agree with those determined by EXPRESS simulations.

4.1.2 Anisotropies for Libration in a Plane and in a Cone

An important advantage of the EXPRESS algorithm is that the relaxation anisotropies can be calculated and compared for different motional models before the whole set of spin relaxation experiments is planned. This helps to predict the required time scale of experiments for observation of relaxation in the dendrimer interior and at its surface. For instance, knowing the tendencies with recycle delays depending on temperature from QE experiments, it is possible to establish motional regime scales, and corresponding optimized delay tables for T_{1Z} and T_{1Q} experiments. Our previous observations showed that longer recycle delays are needed to achieve full relaxation at interior sites (broad powder patterns) with decreasing temperature. Since the rates of molecular motion increase with increasing

temperature, such an observation indicates that the rates describing planar libration at spacers and branching sites are on the slow side of T_{1Z} minimum, $k_1 \sim 10^5$ - 10^8 s^{-1} (Fig. 4.3a).

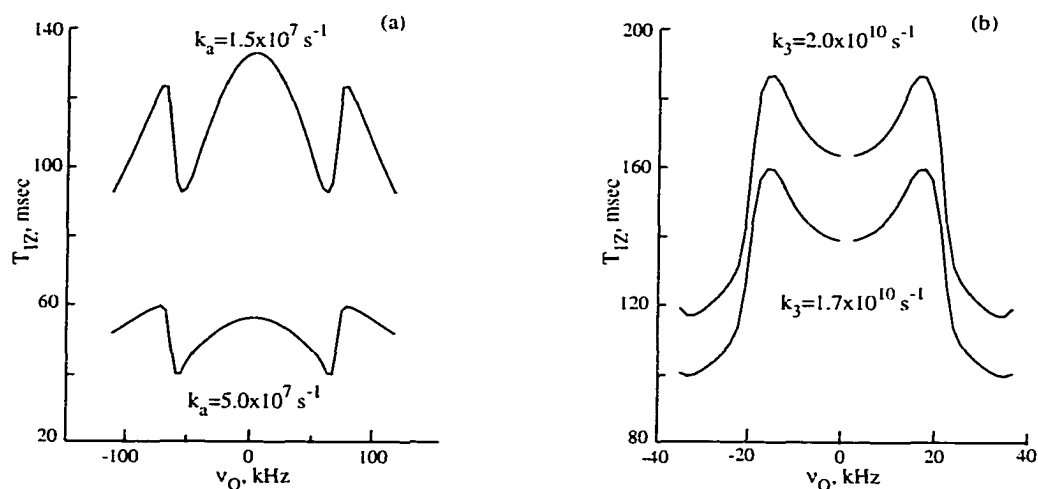


Figure 4.3

EXPRESS simulated anisotropies for the model of planar libration (a), and three-fold rotation with libration in asymmetric cone (b). The rates determining the anisotropies are noted on the Figure. The quadrupole coupling parameters in PAS were $\chi_{PAS} = 162$ kHz, $\eta_{PAS} = 0.05$. The arc amplitude was 11° , and unequal rotational and librational site populations were the same as in Fig. 4.1. Notice the opposite tendencies in T_{1Z} with increasing rate of the molecular motion for the two models.

For ammonium groups, relaxation in the experimentally accessible temperature range is determined by the fast pseudo-three-fold rotation. This is confirmed by observation of completely averaged quadrupole powder patterns and intermediate regime rates of cone libration $k_c < k_3$. Therefore, the relaxation behavior of terminal ammonium groups corresponds to rates on the fast side of the T_{1Z} minimum, $k_3 \sim 10^8$ - 10^{11} , and required recycle delays that increase with increasing temperature (Fig. 4.3b).

Due to spectral overlap of the powder patterns, it is useful to predict the anisotropy pattern for the dendrimer interior and termini a priori, and then look for the predicted trends in experimental data. This helps to validate the motional models (Chapter 3), and to unravel overlapping anisotropies from unselectively labeled deuteron sites. In general the overlap of spectral features, with single exponential relaxation at different rates, produces

multiexponential recovery curves. The best way to analyze these directly would be to separately simulate model dependent recovery curves and compare their weighted sum with experimental results.

From EXPRESS simulations we can calculate T_{1z} anisotropy of each of the spectral components, using nonlinear regression (three parameter) fits to single exponential functions. This also helps to choose the set of delay values to cover termini and interior relaxation trends in a single experiment. Simulations for the models of planar libration (R_2ND and R_3ND^+ , Fig. 3a) and isotropic motion (for narrow central features, producing frequency independent spin lattice relaxation time) show that T_{1z} values of the spectral features underlying ammonium powder pattern do not vary substantially across the middle of the spectrum.

4.2 Log-Normal Rate Distribution

The observation of nonexponential relaxation behavior in glassy polymers is usually associated with the presence of wide rate distributions, often over several decades [121, 122]. Thus, in most cases description of relaxation and motional processes in polymers is based on the log-normal rate distribution [121] or its empirical variations [122]. These distributions are normal on the "log" scale, and are therefore skewed, with long tails towards higher rates, on the linear rate scale. The simplest form found to be adequate for description of some trends in our experimental data is

$$G(k_i) = N^{-1} \exp\left(-\frac{1}{2} \left(\frac{\log_{10}(k_i) - \log_{10}(k_{mp})}{\sigma_k}\right)^2\right), \quad \text{where} \quad [4.1]$$

$$N = \sum_{i=0}^{n_k-1} \exp\left(-\frac{1}{2} \left(\frac{\log_{10}(k_i) - \log_{10}(k_{mp})}{\sigma_k}\right)^2\right) \quad [4.2]$$

For each rate, k_i , the simulated spectrum has to be normalized to unit total intensity before multiplying by the corresponding weight $G(k_i)$. Then the total spectrum is calculated

as a sum of subspectra for n_k k_i values sampled from the distribution,

$I(\nu) = \sum_{i=0}^{n_k-1} I(\nu, k_i) G(k_i)$. It is usually sufficient to use three to five rates with

$k_i = k_{mp} \times 10^{\pm i \cdot \sigma_k}$, $i = 0, \frac{n_k-1}{2}$, chosen symmetrically around the most probable value k_{mp} for

an adequate sampling of a narrow distribution ($\sigma_k < 1$), expected for dendrimers. In this case

corresponding weights reduce to

$$G(k_i) = \frac{\exp(-\frac{i^2}{2})}{1 + 2 \sum_{i=1}^{\frac{n_k-1}{2}} \exp(-\frac{i^2}{2})} \quad [4.3]$$

We emphasize here that according to log-normal rate distribution model, the most probable rate, k_{mp} , is always less than the average rate, $\bar{k} = \sum k_i G(k_i)$, due to the logarithmic form of the distribution. The fraction of spins with rates faster than k_{mp} is larger than that with the rates slower than k_{mp} , and will contribute more intensity to the spectrum. Thus, the prevailing contribution to the spectral intensity will come from spins moving with the rates closer to \bar{k} . This is the motional parameter which can be associated with the average activation energy of motion, if latter is to be derived from the experimental results.

4.3 Unraveling Overlapping Anisotropies

For all T_{1Z} experiments the standard non-selective inversion recovery with quadrupole echo detection pulse sequence was used (section 2.4.2, Fig. 2.7) with a 16 step phase cycle to suppress artifacts [67]. Typically, adequate signal to noise ratios were obtained by accumulating 3,500 to 4,000 transients of 1024 complex data points for each of 10 to 12 relaxation delays, τ . The 90 degree pulse length was 1.6 μ s, resulting in acceptable spectral coverage over the spectral width ± 200 kHz. The pre-acquisition delay was varied so as to

place a sampling point precisely at the top of the quadrupole echo. In most experiments, a 40 μs delay between pulses was chosen to shift the echo well outside the spectrometer dead time. A few experiments performed with 20 μs delay showed that for 40 μs transverse relaxation caused no deleterious effects. Lineshapes obtained for pulse spacings longer than 60 μs are strongly attenuated due to dipolar coupling with relaxing ^{14}N [123], and can therefore not be fit using procedures described in this paper. Temperature dependent relaxation studies were performed for generations 2, 3 and 9. For generations 1, 5 and 7 only room temperature data were obtained. Since all recovery curves were multi-exponential functions of the relaxation delay, delay values were chosen to uniformly sample intensity for both the shortest and the longest relaxation times in the experiment. The recycle delay (typically 2–5 s) was chosen to ensure more than 90 % magnetization recovery for the slowest relaxing component.

For each sample the full T_{1Z} experiment took from 2 to 3 days, depending on the temperature, required recycle delay, and the number of τ values. Over this long acquisition period, the relative error for total intensity in the spectrum due to electronic instabilities is estimated to be 10 to 15 %. This limited the range of temperatures at which experiments could be performed with reasonable accuracy. At temperatures lower than 15 $^{\circ}\text{C}$, the limiting factor was the long T_{1Z} (≥ 1 sec) of secondary amide and deuterated tertiary amine groups. At temperatures above 55 $^{\circ}\text{C}$, prohibitively low signal to noise ratio was caused by the small fraction of rigid material for generations 2 and 9, and by long T_{1Z} values for terminal ammonium groups of generation 3.

A few complementary T_{1Q} experiments were performed for generations 3 and 9 to check consistency of the motional models used to analyze the T_{1Z} data. The broadband Jeener-Broekaert sequence [89, 90] (section 2.4.2, Fig. 2.8) was used with a 32 step phase cycle [67], with the same experimental conditions as described above for T_{1Z} experiment. The t_p value, 12 μs , was chosen so to achieve uniform excitation of quadrupole order across the frequency range from 5 to 35 kHz, covering most of the RND_3^+ powder pattern. The last

delay before acquisition was adjusted to obtain an acquisition point at the zero crossing for the imaginary signal component.

4.3.1 Data Fitting Procedures

Spin relaxation data manipulations and simulations were performed on O2 Silicon Graphics workstations using the data visualization package PV-WAVE and a locally written simulation package, EXPRESS [55, 67]. Exponential apodization, corresponding to 500 Hz Lorentzian broadening, was applied to the time domain signals. The data were then left shifted so that the first point occurred precisely at the top of the echo for T_{1z} and at the first zero crossing for T_{1Q} signals. A frequency independent phase correction of 5-15 degrees was used to minimize the signal in the out of phase channel. The relatively small residual asymmetry in the Fourier transformed spectra may arise from instrumental artifacts and second order effects not eliminated by phase cycling. Prior to generating recovery curves from partially relaxed spectra, small baseline shifts were applied to ensure that the average baseline was exactly zero. Otherwise, natural logarithms of recovery curves could have different large shifts for each data set hampering comparison to simulated curves.

Wide distributions of motional parameters are usual for glassy linear polymers, and can in many cases account for non-exponential relaxation of overall Zeeman and quadrupolar polarization [124]. However, there is a growing awareness that phenomenological distribution functions used to parameterize relaxation of the total polarization are not adequate to account for orientational anisotropy of the relaxation times [51, 52, 125]. Instead, detailed insight into the microscopic dynamics can be obtained by fitting the anisotropy of observed relaxation times to specific motional models [126].

For PAMAM dendrimer salts, the data fitting procedure is greatly complicated by overlapping powder patterns, but because different motional models have different patterns of anisotropy, it is still possible to obtain reliable values of motional rates for specific

dendrimer sites. Due to low polydispersity of the studied materials, and according to conclusions from our QE lineshape analysis (Chapter 3), no substantial distribution of motional parameters is expected. Their contribution, if present, can be accounted for as a "second order" effect for relaxation anisotropies. So, at the first step of analysis this can be neglected. Then, if other descriptions fail, narrow rate distribution can be included as a second order correction. Thus, in the first approximation, the observed multi-exponential character of the recovery curves can be assumed to originate from single exponential contributions of overlapping spectral features:

$$\begin{aligned}
 M_{\infty}(\nu) - M_{\tau}(\nu) &= \sum_{i=1}^N I_{total}^i (m_{\infty}^i(\nu) - m_{\tau}^i(\nu)) e^{-\tau/T_i} \\
 &= \sum_{i=1}^N I_{total}^i (m_{\infty}^i(\nu) - m_{\tau}^i(\nu))
 \end{aligned}
 \tag{4.4}$$

Here, $M(\nu)$ is the overall spectral signal intensity at frequency ν (with *maximum* intensity normalized to 1), $m(\nu)$ is the signal intensity of a contributing feature (with *integrated* intensity normalized to 1), and I_{total} is the weighting factor for each overlapping component (determined from the equilibrium lineshape deconvolution, Chapter 3). Subscript " τ " indicates the delay time and the summation index "i" labels the spectral component. N is the number of spectral features overlapping at a particular frequency ν . For the present study, the following was approximately valid: $N = 1$ for $|\nu| > 110$ kHz (contribution only from R_2ND deuterons), $N = 2$ for $45 < |\nu| < 110$ kHz (contribution from R_2ND and R_3ND^+), and $N = 5$ for $|\nu| < 45$ kHz (rigid, glassy R_2ND , R_3ND^+ , RND_3^+ , a broad and a narrow isotropic component). In practice, low signal to noise ratio prevented accurate analysis of signal intensities for $|\nu| > 100$ kHz. We also found for adequate fits of recovery curves, two contributions from ammonium deuterons had to be included for frequencies in the interval $|\nu| < 45$ kHz, so in this spectral region $N = 6$ (see later sections and Appendix B). The latter two contributions differ only in relaxation time and relative intensity; their lineshapes are superimposable. The procedure used to fit recovery curves for frequencies between 45 and

110 kHz is described in section 4.3.2 below, while the more complicated procedure needed for frequencies inside RND_3^+ powder pattern ($|v| < 45$ kHz) is discussed in section 4.3.3 and Appendix B.

For each m_i simulations were done by solving the stochastic Liouville equation for the time evolution of the density matrix of a single deuteron undergoing Markovian jumps among different sites according to specific motional models (Chapter 3). The computations were performed using EXPRESS [55, 67], a simulation package developed to calculate T_{1Z} and T_{1Q} relaxation time anisotropies. For each spectral component the motional model is defined by the orientations of deuteron principal axes system (PAS) of the electric field gradient tensor and the rates of instantaneous jumps between orientational sites. The individually simulated spectral features were added (according to Eq. 4.4) with appropriate relative weights. The total lineshapes were then multiplied by a factor, $f(v) = v_0^2 / (v_0^2 + Q^2(v - v_0)^2)$, to correct for the finite bandwidth of the probe. The deuteron Larmor frequency was $v_0 = 46.06$ MHz, and the probe quality factor, $Q = 105$. A finite pulse width correction is incorporated in EXPRESS algorithm and does not need to be done separately.

The experimental and simulated recovery curves were compared for several points on the lineshape which had good signal to noise ratios. The simulations were repeated until the smallest global difference was achieved between experimental and simulated recovery curves for all these points. Quoted error bounds on the rates of motion correspond to rates which noticeably increase the difference between experimental and simulated recovery curves. This unwieldy procedure was necessary in order to account for non-exponential anisotropic relaxation of overlapping powder patterns, especially in the frequency range $|v| < 45$ kHz. It also helped to determine to what extent the experimentally observed multiexponential behavior can be influenced by rate distributions. The first step (excluding the rate distribution) was also necessary since for the whole T_{1Z} experiment each computation takes, on average, 20 to 40 minutes of CPU time on a SGI O2 workstation. So, the task of fitting

the data for several dendrimer generations at different temperatures is somewhat daunting. Thus, including the influence of narrow rate distributions should be postponed, whenever possible.

Fortunately, much simplification is achieved due to intrinsic physical properties of the system. For most deuterons, the rates are fast enough to have at most minor effects on the equilibrium lineshapes. Thus, before invoking EXPRESS to analyze the recovery curves, deconvolution of the equilibrium spectra can be performed rapidly (as described in Chapter 3) to yield the quadrupole coupling parameters, librational angles and relative intensities for spectral features originating from R_2ND , R_3ND^+ , and RND_3^+ groups. During the computationally intensive dynamic simulations, these parameters were held constant and only the relevant motional rates were varied.

4.3.2 Relaxation anisotropies at Spacers and Branching Sites

We found that the model of planar libration on an arc provides an adequate description of deuteron relaxation for R_2ND and R_3ND^+ groups. The number of jump sites on the arc was fixed at six in order to reproduce previously analyzed static QE lineshapes with minimum error and computation time. The site orientations were chosen to uniformly sample the libration arc between 0° and ϕ_0 . Equiprobable jumps among all six sites were allowed in the simulations. The distribution of quadrupole coupling parameters was modeled only as a homogeneous Gaussian broadening of 7 kHz half width, which was applied to all spectra after simulation. This broadening cannot not reproduce the generation and temperature dependent intensities, skewed due to H-bond length distributions, and thus introduces small errors in simulated lineshape intensities, which are more pronounced in the middle of the spectra. These errors can be neglected in the present study because the resulting uncertainty in the motional rates lies within experimental error bounds. Thus, the

introduction of additional variable simulation parameters is not warranted by the precision of the relaxation data.

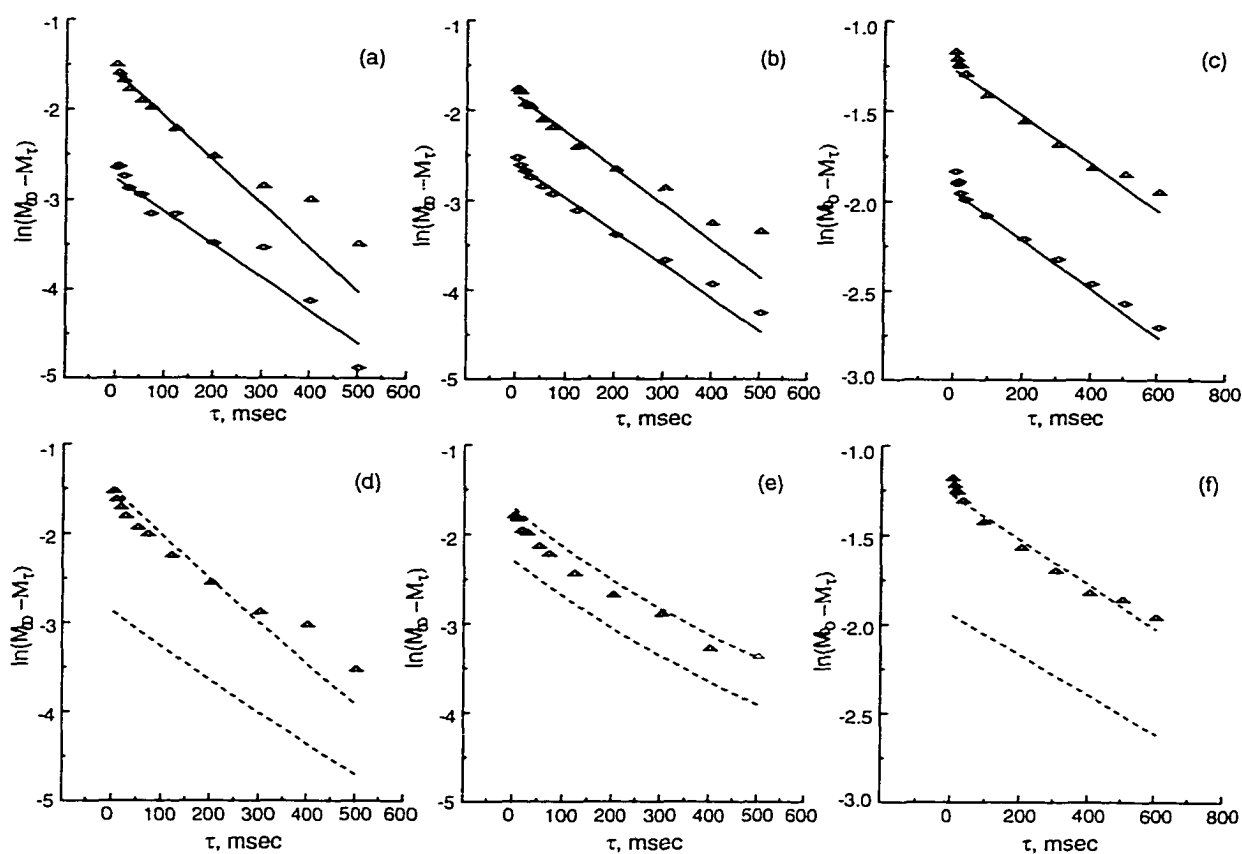


Figure 4.4

Room temperature experimental recovery curves for: (a, d) G1, (b, e) G3, (c, f) G5 at 50 kHz (triangles) and 80 kHz (diamonds). Solid lines in (a, b, c) represent a single exponential fit to experimental data. The “effective” fit T_{1Z} values for G1: 272 ± 44 ms @ 80 kHz, 206 ± 30 ms @ 50 kHz; G3: 270 ± 26 ms @ 80 kHz, 248 ± 36 ms @ 50 kHz; G5: 739 ± 54 ms @ 80 kHz, 767 ± 67 ms @ 50 kHz. Dashed recovery curves in (d, e, f) are results of EXPRESS simulation for two overlapping spectral features from R_2ND and R_3ND^+ deuterons at 50 kHz (upper) and 5 kHz (lower). See Tables 4.1-4.3 for corresponding fit parameters.

Attempts to improve the fit by incorporating wide log-normal distributions, $\sigma_k > 2$, of libration rates appropriate for linear polymers were completely unsuccessful with the dendrimers. Rates which give the best overall fit yield T_{1Z} values close to the minimum. If hundred-fold slower rates are included in the distribution, the simulated relaxation times,

derived from single exponential fit to recovery curves, are not greatly affected. This is because the single exponential three-parameter fit procedure gives more weight to the first points of recovery curve, and correspondingly, to higher rates of the skewed distribution. However, the slow rates introduce characteristic lineshape distortions which are not observed experimentally. Including faster rates in the distribution yields relaxation time anisotropies

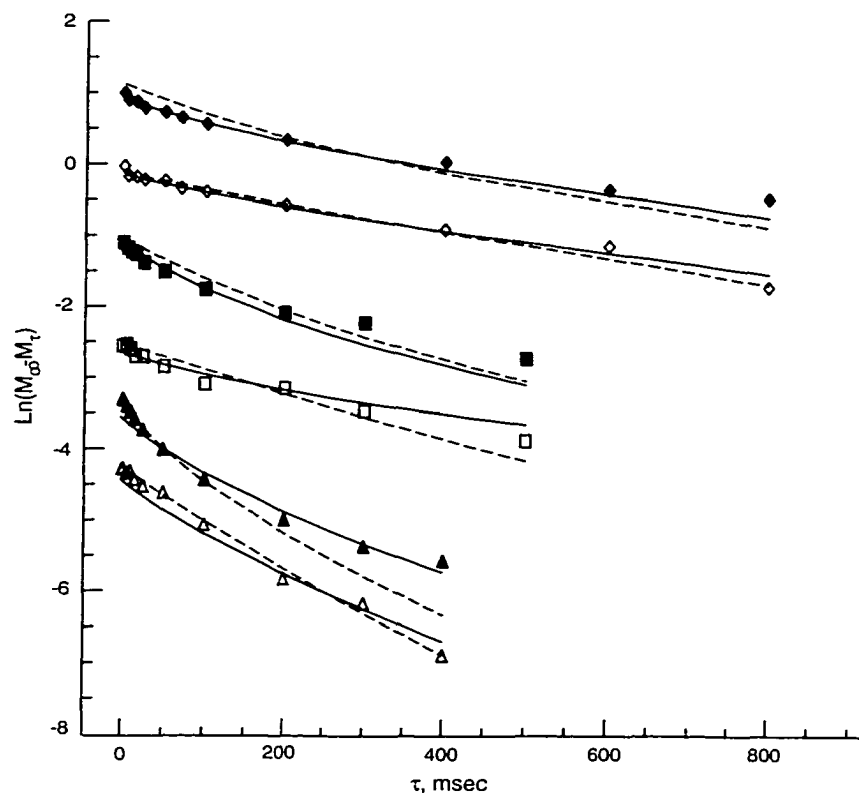


Figure 4.5

Experimental (symbols) and EXPRESS simulated (lines) T_{1Z} recovery curves for G2 at 25 °C (diamonds), 35 °C (squares) and 45 °C (triangles). Filled symbols correspond to a 50 kHz, and open symbols to 80 kHz slices. Dashed lines: $\sigma_k = 0.0$; solid lines: $\sigma_k = 0.5$ for both underlying powder patterns at 25 °C and 35 °C, and $\sigma_k = 0.4$ and 0.6 for spacers and branching points respectively at 45 °C. The most probable fit rates and amplitudes of the planar libration are the same as listed in Tables 4.1 and 4.2, except for the most probable librational rate in the rate distribution simulation for R_3ND^+ at 45 °C, $k_{mp} = 1.2 \times 10^7 \text{ s}^{-1}$. The data are vertically shifted for clarity.

significantly smaller than those observed experimentally. These simulations show that for spacers (RND_2) and branches (R_2ND^+), there can be at most a 3-8 fold distribution (wider at higher temperatures, $\sigma_k < 1$) of librational correlation times about the values quoted below. Such narrow distributions can be accounted for as phenomenological corrections after the completion of the first step of unraveling anisotropies from the overlapping spectral features.

Since only two overlapping components (from spacer and branching sites) are observed in the range $|\nu| > 45$ kHz, it is reasonable to start the relaxation analysis in that region, even though the experimental errors are larger there. Information provided by the spectra in this frequency range should be enough to determine the relaxation time anisotropies of secondary amide and deuterated tertiary amine sites. For many frequency points only two parameters are varied in these fits to a first approximation: the rates of librational motion at each of the two chemically distinct sites. The relative intensities of two components are fixed from static lineshape simulations.

Experimental recovery curves for G1, G3 and G5 at ambient temperature are shown for two representative frequencies, 50 kHz (triangles) and 80 kHz (diamonds), in Figs. 4.4a, b and c respectively. At 50 kHz the predominant intensity comes from R_3ND^+ , and at 80 kHz it comes from R_2ND deuterons. Single exponential functions (solid lines) turn out to be reasonable approximations for the relaxation at these frequencies when $T < 30$ °C. However, Figs. 4.4d, e and f show that nonlinearity of the semi-log recovery curves is better approximated by fitting to a weighted sum of exponentials (dashed lines), according to Eq. 4.4, especially for generation 3. Figs. 4.4d, e and f also show nonexponential recovery curves simulated for interior deuterons near the middle of the spectrum (5 kHz, no symbols), using the same parameters which reproduce the experimental data at 50 kHz (triangles). This information is useful for deconvoluting the experimental recovery curves in this spectral region.

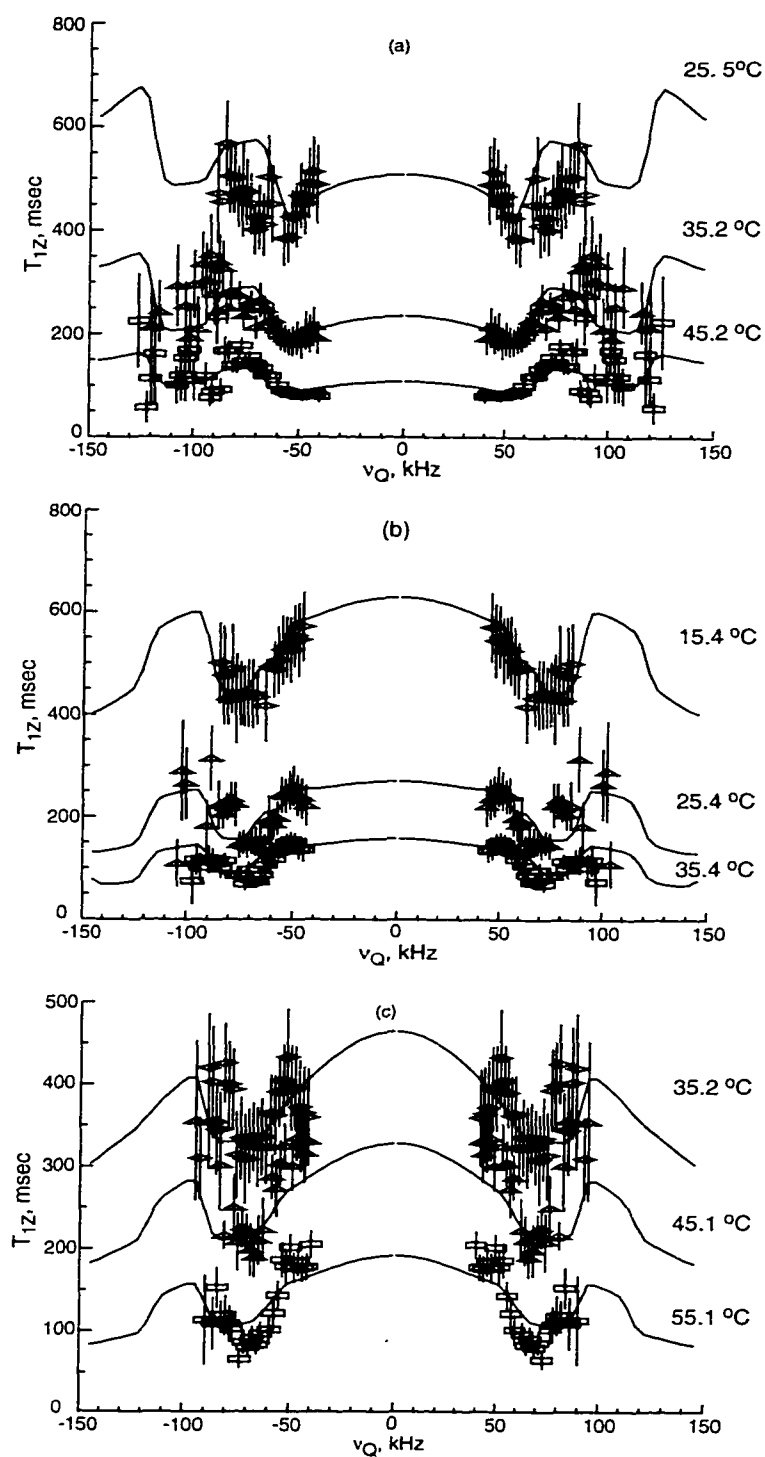


Figure 4.6

Comparison of single exponential T_{1z} fits for temperature dependent experimental relaxation anisotropy data and EXPRESS simulations of overlapping R_2ND and R_3ND^+ powder patterns. Anisotropies are shown with temperature increasing from top to bottom: (a) G2 for $T = 25^\circ\text{C}$, 35°C and 45°C ; (b) G3 for $T = 15^\circ\text{C}$, 25°C and 35°C ; (c) G9 for $T = 35^\circ\text{C}$, 45°C and 55°C .

However, with increasing temperature the fits excluding rate distributions (Fig. 4.5, dashed lines) start to deviate considerably from experimental data at long delay values, $\tau > 200$ ms. It can be concluded that the rate distribution width is changing with increasing temperature. The extent of these changes can be quantified by introduction of narrow log-normal rate distributions for contributing deuterons. Figure 4.5 shows experimental recovery curves for G2 outside the ammonium powder pattern at several temperatures increasing from top to bottom. The solid lines represent EXPRESS fits with five rates sampled from the log-normal distribution with $\sigma_k = 0.5$, and k_{mp} the same as k_l for the "dashed" fits at 25 °C and 35 °C. At 45 °C, $k_{mp} = 1.2 \times 10^7 \text{ s}^{-1}$, and $\sigma_k = 0.4$ and 0.6 for spacers and branching points respectively. Only minor differences were found between the three-rate and five-rate fits in this rate range. The data marked by filled symbols correspond to intensities at 50 kHz from the center of the spectrum, where the prevailing contribution comes from the R_3ND^+ powder pattern. The open symbols mark the 80 kHz slice, where R_2ND deuterons contribute the most.

In Fig. 4.5 little change can be observed in the distribution width with increasing temperature (other than maybe more narrowing) at 80 kHz. Therefore, at most 3-fold distributions can be expected for amide deuterons, and single exponentials are fairly close approximation for their recovery curves. For the 50 kHz recovery curves, the distribution width increases with temperature, and the fits assuming no distribution reproduce well only the first few data points ($\tau < 200$ ms) with higher average slope (shorter T_{1z} values), corresponding to higher libration rates. For R_3ND^+ , the k_{mp} used at higher temperatures is found to be lower than $k_l = 5 \times 10^7 \text{ s}^{-1}$ used in single rate EXPRESS simulations. The latter were derived by matching intensity contributions for relaxation delays $\tau < 200$ ms (Fig. 4.5), and in that sense should be close to the \bar{k} of the skewed distribution. The wider rate distributions at the branching sites may be associated with the presence of chloride anions. The activation energies derived later for librational motion at the dendrimer interior

disregarding log-normal rate distribution can be identified with the average characteristic temperature dependence of \bar{k} . Of course, explicit introduction of the librational rate distribution would increase uncertainty of the best fit rates and activation energies, but would not alter the basic trends and conclusions.

Table 4.1

EXPRESS fit parameters for R₂ND groups of all studied dendrimer generations.

Generation # χ_{PAS}, η_{PAS}	T \pm 0.05, (°C)	I _{total} [†]	$\phi\pm 1$, (degrees)	k _r × 10 ⁶ , (s ⁻¹)
G1 204 kHz, 0.12	25.40	18	13	3.4 \pm 0.5
G2 209 kHz, 0.12	25.45	32	17	0.7 \pm 0.2
	35.15	21	19	0.9 \pm 0.4
	45.15	10	19	2.0 \pm 0.4
	55.15	4	21	3.9 \pm 0.6
G3 206 kHz, 0.12	15.40	15	17	1.1 \pm 0.3
	25.40	22	18	2.5 \pm 0.3
	35.40	15	18	4.9 \pm 0.4
	45.40	7	18	5.4 \pm 0.4
	55.40	0	-	-
G5 209 kHz, 0.12	27.15	41	18	0.50 \pm 0.05
G7 209 kHz, 0.12	27.12	25	11	1.6 \pm 0.3
G9 210 kHz, 0.12	27.17*	31	11	1.9 \pm 0.3
	35.15	33	14	1.6 \pm 0.3
	45.12	34	17	2.0 \pm 0.3
	55.14	24	17	4.4 \pm 0.4

*A month after annealing at 55 °C for a day. [†]I_{total} is the integrated intensity of an R₂ND group. The total equilibrium spectrum, resulting from addition of all features (R₂ND, R₃ND⁺, RND₃⁺, Gaussian and Lorentzian), is normalized to unity at its highest point. The estimated error in I_{total} is $\pm 20\%$ of the quoted value.

For most of the experimental relaxation data (other than G2) signal-to-noise ratios at longer delay values did not allow quantitative characterization of such narrow rate distributions due to high scatter of recovery curve points. Therefore, keeping in mind the

physical sense of the best fit motional rates for overlapping powder patterns under assumption of single exponential relaxation for each spectral feature, the T_{1Z} simulations can be carried on excluding log-normal rate distributions to save computation time. Therefore, derived characteristic parameters should be interpreted as "averaged" over narrow, $\sigma_k < 1$, distribution of motional rates.

Table 4.2
EXPRESS fit parameters for R_3ND^+ groups of all studied dendrimer generations.

Generation # χ_{PAS}, η_{PAS}	$T \pm 0.05, (^{\circ}C)$	I_{total}^{\dagger}	$\phi \pm 1, (degrees)$	$k_i \times 10^6, (s^{-1})$
G1 162 kHz, 0.05	25.40	18	15	4.3 ± 0.5
G2 162 kHz, 0.05	25.45	8	11	11 ± 2
	35.15	14	11	15 ± 3
	45.15	7	11	50 ± 5
	55.15	3	11	100 ± 30
G3 171 kHz, 0.05	15.40	8	18	0.7 ± 0.1
	25.40	10	19	0.9 ± 0.2
	35.40	10	19	1.7 ± 0.3
	45.40	5	20	2.1 ± 0.4
	55.40	0	-	-
G5 159 kHz, 0.05	27.15	14	14	0.9 ± 0.1
G7 162 kHz, 0.05	27.12	21	14	1.4 ± 0.2
G9 159 kHz, 0.05	27.17*	23	11	3.7 ± 0.2
	35.15	14	11	3.3 ± 0.3
	45.12	17	11	3.9 ± 0.3
	55.14	20	14	4.6 ± 0.4

*A month after annealing at 55 $^{\circ}C$ for a day. I_{total}^{\dagger} is calculated for R_3ND^+ groups as indicated in the caption to Table 4.1. The estimated error in I_{total} is $\pm 20\%$ of the quoted value.

The above considerations suggest that an easy way to visualize the accuracy of the fit for the outer powder patterns is to simply compare anisotropies resulting from single

exponential fits to experimental data with the same procedure applied to simulated two-component recovery curves. Such a comparison, for generations 2, 3 and 9 at three representative temperatures, is shown in Fig. 4.6. Similar fits have been performed for other temperatures and generations, but are omitted for brevity. It is important to appreciate that the error bars shown for experimental data (symbols) come not only from finite signal to noise, but also from trying to fit two-component data with finite σ_k to a single exponential. Still, this picture illustrates the level of detail and the accuracy of the information we can extract from relaxation at interior dendrimer sites.

Deuteron relaxation at spacer (R_2ND) and branching (R_3ND^+) sites gets faster with increasing temperature for all generations as illustrated in Fig. 4.6. This observation can only be valid if the corresponding libration rates are on the slow side of the T_{1Z} minimum, as was expected. The best fit rates of libration range from $k_l = 10^6$ - 10^8 s^{-1} . For the branching R_3ND^+ sites of generation 2 at 55 °C, adequately short T_{1Z} values (50 ms) can only be achieved in simulations using the kinetic model of equiprobable jumps among all sites and the rate of libration close to the T_{1Z} minimum ($k_l \sim 10^8$ s^{-1}). With exchange between nearest neighbors on a chain, the minimum achievable T_{1Z} is inadequate (70 ms). However, this observation does not conclusively validate the all-sites model. Neither model includes the possibility of contributions to relaxation from fluctuating intermolecular field gradients, arising from the motion of nearby chloride ions. Such effects should be considerably larger for R_3ND^+ than for R_2ND deuterons.

For secondary amide sites, the experimental data do not distinguish between all-sites and nearest neighbor jump models. To reproduce the observed relaxation times for the nearest neighbor jumps, motion should occur at a rate more than order of magnitude higher than that for the all-site exchange model. However, the trends observed with changing temperature and generation number would be the same. Since the all-site model is required to describe branching site motion, and an alkyl chain connects both sites in the same dendrimer molecule, the all-site model was adopted for the secondary amide sites as well.

Best fit parameters for dendrimer interior obtained for all generations and temperatures are summarized in Tables 4.1 and 4.2.

4.3.3 Overlapping Anisotropies Across Ammonium Powder Pattern

Since interior deuterons associated with chloride anions exhibit increasing rate distribution width with increasing temperature (Fig. 4.5), it is reasonable to expect the same behavior for librational rates of ammonium termini. However, experimentally observed relaxation anisotropies for RND_3^+ deuterons are not determined by the rates of cone libration, but by the rates of fast ammonium rotation instead. This fast rotation is not expected to be noticeably influenced by the Cl^- presence [115, 116, 127]. It is then reasonable to assume that narrow or no rate distributions also suffice to characterize motion of the RND_3^+ groups. Strong support for this hypothesis is provided by the experimental data for G3 at high temperature. For example, at 55 °C, powder patterns for spacer and branch point deuterons have collapsed, and recovery curves for the remaining ND_3^+ powder pattern are well described by single exponential functions (see Appendix B, Fig. B.1). This would not be the case if there were log-normal distribution of rotational jump rates, σ_k increasing with temperature.

Simulating recovery curves has to be done separately for each of the spectral components overlapping in the frequency range $|\nu| < 45$ kHz, followed by adding the contributions, according to Eq. 4.4. The best signal to noise ratios are observed in this frequency range, but in this region it is difficult to analyze the recovery curves without any constraints due to the large number of overlapping components. Here, knowledge about relaxation anisotropies of the underlying spectral components is essential. It is important to realize that the total contribution to the apparent relaxation time at any given frequency will depend on the relative weights of each spectral component at this frequency, so the nature of the “effective” anisotropy is difficult to predict a priori.

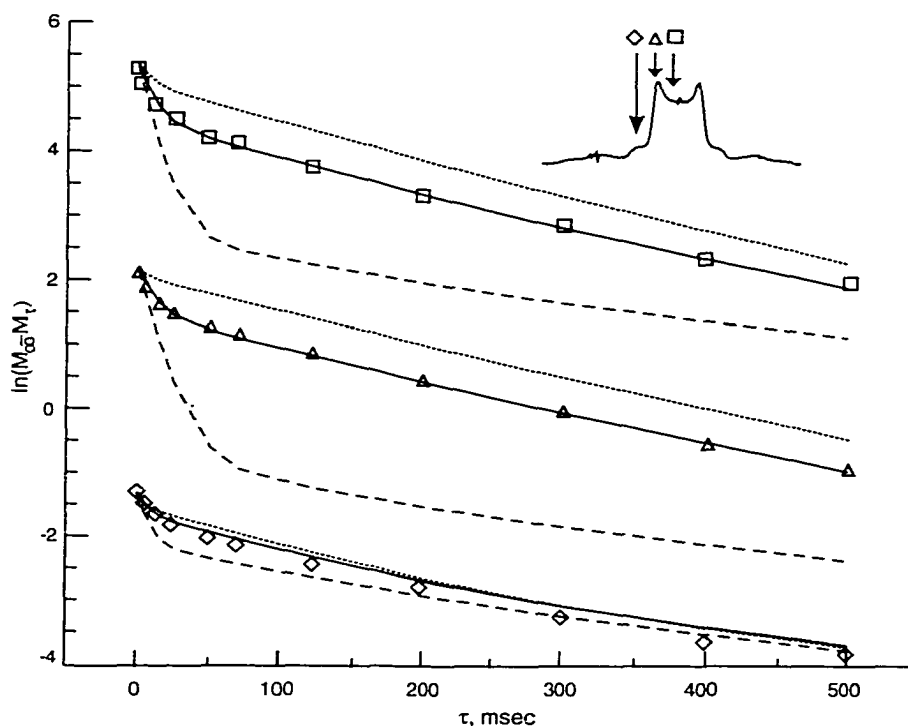


Figure 4.7

Experimental T_{1z} recovery curves for ND_3^+ rotors of G3 at 25 °C (symbols). Recovery curves are shown at frequencies 36 kHz (diamonds), 16 kHz (triangles, shifted vertically by 1.5 for clarity) and 5 kHz (squares, shifted vertically by 5), and their corresponding position on the lineshape is illustrated by the insert. Constrained multiexponential fits correspond to only slow (dashed lines), only fast (dotted lines), and both (solid lines) slow (48 %) and fast (52 %) ND_3^+ rotors.

Typical recovery curves, obtained at 25 °C for G3 PAMAM dendrimers, at three frequencies within the boundaries of the RND_3^+ powder pattern, are shown in Fig. 4.7. The solid lines represent best fits to experimental data (symbols), obtained by procedures described below. It is noted in passing that for some dendrimers, at some temperatures, normalized recovery curves of this type can be fit reasonably well phenomenologically, using a bi-exponential function of the form: $A_f e^{-\tau/T_{1f}} + (1 - A_f) e^{-\tau/T_{1s}}$, where the subscripts f and s denote fast and slow respectively. However, this procedure ignores the fact that in the indicated frequency range, there are contributions from at least three powder patterns in

addition to Gaussian and Lorentzian lines centered at zero frequency. Unconstrained fits to such multi-exponential recovery curves, especially with limited signal to noise ratio, are notoriously unreliable. To avoid such difficulties, the advantage was taken of the fact that motional models for each type of deuteron predict the anisotropy of the relaxation time, i.e., its orientation dependence, in terms of a limited number of parameters. When underlying powder patterns contribute to the recovery curves, this approach can still be used to obtain quantitative information about RND_3^+ motion.

The fit to two "effective" exponentials was successfully applied in recovery curve simulations across ammonium powder pattern to get first approximation rates for two overlapping RND_3^+ contributions with 10-fold different rotational rates. This procedure turned out to be useful also for the recovery curve analysis at a few temperatures where the relaxation rates of ammonium groups were very different from those in the dendrimer interior. In such cases, bi-exponential fit could effectively separate RND_3^+ anisotropy from the rest of the contributions. Thus, it was possible to directly compare experimental data with single exponential fit anisotropy from EXPRESS simulations. The empiric double exponential fit procedure and its implications are discussed in Appendix B.

Fitting the observed recovery curves was accomplished in stages. First, recovery curves for the underlying R_2ND and R_3ND^+ powder patterns were computed in the frequency range $|\nu| \leq 45$ kHz. As described in previous section, the rates and librational amplitudes used to generate these contributions were determined by fitting data *outside* this interval, and were not further adjusted. Next, the contributions from the central features were estimated by performing unconstrained, bi-exponential fits to experimental data for frequencies in the range $|\nu| \leq 5$ kHz. It was found that the "fast" time constant for these recovery curves was isotropic (orientation independent) and temperature independent, approximately equal to 10 ms for all dendrimer generations. Recovery curves with this time constant, generated for Gaussian and Lorentzian central features, were added to the recovery curves computed for R_2ND and R_3ND^+ powder patterns. The relative weight assigned to these contributions was

fixed by independent fitting of equilibrium spectra, as described in Chapter 3. Then recovery curves for RND_3^+ powder patterns were generated based on the two-frame model of (rapid) three-fold jumps combined with (slower) jumps of the three-fold jump axis among four sites defining a cone. The results were added to the fixed contributions from the other spectral components and compared with experimental recovery curves. These simulations, as well as those for librational motion of the R_2ND and R_3ND^+ groups, were all done by solving the stochastic Liouville equation using EXPRESS [55, 67]. This time consuming calculation was necessary because even though the three-fold jumps are fast, libration of the three-fold axis is not. The calculations confirm that while T_{12} is determined primarily by the three-fold jump rate, the lineshape is dependent on all the site populations and the rate of the slow motional process. The latter parameters were fixed by fitting equilibrium lineshapes. Thus, for purposes of simulating a RND_3^+ recovery curves, only one parameter remained adjustable: the three-fold jump rate, k_3 .

The dashed and dotted lines shown in Fig. 4.7 were determined from simulated spectra obtained as functions of the relaxation delay by adding correctly weighted underlying contributions to simulated RND_3^+ powder patterns according to Eq. 4.4. The RND_3^+ jump rate for the dashed lines, $k_3 = 1.3 \times 10^9 \text{ s}^{-1}$, was chosen to best match the short time behavior of the experimental recovery curves. However, these simulations fail to match the data for recovery times greater than 50-150 ms (depending on frequency). The dotted lines, with $k_3 = 2.0 \times 10^{10} \text{ s}^{-1}$, give the best slopes for long recovery times but fail to fit the short time behavior. These results demonstrate that no single value of k_3 can account for the observed recovery curves. The solid lines were obtained by adding a weighted sum of two different RND_3^+ contributions, with different values of k_3 . Additional simulations for G3 at $T < 35 \text{ }^\circ\text{C}$ (data not shown) indicate that comparable fits can be obtained using a narrow ($\sigma_k < 0.3$) log-normal distribution of k_3 values, but only if the distribution is sharply bi-modal with maxima near the two values used in Fig. 4.7. Thus, for G3 at $25 \text{ }^\circ\text{C}$, the data indicate the existence of two RND_3^+ environments, distinguishable only by different three-fold jump rates.

Parameters obtained by this procedure for other temperatures and other dendrimer generations are summarized in Table 4.3. The quoted error limits are qualitative estimates, based on visual comparison of simulated and experimental recovery curves as well as the computed sum of squares of deviations between calculated and experimental points.

Table 4.3

EXPRESS fit parameters for RND_3^+ groups of all studied dendrimer generations.

G # [†]	T \pm 0.05, (°C)	I _{total} [†]	$\beta_c \pm 2, ^\circ$	$p_3(\Omega(240^\circ, \beta_c, 0^\circ));$ $p_1=p_2=(1-p_3)/2;$ $p_3 \pm 0.001$	% "fast" ± 5	$k_3 \times 10^{10},$ (s ⁻¹) "fast"	($k_3 \pm 0.2$) $\times 10^9, (s^{-1})$ "slow"
G1	25.40	68	28	0.348	30	1.8 \pm 0.2	1.3
G2	25.45	67	31	0.350	20	1.1 \pm 0.3	1.1
	35.15	56	35	0.350	10	1.7 \pm 0.5	1.1
	45.15	18	42	0.346	0	-	1.1
	55.15	7	50	0.348	0	-	1.1
G3	15.40	81	20	0.352	45	1.3 \pm 0.2	1.3
	25.40	73	20	0.352	52	2.0 \pm 0.2	1.3
	35.40	64	23	0.346	60	2.7 \pm 0.3	1.3
	45.40	45	23	0.346	85	3.0 \pm 0.3	1.3
	55.40	9	22	0.348	100	3.7 \pm 0.2	-
G5	27.15	76	25	0.350	20	1.9 \pm 0.4	1.3
G7	27.12	76	25	0.350	15	1.3 \pm 0.5	1.2
G9	27.17*	72	32	0.350	0	-	1.2
	35.15	77	32	0.350	10	1.1 \pm 0.4	1.1
	45.12	73	36	0.346	0	-	1.2
	55.14	57	45	0.346	0	-	1.2

*A month after annealing at 55 °C for a day. [†]I_{total} is calculated for RND_3^+ groups as indicated in the caption to Table 4.1. The estimated error in I_{total} is ± 10 % of the quoted value. [†] $\chi_{\text{PAS}} = 165$ kHz, $\eta_{\text{PAS}} = 0.06$.

The presence of ammonium groups with different relaxation behavior is also found for high and low generation dendrimers. For these materials, the fraction of slow ammonium rotors is large at most temperatures studied. The introduction of narrow log-normal distributions for the "slow" ammonium rotors with temperature dependent width may

slightly improve the fit to recovery curves for high and low generation dendrimers. While distributions with $\sigma_k > 0.5$ for "fast" rotors worsen the fits for all PAMAM generations. When log-normal distributions for underlying powder patterns are included, the fits should reproduce better the recovery curves for G2 and G9, especially at higher temperatures. However, these improvements were within experimental error for a few simulations tried. Therefore, the distributions were excluded from quantitative analysis of ammonium relaxation anisotropies.

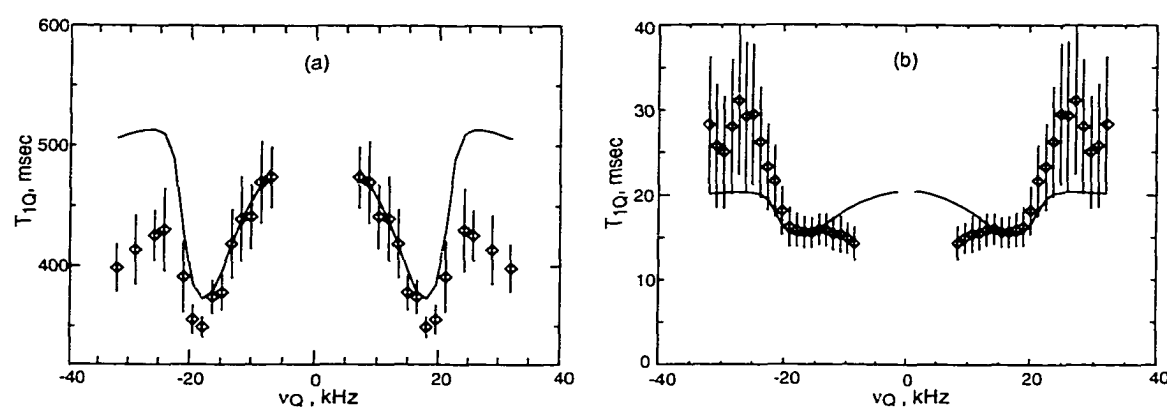


Figure 4.8

Single component experimental (symbols) and simulated (lines) T_{1Q} anisotropies for (a) G3 at 45 °C slow component and (b) G9 at 27 °C (a month after annealing at 65 °C) fast component. The motional parameters used were derived from T_{1Z} data, and are listed in Table 4.3.

G3 is the only generation for which the fraction of fast ammonium rotors increases with increasing temperature. For instance, at 45 °C the fraction of slowly rotating ammonium groups was only 15 %. In this case, an unconstrained bi-exponential fit procedure yields reliable values for T_{1Z} (slow). These are found to be in good agreement with single component EXPRESS simulation for slowly relaxing fast ammonium rotors not only for T_{1Z} , but also for T_{1Q} (see Fig. 4.8a). Single component comparison for RND_3^+ is likewise facilitated by the small fraction of intensity coming from fast relaxing underlying powder patterns at this temperature.

The experimental T_{1Q} values (the slow component from the bi-exponential fit) are slightly shorter than those predicted by single component simulations for fast ammonium rotors, due to contributions from the underlying powder patterns. The latter relaxation times are short at this temperature (see e.g. Fig. 4.6 above), but the bi-exponential fitting procedure does not remove them completely from T_{1Q} (slow), thereby pulling down the apparent slow component. This effect is most pronounced on the shoulders of RND_3^+ T_{1Q} anisotropy, where the fraction of intensity from underlying powder patterns is still relatively high.

Table 4.4
Integrated fit intensities of Lorentzian and Gaussian components for all studied dendrimer generations.

Generation #	$T \pm 0.05$, ($^{\circ}C$)	I_{total}^{\dagger} (Gaussian)	I_{total}^{\dagger} (Lorentzian)
G1	25.40	25	1.3
G2	25.45	18	0.5
	35.15	12	9.7
	45.15	4	12.2
	55.15	0	14.8
G3	15.40	9	0.5
	25.40	19	0.6
	35.40	21	4.1
	45.40	19	8.0
	55.40	0	14
G5	27.15	18	0.5
G7	27.12	15	0.0
G9	27.17*	24	0.0
	35.15	13	0.0
	45.12	16	0.0
	55.14	19	1.9

*A month after annealing at 55 $^{\circ}C$ for a day. I_{total}^{\dagger} is calculated for Gaussian and Lorentzian components as indicated in the caption to Table 4.1. The estimated errors in I_{total} are $\pm 10\%$ of the quoted value for Gaussian, and $\pm 5\%$ for Lorentzian. The half width of Gaussian and Lorentzian were fixed to 14 kHz and 2 kHz respectively for all generations.

For G9 dendrimer room temperature data obtained after annealing show a dominant contribution from slow ammonium rotors (more than 95 %). Once again, the fit for experimental T_{1Q} data (Fig. 4.8b) can be compared with EXPRESS simulations, but in this case the fast relaxing component from bi-exponential fits to experimental data is used, since most of the contribution to the slowly relaxing component comes from the underlying powder patterns at this temperature. The fit is not as good as for G3 because the fraction of underlying powder pattern intensities is high, and produces distortions in the bi-exponential fit, which is reflected in the reported error bars. As expected, this effect is especially noticeable at the shoulders of the ammonium powder pattern (Fig. 4.8b). In contrast to G3 data, the experimental values are now too long, because relaxation times for the underlying powder patterns are longer than for the ammonium groups. Despite these minor discrepancies, the general agreement between measured T_{1Q} anisotropies and those computed using parameters determined from the analysis of T_{1Z} data provides reassurance that the motional models are correct and derived parameters do not suffer from serious systematic errors.

T_{1Q} data are known to be more sensitive to the presence of distributions of rates and slow motion [55, 67]. Full deconvolution of multi-exponential T_{1Q} recovery curves would require taking into consideration the excitation profile and lineshape distortions due to slow motion of the C_{3v} symmetry axis, in addition to contributions from underlying powder patterns. In light of the number of fit parameters demanded, this task was deemed too complicated. Adequate fits of T_{1Q} anisotropies for ND_3^+ groups required the presence of a large excess population at one of the four librational sites, which consequently was fixed at 0.91 in all simulations. If site dependent PAS quadrupole coupling parameters were used as well, the differences in populations of these sites would be much lower. Other fit parameters were the same as in corresponding T_{1Z} simulations.

The quadrupole coupling parameters were assumed to be the same for both ammonium contributions, distinguished by three-fold rotational jump rates which differ by a factor of

ten. Although the possibility of different librational amplitudes and site populations for these deuterons cannot be ruled out, the broadened lineshapes do not provide enough resolution to constitute experimental evidence. Small deviations between simulated lineshape intensities and experimental values which were observed for some high temperature data sets (at the shoulders of the RND_3^+ powder pattern) may be a result of this approximation.

Best fit parameters obtained for ND_3^+ groups and molten fraction of all generations and temperatures are summarized in Tables 4.3 and 4.4. The tabulated total intensities, I_{total} , were calculated for the best fit equilibrium spectrum of the contributing feature, normalized to maximum intensity of superposition spectrum. Such a representation is more meaningful for spectral simulations and comparison with experimental results. If necessary, the corresponding relative intensities can readily be estimated from these data. Error bounds on PAS values of quadrupole coupling parameters are the same as reported in Chapter 3.

The appearance of narrow peaks in the middle of the spectrum is associated with the onset of the glass transition. DSC measurements (Chapter 3) show that for G2 the transition starts near room temperature. The fact that both Gaussian and Lorentzian components appear in appreciable amounts at higher temperatures for high generation materials is consistent with their higher T_g . For all generations, the total intensity of the Gaussian component, which decreases from $< 10\%$ at $15\text{ }^\circ\text{C}$ to $< 1\%$ at $-30\text{ }^\circ\text{C}$, suggests that residual solvent may exert a plasticizing effect below T_g . However, for many glassy polymers, local large amplitude motion can produce a narrow NMR lineshape component well below the onset of the glass transition as determined by DSC, even when there is no residual solvent [124]. The Lorentzian component, which appears only at temperatures well into the glass transition region, may be assigned to molten material.

4.4 PAMAM Generation Dependent Kinetics

Representative fits for full inversion-recovery T_{1Z} experimental data of generations 2, 3, and 9 at 35 °C, are shown in Figs. 4.9a, c and e, together with deconvoluted single exponential anisotropies from contributing deuterons, in Figs. 4.9b, d and f. The amount of information obtained from these fits is appreciable.

From the data presented in Tables 4.1-4.3 and Fig. 4.9, it can be seen that the relaxation times of R_3ND^+ deuterons at 35 °C increase monotonically with increasing generation, while the relaxation times of R_2ND deuterons pass through a minimum around G3. Relaxation times of the fast rotating fraction of RND_3^+ groups pass through a maximum at G3, while the relaxation times of slow rotating RND_3^+ groups are essentially independent of generation. For librational motion, the relaxation time must decrease as the libration amplitude increases, and on the slow side of the T_{1Z} minimum it will decrease with increasing libration rate. Perusal of Tables 4.1-4.3 shows that the trends illustrated in Figure 4.9 reflect changes predominantly in libration rate rather than amplitude. For example, the large almost 4-fold increase in R_3ND^+ relaxation time for G3 and G9 (compared to 100 ms for G2), is due to an approximately ten fold decrease in libration rate at the branching sites. Simultaneously, the libration rate of spacer R_2ND groups passes through a maximum at G3, decreasing their relaxation time to about 80 ms at 35 °C.

For identical motional parameters, libration-induced relaxation of R_2ND deuterons would be faster than that of R_3ND^+ deuterons by the square of the ratio of their corresponding quadrupole coupling constants (1.6). However, for generation 2 the R_2ND deuterons are observed to relax approximately 2.9 times slower than R_3ND^+ deuterons. Since the librational amplitudes are nearly the same, this difference can only be due to the much faster libration rate of the R_3ND^+ deuterons. This trend is reversed for the spacers and branching points of higher generations, where the spacer secondary amide deuterons relax

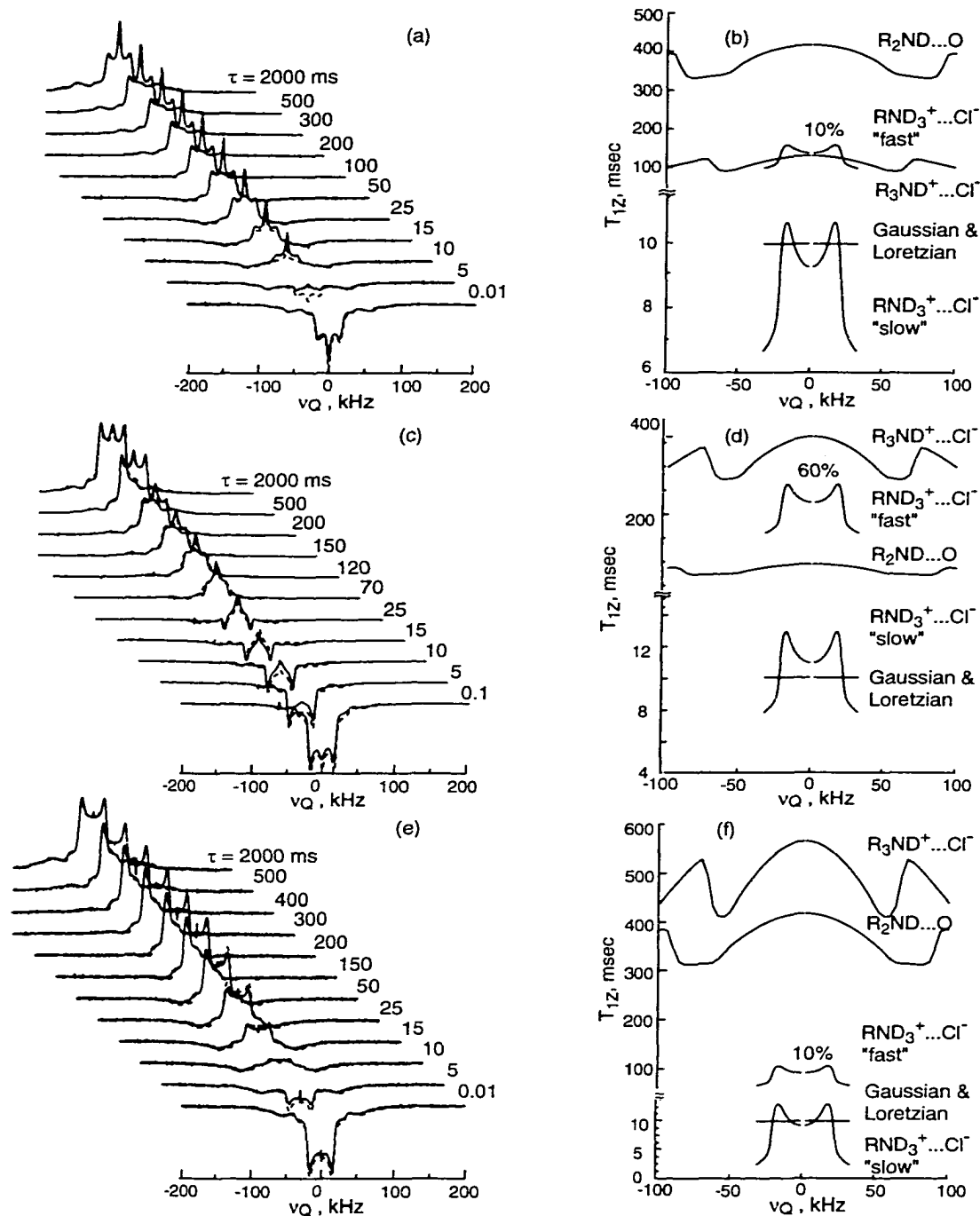


Figure 4.9

T_{1z} experimental lineshapes (solid lines) and overall fit (dashed lines) from EXPRESS simulation for (a) G2, (c) G3 and (e) G9 at 35 °C. Corresponding delay values, τ (ms), are listed to the right of the spectra. The derived relaxation time anisotropies of each contributing deuteron is shown in (b) G2, (d) G3 and (f) G9 (notice the change in T_{1z} scale around 100 ms). The fraction of "fast" ammonium rotors, RND_3^+ , is 10 ± 5 % for G2 and G9 and 60 ± 5 % for G3 at this temperature (see Tables 4.1-4.3 for fit parameters).

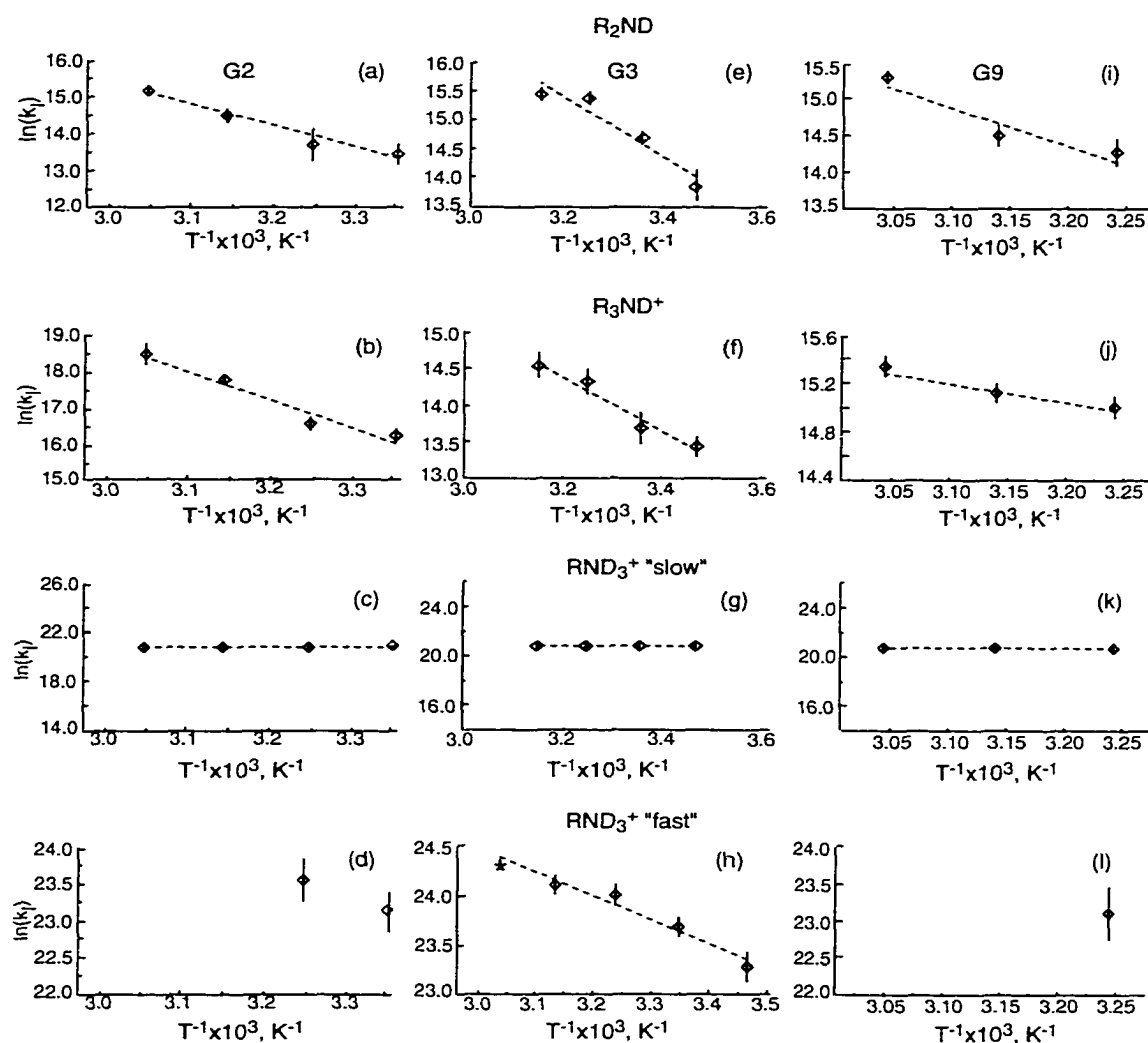


Figure 4.10

Temperature dependence of the rates of molecular motion (symbols) and Arrhenius fits (dashed lines) in (a-d) G2, (e-h) G3 and (i-l) G9. Contribution from “fast” RND_3^+ rotors was not observed at all temperatures studied in (d) G2 and (l) G9 (corresponding symbols are missing). For G3 at 55 °C the only contribution observed was from the “fast” RND_3^+ deuterons (star, (h)).

faster (3 times for G3 and 1.3 times for G9) than those at the branching sites, and the librational rates at both sites are more nearly equal.

For the temperature range investigated, the Arrhenius plots for all deuterated sites of generation 2, 3 and 9 dendrimers are shown in Fig. 4.10. The best fit Arrhenius activation

parameters are summarized in Table 4.5. Due to the presence of narrow log-normal rate distributions, derived activation energies are average characteristics for librational motion in dendrimer interior.

Table 4.5

Average activation energies, logarithm of collision frequencies and rates of motion for generation 2, 3 and 9 PAMAM dendrimers.

Group	G#	E_A , kJ/mol	$\ln(A)$	k , s^{-1} at 35°C
R_2ND	G2	48±7	33±3	$(0.9±0.4)10^6$
	G3	42±8	28±3	$(4.9±0.4)10^6$
	G9	42±10	31±6	$(1.6±0.3)10^6$
R_3ND^+	G2	64±10	42±4	$(1.5±0.3)10^7$
	G3	30±4	26±2	$(1.7±0.3)10^6$
	G9	14±3	20±1	$(3.3±0.3)10^6$
RND_3^+ , "fast"	G2	~30	~30	$(1.7±0.5)10^{10}$
	G3	20±2	32±1	$(2.7±0.3)10^{10}$
	G9	-	-	$(1.1±0.4)10^{10}$

4.4.1 Planar Libration at Branching Sites

Although the data do not permit highly accurate determination of the rates of slow libration of the ammonium symmetry axis, the values used in simulations are comparable to the rates of libration at the secondary amide of the dendrimer interior. This suggests a possible correlation of librational motions at both sites, presumably mediated by covalent bonds of the dendrimer arms. If this is true, then it is far from obvious why the librational rates at R_2ND and R_3ND^+ sites are so different; they only are separated by a pair of methylene groups. One possibility is that the electric field gradient tensor of R_3ND^+ deuterons is determined, in part, by nearby chloride ions. Anion motion would then contribute to an apparent "libration" of these sites. If this is indeed the case, then the large values of apparent libration rate observed for R_3ND^+ in generations lower than 3 are simply

a consequence of increased anion mobility in the more open structure of low generation materials.

The activation energy of “libration” at branching R_3ND^+ sites decreases with increasing dendrimer generation. It is larger than the activation energy of R_2ND sites for G2, almost equal for G3 and smaller for G9 (see Table 4.5). This supports the hypothesis that chloride ion motion modulates the R_3ND^+ electric field gradient tensor. If this picture is correct, activation energies derived from spin lattice relaxation of chloride ions should follow the same trend as those of R_3ND^+ deuterons.

The hydrogen bond energy between charged atom pairs in salts is generally larger than between neutral atoms [106, 128]. Therefore, the low activation energy at the branching sites of G9 suggests that hydrogen bonds between nitrogen and chlorine remain intact during librational motion. The motion of R_3ND^+ and Cl^- fragments could be “synchronized” by the highly constrained environment associated with backfolded arms of the dendrimer molecules. For generation 3, looser backfolding produces weaker constraints, allowing higher amplitudes of libration (Table 4.2) and presumably breaking of hydrogen bonds. On the other hand, since there is no appreciable interpenetration of neighboring molecules, the intermediate activation energy indicates that only one branch is involved. For generation 2, significant tangling between dendrimer molecules again hinders the motion, decreasing the librational amplitude (see Table 4.2), and almost doubling the activation energy (see Table 4.5). This could be due to the fact that breaking $R_3ND^+ \dots Cl^-$ hydrogen bonds now requires motion of two branches belonging to different dendrimer molecules.

4.4.2 Planar Libration at Spacers

The observation of similar libration rates of spacer R_2ND deuterons for low (G2, G3) and high (G9) generation dendrimers, at any given temperature, implies that the dendrimer arms in both environments experience similar constraints. This agrees with the expectation

that high generation materials are extensively backfolded while low generation dendrimers are not [37-39, 103]. The similarity of R_2ND librational rates therefore suggests that structure(s) associated with tangled, interpenetrated dendrimer arms belonging to different molecules in low generation materials resemble those of backfolded, high generation dendrimers. For generation 3, the onset of backfolding reduces the extent of intermolecular penetration and leads to an increase in libration rate. This picture is also consistent with the maximum in libration amplitude of R_3ND^+ sites for G3 (see Table 4.2).

The activation energy for spacer R_2ND libration, $E_A = 44 \pm 5$ kJ/mol, is essentially independent of generation. It follows that the activation mechanism does not depend on whether the librating spacer units belong to interpenetrated or backfolded dendrimer arms. Independent of packing, the $ND \dots O$ hydrogen bonding implies that two dendrimer arms are always involved in this motion. The relatively large amplitude libration in the dendrimer interior could break $R_2ND \dots O$ hydrogen bonds, which accounts for the unusually large activation energy. The typical hydrogen bond energies for amide bonds are known to range from 30 to 60 kJ/mol [106] and depend on the donor-acceptor environment, as well as on the number of hydrogen bonds per amide group. Ordinarily, simple libration in the bottom of a potential would not be expected to exhibit a strong temperature dependence [54]. For $R_2ND \dots O$ hydrogen bonds two spacer units are always involved, since the trans conformation dominance for amide bonds prevents hydrogen bond formation within a single spacer. From the derived absolute value of the activation energy the average number of bonds formed for the same spacer is estimated to be ~ 1.5 [106]. It means that at least every other spacer has its carbonyl involved in hydrogen bonding together with the adjacent ND group. The formation of more than one hydrogen bond for the same amide usually indicates compact environments [106].

4.4.3 Fast Rotation of Ammonium Termini

Relaxation data show more sensitivity to the fast rotation of ammonium termini than to their libration. So, for the former, quantitative characterization can be achieved from inversion recovery experiments while termini libration is better characterized using ^2H MAS. For G3 the fraction of fast ND_3^+ rotors increases with temperature, and approaches 100 % at 55 °C (Table 4.3). However, this fraction remains small for all other generations, and decreases rapidly with increasing temperature for both G2 and G9. A key to understanding this unusual behavior is the observation that for both G2 and G9, the fraction of fast rotating RND_3^+ groups exhibits thermal hysteresis: e.g. a month after annealing G9 for a day above 55 °C, the fraction drops below the limit of detectability (~3-5 %). The fast rotating RND_3^+ groups must be associated with termini near the dendrimer surface. The thermal hysteresis observed for G2 and G9 (and to a lesser extent for G3) implies that some dendrimer arms are trapped in non-equilibrium configurations during solvent removal. For both G2 and G9, looser configurations which allow fast RND_3^+ rotation are thermodynamically less favored than more constrained, backfolded (high generation) or interpenetrated (low generation) configurations (Table 4.3).

The intensity of the underlying R_3ND^+ and R_2ND powder patterns for G3 decrease rapidly with increasing temperature, and these features (as well as the contribution from the slow ammonium rotors) are completely absent from the 55 °C spectrum. This behavior is different from that of either G2 or G9 dendrimers, for which weak R_3ND^+ and R_2ND powder patterns are still evident at 55 °C (see Figure 4.11).

If the fast rotating ammonium groups are associated with less crowded environments near the dendrimer surface, the unique relaxation behavior of G3 suggests that there is an intermolecular network of weakly associated dendrimer arms, connected by more mobile branches. At 55 °C the amplitudes and rates of spacer motion in the mobile regions are sufficiently high to mimic essentially isotropic motion, so that all deuterons in such regions

contribute only to the large central spike in the spectrum. We were able to model such behavior by allowing rotation about two C-C bonds in the ethylene diamine part of the spacer in addition to the libration of ND bond.

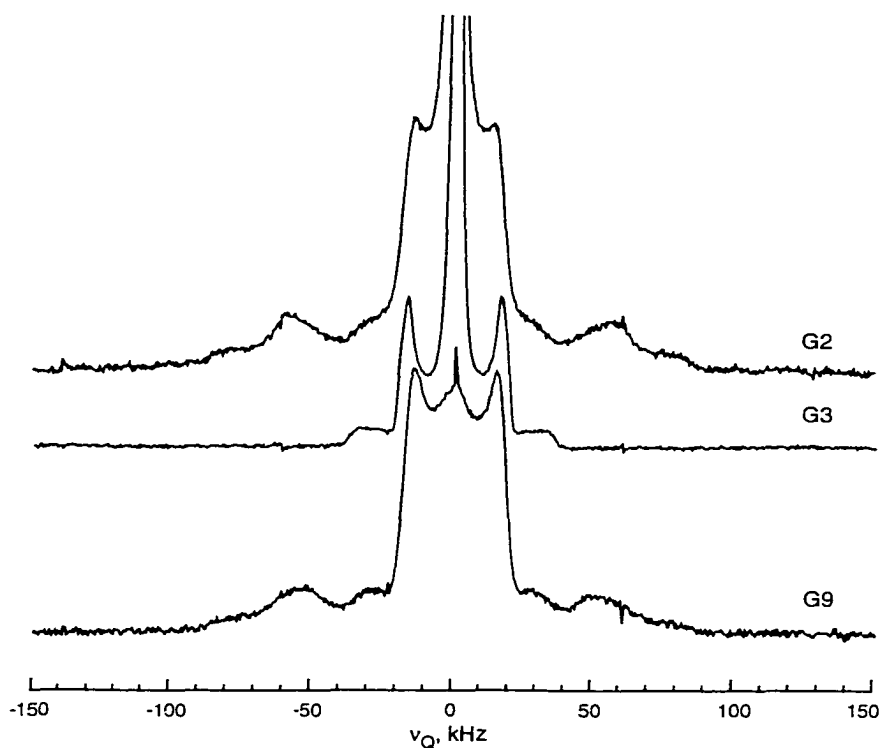


Figure 4.11
Experimental spectra of G9, 3 and 2 (bottom to top) at 55 °C with 5 s recycle time. Notice the absence of outer powder patterns for G3.

The network of termini is not stable for $G < 3$ because the dendrimer arms are too short, while for $G > 3$ globular (backfolded) structures are preferred. For G3 the fraction of RND_3^+ groups participating in the surface network can be estimated on the basis of the appropriate relative intensities. Analysis of integrated intensity data in Tables 4.1-4.4 shows that the increasing proportion of fast versus slow ammonium rotors with increasing temperature (Table 4.3) is actually due to a decrease in the intensity of slow component. In fact, this analysis suggests that the network of dendrimer termini, defined by the fast ammonium rotors, consists of a temperature independent fraction of 60 to 70 % of all

RND₃⁺ groups. It is possible that such a fraction represents a “critical surface concentration”, which allows intermolecular network formation without appreciable backfolding. The backfolded arms, associated with slowly rotating ammonium groups, apparently start to undergo a multifractal motion like the spacers surrounding them, completely averaging their quadrupole coupling tensors, and contribute intensity only to the central spike by 55 °C.

The slowly rotating ammonium deuteron component is associated with restricted environments caused by backfolding for high generations, interpenetration for low generations, and presumably both for generation 3. The fact that the rate of three-fold jumps for these deuterons, $k_3 = (1.3 \pm 0.2) \times 10^9 \text{ s}^{-1}$, is independent of generation number (see Table 4.3) indicates that the nature of these constrained environments is the same for all PAMAM dendrimers. Its independence of temperature is very unusual behavior for three-fold jumps and must be connected to the complexity of dendrimer structure. Phenomenologically, this can arise either from a collision frequency (pre-exponential factor) exponentially decreasing with temperature or an activation energy increasing linearly with temperature. As discussed above, it is also possible that introduction of a narrow log-normal distribution with temperature dependent width ($\sigma_k < 0.8$ at $T > 35 \text{ °C}$) would impart temperature dependence on slow \bar{k}_3 , producing finite average activation energy for these groups. However, it is expected to be small and similar for low and high generations due to the compact environments around slow ammonium rotors and equal rotational rates derived under assumption of no rate distribution. Introduction of the distributions with $\sigma_k > 0.5$ for slow rotors at $T < 35 \text{ °C}$ worsens the recovery curve fit at least for G2. Therefore, the presence of noticeable rotational rate distribution for slow ammonium rotors below the glass transition temperature is unlikely.

Fast ammonium rotors participating in intermolecular surface network do not show the presence of noticeable log-normal distributions of their rotational rates: $\sigma_k < 0.4$ at all temperatures. This might be due to the weaker influence of chloride anions on the surface

associations of ammonium groups compared to backfolded or interpenetrated termini in compact environments of the dendrimer interior. The activation energy of the fast ammonium deuterons could be accurately determined only for G3. Our value is in agreement with the lower limit for crystalline ammonium salts cited in literature [115, 116, 129-131]. This confirms the suggestion of a relatively unconstrained environment for fast RND_3^+ groups. The slight increase in activation energy of fast ammonium rotors for G2, with concomitant decrease in their fraction, is consistent with the generic picture of more constrained environments for interpenetrated low generation dendrimers.

4.5 Libration of Termini Characterized by ^2H MAS

As was mentioned above, experiments measuring relaxation anisotropy showed little sensitivity to librational motion of the dendrimer termini. In contrast, the ^2H MAS lineshapes provide quantitative information about ammonium libration. This method has higher sensitivity in the kinetic window of cone libration, while fast rotation of ammonium termini has negligible effect on ^2H MAS spectra. In addition, ^2H MAS experimental data confirm the surprisingly narrow distributions of librational rates of the dendrimer spacers, found from analyzing relaxation rates. The implications of these results for all PAMAM generations are suggested as well.

All experiments discussed below were performed on G2 PAMAM ammonium chloride dendrimer. Experimental spectra were accumulated using a Chemagnetics MAS triple resonance probe with a 5 mm coil, tuned in single channel mode. The quality factor of the probe is $Q = 220$. $3\mu\text{s}$ 90 degree pulses were applied with 1 s recycle delay in single pulse experiments, spinning at the magic angle at rate $k = 4000 \pm 2$ Hz. The spectral width was set to 100 kHz. The sample was packed under nitrogen atmosphere into a rotor sealed with two finned spacers to protect it from moisture. Thermal equilibration proceeded for 20 minutes

before data acquisition. The number of scans and experimental time was limited by heat conduction to the magnet (typically, less than an hour including thermal equilibration).

Simulations were performed by numerically solving the stochastic Liouville-von Neumann equation for a statistical ensemble of deuterons subject to discrete random reorientation under MAS conditions [56], according to specified motional models (Chapter 3). For the spacer (R_2ND) and branching site (R_3ND^+) deuterons we used the model of random jumps between six sites on a planar arc of amplitude ϕ , at rate k_1 . For terminal (RND_3^+) deuterons, single frame libration in a cone, β_c , was modeled by jumps among four sites, in accord with EXPRESS relaxation anisotropy simulations. A large population, p_4 , was used for the single orientation described by Euler coordinates $\Omega_i(240^\circ, \beta_c, 0^\circ)$, and equal populations, $p_{1,2,3} = (1 - p_4) / 3$, were assigned to the other three sites. Quadrupole coupling parameters, averaged by a fast three-fold rotational motion ($k_3 > 10^9 \text{ s}^{-1}$), were fixed to the values $\eta = 0$ and $\chi = 55 \text{ kHz}$. The inclusion of an additional frame with an explicit three-fold motion was not necessary due to the fast rate of this motion (see Table 4.3), and would only lengthen the simulation time. Each calculation took 100-120 minutes of CPU time on an SGI O2 workstation.

Due to hardware limitations (narrow probe bandwidth, relatively long pulses, and imperfect thermal isolation), adequate spectral coverage was not achieved for broad spectra from R_2ND and R_3ND^+ deuterons ($\chi \sim 150\text{-}200 \text{ kHz}$).

4.5.1 Overlapping Sidebands

After proper correction for the finite pulse width and the probe Q-factor, the simulation of underlying powder patterns (Fig. 4.12b) shows an almost flat intensity pattern across the frequency range of the motionally averaged spectrum of ammonium termini. Therefore, these contributions do not influence the intensity pattern in the middle of the spectra, which

are to be analyzed in terms of RND_3^+ dynamics. Also, at any temperature, the contribution from the spacers will not exceed the values observed between 50 and 70 kHz. This allows complete neglect of spacer contributions for temperatures above 20 °C (see insert (c) in Fig. 4.12).

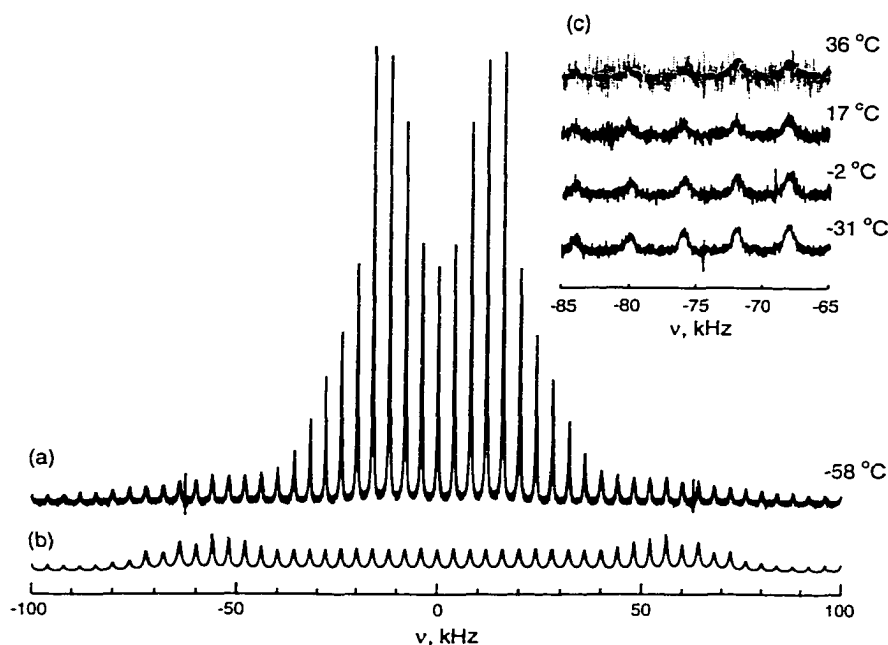


Figure 4.12

The experimental ^2H MAS spectrum (a) for PAMAM G2 at 215 K is compared with a one-frame arc libration simulation (b) for R_3ND^+ , $k_1 = 4.0 \times 10^5 \text{ s}^{-1}$, $\phi = 11^\circ$, and R_2ND , $k_1 = 1.0 \times 10^6 \text{ s}^{-1}$, $\phi = 19^\circ$. The motion is modeled by jumps between 6 sites of equal populations on an arc of amplitude ϕ , with quadrupole coupling parameters: $\chi_{\text{PAS}} = 162 \text{ kHz}$, $\eta_{\text{PAS}} = 0.05$, and $\chi_{\text{PAS}} = 209 \text{ kHz}$, $\eta_{\text{PAS}} = 0.12$, for above mentioned deuteron sites, respectively. The insert (c) illustrates the broadening and decreasing S/N for the outer parts of the experimental spectra with the increasing temperature. The bold line through the spectrum at 36 °C shows the fit for R_2ND component only, with $k_1 = 0.9 \times 10^6 \text{ s}^{-1}$, $\phi = 19^\circ$.

Spinning side bands for the secondary amide and the tertiary amine deuterons become slightly narrower with decreasing temperature, which can be accounted for in simulations either by slightly increasing the rate of libration or by decreasing the arc angle. The latter makes more physical sense. Extrapolation of librational rates to lower temperatures from

Arrhenius fits obtained previously for $T > 20$ °C, is definitely not possible. If done, this would give very broad lines even for angles as small as 1° - 5° , which is not observed experimentally. Instead, librational rates, k_l , on the order of 10^5 - 10^6 for both R_2ND and R_3ND^+ deuterons provide adequate fits for $T < 20$ °C. At these temperatures the values show almost no temperature dependence, which is expected behavior for librational motion [54, 105]. Therefore, the unusually high activation energies, derived from the relaxation anisotropy analysis for libration at the dendrimer interior at higher temperatures, must be connected with the onset of the glass transition around $T = 21$ °C (Chapter 3). Any extrapolation from the corresponding Arrhenius fits must be confined to the glass transition region for the dendrimers. In addition, the low temperature data allow us to address the question of motional rate distributions, putting strict limits on their width.

The distribution of rates can have major effects on the line width of the MAS side bands, even when the intensity pattern is not greatly affected. The side band intensities depend predominantly on the librational amplitude and site populations. For the low temperature data no distribution is necessary. In fact, any distribution with $\sigma_k > 0.4$ would yield both very narrow and very wide components for the spinning side bands, and this is not observed experimentally. For the high temperature data, the S/N of 2H MAS spectra is insufficient for a quantitative analysis. However, attempts to fit the spectrum at 35 °C with the same rates as derived from T_{1Z} data show that the model is sufficient for R_2ND deuterons (Fig. 4.12, insert). For R_3ND^+ libration, $k_{mp} = k_l \sim 10^7$ s $^{-1}$, derived from T_{1Z} data, produces very narrow side bands which are not present in the spectrum. If instead, k_l assumes a sense of \bar{k} , and $k_{mp} < k_p$, 2H MAS side bands for R_3ND^+ at higher temperatures can be fit with log-normal distributions of increasing width ($0.5 < \sigma_k < 0.8$) and slightly decreasing k_{mp} values. This would also be consistent with the phenomenological correction for finite rate distributions at the temperatures within the broad glass transition region for relaxation anisotropy data of G2 in section 4.3.2 above (Fig. 4.5). As was explained before, the introduction of log-normal distribution was not necessary for the consistent

interpretation of the relaxation data. Nevertheless, ^2H MAS spectra show high sensitivity even to narrow librational rate distributions. The conclusions derived from the analysis of deuteron relaxation and magic angle spinning experimental data are consistent as long as the explanations are based on "average" characteristic parameters derived for the same motional models.

4.5.2 Librational Rate Distribution for Ammonium Termini

For the ammonium termini, interpretation of the MAS spectra (Fig. 4.13) is complicated due to a possible distribution of librational angles, β_c , which can produce changes both in intensities and in side band line widths. However, it is natural to assume that a distribution of hydrogen bond length (as is the case for the branching site deuterons R_3ND^+ , Chapter 3) has been at least partially responsible for the observed 5 kHz line width of the RND_3^+ powder pattern in the quadrupole echo experiments. If the distribution of PAS ammonium quadrupole coupling constants has the same width as for tertiary amine deuterons at the branching points, $\sigma_\chi \sim 8$ kHz, averaging over the fast three-fold rotation, leaves less than 2 kHz width to be accounted for by β_c distribution. Thus, σ_β is at most 5° - 6° . Such a narrow distribution of librational angles can be neglected for MAS spectra interpretation, since $\sigma_\beta > 15^\circ$ is needed to noticeably affect the MAS line width or intensity patterns. Introduction of a hydrogen bonding length distribution, causing the distribution of quadrupole coupling parameters in the principle axes system (PAS), does not influence the line width of MAS spectra. Consideration of two overlapping powder patterns, coming from "fast" and "slow" ammonium rotors, suggested by our previous results, can match the intensity pattern and width for low temperatures ($T < 20$ °C), but introduces double the number of fit parameters. Also, this does not apply to higher temperatures ($T > 35$ °C), where the fraction of "fast" ammonium rotors for G2 is less than 5 % (Table 4.3).

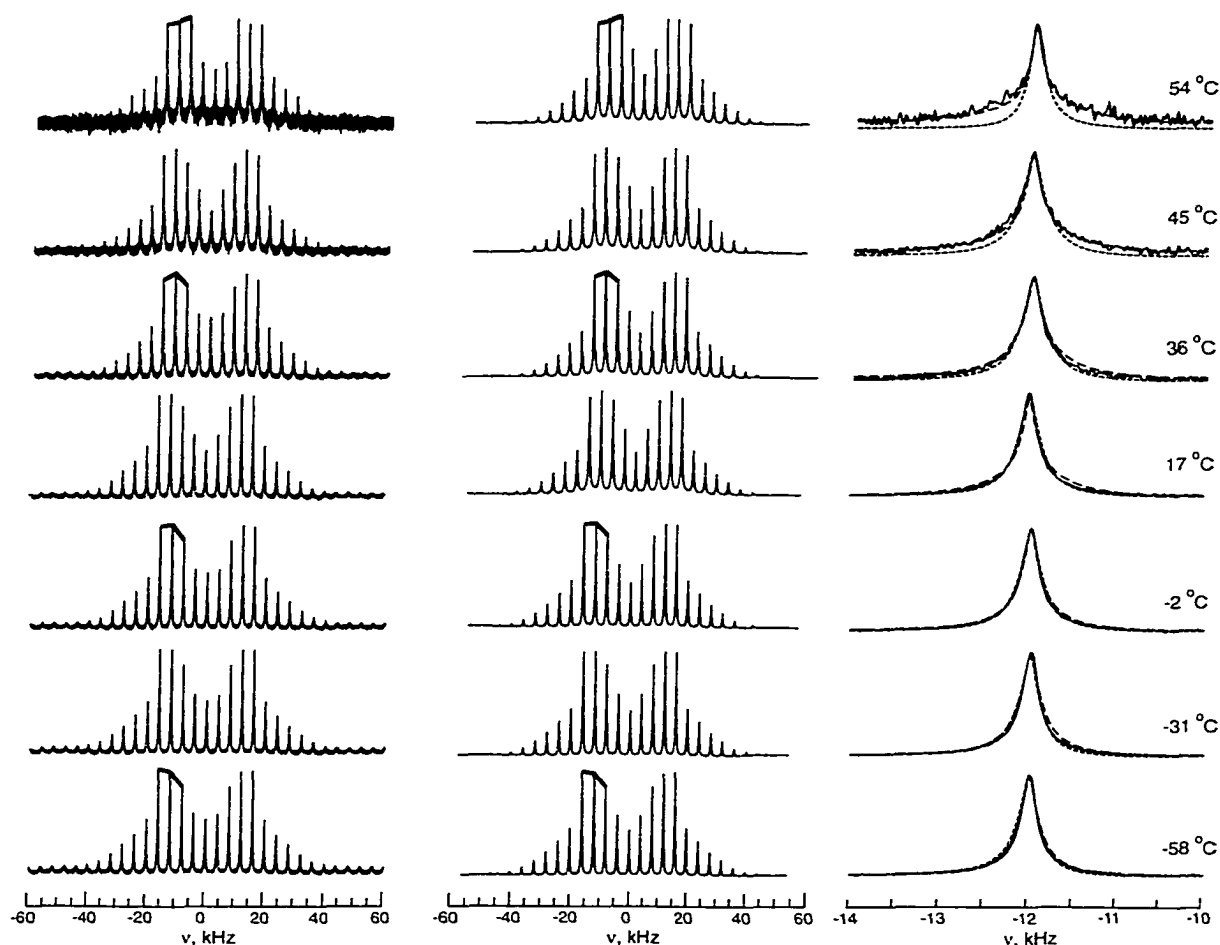


Figure 4.13

Experimental temperature dependent ^2H MAS spectra (left column) and best fits (middle column) for RND_3^+ groups of G2 dendrimer. The right column compares experimentally observed line width for rotation side band of the highest intensity with the simulations assuming zero (short dashes) and finite (long dashes) distribution width for cone libration rates, k_c . All corresponding fit parameters are listed in Table 4.6. The bold line over the left horn of every other experimental and simulated spectrum is shown to illustrate the change in intensity pattern with increasing temperature.

Searching for a single model with the least number of fit parameters to produce adequate fits for both the intensity pattern and the line width of all the temperature dependent MAS data for G2 (Fig. 4.13), we settled on the model of librational motion in an asymmetric cone. The asymmetry is modeled by a high population at one of the cone sites (in accord with relaxation anisotropy simulations). This population difference is essential to reproduce the

intensity pattern around the horns of the RND_3^+ powder pattern. Temperature dependent changes in the intensity pattern across the horns from concave downward to concave upward (see Fig. 4.13, bold lines), and also the change in the line widths, were accounted for by introduction of a log-normal distribution of the librational rates with fixed librational angle, β_c , and unequal cone populations. Without this distribution, reasonably good fits may also be obtained for the low temperature data with a fixed rate $1.6 \times 10^6 \text{ s}^{-1}$, and β_c changing from 30° to 40° . However, for temperatures above $T = 30^\circ \text{C}$, the line width cannot be fit properly (Fig. 4.13, right column) using the single rate model. On the other hand, the three rates sampled from the log-normal distribution as described above ($k_0 = k_{mp}$, $k_{1,2} = k_{mp} \times 10^{\pm\sigma_k}$) were enough to obtain adequate fits for all temperature dependent MAS spectra (Fig. 4.13). The corresponding fit parameters are listed in Table 4.6.

Table 4.6

Best fit parameters for temperature dependent ^2H MAS spectra of G2 PAMAM dendrimer.

$T \pm 0.3, ^\circ\text{C}$	$\beta_c \pm 1, \text{ degree}$	$p_i \pm 0.003$	$k_{mp} \times 10^6, \text{ s}^{-1}$	$\sigma_k \pm 0.02$	$\bar{k}_c \cdot 10^6, \text{ s}^{-1}$
-58.2	33	0.880	1.5 ± 0.1	0.20	2.1 ± 0.5
-30.5	33	0.871	1.4 ± 0.1	0.24	2.2 ± 0.5
-1.6	34	0.874	1.3 ± 0.1	0.33	3.1 ± 0.8
16.7	35	0.877	1.2 ± 0.1	0.37	3.5 ± 0.9
35.7	36	0.871	0.90 ± 0.05	0.48	4.8 ± 0.9
44.9	36	0.862	0.70 ± 0.05	0.62	6.9 ± 1.1
54.4	45	0.892	0.43 ± 0.02	0.91	9.9 ± 0.7

The experimentally derived distributions are plotted in Fig. 4.14. It can be seen that even for such narrow distributions the center of mass is shifted considerably from the most probable rate, k_{mp} , towards higher rates already for $\sigma_k > 0.3$. Therefore, it is really \bar{k} that characterizes the prevailing spin contribution to spectral intensity for the rates distributed according to Fig. 4.14.

The presence of considerable libration rate distributions is confined to the glass transition region of G2 dendrimer. This does not influence the rates of the three-fold

rotation determined from the spin relaxation data. As was pointed in above discussion of relaxation at ammonium termini, a few EXPRESS simulations including the distribution of rotational rates for slow ammonium termini had shown that introduction of k_3 distributions more than 0.5 wide with $k_{mp} = k_3$ worsened the fit for recovery curves across the RND_3^+ powder pattern at 25 °C and 35 °C. With the narrower distributions the contribution of "fast" rotors may still be distinguished at these temperatures, although with higher uncertainty in the rate values. The insert in Figure 4.14 shows that it should be possible to discriminate between "slow" and "fast" rotors only for the reasonably narrow distributions, $\sigma_k < 0.7$. Therefore, the increasing distribution width for the three-fold rates of slow rotors with increasing temperature may be responsible for the "vanishing" contribution of "fast"

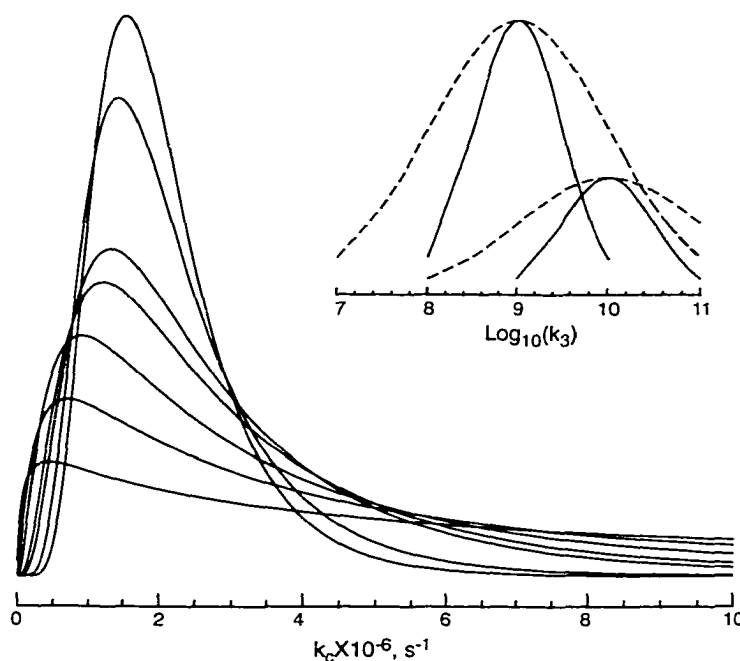


Figure 4.14

Best fit log-normal distributions of cone libration rates, $G(k_c)$, for -58, -30, -2, 16, 35, 45, and 55 °C, temperature increasing bottom to top. The insert shows possible distributions of rotational rates, $G(k_3)$, for RND_3^+ deuterons on a Log_{10} scale assuming 30 % "fast" rotors, $(k_3^f)_{mp} = 10^{10} \text{ s}^{-1}$, $(k_3^s)_{mp} = 10^9 \text{ s}^{-1}$; $\sigma_k = 0.5$ (solid lines) and $\sigma_k = 1.0$ (dashed lines).

rotors in low and high generation dendrimers (Table 4.3). As for the intermediate G3, the distributions were narrow enough to allow quantitative analysis of the temperature dependent rates for the "fast" rotors in the course of the glass transition. It may be connected to the fact that the termini involved in the intermolecular surface network of transition generations are in more uniform environments than the back folded or interpenetrated ammonium groups of high and low generation dendrimers.

4.6 Rate Distribution Evolution During Glass Transition

The distribution width for the rates of termini libration is small for the temperatures below 35 °C, and increases within the glass transition region of G2. In fact, plotting σ_k vs. T (see Fig. 4.15 (triangles), right scale) shows a sharp increase in the width of the distribution in the temperature range between 20 °C and 30 °C. This is the range of the glass transition onset. Therefore, the considerable increase in the distribution width for PAMAM termini libration is correlated with the glass transition in the dendrimer. This seems also be the case for PAMAM interior. The most probable rates, k_{mp} , decrease for higher temperatures. But, as was emphasized above, it is the average rate, \bar{k}_c , that carries information about the prevailing spin contribution to the spectral intensity. The presence of considerable libration rate distribution is confined to the glass transition region of the G2 dendrimer, and does not influence the rates of three-fold rotation determined from spin relaxation data.

The temperature dependence of the average librational rates, \bar{k}_c , for ammonium termini of G2 dendrimer is shown in Fig. 4.15. It is obvious that a single Arrhenius plot is impossible to construct for the full temperature range. However, two temperature regions can be identified where the fits are reasonably accurate. The first is for temperatures below 20 °C, and gives a very low activation energy $E_A = 3.8$ kJ/mol (Fig. 4.15), which is

physically reasonable for librational motion [54, 105]. The other, for temperatures within the glass transition region, shows a much higher slope with $E_A = 32.8$ kJ/mol.

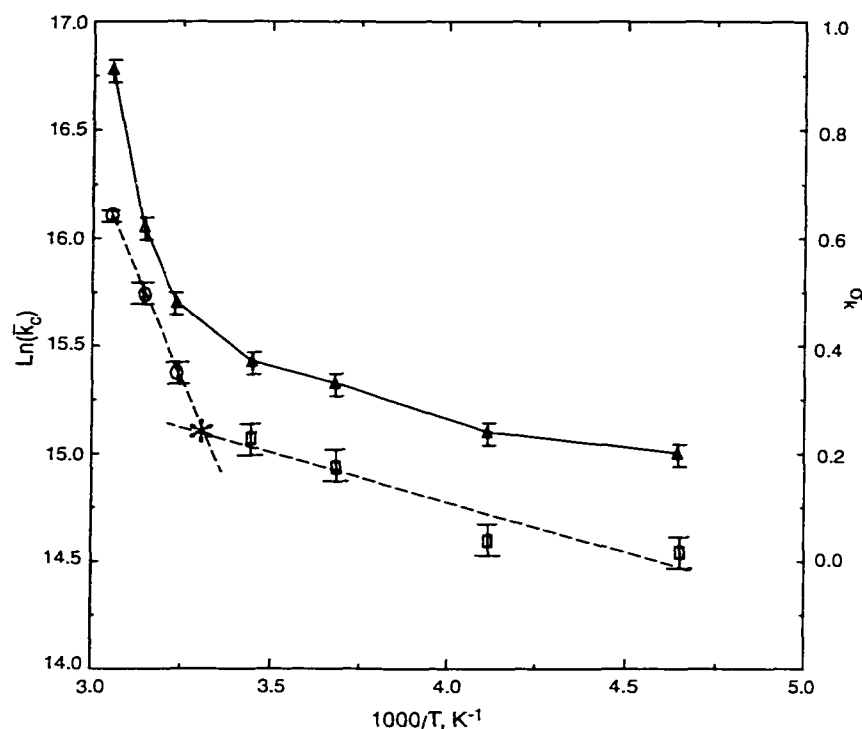


Figure 4.15

Temperature dependence of the rate distribution width (triangles) and average rates of termini libration (squares and circles), and Arrhenius fits (dashed lines, left scale) for the temperatures below T_g (squares, $E_A = 3.8 \pm 0.9$ kJ/mol, $\ln(A) = 16.6 \pm 0.4$) and within the glass transition region (circles, $E_A = 32.8 \pm 0.1$ kJ/mol, $\ln(A) = 28.2 \pm 0.1$), are plotted for G2 dendrimer. The star marks a change in the slope at $T = 27 \pm 1$ °C. The \bar{k}_c rates were calculated for the discrete distributions sampled from 6×10^3 to 3×10^7 with the step 5×10^3 . The solid line for σ_k (triangles, right scale) is drawn to guide an eye. The characteristic distribution parameters were derived from fitting experimental ^2H MAS spectra for G2. The quoted error limits for $\ln(\bar{k}_c)$ are obtained by error propagation from the uncertainties for k_{mp} and σ_k determined from the simulations.

The meaning of the activation energy introduced here is different from that adopted by Wherle, *et.al.* [121], where it was associated with k_{mp} rather than \bar{k} . However, the association of the observed activation energy with the average instead of the most probable rate carries more physical sense for highly skewed log-normal distributions. It is interesting that the

approximate point of change in the slope ($T = 27\text{ }^{\circ}\text{C}$) is very close to the onset of the glass transition ($T = 21\text{ }^{\circ}\text{C}$) for G2 determined from DSC data. Therefore, it can be argued that the observation of unusually high librational activation energies is connected with the glass transition.

This is supported by MAS and T_{1z} data for interior deuterons discussed above. It seems reasonable to conclude that for $R_2\text{ND}$ deuterons the distribution of rates (if any) stays narrow with the increasing temperature. So, the k_{mp} values stay close to \bar{k} or at least have the same temperature dependence since the distribution skew does not change much with the temperature. On the other hand, the motional rate distribution width increases slightly for $R_3\text{ND}^+$ libration (up to $\sigma_k = 0.6\text{--}0.8$ within the glass transition region). The difference in behavior of librational rate distribution width with increasing temperature for deuterons at the branching points, $R_3\text{ND}^+$, and spacers, $R_2\text{ND}$, suggests that chlorine anions associated with deuterated branching points are at least partially responsible for increasing σ_k in the course of the broad glass transition. The activation energies derived from T_{1z} data are associated with \bar{k} . Like for the PAMAM termini, the observation of thermally activated libration in the dendrimer interior is confined to the glass transition region.

Finally, it should be stressed that both relaxation anisotropy and ^2H MAS experimental results rule out any broad distribution, $\sigma_k > 1$, of motional rates for solid dendrimer salts. Thus, solid PAMAM dendrimers behave very differently from linear glassy polymers [121] or dendrimers in solution, where at least three-decade distributions have been reported [35, 36].

4.7 Conclusions

A detailed description of procedures for deconvolution of model dependent spin relaxation anisotropies in unselectively labeled solid dendrimers is provided in application to

PAMAM salts. Advantage is taken of complementarity of the SUMS, EXPRESS and MAS simulation packages to considerably speed up deuteron dynamics characterization for these complex polymeric systems. Quantitative description of motional parameter distributions is achieved for interior and surface regions of solid dendrimers. Multi-exponential deuteron relaxation behavior of PAMAM salts has been analyzed as a sum of contributions from branching R_3ND^+ , spacer R_2ND and terminal RND_3^+ deuterated sites. The site geometry, rates, distributions, and activation energies of each motion has been determined for low and high generation dendrimers.

Analysis of librational motion at the spacer R_2ND sites reveals similarities in the mobility of these sites for low and high generation molecules. This rather surprising result is ascribed to the stabilization of N-D...O hydrogen bonds by interpenetration of extended dendrimer arms for low generation dendrimers and backfolding of arms for high generation materials. Librational motion, $k_l \sim 10^5-10^6 \text{ s}^{-1}$, involves breaking the hydrogen bonds between neighboring branches. According to [106], the derived value for activation energy of spacer libration ($E_A \sim 44 \text{ kJ/mol}$) reports that each spacer is involved in ~ 1.5 hydrogen bonds. The thermally activated libration is confined to the glass transition region. The rate distributions at amide sites are absent at lower temperatures and very narrow, $\sigma_k < 0.4$, for $T > T_g$. Analysis of spin relaxation time anisotropies confirms the presence of extensive hydrogen bonding network. However, static lineshapes and anisotropies do not unambiguously distinguish intramolecular from intermolecular association of the secondary amide spacer units. Intra- and inter-molecular hydrogen bonding and dynamics has been found to be similar at spacer sites of low and high generation materials.

For R_3ND^+ deuterons, the analysis is complicated by fluctuating intermolecular field gradients arising from nearby chloride ions. Nevertheless, this motion is adequately modeled by equally probable jumps among all orientational sites on an arc with $k_l \sim 10^6-10^8 \text{ s}^{-1}$. For these sites, we believe that during glass transition the observed decrease in activation energy with increasing generation number is due to a decrease in the probability of breaking

hydrogen bonds between ND^+ groups and nearby Cl^- ions. This is consistent both with intramolecular backfolding for high generation dendrimers and interpenetration of neighboring molecules for $G < 3$. The presence of chloride anions results in broader rate distributions, $0.5 < \sigma_k < 0.8$, within the glass transition region, compared to those of amide deuterons. The study of dynamics at branching R_3ND^+ sites reveals generation dependent contributions from fluctuating electric field gradient tensors caused by nearby chloride anion motion. In general, the anions act to increase relaxation efficiency. Therefore, such materials (especially low generation salts) may be useful for imaging applications [33], where increasing relaxivity of medium with contrasting agents is an issue.

Two fractions of rotating RND_3^+ groups, distinguished by approximately ten-fold different rotation rates, are found for all dendrimer generations. The fact that both fractions are observed for all generations supports the idea that the local environment of extensively interpenetrated arms of low generation dendrimers is similar to that of backfolded arms of high generation materials. The unique behavior of motional parameters for G3 indicates that, in the solid, its configurations and internal dynamics are determined by a nearly equal balance between intramolecular backfolding and intermolecular association of extended dendrimer arms. The latter allows relatively stable intermolecular surface networks to form in solid dendrimers. Results reported here are in agreement with molecular dynamics simulations [37], which predict a structural transition to a more compact backfolded architecture for dendrimer generations $G \geq 3$. On the other hand we have found no indication of dense shell formation in solid dendrimers of either low or high generations, which is more consistent with a kinetic model [40]. Simulations performed here reveal different environments for surface and constrained termini, which is especially well pronounced for the “transition” generation G3. Such transition generations, being capable of surface network formation, might be more effective as sequestering agents [32].

^2H MAS lineshapes provide quantitative information about librational motion in solid PAMAM dendrimers, which is not accessible either from quadrupole echo or Zeeman

relaxation time experiments. In particular, it is possible to characterize log-normal librational rate distributions at all major dendrimer sites: branching points, spacers and termini. Taking into account the motional rate distributions also produces better fits for experimental Zeeman recovery curves. ^2H MAS data support the validity of the motional models used for the analysis of temperature dependent quadrupole echo lineshapes and relaxation anisotropies. The onset of temperature activated librational motion and the sharp increase in librational rate distribution width coincide with the onset of the glass transition. This suggests that dry dendrimers below their T_g possess highly uniform intra- and inter-molecular environments, in agreement with a kinetic dendrimer growth model [40]. The fact that in solid PAMAM dendrimers the distribution width is more strongly temperature dependent for the branching and terminal sites (with associated chlorine anion) demonstrates the sensitivity of dendrimer glass transition dynamics to the presence of foreign inclusions.

In distinct contrast to solution studies [35, 36], narrow distributions of structural and dynamic parameters are observed in solid dendrimers of all generations. Despite the tendency of low generation dendrimers to adopt open, quasi-planar structures in solution, the rates and amplitudes of local segmental motion in solid dendrimers are very similar for low and high generation materials. This implies that dynamic constraints on highly backfolded arms in high generation dendrimers are very similar to those found for strongly interpenetrated arms in low generation materials.

Chapter 5

REDOR Experiment and Analysis Optimization

Rotational-Echo Double-Resonance (REDOR) experiments on dendrimers have the potential to unequivocally distinguish between inter- and intra-molecular distances [57]. This would not only provide quantitative distance information, but also allow unambiguous correlation to be established between generation dependent morphology and the dynamics revealed by spin relaxation measurements. Considering the complexity of the system, the proper isotopic labeling strategies and experimental conditions should be carefully preplanned to reduce the significant cost and time of the experiments. Experimental conditions can be optimized in advance, based on acquired knowledge about structural and motional parameter distributions in the dendrimers as well as REDOR measurements on model compounds.

This chapter presents the general REDOR optimization scheme both for the experiment and data analysis. First, amide-carbonyl distances are estimated, on the basis of hydrogen bond geometry and above mentioned quadrupole coupling measurements, to substantiate the proper labeling strategies. Next, ways to enhance sensitivity of the experiment to the long distances ($> 3 \text{ \AA}$) anticipated are discussed. The following section develops an algorithm for

structural parameter distribution extraction from the calculated dephasing curves, which puts limits on experimental resolution. Finally, measurements performed on the doubly labeled model compounds are analyzed to describe hardware capabilities and limitations in a triple resonance mode. The highlighted points are relevant to long distance REDOR measurement with available equipment.

5.1 Planning REDOR for PAMAM Dendrimers

Chemical structure of the polyamidoammonium dendrimer salts suggests that possible REDOR options involve dipolar coupling measurements between carbon, nitrogen and/or deuteron in pairs. The least demanding technically and analytically is ^{13}C - ^{15}N REDOR. If we choose to label the carbonyl carbon, we can benefit from the knowledge acquired from ^2H NMR measurements of hydrogen bonding [4] and motion [5] at the dendrimer spacer amide sites.

5.1.1 ^{13}C - ^{15}N Distance Estimation

Typical geometries of amide and carbonyl sites [118] are determined by chemical bonds within the molecules and should not deviate much for dendrimers. Thus, assuming no isotope effect, if carbon and nitrogen are in a line with $r(\text{D}\cdot\text{O}) = r(\text{H}\cdot\text{O})$, which is no more than 2.3 Å (quadrupole constant measurements), the maximum possible separation between C and N labels, involved in amide hydrogen bonding among the dendrimer branches, will be $r(\text{C}\cdot\cdot\text{N}) = r(\text{C}\text{-O}) + r(\text{H}\cdot\text{O}) + r(\text{N}\text{-H}) = (1.2 + 2.3 + 1.0)$ Å. Here, solid "dash" marks the actual chemical bond. However, hydrogen bond energy minimization and atomic electron orbital geometry usually requires that C-O..H-N departs from linearity [106]. It is established that the oxygen lone electron pair acts as a proton acceptor in the amide hydrogen bond and is

oriented at 120° with respect to C-O. As to the amide proton donor, in most cases, e.g. in polypeptides, $\angle\text{N-H}\cdots\text{O}$ angle is found to deviate from 180° by $10\text{-}30^\circ$ at most [106]. If nitrogen lone pair gets oriented towards carbonyl carbon, this deviation may rise to 60° . Thus, in case of PAMAM dendrimers simple geometric considerations show that the largest expected distance will be 4.04 \AA (when $\angle\text{N-H}\cdots\text{O} = 180^\circ$), while the shortest is 3.40 \AA ($\angle\text{N-H}\cdots\text{O} = 120^\circ$) (Fig. 5.1).

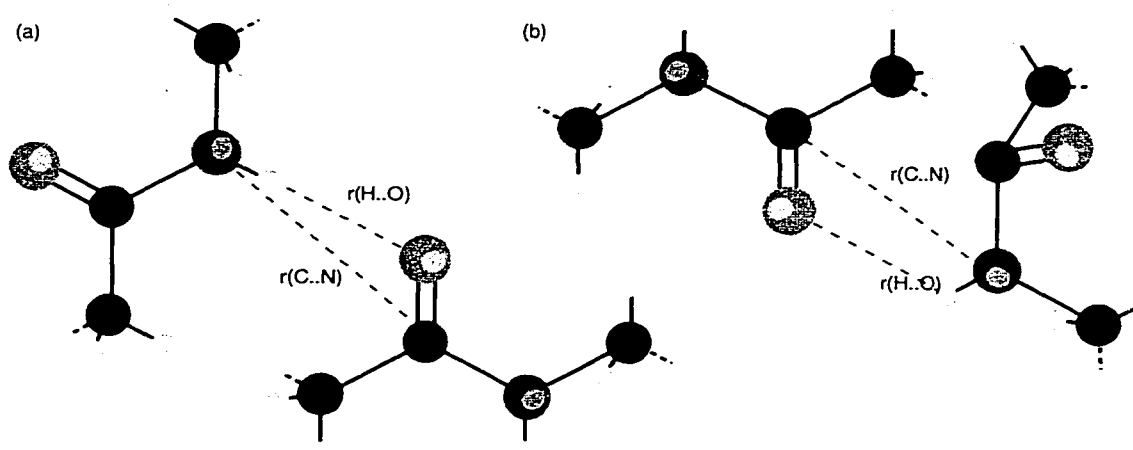


Figure 5.1

Two limiting hydrogen bond length geometries between the dendrimer branches: (a) $r(\text{C}\cdots\text{N}) = 4.04 \text{ \AA}$; (b) $r(\text{C}\cdots\text{N}) = 3.40 \text{ \AA}$.

Shorter distances are more plausible for highly crowded solid dendrimer molecules. It is known that larger deviations from N-H \cdots O linearity are expected when the same amide is involved in two hydrogen bonds [106] (both carbonyl and its chemically bonded nitrogen participate). The activation energies of fast libration at the spacers (see section 4.4.3) indicate that the average number of hydrogen bonds for each dendrimer spacer amide is 1.5. This is also evidence of shorter C \cdots N distances.

5.1.2 Isotope Labeling Strategy

To characterize the change in the dendrimer morphology with increasing generation number, at least three REDOR experiments are needed. For low generation materials the evidence of molecular interpenetration can be obtained by studying a mixture of singly labeled molecules: one part with ^{13}C labels, and another with ^{15}N labels. The same can be done for high generation dendrimers to ensure that no interpenetration is present. Since the ethylene diamine required for PAMAM synthesis can be obtained only with both nitrogens labeled, the N-labeled sites may be either terminus and spacer or spacer and branching point of the same branch. To check for the depth of interpenetration, carbonyl labels should be placed close to the dendrimer core (at G0 or G1), and the nitrogen labels either on the last or one before last step of the divergent synthesis. To exclude intramolecular couplings between labels, the labeled material should be diluted at least to 30-40% in natural-abundance compounds. Of course, this will limit the experimental sensitivity. The problem of coupling between two nitrogen labels on the same branch, which would violate the "single spin pair" approximation, should be alleviated by the three-bond separation. On the other hand, sufficient ^{15}N chemical shift resolution may allow measuring the distances to carbonyl from each nitrogen separately in a N-observe, C-dephase REDOR. In all N-observe experiments the contribution of directly bonded natural-abundance methylene and carbonyl carbons has to be calculated from the known chemical bond distances, and subtracted.

To characterize intramolecular backfolding in high generation materials, the same molecule should be labeled with carbonyl at certain generation (close to the core), and with nitrogens at or close to the termini. These doubly labeled molecules would have to be diluted with natural-abundance dendrimers, this time to exclude intermolecular C-N couplings. For intermediate generation, both backfolding and interpenetration can be tested as described above. In addition, the termini network formation can be probed if the REDOR is performed on mixture of molecules: one part fully labeled with nitrogen at the termini, and another -

fully labeled with carbon at the last generation. Here the contribution from coupling between carbonyl carbon and ammonium nitrogen may have to be calculated (or estimated from the preceding measurements) and subtracted from the experimental data if C-observe experiment is chosen. In other words, two separate couplings can be determined.

5.1.3 Observation of ^{13}C versus ^{15}N

For generation 2 dendrimer, ^{13}C , ^{15}N CP MAS experiments performed on the C, N natural-abundance deuterated sample (Fig. 5.2) establish the limits for resolution, optimum

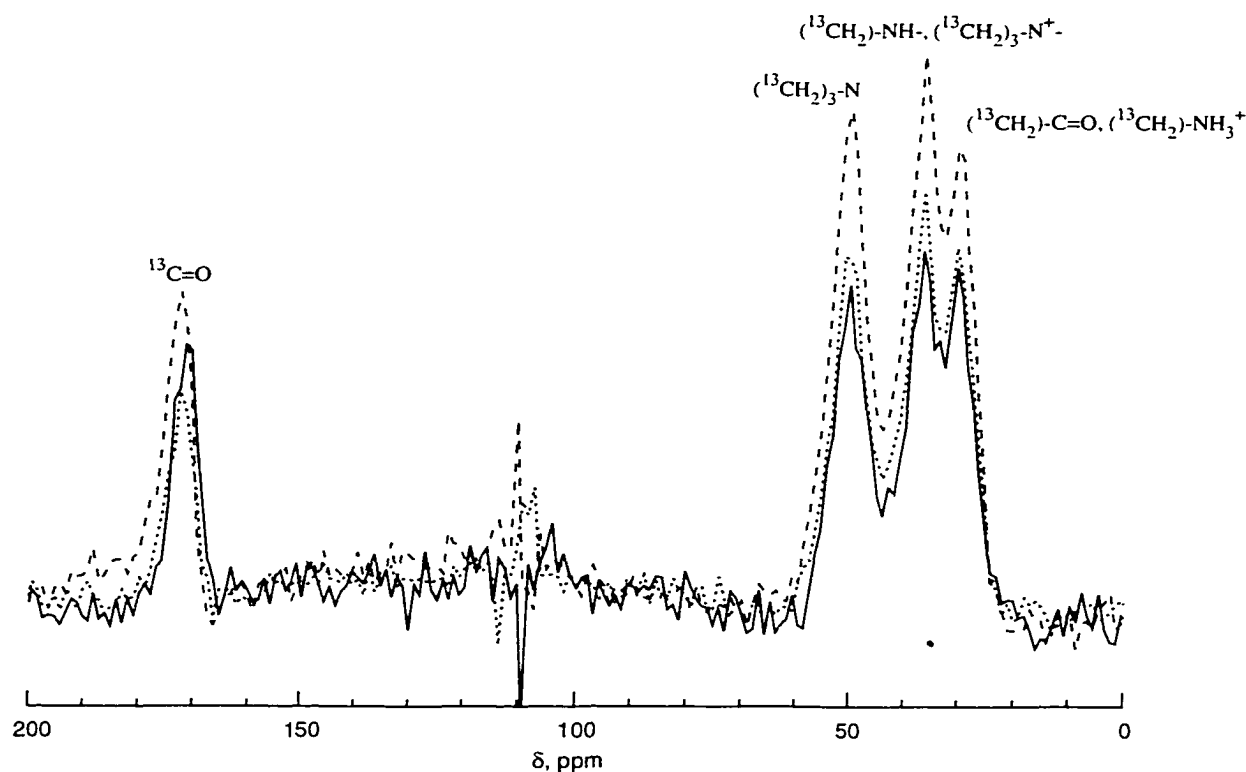


Figure 5.2

CP MAS ^{13}C experimental spectra of the deuterated G2 PAMAM dendrimer. The data acquired with $3.5 \mu\text{s}$ 90° proton pulses, 20 kHz SW, 512 acquisition points, $\nu_r = 4$ kHz, and 1050 transients. Solid line – $T_r = 5$ s, $\tau_{\text{CP}} = 1$ ms; dashed – $T_r = 10$ s, $\tau_{\text{CP}} = 0.5$ ms; dotted – $T_r = 5$ s, $\tau_{\text{CP}} = 0.5$ ms. The chemical shifts are referred to TMS. Assignments are done on the basis of chemical shift correlation to environment [63] and liquid state NMR measurements for carboxyl terminated dendrimers [36].

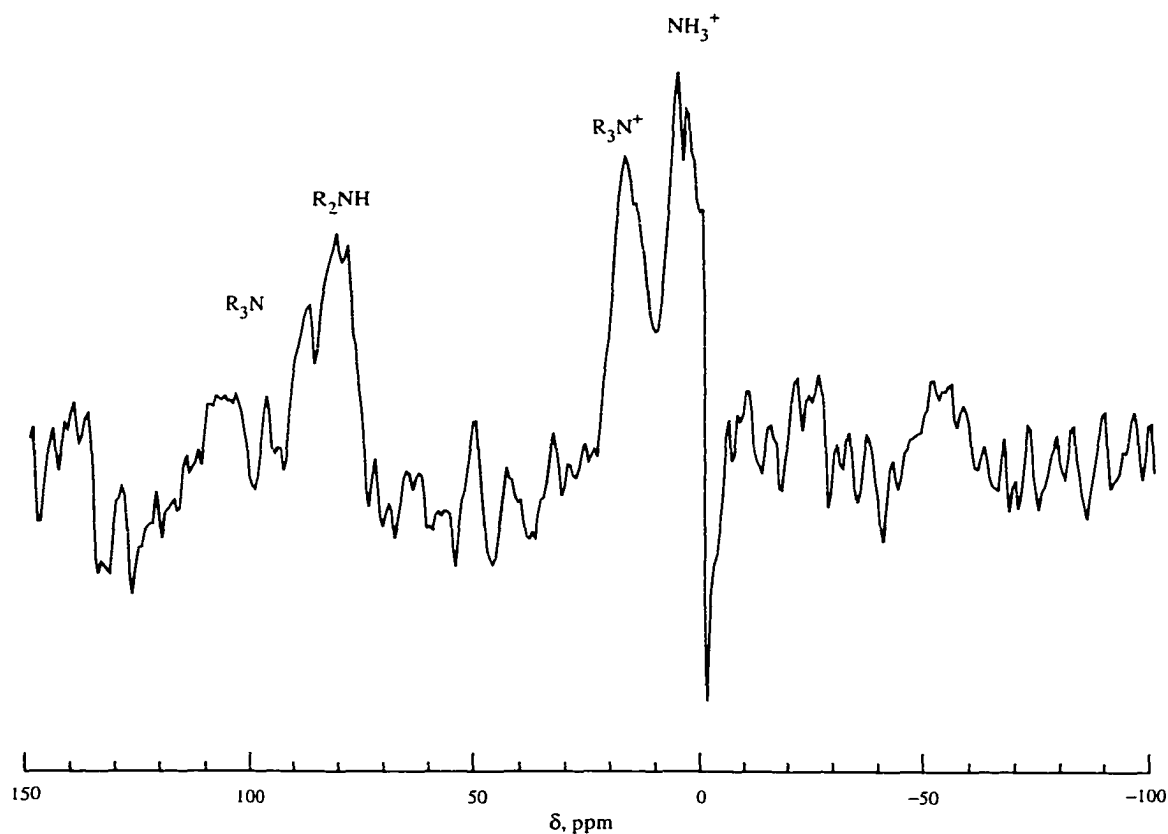


Figure 5.3

CP MAS ^{15}N experimental spectrum of the deuterated G2 PAMAM dendrimer after 50 Hz exponential apodization. The data acquired with $5\ \mu\text{s}$ 90° proton pulses, 10 kHz SW, 1024 acquisition points, $\nu_r = 4\ \text{kHz}$, $T_r = 3\ \text{s}$, $\tau_{\text{CP}} = 2\ \text{ms}$, and 35240 transients. The chemical shifts are referred to glycine. Assignments are done on the basis of literature chemical shifts of similar monomeric materials [63, 132, 133], and liquid state NMR measurements for poly(propylene) imine dendrimers [60].

cross polarization and recycle delays. The most efficient cross polarization is achieved at 0.5 ms for the methylene carbons, and at 1 ms for the carbonyl. Relative intensities of the peaks in the methylene region suggest incomplete protonation (~40 %) at the branching sites, though quantitative conclusion is not possible due to interfering effect of the cross polarization from protons. Contributions from the carbonyl carbons of interior and termini overlap. Although selective labeling should increase spectral resolution, such overlap still may require that for proper correction for natural-abundance in C-observe REDOR the

contribution from the unlabeled carbonyl throughout the whole molecule should be subtracted. The fact that full intensity in the ^{13}C CP MAS spectrum requires relaxation delays longer than 10 s (see Fig. 5.2, dashed lines) implies long experimental times for REDOR measurements.

Poor signal-to-noise ratios observed in ^{15}N CP MAS experiment (Fig. 5.3) did not permit determination of the optimum cross polarization and relaxation delays. However, the spectra do show relatively high resolution. In principle, there is a possibility to detect amide nitrogens separately from the nitrogens of the termini and branching sites. The low S/N of ^{15}N natural-abundance spectra compared to carbon is caused by the three times lower natural-abundance of ^{15}N isotope, as well as by the absence of directly bonded protons (exchanged for deuterons), and long relaxation delays needed for methylene protons. Still for the undeuterated ^{15}N labeled sample, the spectral resolution will be better than for ^{13}C labeled carbonyls. Smaller spectral width is required. However, long recycle delays may be needed, and more scans must be acquired to ensure appropriate S/N ratios for N-observe REDOR.

5.2 Long Distance Measurement with REDOR

The need to measure long (3.5-4.5 Å) C..N distances with REDOR frequently arises in peptide studies [134-136]. Because of this, much experience is gained in predicting and solving the problems related to equipment limitations [137-139], natural-abundance contribution [134, 135, 140, 141], and low sensitivity of REDOR to the corresponding dipolar couplings $D < 100$ Hz [134-136, 140]. Summarizing this experience and evaluating it for the available experimental equipment and the particular system under investigation is the most important preparatory step.

5.2.1 Reduction of Artifacts

Due to small dipolar coupling values associated with both long internuclear distance and low gyromagnetic constants for nitrogen and carbon, long times are required to achieve noticeable REDOR dephasing in experiment. For example, if $D = 100$ Hz, only 20 % dephasing would be observed after 5 ms, corresponding to 25 rotor cycles when spinning at 5 kHz. To accumulate a few more experimental points of efficient dephasing or reach universal REDOR curve oscillations [137] we need to go even longer in time. Therefore, long distance measurements require struggling with low signal-to-noise (due to considerable T_2 effects at long dephasing times), ensuring efficient and stable long-time proton decoupling, perfect dephasing and refocusing pulses, and stable rotor spinning.

Since the train of pulses in a REDOR experiment is applied synchronously with sample rotation, it is important to maintain the spinning speed stable during the experiment. Otherwise, phase distortion and echo reduction may be observed. Accuracy of ± 2 Hz is usually enough [137] and can easily be achieved with available feed-back LED fiber optics spin rate controllers, providing the pressure of the bearing gas does not oscillate much during the experiment. It is also crucial that the bearing gas be clean and moisture free.

Pulse imperfections (< 10 %) coupled with even small (< 0.5 kHz) carrier frequency offsets may cause severe experimental problems and lead to uninterpretable REDOR results [137, 142]. Sometimes it is useful to have the carrier frequency offset up to a few kHz off resonance to avoid electronics or grounding noise interference with the data. Also the carrier frequency may drift for a few hundred Hertz during the experiment. For a long train of pulses of the same phase, such errors are intolerable. The problem with imperfect pulses of the same phase is that they can preserve only one projection of magnetization, while scrambling the others, and affecting the system Hamiltonian. Fortunately, this problem is solved easily by application of XY-8 phase cycles $(xyxy\ yxyx)^n$ [143], which preserve all three magnetization components, even for carrier offsets as large as ± 7 kHz [137]. This

phase cycle may be incorporated in the Tecmag pulse sequence of both "observe" and "dephase" channels in a loop over eight pulses (Fig. 5.4). With this, increasing dephasing time is achieved by increasing the loop number without affecting the phase cycle. The timing of the loop start and end should be carefully adjusted to ensure equal delay between all pulses. Otherwise, phase errors will accumulate over long runs. Since all π -pulses are of finite length, the middle point of the pulse is to be synchronized with the rotor.

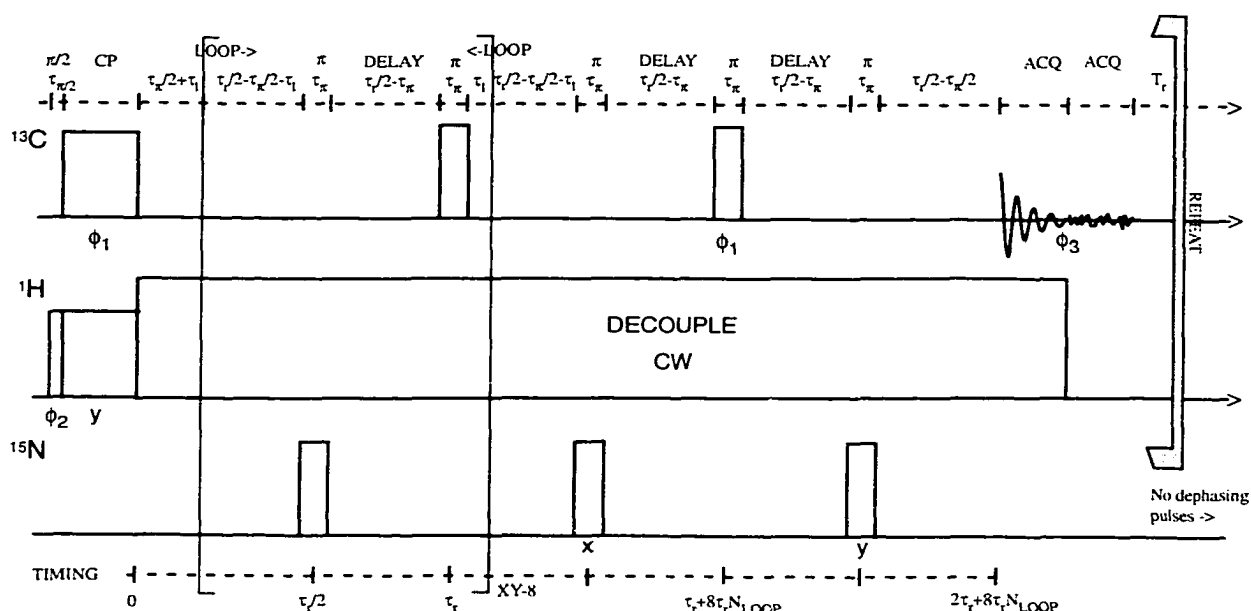


Figure 5.4

The pulse sequence for REDOR experiment with one dephasing and refocusing pulse per rotor period. Pulses are applied independently to ^{13}C , ^1H and ^{15}N nuclei. Proton magnetization is transferred to carbons by applying two RF pulses simultaneously at ^{13}C and ^1H resonance frequencies during the contact pulse (CP). The carbon signal is observed, while high power proton decoupling is used to average the ^{13}C - ^1H dipolar couplings. Then another acquisition is done with no decoupling. The decoupler also averages ^{15}N - ^1H dipolar couplings during ^{15}N dephasing pulses. The reduced echo experiment is followed by a full echo measurement with the same timing, but no dephasing pulses. ϕ_1 marks the phase of the pulse in ^{13}C spin echo sequence phase cycle during the transient acquisition. τ_1 stands for the length of "loop event"; τ_π - π -pulse length; τ_r - rotor period; T_r - recycle delay.

The reduction of π pulse strength imperfection up to $< 2\%$ can be achieved by precise setting of the 2π -pulse length (to $< 4\%$) in a 2D tuning experiment. The corresponding

pulse sequence is shown on Figure 5.5. This pulse sequence [144] has a big advantage in sensitivity over the simple "one pulse proton decoupled" (OPPD) sequence due to the involvement of proton magnetization sink. Therefore, it can be applied directly to the diluted sample (< 10 % labeled material) under investigation to determine precise power levels for dephasing and refocusing pulses in a short time. For comparison, the experiment required to set the levels with the same precision using OPPD would be approximately 10 and 20 times longer in case of ^{13}C and ^{15}N respectively.

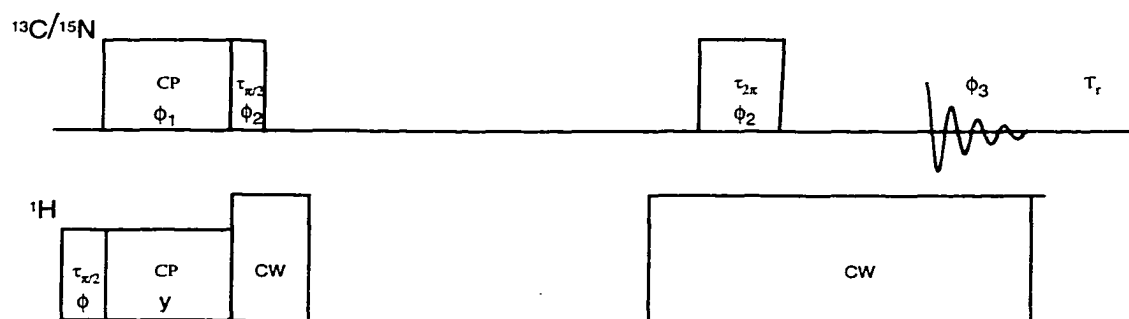


Figure 5.5

π -pulse length tuning sequence for ^{13}C or ^{15}N . The cross polarization from protons is followed by $\pi/2$ -pulse on the observed nucleus. Magnetization is then allowed to dephase under dipolar coupling to protons for 10 ms. This is followed by the application of 2π pulse, which length is set properly, when the acquired signal is zero.

Amplitude and phase fluctuations due to electronic instabilities can still occur during long experiments. This is unavoidable for low S/N ratios and long recycle delays. Since the experimental universal REDOR curve is calculated from the ratio of two experimental signals (w/dephasing and wo/dephasing), fluctuating electronic instabilities cancel in the ratio if both experiments are performed back-to-back on each scan. With this in mind, in a single pulse sequence two data sets (of full and reduced intensity) are accumulated (Fig. 5.6). After Fourier transformation of each data set the total intensity coming from the observed labeled site is calculated, including side bands when present. The ratio of the total intensities for full and reduced echoes for each multiple of rotor cycles provides a data point

on the dephasing curve. Repeating the experiment several times helps to determine error bound statistics.

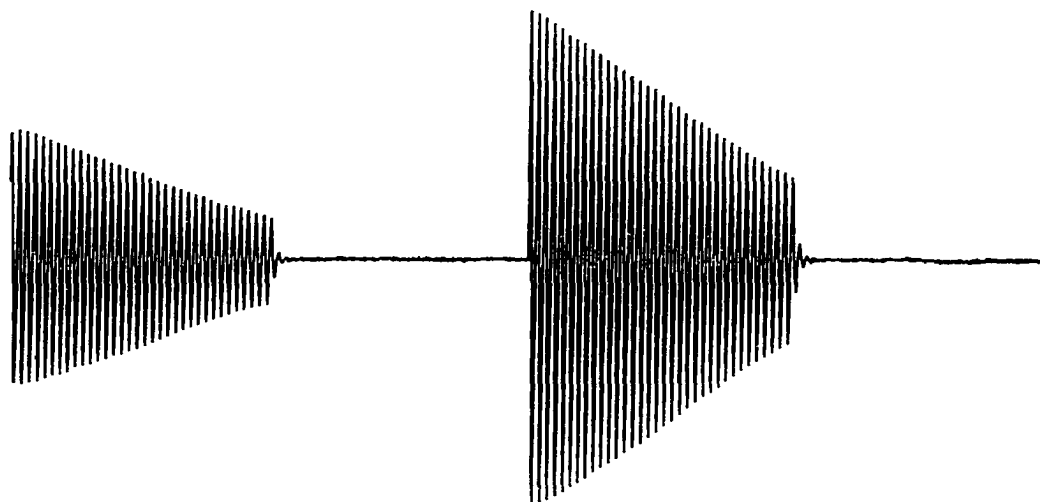


Figure 5.6

Experimental free induction decay signal observed for 10% doubly labeled $1\text{-}^{13}\text{C}\text{-}^{15}\text{N}$ glycine after 18 rotor cycles of REDOR dephasing according to the pulse sequence in Figure 5.4. $\tau_{\text{CP}} = 2$ ms, $T_r = 2$ s, 128 transients, 5.12 acquisition points, SW = 20 kHz. Reduced echo is acquired first. Each echo signal acquisition is followed by a calibrating acquisition with no proton decoupling.

5.2.2 Proton Decoupling

Proton decoupling in REDOR experiments involves an inevitable compromise between high power (reducing linewidths and improving sensitivity) and long acquisition times (which severely strain the triple resonance probe circuitry). The safe upper limit for the length of proton decoupling time in our Chemagnetics probe is 100 ms. Therefore, to get points at longer dephasing times we must reduce the acquisition time. This is achieved either by increasing the spectral width (and introducing more noise to the spectra), or by decreasing the number of acquisition points (and losing spectral resolution). Even with such sacrifices, we are not able to observe more than two oscillations in the dephasing curves for long distances.

Going to dephasing times longer than 50 ms does not necessarily bring more information because for these times T_2 reduces S/N considerably. Moreover, prohibitively long experiments would be required to obtain such data. In fact signal-to-noise reduction makes it very difficult to observe REDOR even after 20-30 ms dephasing time. In principle, the narrower the spectral line at the labeled site, the longer REDOR can be observed.

The line width depends on the strength and homogeneity of the external magnetic field. In our spectrometer the 7.048 T field is strong enough, while good homogeneity is achievable through shimming. Also, the T_2 line width can be efficiently reduced by application of strong proton decoupling fields, especially when the observed nucleus has directly bonded protons [138, 139]. In fact, the line width of the observed nucleus is proportional to the square of decoupler offset and inversely proportional to the square of the decoupling field [145]. In addition, providing decoupling fields much stronger than cross polarization (or proton $\pi/2$ fields) reduces REDOR artifacts, which may be caused by back cross polarization during dephasing and refocusing pulse application [138, 139]. In effect, this changes the T_2 of reduced and full echo signals in different ways, so that contributions no longer cancel in the ratio S/S . For long REDOR sequences this may account for 10-20 % reduction in experimental dephasing compared to the theoretical.

Most commercially available triple resonance probes do not allow application of strong pulses in the proton channel. For example, the safe limit of decoupling field strength for our Chemagnetics 5 mm triple resonance probe is < 75 kHz (corresponding to < 18 G). At this field and less than 1.0 kHz proton resonance frequency offset, the observed lines are up to 40 % wider than at 110 kHz decoupling field [137]. The low decoupling field is also too close to the cross polarization field applied (usually ~ 50 kHz). When high decoupling fields are not available, this problem can be alleviated by observing nuclei not directly bonded to protons (e.g. carbonyl carbons), decreasing the number of refocusing pulses in the "observe" channel, and increasing decoupling efficiency by introduction of special phase cycles in the proton channel [138, 139].

Since efficient proton decoupling is an issue in many branches of solid state NMR, phase cycles are already available [138, 146, 147]. The TPPM phase cycle is based on application of a train of two pulses $P\bar{P}$ ($P = 165^\circ$) with phases 10° and -10° respectively instead of CW decoupling. SPINAL sequences use $Q\bar{Q}$ combinations, where $Q = 165(10^\circ)165(-10^\circ)165(15^\circ)165(-15^\circ)165(20^\circ)165(-20^\circ)165(15^\circ)165(-15^\circ)$, and for \bar{Q} the phase signs are opposite. The most efficient SPINAL sequence is SPINAL-64 = $(Q\bar{Q}\bar{Q}Q\bar{Q}Q\bar{Q})^n$ [147]. The latter is not easily implemented with Tecmag hardware, synchronized in all channels. Its introduction into dephasing loops would produce very long pulse sequences. Unfortunately, decoupler phase alternation during acquisition is completely impossible with Tecmag Libra. However, the TPPM phase cycle can still be incorporated to compensate at least for 10-15 % reduction in dephasing efficiency [138].

5.2.3 Natural Abundance Correction

Even for perfectly tuned and performed REDOR experiments there is an important intermediate step in data processing that must be performed before any quantitative internuclear distances can be derived. This involves a correction for natural-abundance contributions to the observed dephasing. In the general case, these include contributions from both enriched and non-enriched components in mixture [137]. There also may be an interference from the spins in neighboring molecules. If the observed line in the spectrum overlaps with natural-abundance signals from other chemically different sites, their contribution must also be calculated. Using multiple labels at different sites, and mutually subtracting experimental data for such compounds, may help to suppress natural-abundance background [134, 140], but this considerably increases the cost of investigation.

The general scheme for natural-abundance correction calculation [137] can be illustrated by an example. Let us consider the system where the observed nucleus A1 is coupled to B1

and its resonance frequency overlaps with the resonance for A2, whose distance from B1 is known. Then the observed REDOR difference signal is

$$\Delta S = \Delta S_1 + \Delta S_2 \quad [5.1]$$

and the measured universal REDOR curve data points are

$$\Delta S/S = \Delta S_1/S + \Delta S_2/S \quad [5.2]$$

where S is the full echo signal. The fraction of isotopically labeled spins at A1 position with B1 neighbors is $\alpha = S_1/S$, and the fraction of natural-abundance A spins at the A2 position with B1 neighbor is $\beta = S_2/S$. These factors are determined from known isotopic enrichment and dilution in natural-abundance material. Then, substitution in Eq. 5.2 gives the relation

$$\Delta S_1/S_1 = \Delta S/\alpha S - \beta \Delta S_2/\alpha S_2 \quad [5.3]$$

From it the REDOR curve for labeled A1 spins only can be obtained, if β is experimentally determined or known, and $\Delta S_2/S_2$ is calculated (from the known distance) or measured in a separate experiment. Correspondingly, if more A2 resonances overlap at A1 frequency, and the coupling between A2 nuclei can be neglected, the second term in Eq. 5.3 will be a sum over all of them.

When long intramolecular distances are of interest, the contribution of the intermolecular background can either be calculated according to the above scheme (if the X-Ray lattice structure is known) or annihilated by extrapolation to infinite dilution [134, 135]. The latter is achieved when REDOR data (typically 2-4 points) are acquired for a few samples with different percent isotopic dilution. When intermolecular distances are to be measured, the intramolecular contribution from natural-abundance nuclei at known distances to the labeled site have to be subtracted.

If ^{13}C is the experimentally observed nucleus, coupling to natural-abundance ^{15}N sites other than the labeled one can be neglected. Due to higher gyromagnetic ratio the sensitivity in the ^{13}C frequency domain is better than with ^{15}N observation. Unfortunately, resolution is

seldom good enough, and many peaks from morphologically or chemically distinct natural-abundance sites may overlap at the observed frequency. In cases when the distances between them and the ^{15}N label are not known (as for natural-abundance carbonyls of unlabeled dendrimer branches), different models must be tried for consistent background correction calculations [141]. Otherwise their contribution may produce large experimental errors in determination of long internuclear distances. On the other hand, observation of ^{15}N signals usually involves relatively narrow well resolved lines from chemically and morphologically different sites [63, 132, 133]. Even at moderate spinning speeds, $\nu_r < 3$ kHz, chemical shift anisotropies are averaged for most nitrogens. The chemical shift range is smaller than for ^{13}C , and 5-10 kHz spectral width is sufficient to record all chemically inequivalent nitrogens in PAMAM dendrimers. Natural-abundance overlap, if any, can be neglected due to the very low percent of isotopes involved. However, because of the relatively high percent of natural-abundance ^{13}C , many couplings to the carbons with shorter internuclear distances may interfere with the measurement of the distance to a remote site, producing large experimental errors.

5.3 Universal REDOR Curve Calculation

5.3.1 Phase Accumulation

As was shown in previous sections, the reduction of pulse imperfection artifacts in REDOR experiments with a large number of dephasing loops requires the application of XY phase cycling schemes. This necessitates equal time delays between pulses. For the general case of n equally spaced pulses per rotor period, τ_r , it is useful to estimate the accumulated phase to predetermine the most efficient experimental conditions. The time delay between pulses should, therefore be τ_r/n . Let us assume that the first pulse is placed at half the delay

between pulses. Although other initial delays are permitted, half-delay is usually preferred for simplicity it renders to phase loop in a pulse sequence.

The anti-derivative of spin pair dipolar frequency (Eq. 2.101), depending on time, and azimuthal, α , and polar, β , angles, which describe internuclear vector orientation within the MAS spinner, is

$$\Phi(\alpha, \beta, t) = \frac{\tau_r}{4\pi} \left(\sin^2 \beta \sin 2\left(\alpha + \frac{2\pi}{\tau_r} t\right) - 2\sqrt{2} \sin 2\beta \sin\left(\alpha + \frac{2\pi}{\tau_r} t\right) \right) = \frac{\tau_r}{4\pi} P(\alpha, \beta, t) \quad [5.4]$$

Then, the phase accumulated over one rotor period

$$\Delta\phi(n) = \pm \frac{D\tau_r}{4} \left(\begin{array}{l} P\left(\frac{\tau_r}{2n}\right) - P(0) + (-1)^n \left[P(\tau_r) - P\left(\frac{\tau_r(2n-1)}{2n}\right) \right] \\ + \sum_{k \geq 1}^{n-1} (-1)^k \left[P\left(\frac{\tau_r(2k+1)}{2n}\right) - P\left(\frac{\tau_r(2k-1)}{2n}\right) \right] \end{array} \right) \quad [5.5]$$

Substituting Eq. 5.4 into Eq. 5.5 and calculating the sum (see Appendix C), we arrive at the general expression

$$\Delta\phi(n) = \pm \frac{D\tau_r}{4} \left(\begin{array}{l} \left[\begin{array}{l} \left\{ (-1)^n - 1 + 0.5 \cos^{-1}\left(\frac{2\pi}{n}\right) \left((-1)^{n-1} + 1 \right) \right\} \sin 2\alpha \\ \sin^2 \beta \left[\begin{array}{l} + \sin 2\left(\alpha + \frac{\pi}{n}\right) - (-1)^n \sin 2\left(\alpha - \frac{\pi}{n}\right) - 0.5 \cos^{-1}\left(\frac{2\pi}{n}\right) \\ \times \left\{ \sin 2\left(\alpha + \frac{2\pi}{n}\right) - (-1)^n \sin 2\left(\alpha - \frac{2\pi}{n}\right) \right\} + 2\delta_{n+} \cos 2\alpha \end{array} \right] \end{array} \right] \\ \left[\begin{array}{l} \left\{ (-1)^n - 1 + 0.5 \cos^{-1}\left(\frac{\pi}{n}\right) \left((-1)^{n-1} + 1 \right) \right\} \sin \alpha \\ -2\sqrt{2} \sin 2\beta \left[\begin{array}{l} + \sin\left(\alpha + \frac{\pi}{n}\right) - (-1)^n \sin\left(\alpha - \frac{\pi}{n}\right) - 0.5 \cos^{-1}\left(\frac{\pi}{n}\right) \\ \times \left\{ \sin\left(\alpha + \frac{2\pi}{n}\right) - (-1)^n \sin\left(\alpha - \frac{2\pi}{n}\right) \right\} + 2\delta_{n2} \cos \alpha \end{array} \right] \end{array} \right] \end{array} \right) \quad [5.6]$$

There the terms proportional to δ_{n+} and δ_{n2} arise due to the undefined $\cos(2\pi/4)^{-1}$ and $\cos(\pi/2)^{-1}$ respectively, neglected in the sum calculation of *sin* series (Appendix C). For the cases of odd, $n = 2l+1$, and even, $n = 2l$, number of pulses per rotor period, the accumulated phase is given below

$$\Delta\phi(2l+1) = \pm \frac{D\tau_r}{2} \left(\begin{array}{l} \sin^2 \beta \sin 2\alpha \left[1 - \cos \frac{2\pi}{2l+1} \right] \cos^{-1} \frac{2\pi}{2l+1} \\ -2\sqrt{2} \sin 2\beta \sin \alpha \left[1 - \cos \frac{\pi}{2l+1} \right] \cos^{-1} \frac{\pi}{2l+1} \end{array} \right) \quad [5.7]$$

$$\Delta\phi(2l) = \pm D\tau_r \left(\delta_{42l} \sin^2 \beta \cos 2\alpha - \delta_{22l} 2\sqrt{2} \sin 2\beta \cos \alpha \right) \quad [5.8]$$

It is interesting to notice that for the case of even number of pulses per rotor period, no phase is accumulated if $n > 4$. The comparison of the dephasing efficiency for dipolar coupling of 100 Hz and MAS spinner frequency of 5 kHz is shown on Figure 5.7, for several n values.

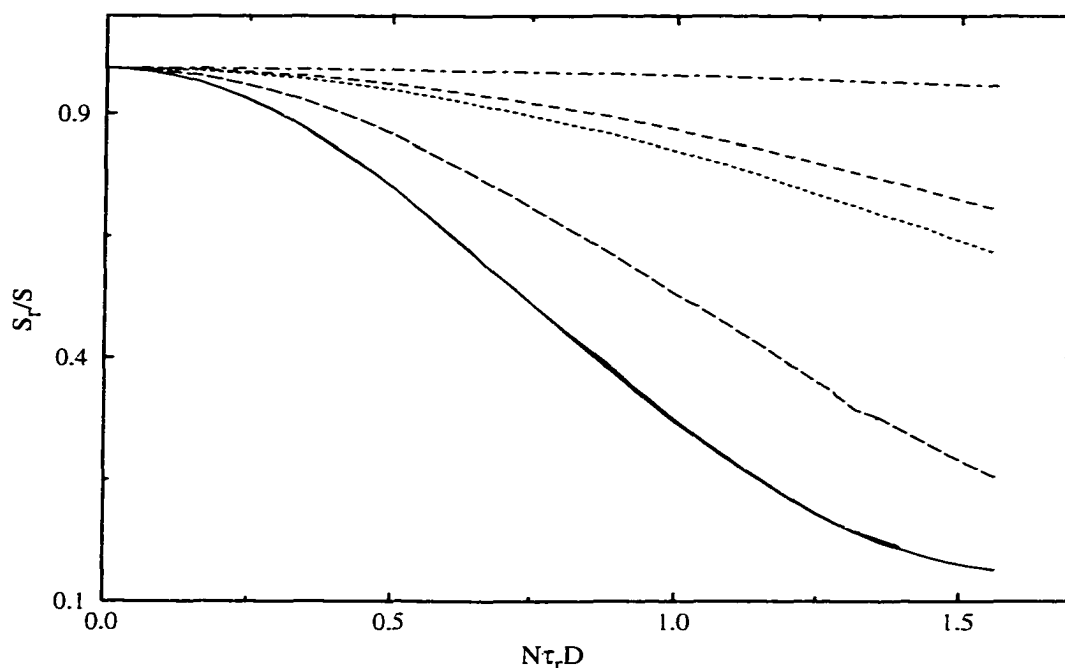


Figure 5.7

Comparison of REDOR dephasing efficiency, S_r/S , for $n < 8$ equally spaced dephasing pulses per rotor period as a function of dimensionless time $N\tau_r D$. N is the number of rotor cycles, $\tau_r = 200 \mu\text{s}$ is the rotor period, $D = 100 \text{ Hz}$ is the dipolar frequency. $n = 1, 2$ – solid; $n = 3$ – long dashed; $n = 4$ – dashed; $n = 5$ – dotted; $n = 7$ – dash-dotted line.

To compute the data plotted in Figure 5.7, it is necessary to evaluate the integral for $N = 2$ to $N = 80$ rotor cycles,

$$1 - \Delta S/S = S_r/S = \frac{1}{4\pi} \int_0^{2\pi} d\alpha \int_0^{\pi} d\beta \sin \beta \cos(\Delta\phi_N) \quad [5.9]$$

$$\Delta\phi_N = N\Delta\phi \quad [5.10]$$

This was done on SGI O2 workstation, using a home written C program with numerical double integration according to Simpson rule. Figure 5.7 shows that the most efficient dephasing corresponds to $n = 1$ and 2 pulses per rotor cycle. With increasing number of

pulses, efficiency drops down, although it is slightly better for $n = 5$ than for $n = 4$. In practice, a high number of pulses per rotor period is difficult to apply due to electronics ring down times and amplifier duty cycles. $50 \mu\text{s}$ is the safe delay between pulses for our experimental setup. This means that no more than 4 pulses per rotor period should be applied for spinning at 5 kHz. For lower spinning speeds more pulses can be applied. It is advisable to have a long delay between the last pulse and the start of an acquisition because of pulse breakthrough between "dephase" and "observe" channels. This will corrupt the first few echo data points. To avoid this and to have the best dephasing efficiency, a small number of pulses ($n = 1, 2$) per rotor period is preferable.

Having in mind all the above mentioned limitations, we choose to apply the sequence with one or two pulses per rotor period. In this case the expression for accumulated phase assumes the simplest form

$$\Delta\phi(n = 1, 2) = \pm(-1)^{n-1} D\tau_r \sin 2\beta \sin(\alpha + \frac{(n-1)\pi}{2}) \quad [5.11]$$

Evaluation of the double integral in Eq. 5.9 for $n = 1, 2$ can be done analytically in terms of cylindrical Bessel functions of the first kind [148, 149], producing

$$S_r/S = \frac{\sqrt{2}\pi}{4} J_{1/4}(\sqrt{2}ND\tau_r) J_{-1/4}(\sqrt{2}ND\tau_r) \quad [5.12]$$

It should be possible to find such analytical solution for the general cases of Eq. 5.7 and 5.8, but such calculations would involve more complex integration patterns and are beyond the scope of the dissertation.

5.3.2 REDOR Dipolar Transform

The dipolar frequency and internuclear distance can be derived from minimizing the error between experimental curve and numerical results (Eq. 5.12) iteratively substituting certain D values. However, fast, direct extraction of D from experimental data is more

desirable. In principle this can be accomplished by means of the REDOR dipolar transform [97, 149]. The basic idea is to seek solution to a Fredholm integral equation of the first kind:

$$f(t) = \int_{D_1}^{D_2} K(D,t)F(D)dD + \varepsilon(t) \quad [5.13]$$

Here $f(t)$ is an experimentally observed time-domain dipolar signal, $F(D)$ is the dipolar frequency-domain solution sought, $K(D,t)$ is a kernel function (given by Eq. 5.12), and $\varepsilon(t)$ is the error perturbation of experimental data (e.g. noise). The solution of this equation is especially valuable for the case of multiple two-spin couplings or their distributions. In such cases, the iterative fitting of Eq. 5.12 involves many calculations, is slower and less reliable, while REDOR dipolar transform ideally should yield direct information on

$$F(D) = A_i \delta(D - D_i) \quad [5.14]$$

Where A_i can be related to the population of spin pair with dipolar coupling D_i , or to the distribution of populations [149].

Unfortunately, Eq. 5.13 describes an ill-posed (or "ill-conditioned" in discrete variables) problem because even for the smallest $\varepsilon(t) \neq 0$, there can be found a ν making $F(D) + A \cdot \sin(D\nu)$ a solution for any arbitrary value of A [97]. Therefore, the analytic inverse of the kernel function Eq. 5.12, which can be calculated in terms of Bessel functions [149], allows the REDOR dipolar transform to be performed without unrelated solutions only for exact data. This is of no practical value except for model calculations.

Luckily, there are methods designed to overcome the instabilities of ill-conditioned problems using physical constraints (like positivity, or spectral width for dipolar spectra). For, example, the self consistent (SC) Tikhonov regularization (TR) algorithm [150, 151] minimizes a discrete linear least square problem

$$\Psi(\lambda) = \sum_{j=1}^m \left\| f_j + \varepsilon_j - \sum_{k=1}^m K_{jk} F_k \right\|_2 + \lambda \left\| \nabla^2 F_j \right\|_2 \quad [5.15]$$

Here Ψ is a function to minimize, λ represents a regularization parameter, $f_j + \varepsilon_j$ refers to a combination of a time domain signal and the experimental noise, and ∇^2 is the second derivative regularization operator. The scaling parameter, λ , is found automatically by the SC algorithm [150, 151]. The method does not require analytical inverse of $K(D_i, t_j) = K_{ij}$ and has excellent noise handling capabilities provided there is sufficient sampling of $f_j + \varepsilon_j$ oscillations with desired spectral width. The overall operation count for this method is proportional to the cube of experimental point number, which is usually small (< 50) for the REDOR experiment. Also, the kernel table can be built up fast from Eq.5.12.

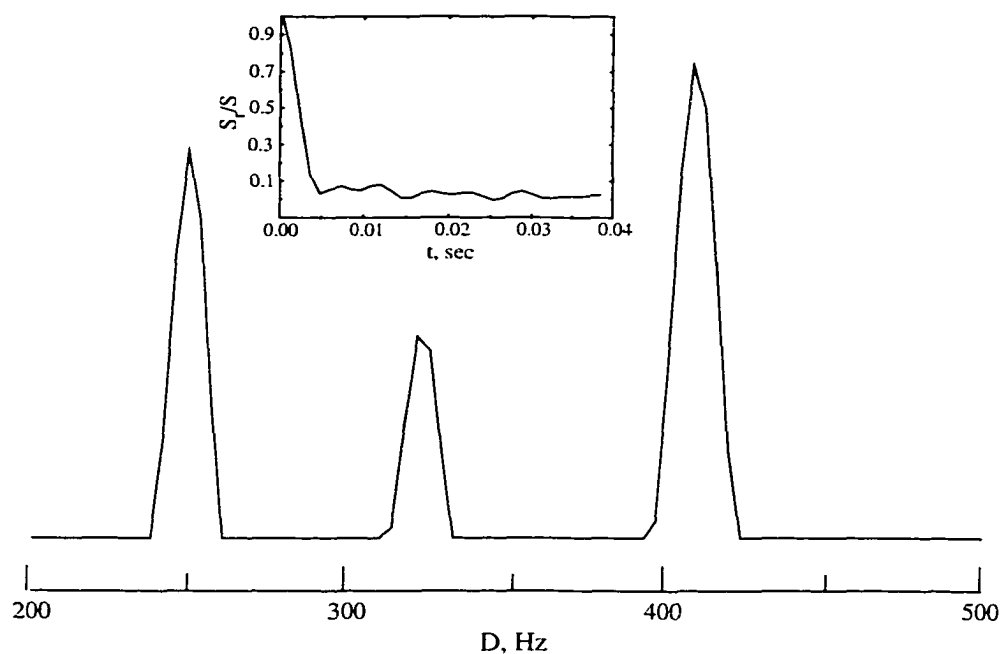


Figure 5.8

Self consistent Tikhonov regularization (SCTR) REDOR dipolar transform of the simulated three-coupling 32 point dephasing curve (insert), with $D = 250, 320$ and 410 Hz, with intensity ratios 2:1:3.

A FORTRAN program for self consistent Tikhonov regularization (SCTR) is available on-line from the CPC program library [151]. Its version with the kernel modified in accordance to Eq. 5.12 has been used here to determine appropriate experimental conditions, allowing extraction of multiple dipolar constants and their distributions from the

experimental data. This will be discussed in the following section. In general, the program provides exact solution only if no less than four oscillations of the REDOR curve with the smallest dipolar frequency are sampled by no less than 32 equally spaced data points. Otherwise, small spurious dipolar peaks arise, and the amplitudes of "real" peaks no longer reflect the correct intensity ratio. The program has the best performance when the difference between the smallest and the largest dipolar couplings allows the use of smaller spectral width in the dipolar domain (Fig. 5.8). In case of a single internuclear distance, the performance of the program is comparable to that of a direct iterative fitting Eq. 5.12 to experimental data.

In the limit of small dephasing angles, the initial behavior of the Bessel functions [148] (Eq. 5.12) gives parabolic dependence for dephased signal on dipolar frequency

$$S_r/S = 1 - \frac{16}{15}(ND\tau_r)^2, \quad \text{when} \quad [5.16]$$

$$ND\tau_r < 1 \quad [5.17]$$

from which the direct "inverse transform" for each data point satisfying the condition of Eq. 5.17 can easily be derived

$$D = \frac{\sqrt{\frac{15}{16}(1 - S_r/S)}}{N\tau_r} \quad [5.18]$$

This is useful for coupling estimation when tuning, or measuring very long internuclear distances, if only a few initial points of the dephasing curve are (or can be) acquired.

5.3.3 Planar Libration and Internuclear Distance Distribution

The models used to describe ^2H QE echo lineshapes of the deuterated dendrimers include fast planar libration of the spacers as well as the distribution of hydrogen bond length (see section 3.5.1). Therefore, it is useful to determine the impact of such models on REDOR data to define the best experimental conditions to optimize the accuracy of distance

determination. The Gaussian distribution of the structural parameters typical for polymeric systems [152], is correlated with the observed internuclear distances, and results in a skewed distributions in the dipolar frequency domain. In principle, the skew and characteristic width should be detectable in REDOR experiments. The resulting distributions in the dipolar frequency domain can be monitored directly by the aid of the above discussed REDOR dipolar transform.

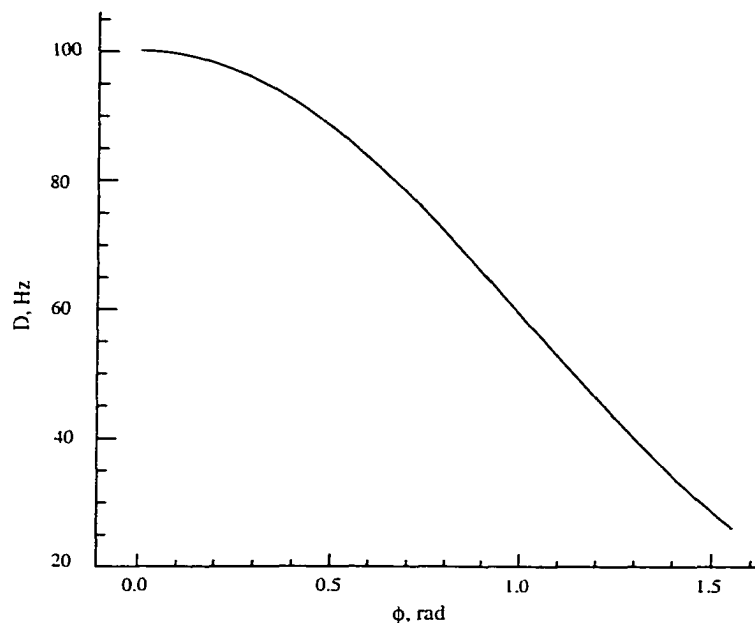


Figure 5.9

Dipolar frequency as a function of planar libration amplitude for the case of fast librational motion; $D_{PAS} = 100$ Hz.

In case of molecular motion, its averaging effect is in the fast regime with respect to REDOR when its rate is much higher than the dipolar frequency. Estimated dipolar frequency range for the PAMAM dendrimers is less than 100 Hz. So, the detected planar libration of the dendrimer spacers, occurring with the rates higher than 10^5 Hz (Table 4.1) [5, 6] is definitely "fast" on a dipolar scale. The circular term of a dipolar Hamiltonian will undergo additional transformation from PAS to crystal fixed frame, $\Omega_{PC}(0, \phi(t), 0)$ before Crystal-Rotor, Ω_{CR} , and Rotor-LAB, Ω_{RL} . As a result of this transformation and motional

averaging by planar libration, the zeroth component of the irreducible spherical tensor in crystal fixed frame will be

$$T_0^{(2)} = \langle D_{oo}^{(2)} \rangle T_0^{(2)}(PAS) = \langle D_{oo}^{(2)} \rangle \sqrt{6} \gamma_C \gamma_N \hbar r_{CN}^{-3}, \quad \text{where} \quad [5.19]$$

$$T_0^{(2)} = \langle D_{oo}^{(2)} \rangle T_0^{(2)}(PAS) = \langle D_{oo}^{(2)} \rangle \sqrt{6} \gamma_C \gamma_N \hbar r_{CN}^{-3}, \quad \text{where} \\ \langle D_{00}^{(2)} \rangle = 0.5(3 \langle c^2 \rangle - 1) \quad [5.20]$$

where $\langle c^2 \rangle$ is given by Eq. 3.8 [4]. This brings an experimentally measured dipolar coupling constant into the form

$$D = \frac{1}{4} D_{PAS} \left(1 + 3 \frac{\sin 2\phi}{2\phi} \right) \quad [5.21]$$

Thus, an experimentally determined D is reduced by planar libration (Fig. 5.9), up to one quarter of its PAS value ($0 < \phi < \pi/2$). It is interesting to notice that for relatively small ϕ , $\sin(2\phi)/2\phi \rightarrow 1$, and $D \approx D_{PAS}$. Only for really large librational amplitudes, will D deviate significantly from D_{PAS} . Therefore, it is not surprising that for the largest librational amplitude observed at the dendrimer spacers [5], $\phi = 20^\circ$, the effect on a measured internuclear distance of 3.4 Å is its apparent "lengthening" to 3.47 Å only. This difference would most likely be beyond REDOR accuracy. Nevertheless, for other systems with larger librational amplitudes, such a correction may become important. In general, it is essential to know the dynamics at the site for which internuclear distance is to be determined by REDOR, if correct distances are to be determined.

The question of the impact of a structural parameter distributions on REDOR also deserves detailed consideration. For dendrimers, QE echo lineshapes are influenced predominantly by hydrogen bond length distribution, while the distribution of libration amplitudes, if exists, is very narrow. Even if we assume that the full line width of the amide deuteron powder pattern is accounted for by the Gaussian distribution of the planar libration amplitude, the characteristic half width of such a distribution would only be $\sigma_\phi \leq 18^\circ$. While in the case of hydrogen bond length distribution the same assumption leads to $\sigma_r \leq 0.2 \text{ \AA}$. The librational amplitudes and distribution width is unlikely to be different at the carbonyl

and amide sites due to the rigidity of an amide bond, which possesses partial double-bond character. The distribution of C..N internuclear distances between the dendrimer branches may be broader than determined for D..O. To obtain the picture in a dipolar frequency domain, $r(D)$ has to be found from the relation $r \propto D^{-1/3}$, in case of the distance distribution, and $\phi(D)$ should be determined numerically by solving equation $\sin 2\phi = 2\phi(4D/D_{PAS}-1)/3$. The characteristic skewed distributions are plotted in Figure 5.10.

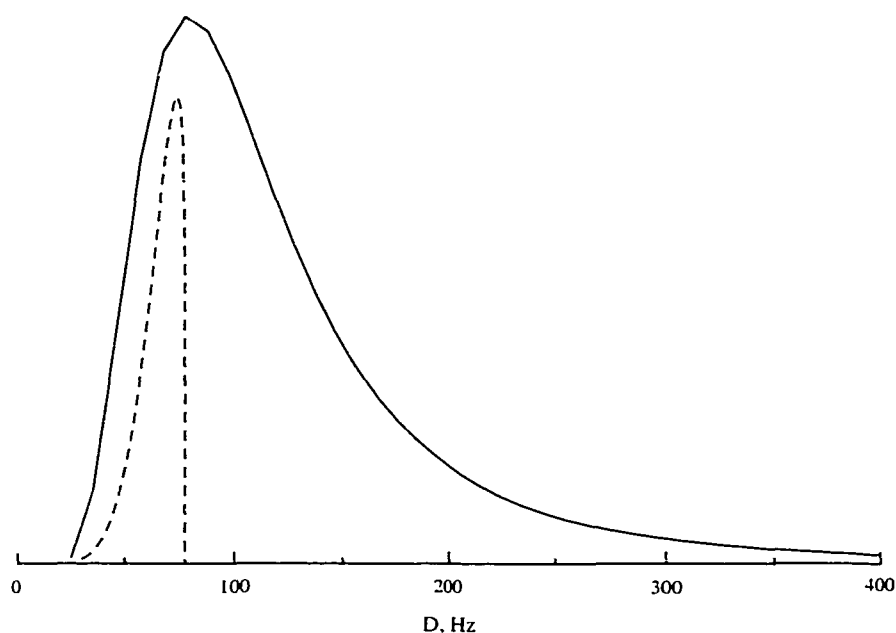


Figure 5.10

Skewed distributions of dipolar couplings in case of Gaussian distribution of internuclear distances (solid line, $\langle r \rangle = 3.4 \text{ \AA}$, $\sigma_r = 0.5 \text{ \AA}$) and planar libration amplitudes (dashed line, $\langle \phi \rangle = 20^\circ$, $\sigma_\phi = 18^\circ$).

It is obvious that the character of the skew in a dipolar frequency domain is opposite for the two models. Also, the libration amplitude distribution will have only a minor effect on REDOR spectrum compared to the distribution of the internuclear distances. This effect was studied for both models using a simulated sum of appropriately weighed REDOR curves with added 15-20 % noise from the spectrum, and applying REDOR dipolar transform through SCTR algorithm. The results are shown in Figures 5.11 and 5.12.

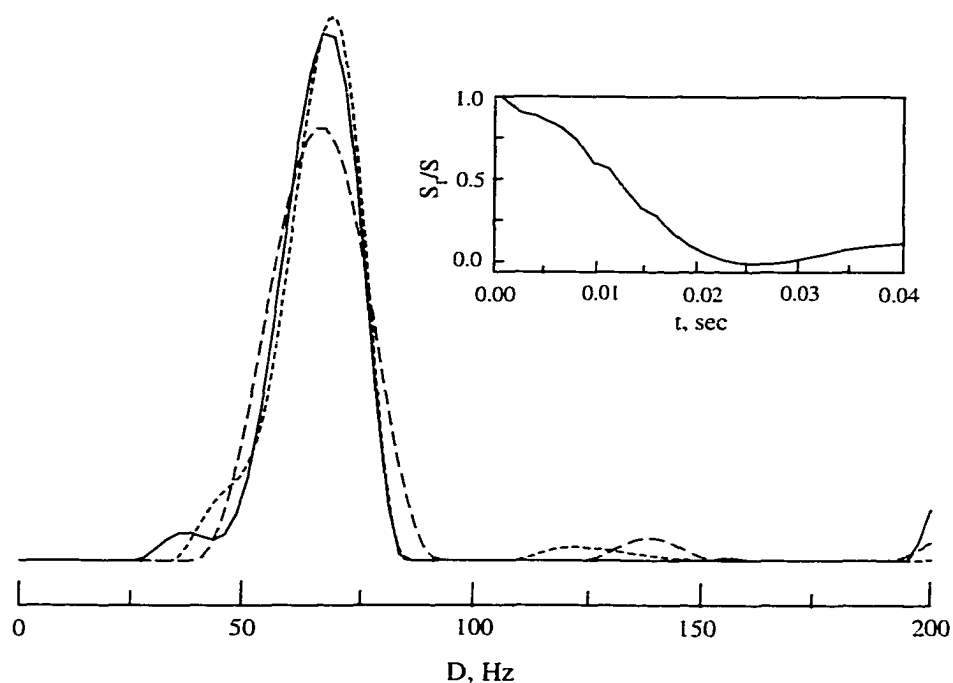


Figure 5.11

Results of SCTR REDOR dipolar transform for the simulated dephasing curves in case of a Gaussian distribution of a planar libration amplitude, $\langle\phi\rangle = 20^\circ$, $\sigma_\phi = 18^\circ$, SW = 200 Hz, 15 % experimental noise is added to the simulated dephasing curves. Solid line – 200 rotor cycles sampled every eighth cycle; long dashed – 200 rotor cycles sampled every fourth cycle; short dashed – 400 rotor cycles sampled every fourth rotor cycle. The insert shows the simulated REDOR curve (25 points) corresponding to conditions close to experimental, and the solid line in SCTR dipolar spectrum.

For conditions close to experimental, when the small number of REDOR points is acquired over a limited time (< 40 ms), no quantitative information can be extracted about the distribution. Nevertheless, the skew can still be detected and related to an appropriate model. With decreasing number of points or increasing noise, the resulting curves get broader, and spurious peaks appear. Therefore, for good resolution many points for many rotor cycles with substantial averaging is required. The quantitative characterization of the planar libration angle distribution from REDOR may be possible only for very broad distributions. When the REDOR dephasing curve is offset from zero (simulating imperfect decoupling conditions), spurious intensity grows close to zero frequency in the inverse transform dipolar spectrum, but the average internuclear dipolar coupling can still be determined. This

implies that SCTR algorithm can be applied experimental data with even inadequate decoupling for direct internuclear distance determination. In this case iterative comparison with simulated curves would require introduction of additional correction procedures. In summary, for long internuclear distances real REDOR experiments have little sensitivity to the distribution of the planar libration amplitudes, but can unambiguously detect the presence of distributions of internuclear distances.

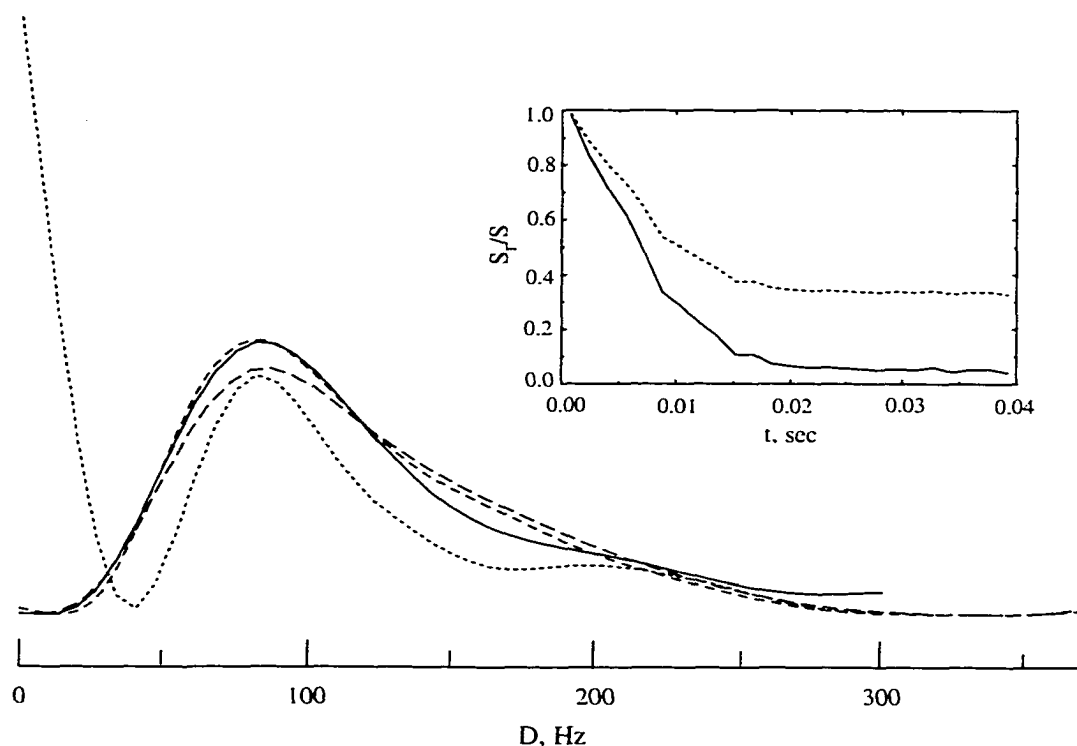


Figure 5.12

Results of SCTR REDOR dipolar transform for the simulated dephasing curves in case of a Gaussian distribution of internuclear distances, $\langle r \rangle = 3.4 \text{ \AA}$, $\sigma_r = 0.5 \text{ \AA}$, $SW = 400 \text{ Hz}$, 15 % experimental noise is added to the simulated dephasing curves. Solid line – 200 rotor cycles sampled every eighth cycle; dotted line – 200 rotor cycles sampled every eighth cycle with "inefficient" decoupling (dephasing reduced by a factor 0.65); long dashed – 200 rotor cycles sampled every fourth cycle; short dashed – 400 rotor cycles sampled every fourth rotor cycle. The insert shows the simulated REDOR curves (25 points) corresponding to conditions close to experimental. The line style is the same in the SCTR dipolar spectrum.

5.4 Experimental Results for Model Compounds

Routine REDOR experiments require pre-tuning the spectrometer using a compound with known internuclear distance before measuring unknown structures. For ^{13}C - ^{15}N REDOR, good reference materials are small amino acids. Their crystalline structures are usually known from X-ray measurements, and REDOR data can be obtained in a short time with a good signal-to-noise ratio.

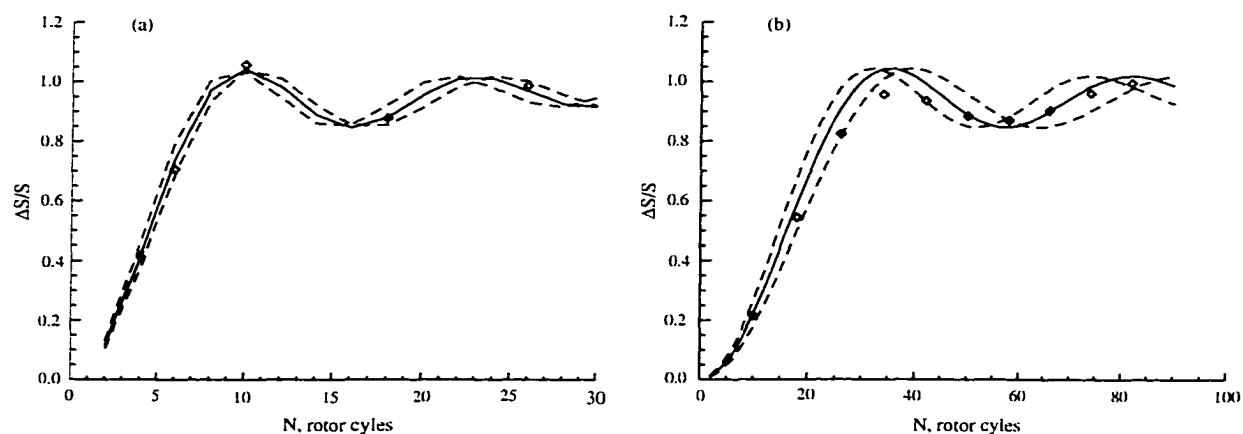


Figure 5.13

Experimental universal REDOR data (diamonds), corrected for natural-abundance contributions, and best fit simulations (solid lines) for 10 % doubly labeled (a) $2\text{-}^{13}\text{C}\text{-}^{15}\text{N}$ glycine (Gly-2), $\nu_r = 4$ kHz, $D = 845 \pm 45$ Hz; and (b) $1\text{-}^{13}\text{C}\text{-}^{15}\text{N}$ glycine (Gly-1), $\nu_r = 5$ kHz, $D = 190 \pm 20$ Hz. The dashed lines are simulated dephasing curves for error limiting dipolar couplings.

Experimental results for doubly labeled glycine samples ($2\text{-}^{13}\text{C}\text{-}^{15}\text{N}$ – Gly-2 and $1\text{-}^{13}\text{C}\text{-}^{15}\text{N}$ – Gly-1), diluted to 10 % in natural abundance material after the correction for natural abundance, are shown in Figure 5.13. Calculation of the correction factor, α , was done by summing all the contributions to the ^{13}C signal (^{13}C coupled to ^{14}N and ^{13}C coupled to ^{15}N) from labeled (50 mg) and natural-abundance (450 mg) fraction of the sample, and finding the ratio of ^{13}C coupled to ^{15}N from the labeled material only to this sum. For both samples $\alpha = 0.89$, $\beta = 0$ (Eq. 5.3). The $10 \mu\text{s}$ (1170 W) dephasing pulses were applied to the ^{15}N

channel every half a rotor cycles. Refocusing pulses of the same length (392W) were applied every rotor period to ^{13}C channel. The length of the π pulses was set within $\pm 0.1 \mu\text{s}$ for ^{13}C and $\pm 0.2 \mu\text{s}$ for ^{15}N . The protons were irradiated with 50 kHz (65 W) field during 90_x and cross polarization pulses. The decoupling field of 75 kHz (146 W) was kept on during dephasing and acquisition. The cross polarization time was 1 ms for the methylene carbon of Gly-2, and 2 ms for the carbonyl of Gly-1. The line width was 20 Hz (15 kHz SW) for the labeled carbonyl, 52 Hz (20 kHz SW) for the labeled methylene, and 18 Hz for ^{15}N (10 kHz SW). The samples were spun at 4000 ± 2 Hz, and 128 transients with 2 s recycle delay were accumulated for each REDOR data point.

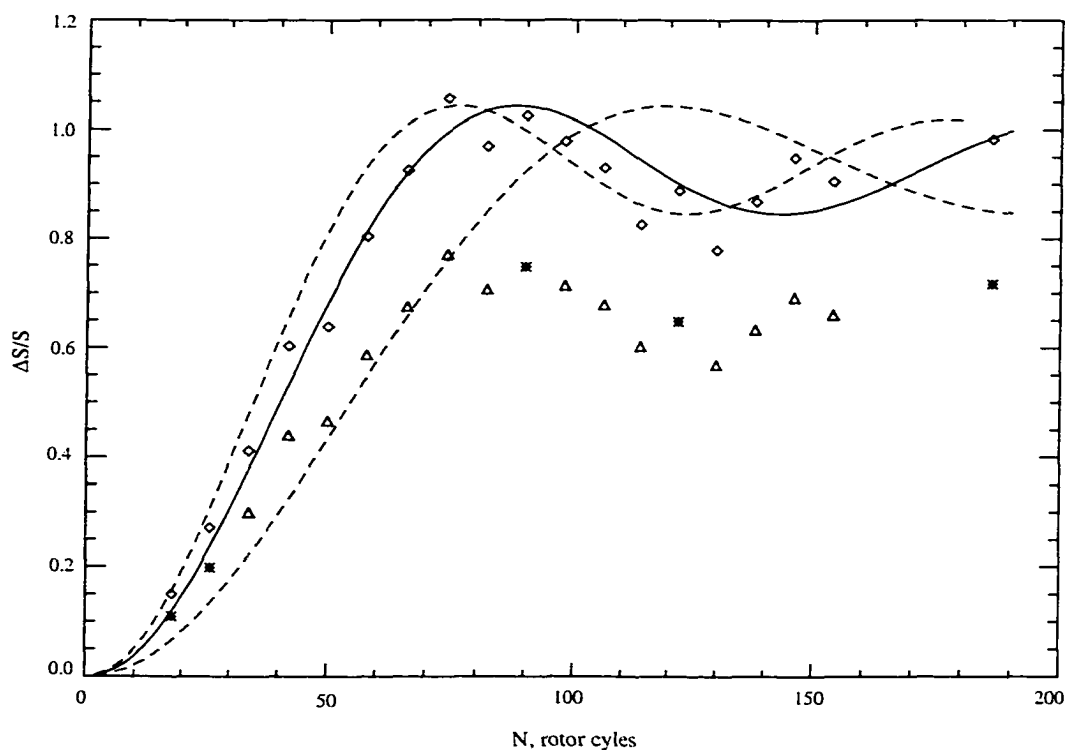


Figure 5.14

Experimental universal REDOR data for (triangles), corrected for natural abundance contributions, and the best fit simulation (solid line) for 9 % doubly labeled cyclo-leuciloglycine (CLG) di-peptide. Stars mark the points with data averaged over 3-4 experiments. Diamonds show the experimental results after "empirical" correction for inefficient decoupling with correction factor 1.34. Best fit $D = 95 \pm 20$ Hz. The dashed lines are simulated dephasing curves for error limiting dipolar couplings.

A small effect of insufficient decoupling is observed for 20-50 rotor cycles data in case of Gly-1. Two side bands were included in intensity calculation for Gly-1 REDOR. The derived distances are 1.52 ± 0.05 Å (1.48 Å, X-ray for Gly-2) and 2.5 ± 0.1 Å (2.47 Å, X-ray for Gly-1). Due to narrower lines and smaller dipolar coupling, the Gly-1 would be the tuning sample of choice if longer distances are to be measured and longer dephasing times with XY-8 pulse in a loop are required.

The technique was likewise tested on small di-peptide, cyclo-leuciloglycine (CLG), where leucine residue is doubly labeled ($4\text{-}^{13}\text{C}\text{-}^{15}\text{N}$). This sample is an object of further research in the lab. The internuclear distance between the labeled sites was numerically calculated [153] for extended relaxed conformation to be 3.8 Å. For better statistical averaging of errors, the experiment was done in three steps. First, after tuning with Gly-1, REDOR data points were acquired for odd dephasing loop numbers (8 pulses in one loop). Then experiment was repeated 2-3 times with different number of scans for some of the data points, and averaged (Fig. 5.14, the data marked with stars). Next, the tuning was repeated, and the data for even loop numbers were accumulated. These 2D experiments were performed with introduction of loop tables in REDOR pulse sequence (Fig. 5.4). The experimental data analysis was automated by home written PVWAVE routine. The determined distance, 3.25 ± 0.25 Å, is smaller than calculated [153]. This provides a distance constraint on CLG conformation in the crystalline state, and rules out a fully extended architecture. The side chain of the CLG has to be slightly bent towards the ring nitrogen. The experimental results after the natural-abundance correction (Eq. 5.3, $\alpha = 0.8885$, $\beta = 0$) are presented in Figure 5.14 (triangles). Artifacts of insufficient decoupling for a labeled carbon, directly bonded to proton (line width 110 Hz at 20 kHz SW) resulting in reduced dephasing (~ 30 % loss) is obvious. 1024 transients were accumulated with 3 s recycle delay for each data point. To empirically compensate for this reduction and compare with calculated curves, the data were multiplied by 1.34 (Fig. 5.14, diamonds).

The performance of the REDOR dipolar transform with SCTR was tested on

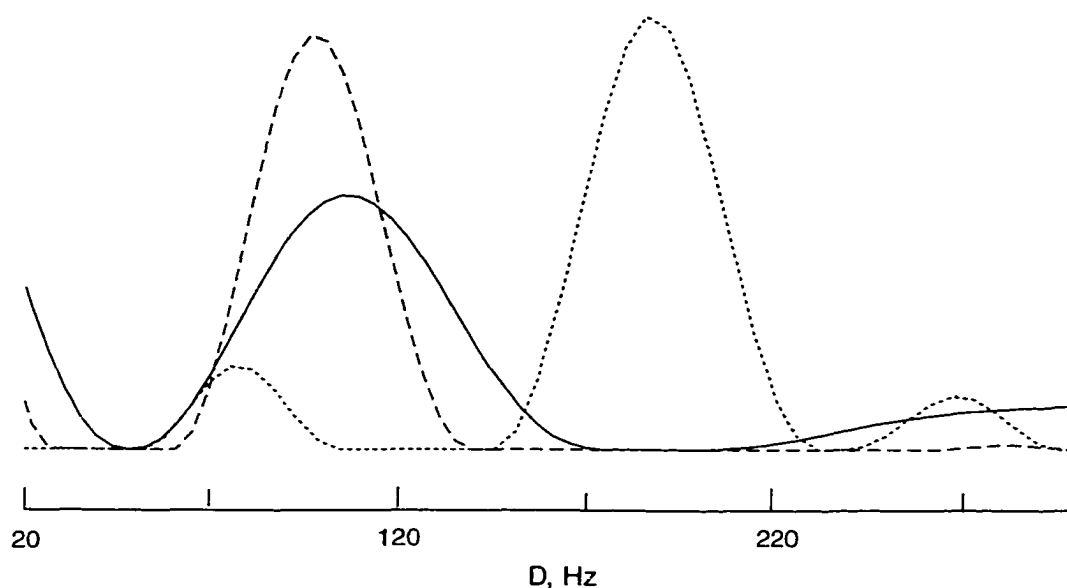


Figure 5.15

Results of SCTR REDOR dipolar transform for experimental CLG data (19 points, solid line); linearly interpolated CLG data (33 points, dashed line); and Gly-1 tuning curve (10 points, dotted line). Dipolar spectral width is 250 Hz.

experimental data (not corrected for reduced dephasing efficiency) for CLG and Gly-1 (Fig. 5.15). The small number of data points results in appearance of spurious peaks and large dipolar line width. This line width is a measure of experimental uncertainty, rather than an indication of any structural parameter distribution. The interpolation of experimental points for CLG, producing narrower lines, is an illustration of this fact. In general, simple linear interpolation between the small number of experimental points may help to increase dipolar resolution in case of a single dipolar coupling. The spurious intensity observed close to zero frequency is due to the reduced dephasing efficiency. Still, even with the small number of data points, single internuclear distance can be deduced immediately and directly from the application of SCTR. This may be useful for tuning (Fig. 5.15, Gly-1 data). In case when structural parameter distributions are of interest, such an experiment would not provide sufficient resolution. It illustrates that more data points with better S/N have to be accumulated for longer dephasing times in order to detect distributions of distances. This may require acquisition of more transients for rotor cycle numbers higher than 50.

5.5 Summary

For PAMAM dendrimers intra- and intermolecular distances between the dendrimer branches can be determined from REDOR experiment using available hardware and software. This would provide solid confirmation of the transition from open interpenetrated structure in low generation ($G < 3$) dendrimers to a backfolded architecture in high generation ($G > 5$) materials through the creation of surface network in "transition" generation ($G = 3-5$) molecules. The REDOR data should allow establishment of general correlation between structure, molecular motion and morphology in complex solid polymeric systems.

The estimated range of distances between ^{13}C and ^{15}N of the dendrimer branches from the hydrogen bonding constraints is 3.4-4.0 Å. Appropriate labeling strategies, optimum experimental acquisition and data analysis techniques have been developed and tested on the model compounds. Prior knowledge of motional parameter distributions suggests that the influence of the small amplitude planar libration and relatively narrow hydrogen bond distribution on observed REDOR curves should be beyond detectability. In general for the correct determination of internuclear distances in polymeric systems, the amplitudes and rates of molecular motion have to be determined beforehand. To measure a single small dipolar coupling, expected in case of the PAMAM dendrimers, it is sufficient to acquire only a few (4-6) initial points of the dephasing curve with a small uncertainty. If spinning at 5 kHz, the curve should be sampled less than for 50 rotor cycles for the pulse sequence (Figure 5.4). Then, the internuclear distance can be directly calculated (from Eq. 5.18) after natural-abundance corrections.

For the case of equally spaced XY-8 pulses optimum dephasing conditions are met when no more than two pulses are applied per rotor period. The signal-to-noise has to be improved by introduction of more efficient proton decoupling schemes. Together with

decreasing the number of refocusing pulses and observing carbonyl carbon (without directly bonded proton), this would likewise help to increase dephasing efficiency over longer time periods, and accurately acquire data as long as a few REDOR curve oscillations. The detection of the oscillation is not necessary for a long distance measurement (Eq. 5.18), but may be important for other systems where distribution of structural and motional parameters are to be characterized.

For moderate internuclear distances ($< 3.5 \text{ \AA}$) the substantial distributions of structural and motional parameters (e.g. $\sigma_\phi > 20^\circ$, $\sigma_r > 0.3 \text{ \AA}$) can be quantitatively characterized (with less than 10 % error) from REDOR data using the REDOR dipolar transform with SCTR, if at least two dephasing cycles are sampled with 50 data points of S/N better than 10 %. It also should be possible to narrow the spectral width in the dipolar frequency domain, if the distribution of very different multiple couplings are not observed. Interpolation between 20-30 experimental data points may be an alternative to long data set acquisitions, helping to increase resolution too. The presence of skewed dipolar frequency distributions always indicate the presence of structural and motional parameter distributions in the system. If motion is fast, the symmetric distributions indicate insufficient signal-to-noise or under-sampling of the dephasing curve. This should prompt further optimization of experimental conditions depending on required accuracy and resolution.

The tuning technique for the NMR spectrometer in a triple resonance mode for REDOR data acquisition was tested on doubly labeled samples of small amino acids. Software performance for the data analysis was adjusted to the required accuracy of extracted information. The hardware and software testing allowed development of the optimum procedure for the experiment performance and data manipulation.

The first REDOR measurement of $4\text{-}^{13}\text{C}\dots^{15}\text{N}$ distance ($> 3 \text{ \AA}$) in crystalline CLG dipeptide have revealed deviations in its structure from extended conformation implying the side-chain bends toward the ring nitrogen.

Chapter 6

General Conclusions and Future Research

The preceding chapters described the progress made in characterization of narrow distributions of structural and motional parameters from temperature dependent dynamics of polyamidoammonium dendrimer salts. In addition, the sensitivity limits were discussed for the techniques of solid state NMR employed in this study. Here, the important results and their implications for polymer science are summarized, and directions for future research are outlined.

Solid state NMR studies of PAMAM salts revealed that these dendrimers possess highly uniform intra- and inter-molecular environments, characterized by extremely narrow distributions of hydrogen bond length ($\sigma_r < 0.25 \text{ \AA}$) and rates of libration ($\sigma_k < 1.0$). No considerable distribution of librational amplitudes is observed. The absence of wide distributions is very different from the dendrimers in solution [35, 36] and linear polymers [121, 122]. These results are in agreement with theoretical predictions of kinetic dendrimer growth model [40]. Dendrimer structures are stabilized by extensive hydrogen bonding between spacer amide and branching site amine groups. PAMAM spacers undergo fast planar libration with very narrow rate distributions of temperature independent width ($\sigma_k <$

0.4). Spacer librations which break amide hydrogen bonds are thermally activated ($E_A \sim 44$ kJ/mol) for all generations only within broad glass transition region. At branching sites librational rate distributions are influenced by Cl^- counterion. These distributions have temperature dependent width ($0.2 < \sigma_x < 1.0$). The activation barrier at the branching sites is higher for low generation materials. Dendrimer termini undergo librations in an asymmetric cone in addition to fast pseudo-three fold rotation. For dendrimer interior and surface, librational amplitudes increase with increasing temperature and motion of the termini becomes more symmetric. Thermal activation of libration at the PAMAM interior and surface is confined to the glass transition region. Kinetics of PAMAM termini is influenced by counterions and reveals the presence of ammonium groups in constrained (interpenetrated or backfolded) and free (surface) environments. Three solid state dendrimer subclasses may be distinguished by their dynamics. Low PAMAM salt generations ($G < 3$) are associations of open and interpenetrated molecules with high relaxation efficiency at branching sites. Intermediate generations ($G = 3-5$) have $\sim 60\%$ of ammonium termini involved in surface network formation, and the rest either backfolded or interpenetrated. They should be effective as sequestering agents. High generation dendrimers ($G > 5$) form extensively backfolded, less flexible structures.

Combination of several solid state NMR techniques enabled full characterization of narrow structural and motional parameter distributions in PAMAM dendrimers. These techniques are indispensable for studies of rigid glassy polymers lacking long range order. When motion is fast, QE lineshapes are descriptive of narrow distributions of librational amplitudes and hydrogen bond length. They provide constraints on motional trajectories independent of the rates. Fast kinetics and rate distribution for a single frame motion are fully characterized from T_1 anisotropy measurements. The range of rates corresponding to the fast regime depends on the motional geometry. In this regime it is possible to unravel overlapping relaxation time anisotropies for unselectively deuterated polymeric materials with the aid of preliminary information on motional amplitudes provided by QE

experiments. In case of multiframe dynamics, the absolute value of the relaxation time is determined by the fastest motion, while the shape of anisotropy depends on both the slower rate and the motional geometry. For two-frame motions ^2H MAS technique allow quantitative description of the rates for the slower motion. This method is very sensitive to the presence of narrow log-normal rate distributions. REDOR experiments can discriminate between backfolding and interpenetrating by measuring inter- and intra-molecular distances between dendrimer spacers ($3.4 \text{ \AA} < r < 4.04 \text{ \AA}$) doubly labeled according to a strategy developed in this dissertation. Skewed distributions of intensity in REDOR dipolar spectra indicate the presence of structural parameter distributions. They can be quantified applying the SCTR dipolar transform directly to the time domain REDOR data. For PAMAM dendrimers, the influence of fast planar libration and hydrogen bond length distribution on dipolar frequencies is negligible.

Fundamental theoretical questions still awaiting solution concern effects of slow molecular motion on REDOR dipolar frequencies, as well as correlation of solid (linear, electrolyte, hyperbranched) polymer dynamics with broad glass transition region observation, and a mathematical description of the effect of hydrogen bonding on conformation and glass transition behavior. With a toolbox of available NMR techniques the directions for future dendrimer research are to do REDOR on doubly labeled PAMAM dendrimers and to establish correlation between dendrimer morphology and spacer length and flexibility for different dendritic polymers. It is likewise of technical interest to monitor dendrimer dynamics with inclusion compounds and as inclusion compounds inside polymer networks. Conformation of inclusion compounds can be determined using distance constraints provided by REDOR.

Morphology and dynamics of polymeric materials are intrinsically interdependent. For complete description of solid polymers accurate information about dynamics has to be acquired. Like structure and morphology, rates and trajectories of molecular motion are correlated with bulk material properties. The distributions of microscopic structural and

motional parameters constitute the origin of macroscopic physical property distributions. Therefore, the distribution characterization, suggesting the means for control, are of general interest for polymer science. This characterization for rigid amorphous polymeric systems is efficiently achieved using solid state NMR techniques.

Appendix A

Derivation of Cartesian EFG Tensor Dependence on the Amplitude of Fast Planar Libration

In passive transition between different coordinate frames, Cartesian tensors transform according to the rule

$$Q(NEW) = R(\alpha, \beta, \gamma)Q(OLD)R^{-1}(\alpha, \beta, \gamma) \quad [A.1]$$

where $R(\alpha, \beta, \gamma)$ are Euler orthogonal matrices in Rose [154] convention, and $R^{-1} = R^T$. In a simple case of planar libration around Y-axis in principle axes (PAS) system of the tensor, Euler angles are: $\alpha = 0$, $\beta = \phi(t)$, and $\gamma = 0$. For EFG tensor the transition from its PAS system to a molecule-fixed frame (active rotation) is described by

$$R = \begin{pmatrix} \cos \phi & 0 & -\sin \phi \\ 0 & 1 & 0 \\ \sin \phi & 0 & \cos \phi \end{pmatrix} \quad [A.2]$$

The physical constraints on Cartesian EFG tensor components in its PAS system ($|q_{xx}| \leq |q_{yy}| \leq |q_{zz}|$; $\eta_{zz} = q_{xx} - q_{yy}$; $q_{zz} = -(q_{xx} + q_{yy})$) allows expressing the tensor in terms of two positive parameters: asymmetry, η_{PAS} , and the largest component, q_{zz}^{PAS} :

$$Q(PAS) = -\frac{q_{zz}^{PAS}}{2} \begin{pmatrix} 1 - \eta_{PAS} & 0 & 0 \\ 0 & 1 + \eta_{PAS} & 0 \\ 0 & 0 & -2 \end{pmatrix} \quad [A.3]$$

The Euler transformation in Eq. A.1 according to Eq. A.2 yields an expression for EFG tensor with nonzero asymmetry parameter, $\eta_{PAS} \neq 0$, in a molecular-fixed frame,

$$Q(MOL) = -\frac{q_{zz}^{PAS}}{2} \begin{pmatrix} \cos^2 \phi (3 - \eta_{PAS}) - 2 & 0 & \cos \phi \sin \phi (3 - \eta_{PAS}) \\ 0 & 1 + \eta_{PAS} & 0 \\ \cos \phi \sin \phi (3 - \eta_{PAS}) & 0 & 1 - \eta_{PAS} - \cos^2 \phi (3 - \eta_{PAS}) \end{pmatrix} \quad [A.4]$$

Ensemble average over the fast libration in an arc of the $Q(MOL)$ components produces diagonal EFG tensor in molecule-fixed frame due to the fact that

$$\begin{aligned} \langle \cos \phi \sin \phi \rangle &= \frac{1}{4\phi_0} \int_{-\phi_0}^{\phi_0} \sin 2\phi d\phi = 0 \\ \langle \cos^2 \phi \rangle &= \frac{1}{2\phi_0} \int_{-\phi_0}^{\phi_0} \frac{1 + \cos 2\phi}{2} d\phi = \frac{1}{2} \left(1 + \frac{\sin 2\phi_0}{2\phi_0} \right) \end{aligned} \quad [A.5]$$

After straightforward algebraic substitution the average values of two independent parameters of EFG tensor in molecule-fixed system become

$$\langle q_{zz}^{MOL} \rangle = \frac{1}{2} q_{zz}^{PAS} \left[\eta_{PAS} - 1 + \langle c^2 \rangle (3 - \eta_{PAS}) \right] \quad [A.6]$$

$$\langle \eta^{MOL} \rangle = \frac{3 + \eta_{PAS} - \langle c^2 \rangle (3 - \eta_{PAS})}{\eta_{PAS} - 1 + \langle c^2 \rangle (3 - \eta_{PAS})} \quad [A.7]$$

Thus, the dependence of Cartesian EFG tensor on the amplitude of fast planar libration is given by Eq. A.5, A.6 and A.7.

Appendix B

T_{1Z} Anisotropy Analysis Procedure for Multiple Overlapping Powder Patterns

Temperature dependent recovery curves of G3 dendrimer provide experimental insight into the origin of multiexponential relaxation behavior observed for all PAMAM generations. Therefore, it is easier to explain procedure of constrained multiexponential fit using G3 as an example. Figure B.1 compares the results of unconstrained biexponential and constrained multiexponential fits for G3 recovery curves at the horns of RND₃⁺ powder pattern at five temperatures from 15 °C to 55 °C. The actual experimental data and corresponding fits at different temperatures were vertically shifted for clarity. The multiexponential fit was done according to Equation 4.4. The “constraints” for anisotropies of the R₂ND and R₃ND⁺ powder patterns were obtained by fitting experimental data outside RND₃⁺ powder pattern.

Biexponential fit was accomplished by first visually choosing the slope change point, τ_c , for recovery curve, and fitting the data for $\tau > \tau_c$, slowly relaxing magnetization component (superscript "s"), to a single exponential using linear least square fit procedure. Then, obtained contribution of M_τ^s

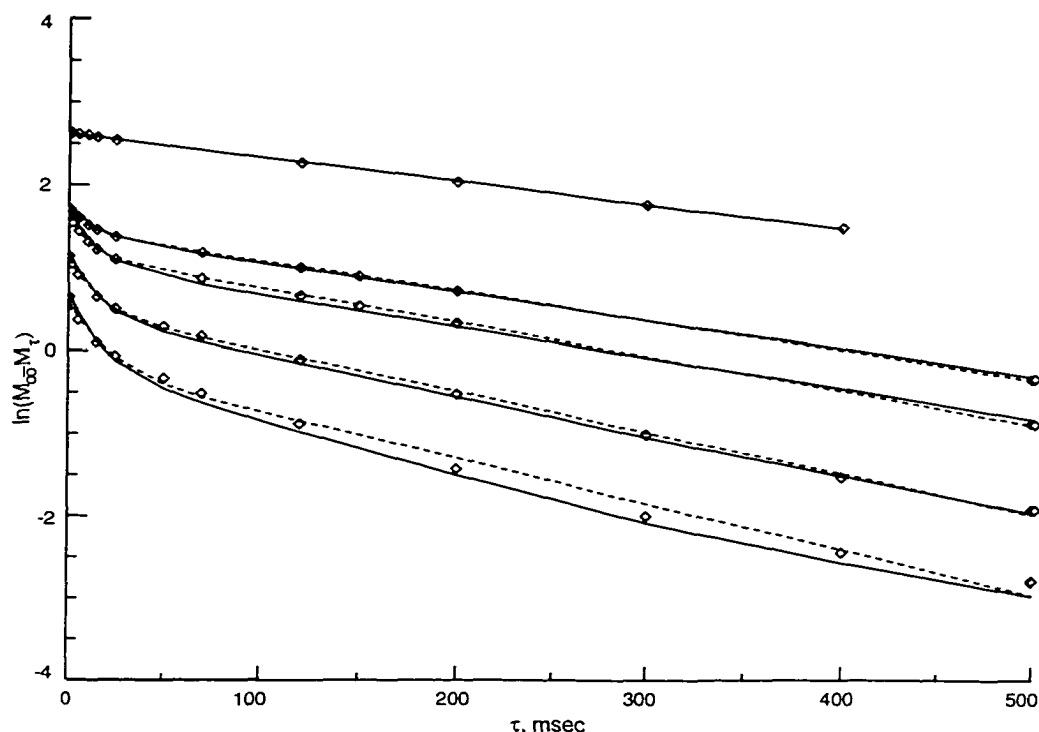


Figure B.1

Comparison of unconstrained biexponential (dashed) and constrained multiexponential (solid) fit for recovery curves at 16 kHz (horns of RND_3^+ powder pattern) of G3 dendrimer @ 15, 25, 35, 45 and 55 °C (temperature growing bottom to top). 25, 35, 45 and 55 °C curves were shifted vertically by 0.5, 1, 1.5 and 2, respectively, for clarity. For biexponential fit @ 15, 25, 35 and 45 °C, the fifth delay value was arbitrarily chosen as τ_c (see Eq. B.3). The single exponential fit was performed for 55 °C data. The best fit "effective" T_{1Z} with growing temperature were: 179, 201, 241, 278 and 341 ms for "slow" component; and 16, 12, 9, 9 ms (no contribution at 55 °C) for "fast" component (see text for nomenclature). Corresponding constrained multiexponential fit parameters are listed in Table 4.3. Errors of fits are deviations of the points from the lines.

was subtracted from total experimental intensity at $\tau < \tau_c$, and single exponential fit was performed for remaining fast relaxing component (superscript "f"). This procedure is mathematically rigorous if $T_{1Z}^s \gg T_{1Z}^f$ and $T_{1Z}^s \gg \tau_c \gg T_{1Z}^f$ (see equations below).

$$M_\infty(\nu) - M_\tau(\nu) = (M_\infty^s(\nu) - M_0^s(\nu))e^{-\tau/T_{1Z}^s} + (M_\infty^f(\nu) - M_0^f(\nu))e^{-\tau/T_{1Z}^f} \quad [\text{B.1}]$$

$$\ln(M_\infty(\nu) - M_\tau(\nu)) = \ln(M_\infty^s(\nu) - M_0^s(\nu)) - \tau/T_{1Z}^s + \ln\left(1 + \frac{M_\infty^f(\nu) - M_0^f(\nu)}{M_\infty^s(\nu) - M_0^s(\nu)} e^{-\tau\left(\frac{1}{T_{1Z}^f} - \frac{1}{T_{1Z}^s}\right)}\right) \quad [\text{B.2}]$$

$$\tau > \tau_c \Rightarrow \ln(M_\infty(\nu) - M_\tau(\nu)) \cong \ln(M_\infty^s(\nu) - M_0^s(\nu)) - \tau/T_{1Z}^s \quad [\text{B.3}]$$

Although unconstrained biexponential method provides acceptable fit for experimental data, it does not bear much physical sense, except for giving two approximate "effective" relaxation rates at a given frequency point, which would depend on the choice of τ_c . Nevertheless, the fact that such a separation is more "accurate" at some temperatures (e.g. 35 °C and 45 °C for G3) and at some frequency points, ν , (e.g. at the horns of RND_3^+ powder pattern vs. its shoulders) suggests to look for the correlation between the changes in contributions to "effective" relaxation times and the temperature dependent changes in lineshapes. Notice also that the above introduced notion of "fast" and "slow" T_{1Z} components is opposite in meaning to the fast and slow ammonium rotors in that fast rotation will slow down the relaxation.

The observation that effective slope of recovery curves gets slightly smaller for $\tau > \tau_c$ (T_{1Z}^s increases) and slightly larger for $\tau < \tau_c$ (T_{1Z}^f decreases) with increasing temperature prompts for at least two different relaxation mechanisms, which are most likely to arise for chemically distinct deuterons. Here, we may recall that many spectral features overlap at the analyzed frequency, and for two of them experimental data at $45 \text{ kHz} < |\nu| < 110 \text{ kHz}$ confirmed the decreasing relaxation time with the increasing temperature (see Fig. 4.6). Therefore, the observed "effective" behavior of T_{1Z}^f could be ascribed to deuterons of the spacers, while the opposite tendency for T_{1Z}^s might originate from the remaining labels - terminal ammonium deuterons in rigid glass phase or deuterons of amorphous phase undergoing isotropic motion. The increase in T_{1Z}^s has to be ascribed to ammonium deuteron contribution since in the studied temperature range the rate of RND_3^+ rotation is known to be on the fast side of minimum [115, 116], which corresponds to T_{1Z} increasing with the temperature.

Although bearing little physical sense, biexponential fit procedure can speed up relaxation analysis providing easy way for getting first approximation motional rates and eliminating the necessity to invoke multiple time consuming EXPRESS simulations. When

biexponential fit is performed for experimental and simulated data sets for a few τ_c delay values chosen along the middle of recovery curves, the best first approximation T_{1Z} values for a certain spectral feature can be obtained, when resulting "effective" experimental and simulated data anisotropies coincide for as many τ_c 's as possible. According to Eq. B.3, choosing different τ_c correspond to including more or less of "intermediate" T_{1Z} contributions to "fast" or "slow" component. This allows to interactively change T_{1Z} values without reference to motional rate till the "best" biexponential fit is achieved.

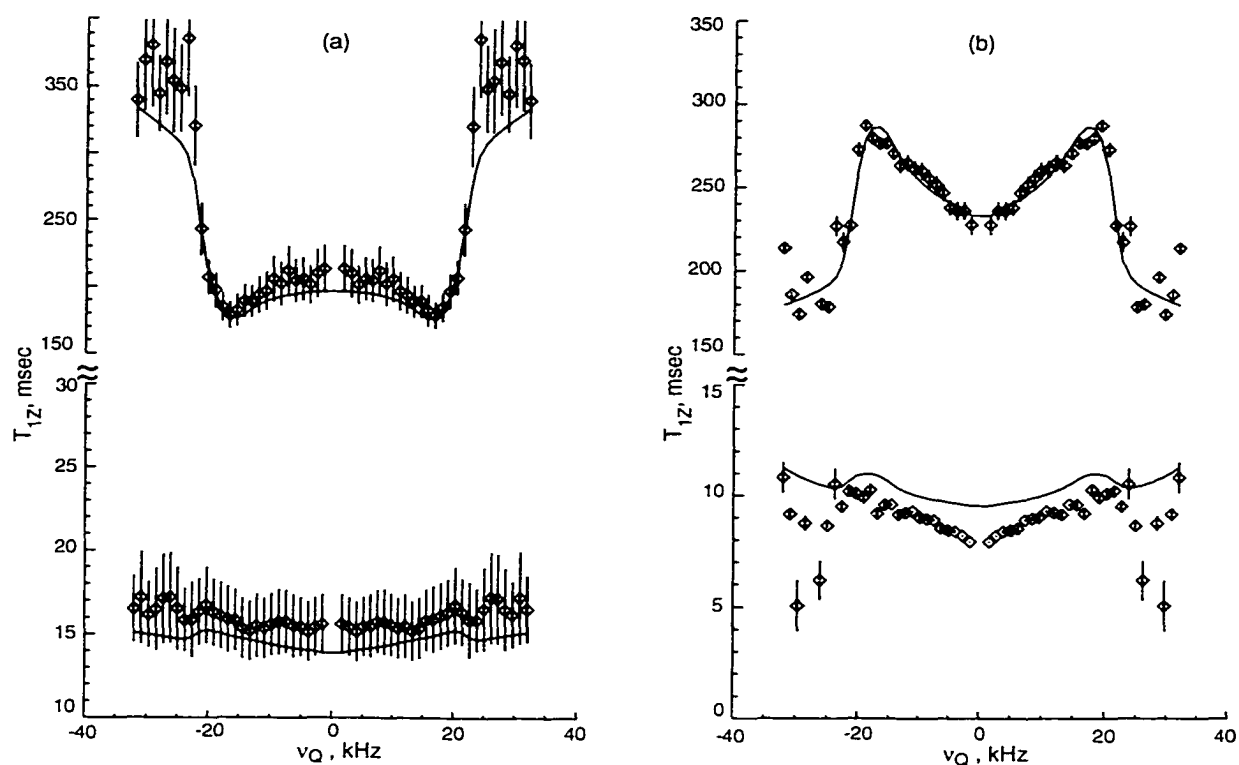


Figure B.2

Unconstrained biexponential fit for experimental (diamonds) and EXPRESS simulated (solid lines) T_{1Z} data for G3 at 15 °C (a) and 45 °C (b). Error bars are shown only for the fit to experimental data and reflect the biexponential fit formalism more than experimental scatter (see Eq. B1). Two "effective" T_{1Z} components are separated by choosing $\tau_c = 100$ ms.

In practice, simulated normalized contributions from underlying powder patterns are first subtracted from normalized experimental data at $\tau = \infty$, to get $M_\infty(\nu)$ for RND_3^+ . Then,

with known $T_{1Z}(\nu)$ for ammonium deuterons from preliminary EXPRESS simulation best fitting the lineshape, Eq. B.3 is used to calculate their $M_\tau(\nu)$ values. Adding back RND_3^+ contribution to the rest of simulated partially relaxed spectra for equally spaced (with required step) frequencies across the region $|\nu| < 45$ kHz, overall T_{1Z} simulation is obtained. Now, performing computerized biexponential fit for 4-5 different τ_c , and shifting $T_{1Z}(\nu)$ up or down by ΔT_{1Z} , the "shift" needed for the best correspondence between experimental and simulated data can be found relatively fast by minimizing the difference between the experimental and simulated T_{1Z}^f and T_{1Z}^s anisotropies in the least squares sense. Then, knowing approximate relationship $\Delta T_{1Z} \propto \Delta k_3$, which holds true in the fast motion limit (valid in the studied temperature range for RND_3^+ deuterons) allows determination of the required increment for the rate constant, Δk_3 , and thus get first approximation k_3 with large savings in CPU time.

In the process of data fitting it was found that at low temperatures for G3 dendrimer the apparent character of "slow" anisotropy is opposite to that at higher temperatures. It is noteworthy that "slow" component anisotropy at 15 °C has the shape of topsy-turvy RND_3^+ powder pattern (Fig. B.2(a)), which is opposite to the single component anisotropy for ammonium deuterons (Fig. 4.3). The reversed character of effective slow component anisotropy arises solely from the contributions of underlying powder patterns, since for 15 °C their T_{1Z} is higher than that of ammonium groups and their contribution to magnetization intensity is relatively high at the shoulders of ammonium powder pattern. On the other hand, at 45 °C "slow" anisotropy in the frequency range of $|\nu| < 45$ kHz is determined predominantly by T_{1Z} of RND_3^+ (relaxation of underlying powder patterns is much faster), Fig. B.2(b). Here, the "effective" anisotropy is the same as obtained from simulation of the single exponential ammonium relaxation governed by the rate of 3-fold jumps, k_3 , around RND_3^+ symmetry axis.

Trying to simultaneously fit the observed "fast" anisotropy, we find that additional contribution from ammonium deuterons has to be taken into account, with order of

magnitude slower rotational rate, to get the correct values and shape of "fast" anisotropy. The first approximation for this rate can be obtained as described above for the "slow" component, but with two fractions of ammonium deuterons and variable ΔT_{1Z}^{sf} . The fraction of slow rotors was found to change with the temperature. Quantitatively, the fraction is best determined looking directly at recovery curves along the lineshape and trying to minimize the error for intermediate delay values.

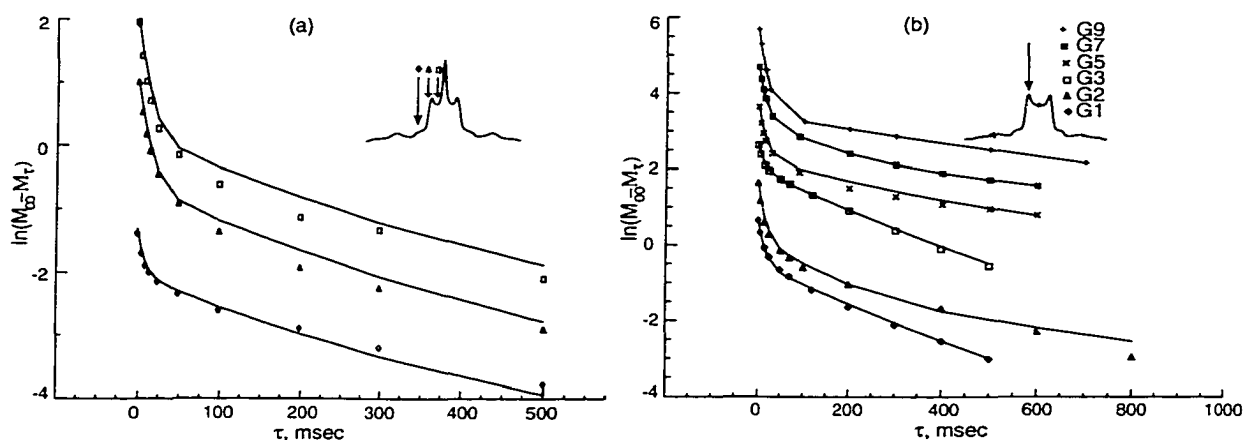


Figure B.3

Experimental recovery curves (symbols) and constrained multiexponential fit results (solid lines) across the spectrum of G2 @ 35 °C (a) and for 16 kHz slice of all studied generations at room temperature (b). Recovery curves for G2 (a) are at 28 kHz (diamonds), 16 kHz (triangles, shifted vertically by 1 for clarity), 5 kHz (squares, shifted vertically by 2). Ambient temperature data for G1, 2, 3, 5, 7 and 9 (b), bottom to top, are vertically shifted by (G-1). The corresponding position of the frequency slice on the lineshape is illustrated by the insert.

Therefore, the complete constrained multiexponential fit procedure in the frequency range of $|v| < 45$ kHz requires the use of three parameters (two k_3 rates and fraction) and constraints for underlying powder patterns and motionally averaged deuterons, contributing Gaussian and Lorentzian components. But, since many recovery curves had to be fit simultaneously, we believe that the three-parameter fit with independent constraints is a reliable procedure for unraveling overlapping anisotropies across ammonium powder pattern. Typical fits obtained this way for G2 dendrimer at the shoulders, horns, and in the

middle of RND_3^+ powder pattern are shown in Figure B.3(a). The fits for all studied generation at room temperature at the horns of ammonium powder pattern (where ammonium deuterons contribute most of intensity) is shown in Figure B.3(b). Considerable deviations between the experimental data and fit would be produced here if only one contribution for ammonium deuterons is taken into account, especially for G3.

The experimental errors for motional rates were determined by changing the rate of one of the components, others being fixed, till noticeable deviation of the fit from recovery curves occurred across experimental lineshape (especially at the frequencies with the best S/N for the component under consideration). The "tweaking" of error bars was done first by the procedure of "effective" biexponential fit described above, and then checked directly on recovery curves from EXPRESS simulations for predetermined approximate rate errors.

Appendix C

Calculation of Trigonometric Sum in Eq. 5.5

$$P(\alpha, \beta, \tau_r, \frac{2k \pm 1}{2n}) = P(\tau_r, \frac{2k \pm 1}{2n}) = \sin^2 \beta \sin 2(\alpha + \frac{\pi(2k \pm 1)}{n}) - 2\sqrt{2} \sin 2\beta \sin(\alpha + \frac{\pi(2k \pm 1)}{n})$$

$$\sum_{k \geq 1}^{n-1} (-1)^k P(\tau_r, \frac{2k \pm 1}{2n}) = \sin^2 \beta \sum_{k \geq 1}^{n-1} (-1)^k \sin 2(\alpha + \frac{\pi(2k \pm 1)}{n}) - 2\sqrt{2} \sin 2\beta \sum_{k \geq 1}^{n-1} (-1)^k \sin(\alpha + \frac{\pi(2k \pm 1)}{n})$$

$$(-1)^k = \exp(ik\pi), \quad \sin y = \frac{1}{2i}(\exp(iy) - \exp(-iy)), \quad \cos(y) = \frac{1}{2}(\exp(iy) + \exp(-iy)),$$

$$\sum_{k \geq 1}^{n-1} \exp(\pm iy) = \frac{\exp(\pm iy) - \exp(\pm iny)}{1 - \exp(\pm iy)} = \frac{\exp(\pm iy / 2) - \exp(\pm i(n+1 / 2)y)}{\exp(\mp iy / 2) - \exp(\pm iy / 2)}$$

$$\sum_{k \geq 1}^{n-1} (-1)^k \sin 2(\alpha + \frac{\pi(2k+1)}{n}) = 2 \cos^{-1}(\frac{2\pi}{n}) \left[(-1)^{n-1} \sin 2\alpha - \sin 2(\alpha + \frac{2\pi}{n}) \right]$$

$$\sum_{k \geq 1}^{n-1} (-1)^k \sin 2(\alpha + \frac{\pi(2k-1)}{n}) = 2 \cos^{-1}(\frac{2\pi}{n}) \left[(-1)^{n-1} \sin 2(\alpha - \frac{2\pi}{n}) - \sin 2\alpha \right]$$

$$\sum_{k \geq 1}^{n-1} (-1)^k \sin(\alpha + \frac{\pi(2k+1)}{n}) = 2 \cos^{-1}(\frac{\pi}{n}) \left[(-1)^{n-1} \sin \alpha - \sin(\alpha + \frac{2\pi}{n}) \right]$$

$$\sum_{k \geq 1}^{n-1} (-1)^k \sin(\alpha + \frac{\pi(2k-1)}{n}) = 2 \cos^{-1}(\frac{\pi}{n}) \left[(-1)^{n-1} \sin(\alpha - \frac{2\pi}{n}) - \sin \alpha \right]$$

$$\sum_{k \geq 1}^{n-1} (-1)^k \left(P(\tau_r, \frac{2k+1}{2n}) - P(\tau_r, \frac{2k-1}{2n}) \right) = 2 \cos^{-1}(\frac{2\pi}{n}) \sin^2 \beta \left[\begin{array}{l} ((-1)^{n-1} + 1) \sin 2\alpha \\ -\sin 2(\alpha + \frac{2\pi}{n}) + (-1)^n \\ \times \sin 2(\alpha - \frac{2\pi}{n}) \end{array} \right]$$

$$- \sqrt{2} \cos^{-1}(\frac{\pi}{n}) \sin 2\beta \left[\begin{array}{l} ((-1)^{n-1} + 1) \sin \alpha \\ -\sin(\alpha + \frac{2\pi}{n}) + (-1)^n \\ \times \sin(\alpha - \frac{2\pi}{n}) \end{array} \right]$$

Bibliography

- [1] G. R. Newkome, C. N. Moorefield, and F. Voegtle, *Dendritic Molecules. Concepts - Synthesis - Perspectives* (VCH Publishers, Inc. NY, 1996).
- [2] C. J. Hawker and J. M. J. Frechet, in *New Methods of Polymer Synthesis*, edited by J. R. Ebdon and e. al. (UK, Glasgow, 1995), p. 290.
- [3] S. Uppuluri, D. A. Tomalia, and P. R. Dvornic, in *Polymeric Materials Encyclopedia*, edited by J. C. Salamone (CRC Press, New York, 1996), Vol. 3, p. 1824.
- [4] D. I. Malyarenko, R. L. Vold, and G. L. Hoatson, *Macromolecules* **33**, 1268 (2000).
- [5] D. I. Malyarenko, R. L. Vold, and G. L. Hoatson, *Macromolecules* **33**, 7508 (2000).
- [6] D. I. Malyarenko, R. L. Vold, and G. L. Hoatson, *Macromolecules*, submitted (2001).
- [7] B. R. Matthews and G. Holan, *Antiviral Polyamidoamine Dendrimers*, AU Appl 94/6,239 (1994) 47 pp.
- [8] S. W. Poxon, P. M. Mitchell, E. Liang, *et al.*, *Drug Delivery* **3**, 255 (1996).
- [9] J. S. Choi, D. K. Joo, C. H. Kim, *et al.*, *J. Am. Chem. Soc.* **122**, 474 (2000).
- [10] M. Enomoto and T. Aida, *J. Am. Chem. Soc.* **121**, 874 (1999).
- [11] P. Welch and M. Muthukumar, *Macromolecules* **33**, 6159 (2000).
- [12] D. A. Tomalia, *Langmuir* **13**, 3136 (1997).
- [13] M. Miyazaki, K. Torigoe, and K. Esumi, *Langmuir* **16**, 1522 (2000).
- [14] G. Nisato, R. Ivkov, and E. J. Amis, *Macromolecules* **33**, 4172 (2000).
- [15] S. Stechemesser and W. Eimer, *Macromolecules* **30**, 2204 (1997).

- [16] A. Topp, B. J. Bauer, D. A. Tomalia, *et al.*, *Macromolecules* **32**, 7232 (1999).
- [17] P.R.L. Melenfant, M. Jayaraman, and J. M. J. Frechet, *Chem. Mater.* **11**, 3420 (1999).
- [18] A. L. Hurley and D. L. Mohler, *Org. Lett.* **2**, 2745 (2000).
- [19] F. Grohn, B. J. Bauer, A. Y. Akpalu, *et al.*, *Macromolecules* **33**, 6042 (2000).
- [20] K. Esumi, A. Suzuki, A. Yamahira, *et al.*, *Langmuir* **16** (2000).
- [21] J. W. Kriesel and T. D. Tilley, *Chem. Mater.* **11**, 1190 (1999).
- [22] F. M. Ottaviani, P. Favuzza, M. Bigazzi, *et al.*, *Langmuir* **16**, 7368 (2000).
- [23] S. Uppuluri, S. E. Keinath, D. A. Tomalia, *et al.*, *Macromolecules* **31**, 4498 (1998).
- [24] S. Uppuluri, F. A. Morrison, and P. R. Dvornic, *Macromolecules* **33**, 2551 (2000).
- [25] C. L. Jackson, H. D. Chanzy, F. P. Booy, *et al.*, *Macromolecules* **31**, 6259 (1998).
- [26] J. Li, L. T. Piehler, D. Qin, *et al.*, *Langmuir* **16**, 5613 (2000).
- [27] S. Uppuluri, *Ph.D. Dissertation, Michigan Technological University*, (1997).
- [28] D. A. Tomalia, H. Baker, J. Dewald, *et al.*, *Macromolecules* **19**, 2486 (1986).
- [29] S. Jockusch, J. Ramirez, K. Sanghvi, *et al.*, *Macromolecules* **32**, 4419 (1999).
- [30] D. A. Tomalia and H. D. Durst, in *Topics in Current Chemistry*, edited by E. Weber (Springer Verlag, Berlin, 1993), Vol. 165, p. 193.
- [31] M. Karplus, *Physica* **263**, 389 (1999).
- [32] Y. Sayed-Sweet, D. M. Hedstrand, R. Spinder, *et al.*, *J. Mater. Chem.* **7**, 1199 (1997).
- [33] E. C. Wiener, M. W. Brechbiel, H. Brothers, *et al.*, *Magn. Res. Med.* **31**, 1 (1994).
- [34] V. V. Tsukruk, F. Rinderspacher, and V. N. Bliznyuk, *Langmuir* **13**, 2171 (1997).
- [35] A. D. Meltzer, D. A. Tirrell, A. A. Jones, *et al.*, *Macromolecules* **25**, 4549 (1992).
- [36] A. D. Meltzer, D. A. Tirrell, A. A. Jones, *et al.*, *Macromolecules* **25**, 4541 (1992).
- [37] A. M. Naylor and W. A. I. Goddard, *J. Am. Chem. Soc.* **111**, 2339 (1989).
- [38] E. J. Amis, A. Topp, B. J. Bauer, *et al.*, *Polym. Mater. Sci. Eng.* **77**, 183 (1997).
- [39] T. J. Prosa, B. J. Bauer, E. J. Amis, *et al.*, *J. Polym. Sci., Part B: Polym. Phys.* **35**, 2913 (1997).
- [40] R. L. Lescanec and M. Muthukumar, *Macromolecules* **23**, 2280 (1990).

- [41] P. G. De Gennes and H. Hervet, *J. Physique - Lett.* **44**, 351 (1983).
- [42] M. C. Moreno-Bondi, G. Orellana, N. J. Turro, *et al.*, *Macromolecules* **23**, 910 (1990).
- [43] F. M. Ottaviani, S. Bossmann, N. J. Turro, *et al.*, *J. Am. Chem. Soc.* **116**, 661 (1994).
- [44] F. M. Ottaviani, F. Montani, N. J. Turro, *et al.*, *J. Phys. Chem. B* **101**, 158 (1997).
- [45] K. R. Gopidas, A. R. Leheny, G. Caminati, *et al.*, *J. Am. Chem. Soc.* **113**, 7335 (1991).
- [46] Y. Gao, K. I. Langley, and F. E. Karasz, *Macromolecules* **25**, 4902 (1992).
- [47] D. E. Valachovic, *Polym. Mater. Sci. Eng.* **77**, 230 (1997).
- [48] A. Topp, B. J. Bauer, T. J. Prosa, *et al.*, *Macromolecules* **32**, 8923 (1999).
- [49] A. Topp, B. J. Bauer, J. W. Klimash, *et al.*, *Macromolecules* **32**, 7226 (1999).
- [50] H. W. Spiess, *Coll. Polym. Sci.* **261**, 193 (1983).
- [51] R. R. Vold and R. L. Vold, *Adv. Magn. Opt. Reson.* **16**, 85 (1991).
- [52] G. L. Hoatson and R. L. Vold, *NMR: Basic Principles & Progress*, (B. Bluemich, Guest Editor) **32**, 1 (1994).
- [53] M. Usha, G. and R. J. Wittebort, *J. Mol. Biol.* **208**, 669 (1989).
- [54] M. G. Usha, W. L. Peticolas, and R. J. Wittebort, *Biochemistry* **30**, 3955 (1991).
- [55] R. L. Vold, G. L. Hoatson, and T. Y. Tse, *Chem. Phys. Lett.* **263**, 271 (1996).
- [56] J. H. Kristensen, G. L. Hoatson, and R. L. Vold, *Solid State NMR* **13**, 1 (1998).
- [57] K. L. Wooley, C. A. Klug, K. Tasaki, *et al.*, *J. Am. Chem. Soc.* **119**, 53 (1997).
- [58] H.-M. Kao, A. D. Stefanescu, K. L. Wooley, *et al.*, *Macromolecules* **33**, 6214 (2000).
- [59] Dendritech, Inc. (Michigan Molecular Institute, www.mmi.org/mmi/dendritech/pamam.html)
- [60] M. H. P. van Genderen, M. W. P. L. Baars, C. Elissan-Roman, *et al.*, *Polym. Mater. Sci. Eng.* **73**, 336 (1995).
- [61] C. P. Slichter, *Principles of Magnetic Resonance* (Springer-Verlag, New York, 1990).
- [62] W. J. Thompson, *Angular Momentum* (John Wiley and Sons, New York, 1994).
- [63] R. S. Macomber, in *A Complete Introduction to Modern NMR Spectroscopy* (John Wiley & Sons, New York, 1998), p. 382.

- [64] J. J. Sakurai, *Modern Quantum Mechanics* (Addison-Wesley, London, 1985).
- [65] D. M. Brink and G. R. Satchler, *Angular Momentum* (Oxford University Press, Oxford, 1993).
- [66] A. G. Marshall and F. R. Verdun, *Fourier Transforms in NMR, Optical, and Mass Spectrometry* (Elsevier, New York, 1990).
- [67] T. Y. Tse, *Ph.D. Dissertation, College of William and Mary*, (1995).
- [68] E. Fukushima and S. B. W. Roeder, *Experimental Pulse NMR. A Nuts and Bolts Approach* (Addison-Wesley, London, 1981).
- [69] Heater wires, (ARI Industries, www.ariindustries.com).
- [70] U. Haeberlen, *High Resolution NMR in Solids: Selective Averaging* (Academic Press, New York, 1976).
- [71] A. Abragam, *Principles of Nuclear Magnetism* (Clarendon Press, Oxford, 1961).
- [72] S. J. Varner, R. L. Vold, and G. L. Hoatson, *J. Magn. Reson. A* **123**, 72 (1996).
- [73] L. D. Landau and E. M. Lifshitz, *Electrodynamics of Continuous Media* (Oxford, New York, 1984).
- [74] N. Bloembergen, E. M. Purcell, and R. V. Pound, *Phys. Rev.* **102**, 679 (1948).
- [75] E. O. Stejskal and J. D. Memory, *High Resolution NMR in the Solid State* (Oxford, 1994).
- [76] M. M. Maricq and J. S. Waugh, *J. Chem. Phys.* **70**, 3300 (1979).
- [77] T. Gullion and J. Schaefer, *Adv. Magn. Opt. Reson.* **13**, 57 (1989).
- [78] T. M. Duncan, *A Compilation of Chemical Shift Anisotropies* (The Farragut Press, Chicago, 1990).
- [79] J. H. Kristensen, H. Bildsoe, H. J. Jakobsen, *et al.*, *J. Magn. Reson.* **100**, 437 (1992).
- [80] A. G. Redfield, *Adv. Magn. Reson.* **1**, 1 (1965).
- [81] R. R. Ernst, G. Bodenhausen, and A. Wokaun, *Principles of Nuclear Magnetic Resonance in One and Two Dimensions* (Oxford, 1987).
- [82] M. J. Brown, *Ph.D. Dissertation, College of William and Mary*, (1997).

- [83] J. H. Kristensen, *Ph.D. Dissertation, University of Aarhus, Denmark*, (1995).
- [84] S. J. Varner, *Ph. D. Dissertation, College of William and Mary*, (1999).
- [85] J. H. Davis, K. R. Jeffrey, M. Bloom, *et al.*, *Chem. Phys. Lett.* **42**, 390 (1976).
- [86] N. Boden, L. D. Clark, S. M. Hanlon, *et al.*, *Faraday Symp. Chem. Soc.* **1979**, 109 (1978).
- [87] M. Bloom, J. H. Davis, and M. I. Valic, *Can. J. Chem.* **58**, 1510 (1980).
- [88] S. Wimperis and G. Bodenhausen, *Chem. Phys. Lett.* **132**, 194 (1986).
- [89] S. Wimperis, *J. Magn. Reson.* **86**, 46 (1990).
- [90] G. L. Hoatson, *J. Magn. Reson.* **94**, 152 (1991).
- [91] S. R. Hartman and E. L. Hahn, *Phys. Rev.* **128**, 2042 (1962).
- [92] T. Gullion, *Magn. Res. Rev.* **17**, 83 (1997).
- [93] A. W. Hing and J. Schaefer, *Biochemistry* **32**, 7593 (1993).
- [94] W. H. Press, B. P. Flannery, S. A. Teukolsky, *et al.*, *Numerical Recipes* (Cambridge University Press, Cambridge, 1986).
- [95] F. J. Harris, *Proc. IEEE* **66**, 51 (1978).
- [96] J. M. Goetz and J. Schaefer, *J. Magn. Reson.* **127**, 147 (1997).
- [97] F. G. Vogt, D. J. Aurentz, and K. T. Mueller, *Mol. Phys.* **95**, 907 (1998).
- [98] A. Schmidt, R. A. McKay, and J. Schaefer, *J. Magn. Reson.* **96**, 644 (1992).
- [99] T. Gullion, *J. Magn. Res.* **139**, 402 (1999).
- [100] I. Sack, A. Goldbourt, S. Vega, *et al.*, *J. Magn. Res.* **138**, 54 (1999).
- [101] I. Sack and S. Vega, *J. Magn. Res.* **145**, 52 (2000).
- [102] T. Gullion, *J. Magn. Res.* **146**, 220 (2000).
- [103] S. Uppuluri, D.A. Tomalia, and P.R. Dvornic, *Poly. Mater. Sci. Eng.* **77**, 116 (1997).
- [104] R. Gerald, T. Bernhard, U. Haeberlen, *et al.*, *J. Am. Chem. Soc.* **115**, 777 (1993).
- [105] R. J. Wittebort, E. T. Olejniczak, and R. G. Griffin, *J. Chem. Phys.* **86**, 5411 (1987).
- [106] S. Sheiner, in *Hydrogen Bonding. A Theoretical perspective.* (Oxford University Press, New York, 1997), p. 375.

- [107] P. Schuster, G. Zundel, and C. Sandorfy, *The Hydrogen Bond* (North-Holland Publishing Company, New York, 1976).
- [108] M. J. Hunt and A. L. Mackay, *J. Magn. Reson.* **22**, 295 (1976).
- [109] M. J. Hunt and A. L. Mackay, *J. Magn. Reson.* **15**, 402 (1973).
- [110] P. Vaughan and J. Donohue, *Acta Cryst.* **5**, 530 (1952).
- [111] T. Chiba, *Bull. Chem. Soc. Jpn.* **38**, 259 (1965).
- [112] N. J. Heaton, R. L. Vold, and R. R. Vold, *J. Am. Chem. Soc.* **111**, 3211 (1989).
- [113] K. D. M. Harris and J. M. Thomas, *J. Chem. Soc. Faraday Trans.* **86**, 2985 (1990).
- [114] LiWang, *J. Magn. Res.* **127**, 54 (1997).
- [115] M. L. H. Gruwel and R. E. Wasylshen, *Z. Naturforsch.* **46A**, 691 (1991).
- [116] M. L. H. Gruwel and R. E. Wasylshen, *Z. Naturforsch.* **47A**, 1073 (1992).
- [117] C. J. Poucher, *The Aldrich Library of ¹³C and ¹H FT NMR spectra* (Aldrich Chemical Company, Inc., U.S.A., 1993).
- [118] D. R. Lide, *Handbook of Chemistry and Physics* (CRC Press, New York, 1997), p.9.
- [119] A.W. Bosman, M.J. Bruining, H. Kooijman, *et al.*, *J. Am. Chem. Soc.* **120**, 8547 (1998).
- [120] M. L. H. Gruwel and R. E. Wasylshen, *Z. Naturforsch., Teil A* **45A**, 55 (1989).
- [121] M. Wehrle, G. P. Hellmann, and H. W. Spiess, *Coll. Polym. Sci.* **265**, 815 (1987).
- [122] T. M. Connor, *Trans. Faraday. Soc.* **60**, 1574 (1964).
- [123] N. J. Heaton, R. R. Vold, and R. L. Vold, *J. Chem. Phys.* **91**, 56 (1989).
- [124] F. A. Bovey and P. A. Mirau, *NMR of Polymers* (Academic Press, San Diego, 1996).
- [125] R. G. Griffin, K. Beshah, R. Ebelhauser, *et al.*, *NATO ASI C228*, 81 (1988).
- [126] R. D. O'Conner, E. J. Ginsburg, and F. D. Blum, *J. Chem. Phys.* **112**, 7247 (2000).
- [127] J. Tang, L. Sterna, and A. Pines, *J. Magn. Reson.* **41**, 389 (1980).
- [128] H.-D. Jakubke and H. Jechkeit, *Concise Encyclopedia of Chemistry* (Walter de Gruyter, Berlin, New York, 1994), p. 510.
- [129] H. Ishida, R. Ikeda, and D. Nakamura, *Bull. Chem. Soc. Japan* **55**, 3116 (1982).

- [130] H. Ishida, R. Ikeda, and D. Nakamura, *J. Phys. Chem.* **86**, 1003 (1982).
- [131] H. Ishida, R. Ikeda, and D. Nakamura, *Bull. Chem. Soc. Japan* **59**, 915 (1986).
- [132] M. Andreis, J. L. Koenig, M. Gupta, *et al.*, *J. Poly. Sci.: Part B* **33**, 1449 (1995).
- [133] C. G. Johnson and L. J. Mathias, *Polymer* **35**, 66 (1994).
- [134] J. R. Garbow and C. A. McWherter, *J. Am. Chem. Soc.* **115**, 238 (1993).
- [135] A. Naito, K. Nishimura, S. Tuzi, *et al.*, *Chem. Phys. Lett.* **229**, 506 (1994).
- [136] G. R. Marshall, D. D. Beusen, K. Kociolek, *et al.*, *J. Am. Chem. Soc.* **112**, 963 (1990).
- [137] T. Gullion, *Concepts in Magnetic Resonance* **10**, 277 (1998).
- [138] D. J. Mitchell and J. N. S. Evans, *Chem. Phys. Letters* **292**, 656 (1998).
- [139] A. K. Mehta, D. J. Hirsh, N. Oyler, *et al.*, *J. Magn. Reson.* **145**, 156 (2000).
- [140] Young Pan, Terry Gullion, and J. Schaefer, *J. Magn. Reson.* **90**, 330 (1990).
- [141] L. M. McDowell, C. A. Klug, D. D. Beusen, *et al.*, *Biochemistry* **35**, 5395 (1996).
- [142] J. R. Garbow and T. Gullion, *J. Magn. Reson.* **95**, 442 (1995).
- [143] T. Gullion, D. B. Baker, and M. S. Conradi, *J. Magn. Reson.* **89**, 479 (1990).
- [144] T. Gullion, personal communication (Prof. of Chemistry, WVU, Morgantown, 2000).
- [145] D. L. VanderHart, W. L. Earl, and A. N. Garroway, *J. Magn. Reson.* **44**, 361 (1981).
- [146] A. E. Bennett, C. M. Rienstra, M. Auger, *et al.*, *J. Chem. Phys.* **103**, 6951 (1995).
- [147] B. M. Fung, A. K. Khitrin, and K. Ermolaev, *J. Magn. Reson.* **142**, 97 (2000).
- [148] K. T. Mueller, *J. Magn. Reson., A* **113**, 81 (1995).
- [149] K. T. Mueller, T. P. Jarvie, D. J. Aurentz, *et al.*, *Chem. Phys. Lett.* **242**, 535 (1995).
- [150] J. Honerkamp and J. Weese, *Cont. Mech. Therm.* **2**, 17 (1990).
- [151] J. Weese, *Comp. Phys. Com.* **69**, 99 (1992).
- [152] P. J. Flory, *Principles of Polymer Chemistry* (Cornell University Press, Ithaca, 1953).
- [153] D. Bebout, personal communication (Prof. of Biochemistry, The College of William & Mary, Williamsburg, 2000).
- [154] M. E. Rose, *Elementary Theory of Angular Momentum* (Wiley & Sons, New York, 1957).

Vita

Dariya Ivanovna Malyarenko

The author was born on July 4, 1972, in Kiev, Ukraine. Graduated from Kiev High School #153 with Honors, June 1989, B.S. Honors, Kiev State Taras Shevchenko University (KSU), 1994. Enrolled in part time graduate school (KSU, Molecular Physics) and worked as engineer-physicist (Physics of Liquids Lab) and translator (Svitanok Enterprises), 1994-1996. The author entered the graduate program at William and Mary in 1996, and received M.S. in Applied Science, 1998. Completed Ph.D. program under scientific supervision of Dr. Robert Vold (Polymer Science, Solid State NMR), June 2001.